**NUREG/CR-0993**
**LA-7968-PR**
Progress Report

# Nuclear Reactor Safety

## Quarterly Progress Report

## April 1—June 30, 1979



University of California

LOS ALAMOS SCIENTIFIC LABORATORY
Post Office Box 1663 Los Alamos, New Mexico 87545

The four most recent reports in this series, unclassified, are NUREG/CR-0385 LA-7481-PR, NUREG/CR-0522 LA-7567-PR, NUREG/CR-0762 LA-7769-PR, and NUREG/CR-0868 LA-7867-PR.

This report was not edited by the Technical Information staff.

Work supported by the US Department of Energy, Division of Reactor Development and Demonstration.

NUREG/CR-0993
LA-7968-PR
Progress Report
R4, R7, and R8

# Nuclear Reactor Safety

## Quarterly Progress Report

## April 1—June 30, 1979

Compiled by

James F. Jackson
Michael G. Stevenson

Los Alamos Scientific Laboratory
Q (Energy) Division
William G. Davey, Division Leader
William L. Kirk, Alternate Division Leader

Manuscript submitted: August 1979
Date published: August 1979

Prepared for
Office of Nuclear Regulatory Research
Division of Reactor Safety Research
Office of Nuclear Reactor Regulation
Division of Systems Safety
US Nuclear Regulatory Commission
Washington, DC 20555

NRC FIN Nos. 00354, AL022, AL023, AL009, A7015, A7013, A7016, B5189, A7014, A7044, A7046, A7049, A7053, A7105, A7112, A7111

UNITED STATES
DEPARTMENT OF ENERGY
CONTRACT W-7405-ENG. 36

CONTENTS

FIGURES

FIGURES (cont)

TABLES

## ABSTRACT

Blind pretest predictions of the nuclear LOFT test L2-3 were performed with the TRAC code. A recent version of TRAC that incorporated the Iloeje minimum film boiling correlation has a good prediction of the peak cladding temperature history measured during the test. A TRAC model of the Three Mile Island nuclear plant was developed and a calculation of the early stages of the recent incident was initiated. Several studies were completed in support of the multinational 2D/3D research program. These included evaluating the need for an extra steam supply for the Slab Core Test Facility, and an evaluation of the Rouths storage tank for the Upper Plenum Test Facility. A pretest prediction of the Cylindrical Core Test Facility Shakedown Test No. 4 was also completed.

A SIMMER-II analysis of the transition phase behavior of a single LMFBR subassembly was completed. The results compared well with a similar SAS3A calculation and will serve as a base case for future parametric calculations. Recent work on the damage potential of energetic excursions in LMFBRs was compiled into a comprehensive evaluation. Significant progress was made in the area of SIMMER experimental verification. This included additional analyses of water flashing experiments, continued development of the USD experiment at LASL, and a sensitivity study to evaluate the consistency between SIMMER predictions and an SRI experiment that simulated HCDA conditions. Finally, a number of improvements were made to the equation-of-state modeling in SIMMER.

In the gas-cooled reactor area, work continued in support of the final series of HTGR core block seismic tests to be performed at the White Sands Missile Range. A report was prepared summarizing the results from the HTGR fuel particle heatup and failure experiments. This included an extensive statistical analysis of the results. Progress continued on the design, construction, and testing of the GCFR low-power safety experimental facility.

Modeling procedure guidelines for nuclear power plant containment subcompartment analyses were developed. Procedures for determining the bulk containment conditions following a steam line break (for use in equipment qualification) were evaluated and several improvements recommended.

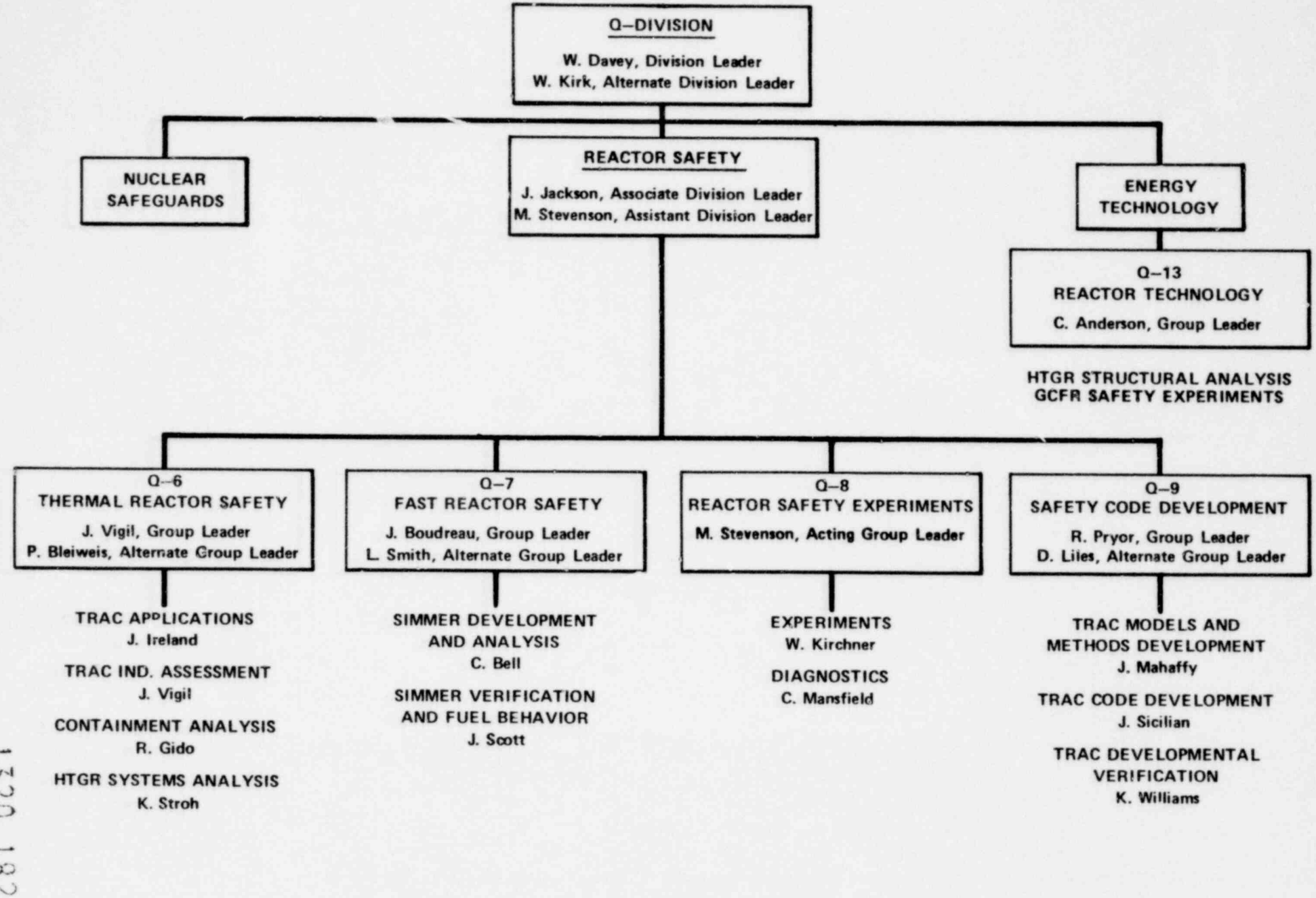
Q–DIVISION
W. Davey, Division Leader
W. Kirk, Alternate Division Leader
NUCLEAR SAFEGUARDS
REACTOR SAFETY
J. Jackson, Associate Division Leader
M. Stevenson, Assistant Division Leader
ENERGY TECHNOLOGY
Q–13
REACTOR TECHNOLOGY
C. Anderson, Group Leader
HTGR STRUCTURAL ANALYSIS
GCFR SAFETY EXPERIMENTS
Q–6
THERMAL REACTOR SAFETY
J. Vigil, Group Leader
P. Bleiweis, Alternate Group Leader
Q–7
FAST REACTOR SAFETY
J. Boudreau, Group Leader
L. Smith, Alternate Group Leader
Q–8
REACTOR SAFETY EXPERIMENTS
M. Stevenson, Acting Group Leader
Q–9
SAFETY CODE DEVELOPMENT
R. Pryor, Group Leader
D. Liles, Alternate Group Leader
TRAC APPLICATIONS
J. Ireland
TRAC IND. ASSESSMENT
J. Vigil
CONTAINMENT ANALYSIS
R. Gido
HTGR SYSTEMS ANALYSIS
K. Stroh
SIMMER DEVELOPMENT AND ANALYSIS
C. Bell
SIMMER VERIFICATION AND FUEL BEHAVIOR
J. Scott
EXPERIMENTS
W. Kirchner
DIAGNOSTICS
C. Mansfield
TRAC MODELS AND METHODS DEVELOPMENT
J. Mahaffy
TRAC CODE DEVELOPMENT
J. Sicilian
TRAC DEVELOPMENTAL VERIFICATION
K. Williams

# NUCLEAR REACTOR SAFETY

Compiled by
James F. Jackson
and
Michael G. Stevenson

## I. INTRODUCTION

(J. F. Jackson and M. G. Stevenson, Q-DO)

This quarterly report summarizes technical progress from a continuing nuclear reactor safety research program conducted at the Los Alamos Scientific Laboratory (LASL). The reporting period is from April 1 to June 30, 1979. This research effort concentrates on providing an accurate and detailed understanding of the response of nuclear reactor systems to a broad range of postulated accident conditions. The bulk of the funding is provided by the U.S. Nuclear Regulatory Commission (NRC), with part of the advanced reactor work funded by the U.S. Department of Energy (DOE).

The report is mainly organized according to reactor type. Major sections deal with Light-Water Reactors (LWRs), Liquid Metal Fast Breeder Reactors (LMFBRs), High-Temperature Gas-Cooled Reactors (HTGRs), and Gas-Cooled Fast Reactors (GCFRs).

The research discussed was performed by several technical divisons and groups within LASL. The names and group affiliations of the individual staff members responsible for the work are given at the beginning of each section. Most of the work was performed in the reactor safety portion of the Energy (Q) Division. An organization chart showing the Q-Division groups with major reactor safety activities is presented on the facing page. Other divisions contributing to the program were the Theoretical (T) Division, Computer Science and Services (C) Division, the Systems, Analysis, and Assessment (S) Division, and the Dynamic Testing (M) Division.

## II. LWR SAFETY RESEARCH

(J. F. Jackson, Q-DO)

Five major projects in LASL's light-water reactor safety research program are reported in this section. The first is the development and testing against experimental data of the Transient Reactor Analysis Code (TRAC). The second concentrates on the application of TRAC to the multinational 2D/3D LWR safety research program. The third area focuses on the independent assessment of the TRAC code by performing blind predictions of pertinent experiments. The fourth project involves component code development and thermal-hydraulic research in key LWR safety problem areas. The fifth, and final effort, is an experimental program that supports model development activities and provides advanced instrumentation for reactor safety experiments.

### A. TRAC Code Development and Assessment

(R. J. Pryor, Q-9)

TRAC is an advanced, best estimate computer program for the analysis of postulated accidents in LWRs. It features a nonhomogeneous, nonequilibrium multidimensional fluid dynamics treatment; detailed heat transfer and reflood models; and a flow-regime-dependent constitutive equation package to describe the basic physical phenomena that occur under accident conditions. It calculates initial steady-state conditions and complete accident sequences.

The first version of TRAC, called TRAC-P1, is primarily directed toward loss-of-coolant accidents (LOCAs) in pressurized water reactors (PWRs). A refinement of this version, called TRAC-P1A, was released to the National Energy Software Center (NESC) in March, 1979. An improved version, designated TRAC-P1A/MOD1, will be released in December and will contain improved reflood and heat transfer models. A fast-running version called TRAC-P2 will be released in March of next year. TRAC-P2 will be capable of treating noncondensible gases and a wider range of accident types, including transients such as the Three Mile Island incident. TRAC-P1B will be

released late next year and will provide detailed analyses of Anticipated Transients Without Scram (ATWS), Reactivity Insertion Accidents (RIAs), and operational transients.

As part of a closely coupled code assessment effort, TRAC is being applied to a broad range of water reactor safety experiments. These experiments are designed to study separate and integral effects that occur during all accident phases. TRAC posttest calculations are compared with experimental results to evaluate the thermal-hydraulic models in the code. Pretest calculations are made to test the predictive capability of TRAC. Both types of analyses are in progress and will continue to receive increased emphasis.

During the past quarter, significant progress was made in the area of adding a noncondensible gas field, and in improving the reflood and heat transfer models in TRAC. A pretest prediction of LOFT test L2-3 was made and a draft of Volume II of the TRAC manual describing the results of the assessment calculations was completed. Details of these efforts and other work follow.

## 1. Hydrodynamics and Heat Transfer Methods

(D. R. Liles, Q-9)

A number of modifications to TRAC-P1A have been implemented. The wall heat transfer correlations have been extensively improved. A new quench front model is being developed and an effort designed to implement a gap conductance code in TRAC was initiated. A noncondensible gas field has been added to the three-dimensional vessel model and testing has begun. A one-dimensional, two-fluid water packing algorithm has been implemented in the preliminary version of TRAC-P2.

### a. Gap Conductance Treatment

(D. A. Mandell, Q-9)

At a meeting held in Washington, DC on April 26, among LASL, Idaho National Engineering Laboratory (INEL), and the NRC, it was decided that the FRAP-T5 code would be modified by INEL so that it could run at LASL and be incorporated into TRAC. (The standard FRAP-T codes cannot be run at LASL due to loader problems.) This work is in progress. It was also decided that the FRAPCON code

would be used for the steady-state gap conductance calculations.[1] This code has been received at LASL and is presently being implemented on the LASL computer system.

b. Improved Heat Transfer Correlations

(D. A. Mandell, Q-9)

Since TRAC-P1A was released, various organizations have run problems, often nonreactor situations, that cover a broader range of heat transfer conditions than had been previously examined. These TRAC runs have indicated some errors and needed model improvements in HTCOR and associated heat transfer subroutines. The corrections are discussed in the TRAC Newsletter.[2] Model improvements for the minimum stable film boiling temperature ($T_{min}$),[3] for the critical heat flux (CHF), and for various heat transfer coefficient correlations are being implemented.

In Ref. 3 it was shown that TRAC with the Iloeje $T_{min}$ correlation predicts the LOFT L2-2 data better than TRAC-P1A. It was suggested during the Denver Heat Transfer Workshop[4] that in order to further qualify the Iloeje correlation, other tests should be examined. A TRAC input deck for the General Electric (GE) Blowdown Heat Transfer (BDHT) facility has been obtained from GE and a 30 s transient run has been made. This run indicated that improved noding may be required, and discussions are being held in order to produce an optimum input deck.[5] Runs with TRAC-P1A and TRAC with the Iloeje correlation will be made as soon as a qualified deck is available.

c. Improved Treatment of Water Packing

(S. B. Woodruff, Q-9)

Logic for detection and prevention of water packing was incorporated into the two-fluid, one-dimensional hydrodynamics. To facilitate this implementation, two new flags were added to indicate packing (or stretching) on the left or right face of a hydrodynamic cell. The network solution procedure was also altered to account for water packing at component boundaries in such a way that packing adjustments in adjacent components occur automatically.

## 1. An Improved TRAC Quench Front Model

(F. L. Addessio and R. J. Pryor, Q-9)

The reflood phase of a postulated LOCA is characterized by a sequence of heat transfer and two-phase flow regimes advancing through the reactor vessel. An understanding of the surface rewetting phenomena is essential for the prediction of fuel rod cladding temperatures during transients. To properly predict these temperatures, an adequate numerical technique is necessary to model the dramatic gradients characteristic of the quench front (QF) motion. For this reason, an improved two-dimensional heat transfer model is being introduced into TRAC.

The leading-edge of the quenched region associated with the rewetting phenomenon during the reflood phase of a LOCA is characterized by large variations in rod surface temperatures and heat transfer coefficients within small axial distances ($\Delta z \sim 1$ mm).[6] At times, the advancement of the front is primarily controlled by axial heat conduction from the dry region ahead of the QF to the wetted region behind the advancing film. This heat is removed by violent nucleate boiling (sputtering) at the leading edge of the front. Although the heat removed ahead of the wetting front is small because of the small heat transfer coefficients characteristic of a film boiling region, it is not insignificant. Indeed, the precursory cooling of the rod associated with heat transfer to the droplets entrained in the rising vapor field has a direct effect on the velocity of the QF. The resulting motion is therefore nonstationary.

Although an inherently local phenomenon, the liquid propagation is also affected by systems properties. Such variables as the pressure, inlet subcooling, wall superheat, reactor power level, and rod gap conductance can be important. These effects must be included if the thermal behavior of the core is to be accurately predicted.

In an effort to adequately model the inherently Lagrangian QF motion and resolve the associated large thermal gradients, an improved heat transfer model is being incorporated into the TRAC code. The model developed at LASL is similar in philosophy to the method employed by the COBRA-TF[7] code. An important feature of the

technique is the capability of modeling more than one front simultaneously. Quenching and dryout are treated automatically.

An integral method has been applied to the two-dimensional (r,z) conduction equation written in conservative form. The effects of internal heat generation due to decay heat and the metal-water reaction, gap conductance, and variable rod properties are included. Differencing in the axial (z) direction is performed explicitly and in the radial (r) direction implicitly. This differencing technique offers the advantage of only requiring the solution of tridiagonal matrices and is capable of modeling the large radial power variations in the fuel. The explicit differencing in the axial direction does place a limit on the axial fine-mesh spacing. This spacing is orders of magnitude less than the coarse-mesh spacing used by the fluid dynamics calculations, however.

The coupling between the conduction and fluid dynamics equations is handled in a semi-implicit fashion. For the time step sizes dictated by the flow equations (they are Courant limited) this appears to be adequate.

The large axial gradients encountered in the vicinity of a QF are resolved by the insertion of radial rows of stationary nodes (Fig. 1). Additional rows are added whenever the temperature difference between nodes exceeds a user-specified value ($\Delta T_{max}$). Temperatures are assigned to the additional nodes such that energy is conserved. Once the front has progressed beyond the location of the inserted rows, the surface temperature difference drops below a prescribed value ($\Delta T_{min}$), and the added rows are removed. The original user-specified nodes always remain.

In an attempt to reduce computing costs in the TRAC code, material properties are computed only at the original node locations. Linear interpolation is used to obtain the properties at additional locations. Heat transfer coefficients, however, are obtained directly from boiling curves for all of the rod surface nodes.

The calculation procedure may be summarized as follows:

- the rod power level ($\dot{q}'''_N$) is calculated,
- rod properties (k, $c_p$, $\rho$, $\varepsilon$) are obtained for the original noding,

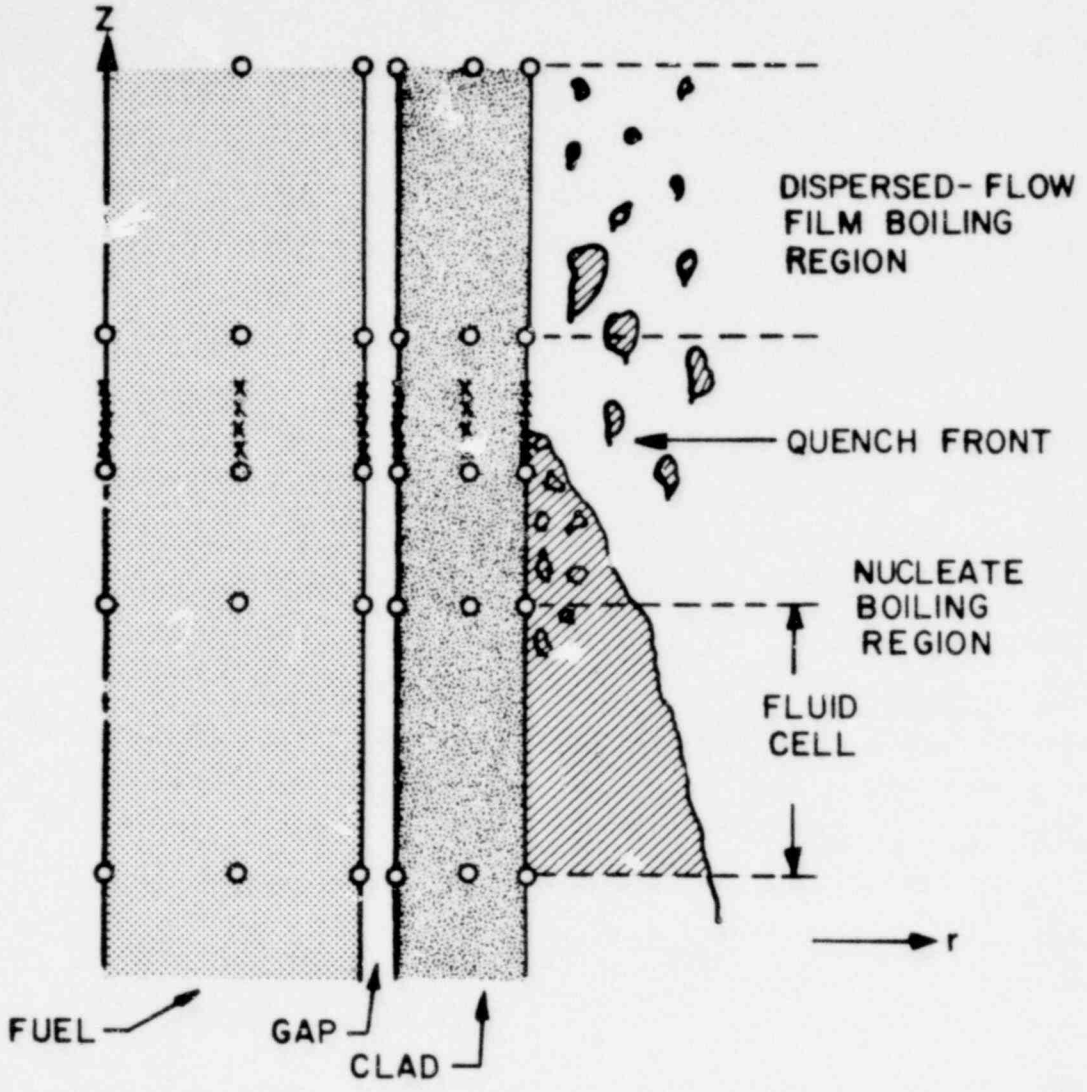


o USER SPECIFIED NODES

x NODES INSERTED IN A REGION OF LARGE $\frac{\Delta T}{\Delta Z}$

Fig. 1. Conduction noding during reflood.

- the number of nodes in the rod is adjusted to resolve the QF,
- heat transfer coefficients ($h_\ell$, $h_v$) are obtained for all of the rod surface nodes,
- averaged properties ($\bar{h}$,$\bar{T}$) required by the fluid dynamics computations are computed,
- the fluid equations are solved ($\alpha$, $\rho$, V, T, ...),
- heat generation resulting from the metal-water reaction ($\dot{q}'''_{MW}$) is computed,

- the gap conductance ($h_{gap}$) is calculated, and
- the conduction equation is solved.

The above steps are performed for each time step until the entire heat transfer, two-phase flow history is predicted for the reflood phase.

The ability of this method to model the QF propagation has been tested by applying the technique to the one-dimensional axial conduction equation. A simple two-regime heat transfer coefficient model was used. The results were compared to the analytic solution of Duffey and Porthouse.[8] A maximum difference of 8% was observed in the rewetting front velocity.

The above numerical procedure is capable of modeling the entire reflood scenario in a complete and consistent fashion. It is anticipated that the model will provide improved understanding of the physical mechanism governing the motion of the rewetting front.

e. A Status Flag Routine for TRAC

(J. H. Mahaffy and J. M. Sicilian, Q-9)

Up to now, status flags have been stored by overwriting real variable arrays. This has led to the unappealing prospect of having the values of these arrays misconstrued during edits.

A new array with the specific purpose of storing status flags (called BITN) has been implemented. The introduction of this storage will allow much more extensive and less confusing use of binary switching logic in future TRAC versions.

f. Addition of a Noncondensible Gas Field

(D. R. Liles and S. B. Woodruff, Q-9)

A single, noncondensible gas field has been added to the three-dimensional hydrodynamics routine in TRAC. Work is proceeding on adding the equations to the one-dimensional, two-fluid model as well as testing the changes incorporated in the three-dimensional routine. The basic assumptions are (NC = noncondensible, s = steam, and v = vapor mixture):

1. summation of partial pressures

$$P = P_s + P_{NC},$$

1320 190

2. thermal equilibrium between the vapor components

$$T_v = T_s = T_{NC},$$

3. a single representative vapor velocity with no diffusion between vapor components

$$V_v = V_s = V_{NC},$$

4. miscibility of components, and

5. a single noncondensible continuity equation to allow the partial pressure of the additional vapor component to be unfolded.

The procedure employed substitutes the continuity equation for the noncondensible gas into the basic field equations to keep the size of the solution matrix blocks from increasing. After an outer iteration (in the one dimensional) or during the final pass (in the three dimensional), the noncondensible mass equation may be used to explicitly unfold the partial pressure of the noncondensible gas ($P_{NC}$).[9]

## 2. TRAC Code Development

(J. M. Sicilian, Q-9)

During the past quarter the TRAC code development effort has provided assistance to outside organizations implementing TRAC-P1A, to LASL users transferring TRAC restart and dump files to other sites, and to the TRAC development community in using new LASL computing capabilities.

Reorganization of the EDIT overlay was completed and reorganization of the INPUT and INIT overlays was begun. Documentation and improvement of the file maintenance system continued, as did location of uninitialized variables and reorganization of TRAC COMMON blocks. The TRAP graphics postprocessing system is in production use at LASL and is being modified to reflect the needs of TRAC users here.

The acquisition of Distributed Processors for the TRAC development project is nearing completion. Competitive benchmarking of these vendor systems was performed and a vendor selected. Purchase of hardware is awaiting final approval from DOE headquarters.

a. Reorganization of Overlays

(M. R. Turner, Q-9)

As reported previously[10] TRAC overlays are being reorganized to take advantage of the common one-dimensional component pointer tables. This quarter the EDIT overlay was completed and the conversion of overlays INPUT and INIT was begun.

b. TRAC Maintenance Systems

(R. P. Harper and M. R. Turner, Q-9)

Documentation of the current state of TRAC code development has been completed. This documentation describes the new TRAC library structure, the new HORSE program, modifications to update libraries, and the comparison utility CMPR. These new procedures were implemented to permit parallel development of multiple versions of TRAC and support programs.

c. Initialization of Variables and COMMON Block Reorganization

(J. R. Netuschil, Q-9)

Because of the ability of the LASL loader to initialize memory to zero, TRAC does not specifically initialize numerous variables. Many other systems, including some which may shortly be in use at LASL, do not provide this initialization. A project has therefore begun to locate those variables which are not currently initialized, and to add their specific initialization to TRAC.

Reorganization of TRAC COMMON blocks as described previously[10] continued this quarter.

d. TRAP Graphics Postprocessor

(J. C. Ferguson, Q-9)

Production use of the TRAP graphics postprocessing system at LASL has led to modification of TRAP to provide capabilities needed by the user community. These include the ability to produce graphs interactively at the user's computer terminal, and improvement of TRAP efficiency by overlaying and data storage reorganization.

e. User Assistance

(J. M. Sicilian, Q-9)

Assistance in implementing TRAC was provided to numerous groups outside LASL. The first of a series of TRAC newsletters was distributed to the TRAC user community. This newsletter describes several errors found in TRAC-P1A, the repair procedure, and information about future TRAC plans.

Programs were developed to translate files between LASL LTSS structures and standard CDC structures to allow transmission of binary files such as TRAC graphics and restart files by users at LASL to remote sites. Instruction in the use of the new Common File System was provided for the LASL TRAC community.

3. TRAC Code Assessment

(K. A. Williams, Q-9)

The effort during the past quarter concentrated primarily on assessment of improvements to the reflood calculational procedure and on the evaluation of an alternative correlation for the minimum stable film boiling temperature ($T_{min}$) as presented by Iloeje, et al.[11] The reflood assessment has utilized a separate effects type experimental facility which employs a single heated tube. This work has lead to the correction of several errors in the logic pertaining to the quench front velocity and to the heat transfer package in general. Evaluation of these changes is still in progress and the conclusions are not yet finalized. Evaluation of the Iloeje $T_{min}$ correlation in TRAC is also in progress with the object being to analyze data from several different experimental facilities. A pretest prediction of LOFT test L2-3 was provided to the NRC using TRAC-P1A with the Iloeje correlation. This calculation predicted the early rewet of the core hot spot as well as the subsequent dryout. In general, the calculated hot rod cladding temperature is in very good agreement with the data.

In the interest of developing a faster running code, work continued on assessing the feasibility of using very coarse noding in the reactor vessel component. Since this is expected to have the strongest influence on the bypass/refill calculation, the Creare ramped transient tests are being analyzed.

a. LOFT LOCE L2-3 Pretest Prediction

(K. A. Williams and D. A. Mandell, Q-9)

LOFT nuclear loss-of-coolant-experiment (LOCE) L2-3 was a 200% cold-leg break test conducted from an initial maximum linear heat generation rate of 39.4 kW/m (12 kW/ft). Pretest predictions were submitted to the NRC using both the release version of TRAC-P1A and a modified version that employed a correlation for $T_{min}$ presented by Iloeje, et al.[11] The TRAC-P1A calculation is part of the independent code assessment task and those results are reported in that section.

The use of the Iloeje $T_{min}$ correlation was the only change made to the P1A version for this calculation. This change was implemented as a result of posttest analyses of LOFT test L2-2.[12] These posttest calculations demonstrated that this single change to the P1A version produced a prediction of the experimentally observed early core rewet. The L2-3 pretest prediction of the cladding temperature response of a central rod at the core midplane is in very good agreement with the data, as shown in Fig. 2. The calculated cladding temperatures for lower power rods at the core outer periphery are also in very good agreement with data, as shown in Fig. 3. Additional code assessment calculations are in progress to ensure that the Iloeje $T_{min}$ correlation accurately predicts the thermal-hydraulic phenomena from a wide range of test facilities. If the comparisons show agreement similar to these LOFT results, this correlation will be incorporated into future versions of TRAC.

b. Semiscale Test S-06-2

(J. K. Meier, Q-9)

Semiscale MOD1 test S-06-2 was the counterpart test to LOFT LOCE L2-2. There are several reasons for selecting this particular test for analysis. The effects of emergency core cooling (ECC) injection from an accumulator are present in this test, where they were not in Standard Problem 5 (SP5) previously analyzed. There is a lower linear power generation range in S-06-2 than in SP5 and consequently the onset of departure from nucleate boiling (DNB) is delayed for about 3-4 s. Thus, the characteristics of the

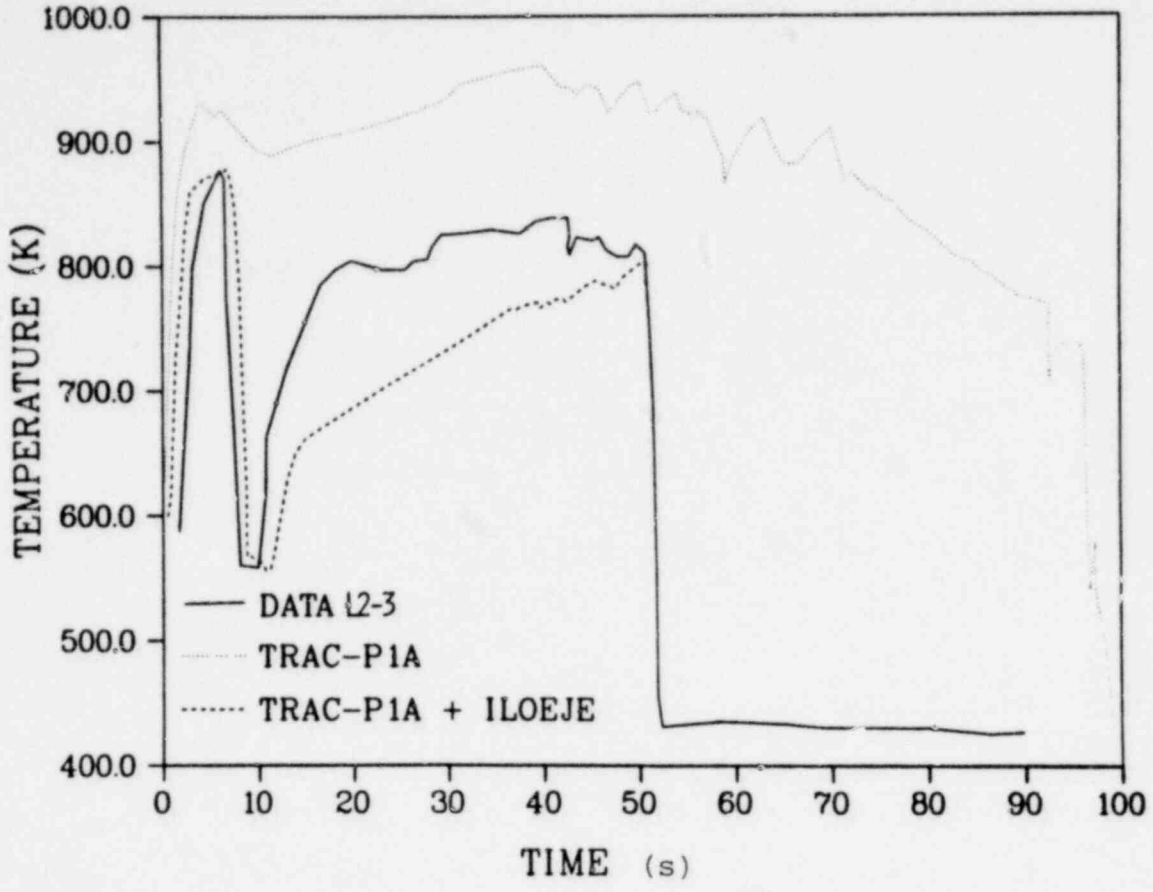


Fig. 2. TRAC pretest predictions of cladding temperature at core midplane during LOFT test L2-3.

blowdown are significantly different than in SP5. The most important reason for performing this calculation is that these test data present an opportunity to assess the Iloeje $T_{min}$ correlation. In this test the rods did not rewet as they did in the LOFT counterpart test L2-2. We will determine if the use of the Iloeje correlation produces an artifical rewet in this calculation. At the present time a steady-state solution has been obtained for S-06-2 and the transient calculation is in progress.

c. Noding Sensitivity Study

(W. H. Lee, Q-9)

During the past quarter, work was initiated on improving the speed of the TRAC-P1A code. Many different techniques have been considered for speeding up the calculations, among them the coarse noding of the vessel is one of the simplest, since it requires no code modification. In order to check the accuracy of

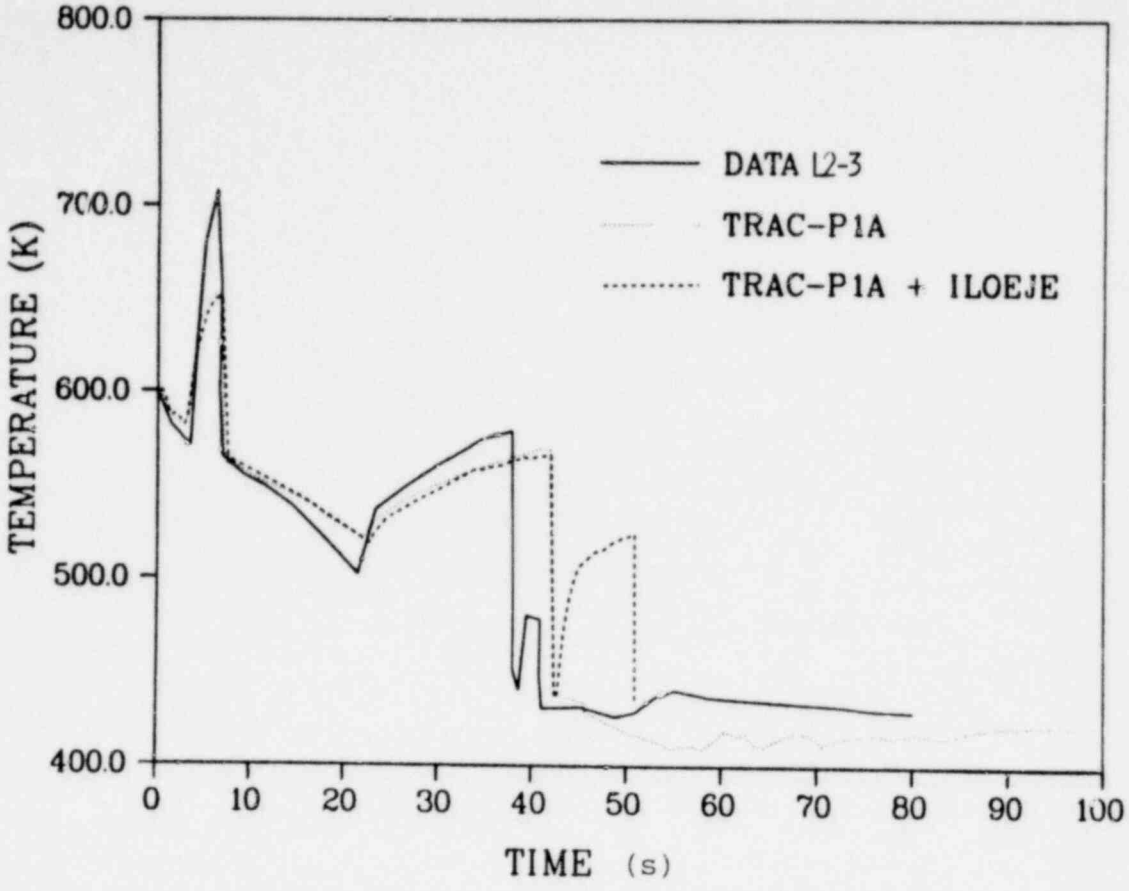


Fig. 3. TRAC pretest predictions of cladding temperatures at outer core periphery during LOFT test L2-3.

calculations using coarse-mesh noding in the vessel, the Creare 1/15-scale ramped transient test data[13] are being used. Test number H75 of the ramped transients has been chosen for the first calculation. In this particular test series, both the transient steam flow and the vessel pressure are decreasing. By using the proper initial and boundary conditions for the transient steam reverse core flow rate, the calculated transient vessel pressure, downcomer steam flow, and ECC delivery can be compared with the experimental data. Currently, the input data have been prepared and the transient calculations are in process.

d. ORNL THTF Analyses

(J. S. Gilbert, Q-9)

A description of the Oak Ridge National Laboratory (ORNL) Thermal-Hydraulic Test Facility (THTF) was received and a model of Test 105 is being developed as part of the effort to assess the

minimum film boiling correlations in TRAC. Based on recommendations by NRC, this test and Test 177 will eventually be analyzed.

## B. TRAC Applications

(J. C. Vigil and P. B. Bleiweis, Q-6)

The work described in this section includes the application of TRAC to full-scale LWR transients and to the planned large-scale German and Japanese 2D/3D experiments. In general, these applications are used to help with the planning, coordination, and analyses of the experiments by providing design assistance, pretest predictions, and posttest analyses. TRAC applications to the experiments also help validate the code for use on full-scale LWR systems. Applications of TRAC to full-scale LWR systems provide best estimate predictions of the consequences of postulated transients. In addition to the above activities, TRAC is being used to analyze a variety of other tests and problems for NRC and outside users.

The TRAC noding model and steady-state calculation of the Three Mile Island Unit 2 plant were completed during the quarter and a transient calculation corresponding to the recent accident was begun. Analysis work for the 2D/3D program continued with a variety of Slab Core Test Facility (SCTF) calculations to analyze the addition of an extra steam supply for combined injection cases to see if reasonable comparisons can be made to the full-scale German PWR. Also, a series of SCTF runs were made for the purpose of instrument ranging for both the cold leg and combined ECC injection modes. Other work for the 2D/3D program involved preliminary design assistance calculations for the Rouths storage tank to be used in the Upper Plenum Test Facility (UPTF). Finally, a double-blind pretest prediction of the Cylindrical Core Test Facility (CCTF) shakedown test No. 4 was performed and the results are reported below.

## 1. Three Mile Island TRAC Model and Initial Results

(J. R. Ireland, Q-6)

The Three Mile Island Babcock and Wilcox (B&W) nuclear plant (Unit 2) was modeled using the TRAC code and preliminary calculations were started during the quarter. The purpose of these calculations is to determine how well TRAC compares overall to the accident scenario that occurred on March 28, 1979 and to help answer safety-related questions about the incident.

The TRAC model for this system is shown in Fig. 4. The model consists of two primary coolant loops and a vessel. The only difference between the two loops is that loop "A" contains the pressurizer. The steam generators are the once-through type as opposed to U-tube and are modeled using the once-through steam generator option in TRAC. In the real system, there are actually two cold legs per loop with a primary pump on each cold leg, but for this model the cold legs and pumps have been combined together as shown in Fig. 4. The ECC injection systems enter the cold legs using TEEs (components 4 and 14 in Fig. 4).

The vessel noding is shown in Fig. 5. The Three Mile Island Unit 2 vessel consists of 177 fuel assemblies with 208 fuel rods per assembly (15 x 15 arrays). These fuel assemblies are modeled in TRAC using three axial levels with one radial ring and two theta segments for a total of six TRAC core cells (levels 2, 3, and 4 in Fig. 5). With this noding, only two average rods (7.4 kW/ft) are used for coupling the fuel-rod heat transfer to the fluid dynamics. Two "hot" rods are also used to model the high power and low power rods in the core (10.9 and 3.6 kW/ft, respectively). The lower plenum, upper plenum, and upper head regions are each modeled using one axial level. The entire TRAC vessel model consists of 2 radial rings, 6 axial levels, and 2 azimuthal segments for a total of 24 vessel cells. The total system consists of 61 TRAC cells.

The pressurizer is modeled as a constant pressure break for the steady-state calculation (component no. 121 in Fig. 4). For the transient calculation, however, the pressurizer is modeled using two pipe components as shown in Fig. 6. The lower pipe component models part of the pressurizer surge line and the bottom part

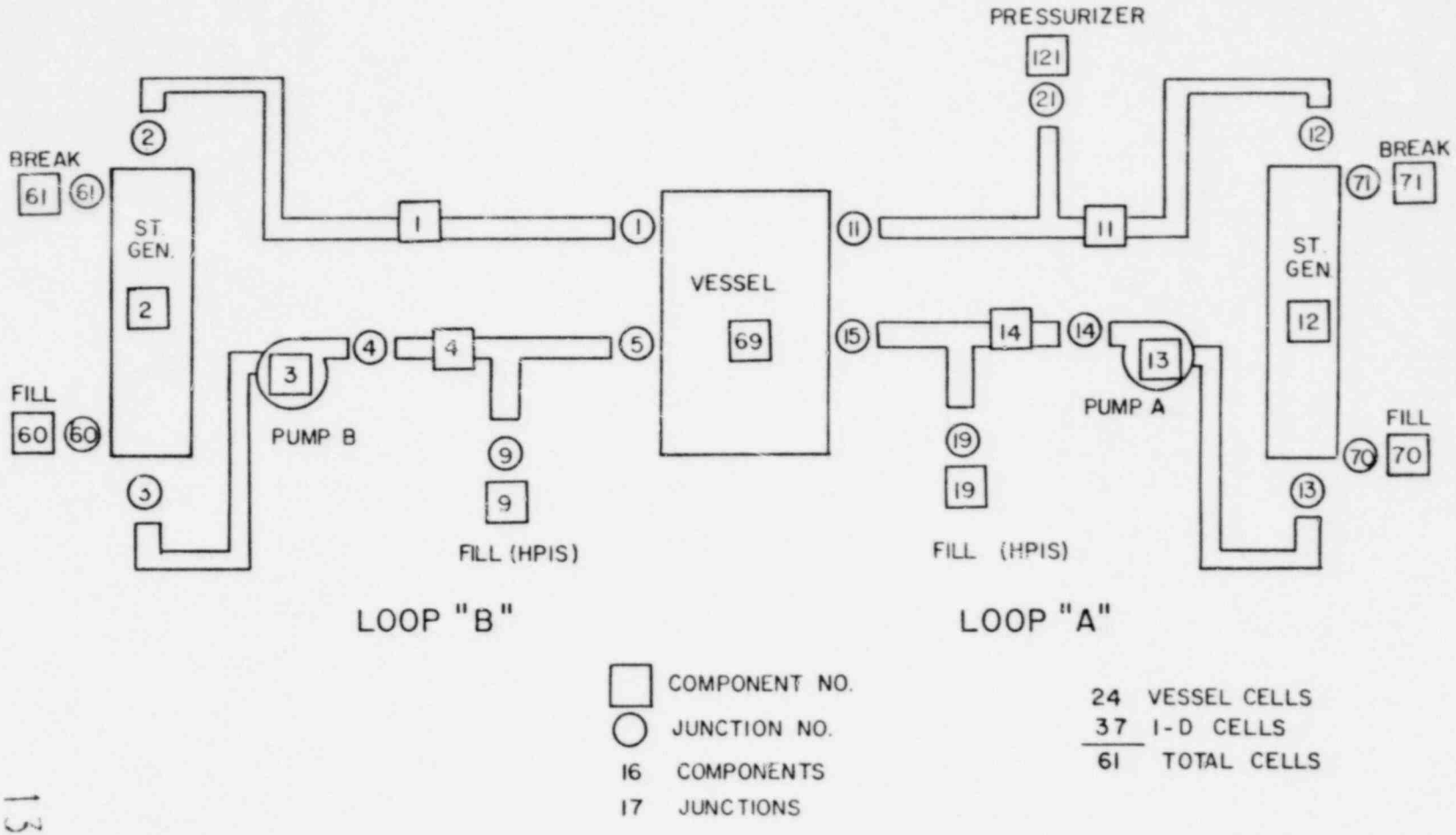


Fig. 4. Three Mile Island (Unit 2) - TRAC schematic.

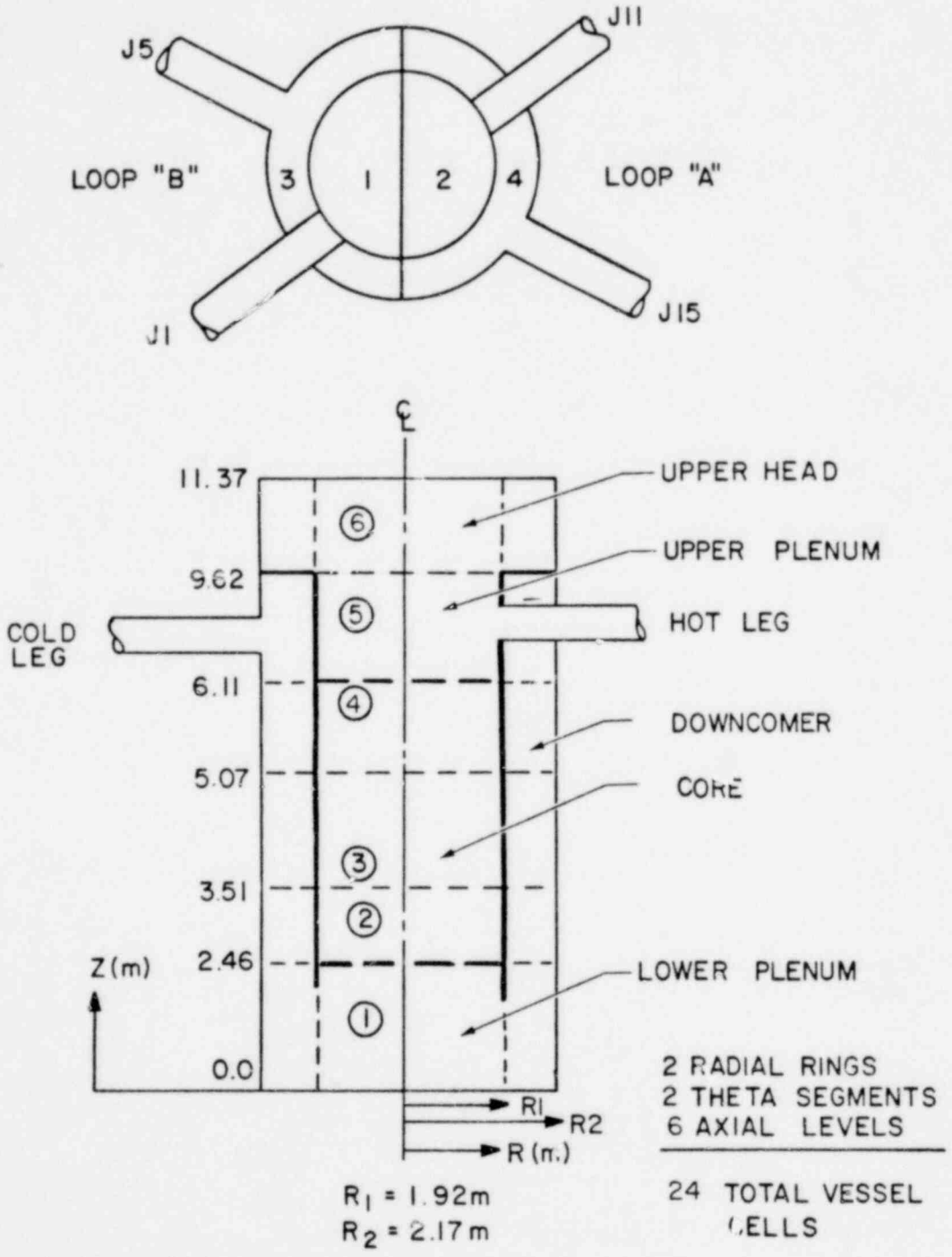


Fig. 5. Three Mile Island (Unit 2) - vessel details.

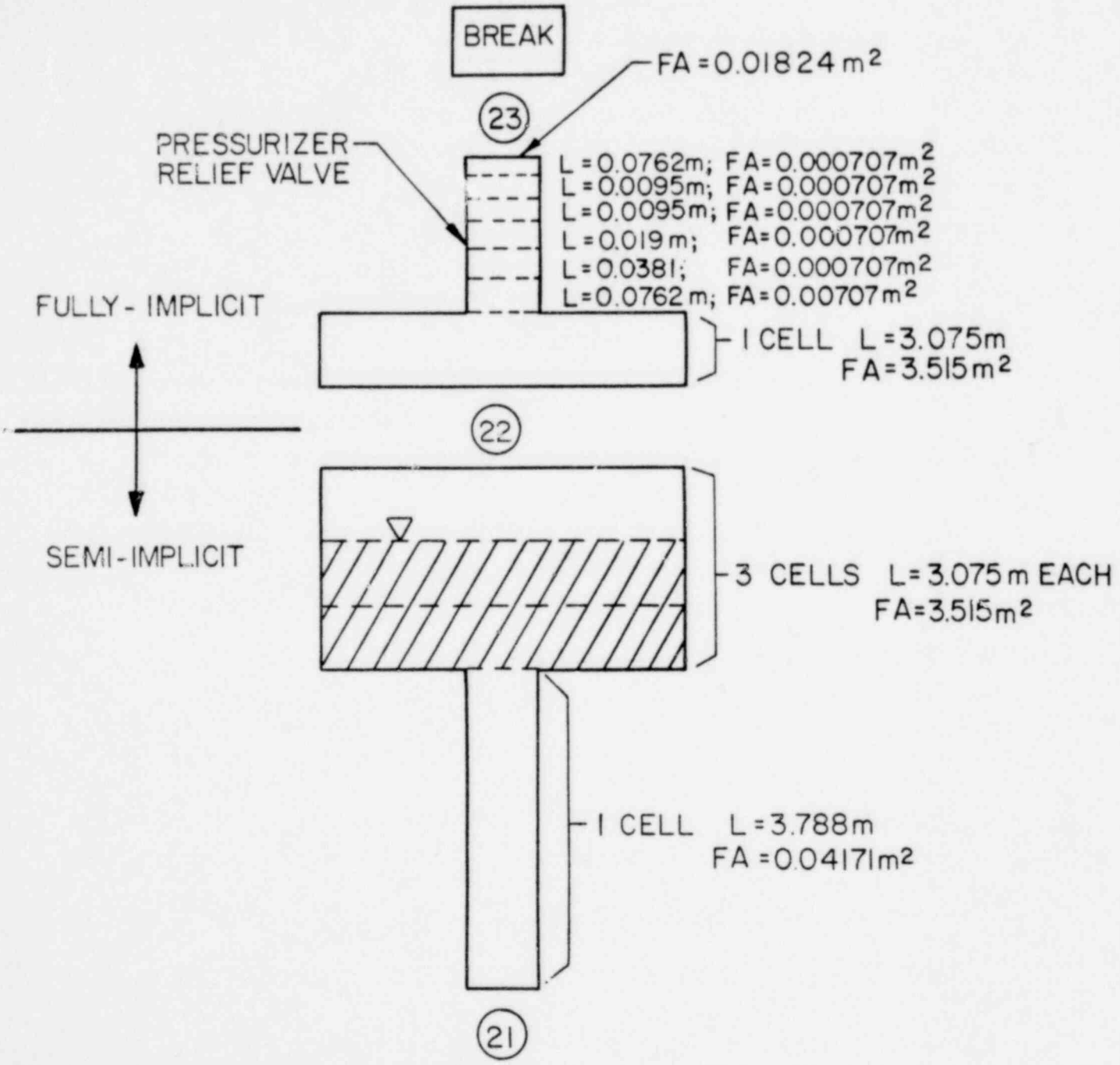


Fig. 6. Three Mile Island (Unit 2) - pressurizer model.

of the pressurizer and the upper pipe models the top of the pressurizer and the pressurizer relief valve. Note that the upper pipe component is modeled using the fully implicit hydrodynamics option in TRAC with very fine noding in the relief valve to naturally calculate choked flow. The pressurizer was modeled this way since the current pressurizer component in TRAC cannot have any other component connected to it except for the surge line.

Based on the geometry and noding described above, a steady-state calculation was performed using the generalized steady-state option in TRAC to obtain initial conditions prior to the transient calculation. The input parameters for the steady-state calculation are shown in Table I. TRAC calculated initial conditions are given in Table II along with a comparison with the results from the B&W code CRAFT-2. The agreement appears to be quite good for all parameters. The difference between the calculated primary system water masses is due to the fact that TRAC includes the mass of the secondary side of the steam generator but CRAFT-2 does not.

Using these steady-state results and the pressurizer model shown in Fig. 6, the transient calculation was initiated. For the transient, boundary conditions were required for the steam generator

TABLE I

THREE MILE ISLAND (UNIT 2) - INPUT PARAMETERS

| | Parameter | Value |
|---|---|---|
| 1. | Initial power (97% of rated) | $2.711\ 78 \times 10^9$ W |
| 2. | Relative axial power shape (3 levels - bottom to top) | 0.64, 1.0, 0.76 |
| 3. | Relative radial power shape | 1.0 |
| 4. | Core average linear power | $2.014\ 4 \times 10^4$ W/m |
| 5. | Peak rod linear power | $2.444\ 2 \times 10^4$ W/m |
| 6. | High-power rod linear power | $3.589\ 2 \times 10^4$ W/m |
| 7. | Low-power rod linear power | $1.197\ 5 \times 10^4$ W/m |
| 8. | Pressurizer pressure | $1.477\ 21 \times 10^7$ Pa |

TABLE II

THREE MILE ISLAND (UNIT 2)
CALCULATED INITIAL CONDITIONS AT STEADY STATE

| | Parameter | TRAC | CRAFT-2 |
|---|---|---|---|
| 1. | Average hot-leg temperature at vessel outlet (K) | 592.2 | 593.0 |
| 2. | Average cold-leg temperature at vessel inlet (K) | 564.3 | 564.5 |
| 3. | Total primary system flowrate (2 loops) (kg/s) | 17 314.0 | 17 375.5 |
| 4. | Average hot-leg pressure at vessel outlet (Pa) | $1.475 \times 10^7$ | $1.472 \times 10^7$ |
| 5. | Average cold-leg pressure at vessel inlet (Pa) | $1.511 \times 10^7$ | $1.534 \times 10^7$ |
| 6. | Pump $\Delta P$ (Pa) | $7.81 \times 10^5$ | $7.87 \times 10^5$ |
| 7. | Steam generator secondary side flowrate (each) (kg/s) | 700.0 | |
| 8. | Average steam generator secondary side pressure (Pa) | $6.55 \times 10^6$ | |
| 9. | Cladding surface temperatures at core level 2 (K) | | |
| | Average rod | 604.5 | |
| | High power rod | 613.5 | |
| | Low power rod | 594.7 | |
| 10. | Total primary system water mass (kg) | $2.775 \times 10^5$ | $2.765 \times 10^5$ |

secondary side, pressurizer relief valve back pressure, etc. These boundary conditions are summarized in Table III and were obtained from data recorded during the accident. A sequence of events was also needed to simulate operator interactions with the system and to simulate the actual plant signals or trips that occurred. Using available information, a preliminary sequence of events for use in the TRAC calculation is shown in Table IV. The transient calculation will only be run until the core uncovers and the cladding

TABLE III

THREE MILE ISLAND (UNIT 2)
BOUNDARY CONDITIONS

1. Reactor power vs time
2. Pump speed vs time
3. High-pressure injection (HPI) flow vs time
4. Pressurizer relief valve back-pressure vs time
5. Steam generator steam line back-pressure vs time
6. Steam generator feedwater flow vs time

temperatures reach 2 200°F at which time fuel rod damage would need to be considered.

The transient calculation is in progress and the initial results are reasonable for the assumptions and information used. As more precise information becomes available and a consistent sequence of events is obtained, the TRAC calculation will be updated and the results reported in the next quarterly.

TABLE IV

THREE MILE ISLAND (UNIT 2)
ASSUMED SEQUENCE OF EVENTS

| | Time (s) | Event |
|---|---|---|
| 1. | 0.0 | Loss of feedwater flow |
| 2. | 6.0 | Pressurizer relief valve opens |
| 3. | 10.5 | Trip reactor power |
| 4. | 120.0 | HPI initiated |
| 5. | 270.0 | Trip one HPI pump |
| 6. | 480.0 | Start auxiliary feedwater flow |
| 7. | 630.0 | Trip second HPI pump |
| 8. | 672.0 | Start HPI - one pump |
| 9. | 4 380.0 | Trip loop B primary pumps |
| 10. | 6 000.0 | Trip loop A primary pumps |
| 11. | 8 280.0 | Pressurizer relief valve closed |

## 2. SCTF Steam Supply Study

(S. T. Smith, Q-6)

Calculations were performed to determine whether an external steam supply for the SCTF will provide a closer match to the German PWR (GPWR) initial and transient conditions during the reflood stage of a LOCA. Table V shows the initial conditions for these calculations. The eight cases calculated are summarized in Table VI and the general operating procedure is given in Table VII.

Figure 7 shows the two-dimensional vessel noding for all cases, except for case 8 which has no break components. Figure 8 is the system component diagram for all cases with extra steam injected at various locations in the vessel. Figure 9 shows the three time-dependent steam supplies considered. Cases 2, 3, and 4 (shown in Table VI) all had the extra steam injected upward at the bottom level of the core. Cases 5 and 6 had the extra steam injected from the side into the core midplane (level 8) and upper plenum (level 12), respectively. Cases 7 and 8 had the extra steam injected into the containment tank modeled as a tee located in the broken hot leg

TABLE V

SCTF INITIAL CONDITIONS

| | |
|---|---|
| Power: | 11.0 MW (ANS decay) |
| Pressures: | System - 6.0 bars |
| | Break - 3.0 bars |
| Temperatures: | Peak Clad - 885 K |
| | Vessel Internals - 430 K (saturation) |
| | Cold-leg ECC - 330 K |
| | Upper Plenum ECC - 400 K |
| | Lower Plenum Liquid - 430 K |
| | Primary Piping - 430 K |
| Lower Plenum: | 68% Full |
| Cold-Leg Injection Flow Rate: | Scaled from German PWR |
| Upper Plenum Injection Flow Rate: | 60 kg/s |

TABLE VI

SCTF CALCULATIONS PREFORMED

| Case No. | Steam Injection Rate (Peak) kg/s | Steam Injection Location |
|---|---|---|
| 1 | Base Case (0) | N/A |
| 2 | 8 | Core Bottom |
| 3 | 0.7 | Core Bottom |
| 4 | 13 | Core Bottom |
| 5 | 13 | Core Midplane |
| 6 | 13 | Upper Plenum |
| 7 | 13 | Containment tank (with breaks) |
| 8 | 13 | Containment tank (no breaks |

between the break component and the valve (case 7) and as a tee replacing the hot-leg and cold-leg breaks (case 8).

Figures 10-17 show the average core pressure, the core steam mass flow rate, the average core midplane temperature, and the average core top temperature for five of the eight SCTF cases and for the GPWR. With little or no steam, core pressures (Figs. 10 and 11) compare reasonably well, but all cases are within acceptable bounds except for case 8. None of the SCTF cases match the GPWR core steam flows (Figs. 12 and 13); the best match is case 5, the

TABLE VII

SCTF OPERATING PROCEDURE

| Time (s) | Events Initiated |
|---|---|
| 0.0 | Power Decay |
| | Hot-leg Valve Opening |
| 2.0 | Extra Steam Injection |
| | Cold-leg Valve (break) Opening |
| | Upper Plenum Injection |
| 10.0 | Cold-leg Injection |

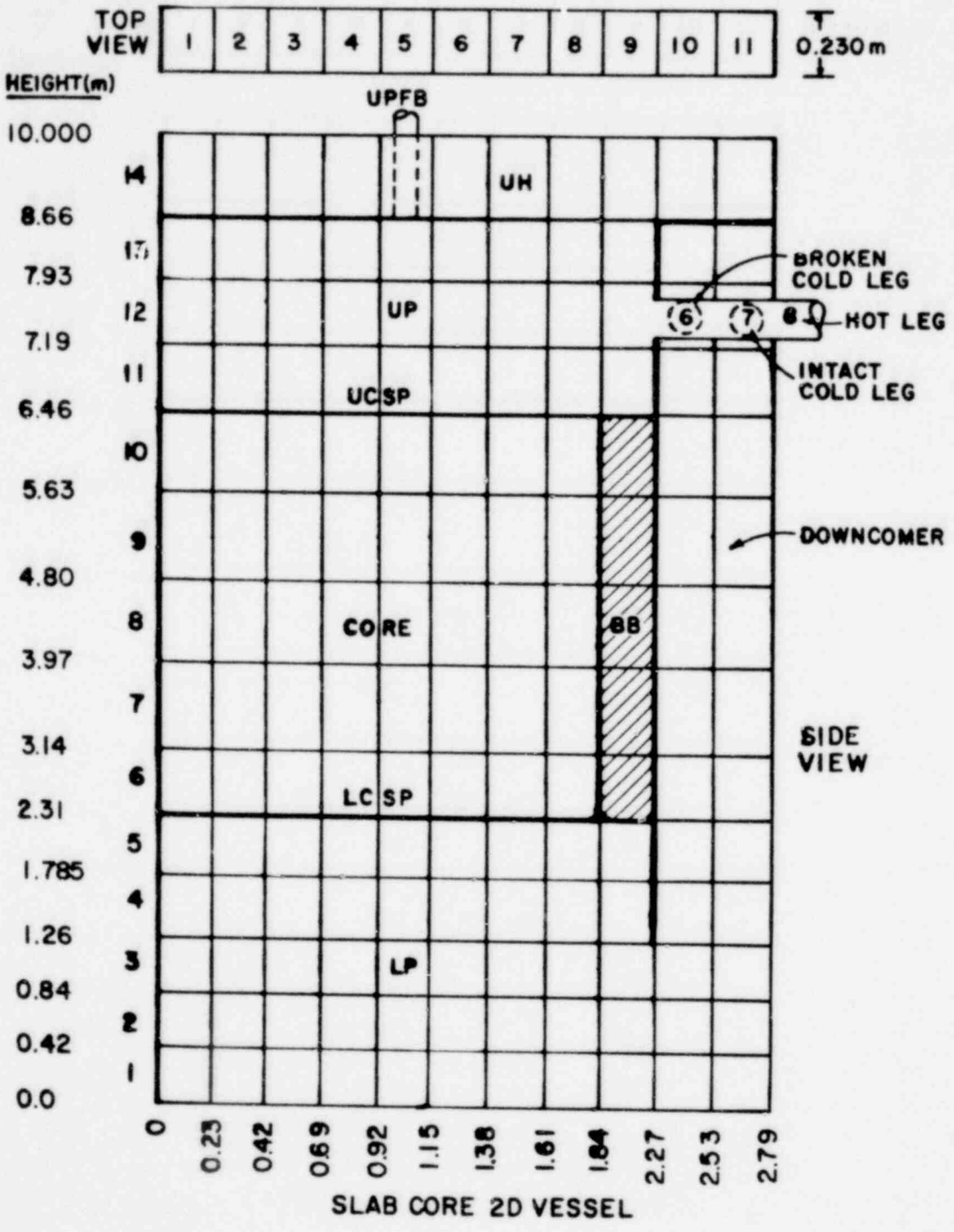


Fig. 7. TRAC model of SCTF vessel.

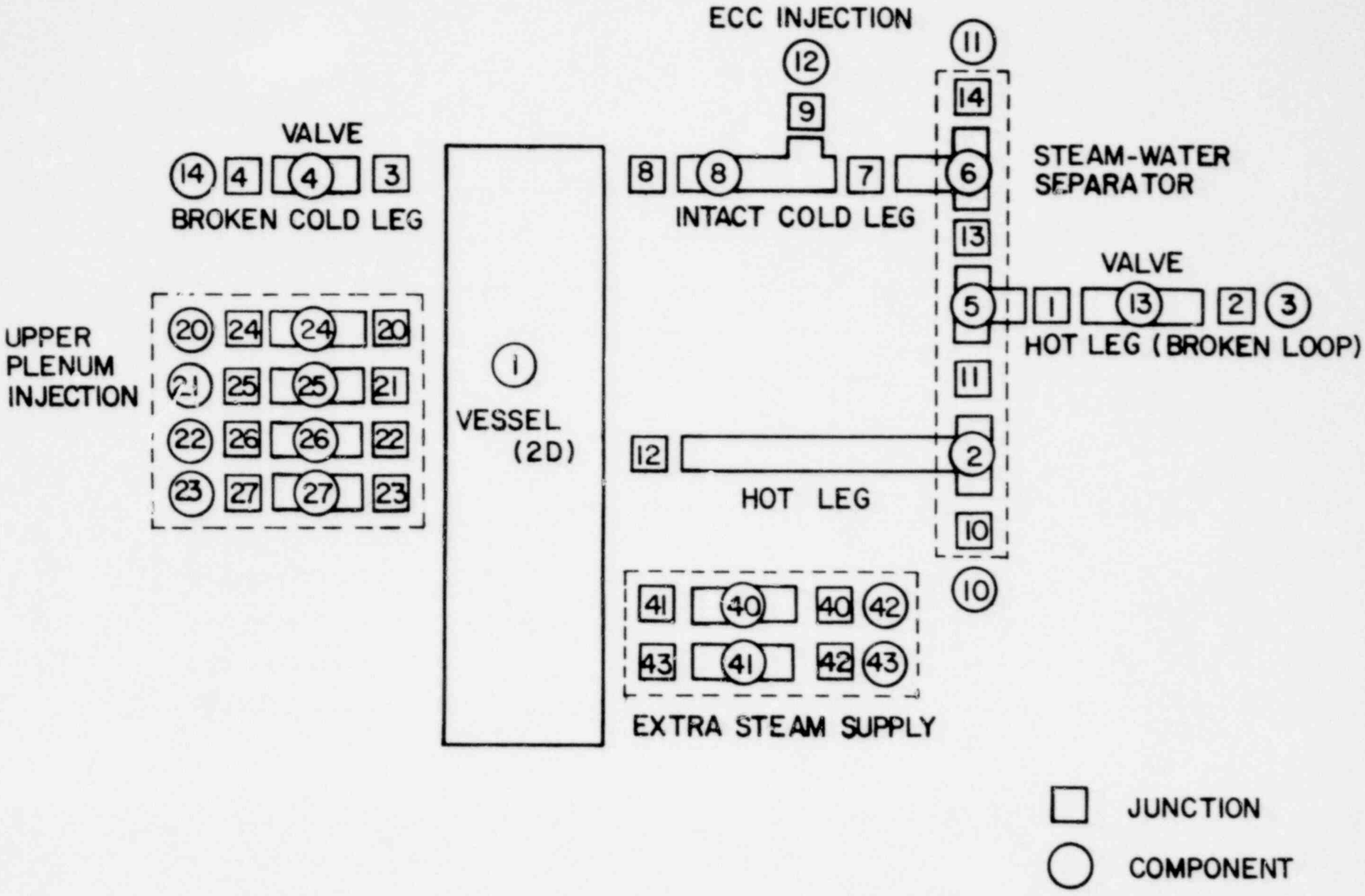


Fig. 8. SCTF system component diagram.

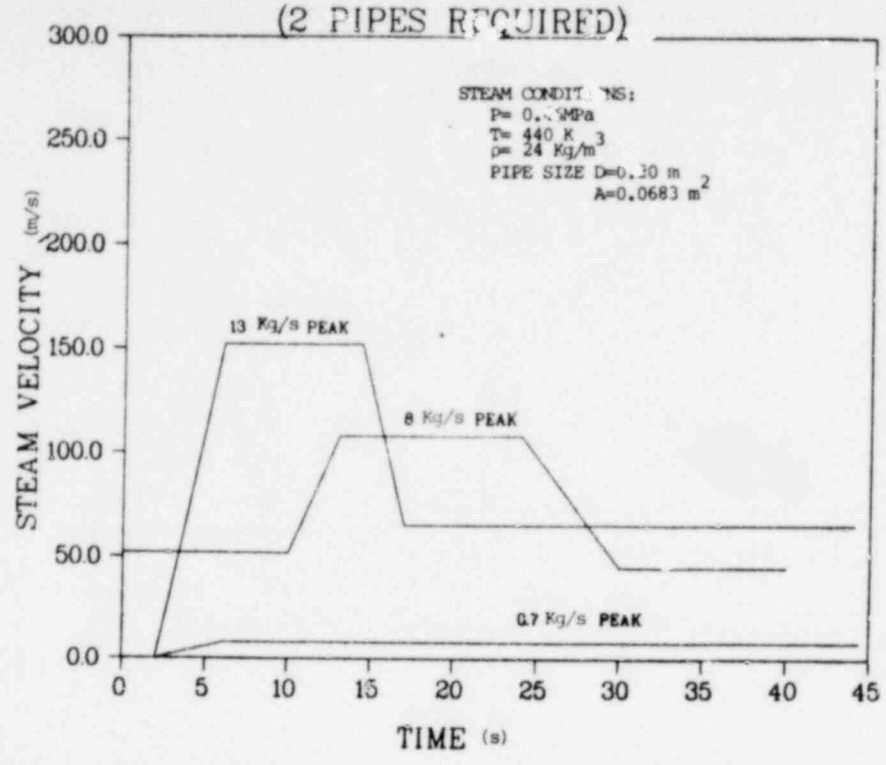


Fig. 9. Time-dependent steam supplies used in SCTF calculations.

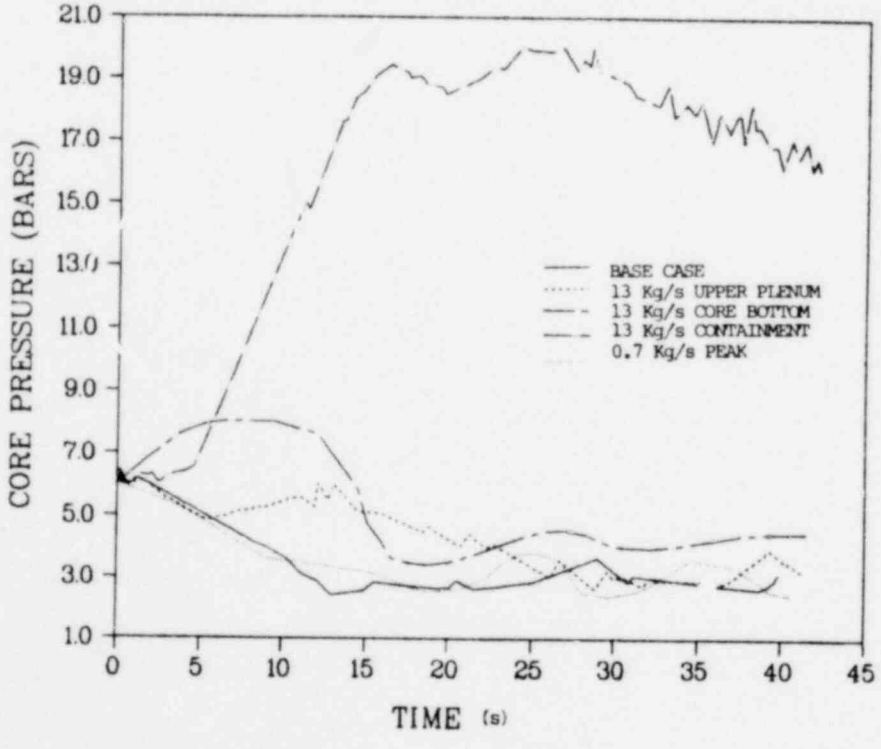


Fig. 10. SCTF core pressure during reflood

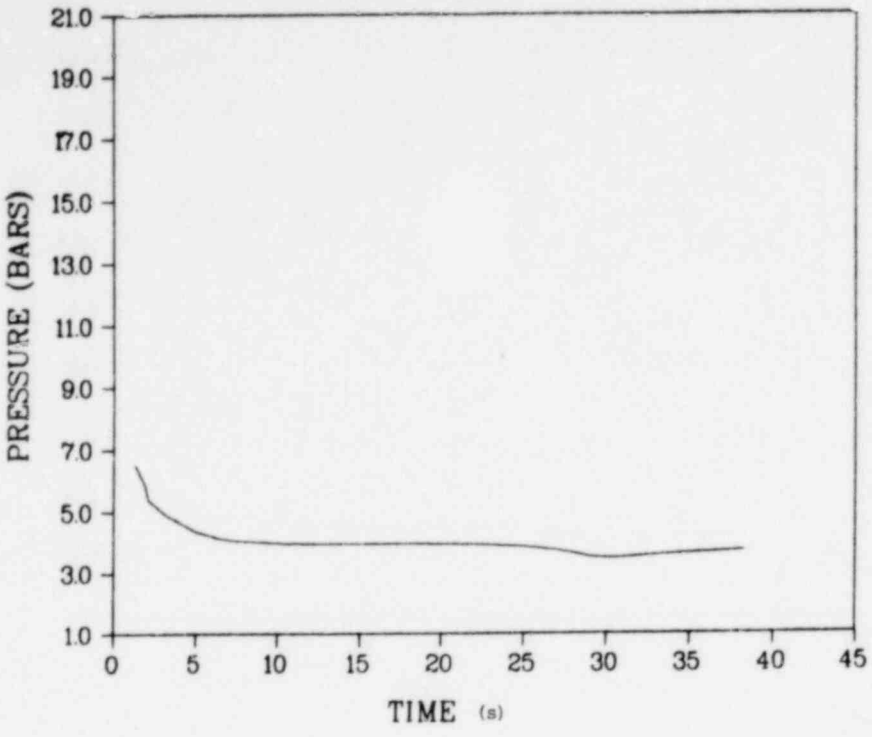


Fig. 11. GPWR average core pressure.

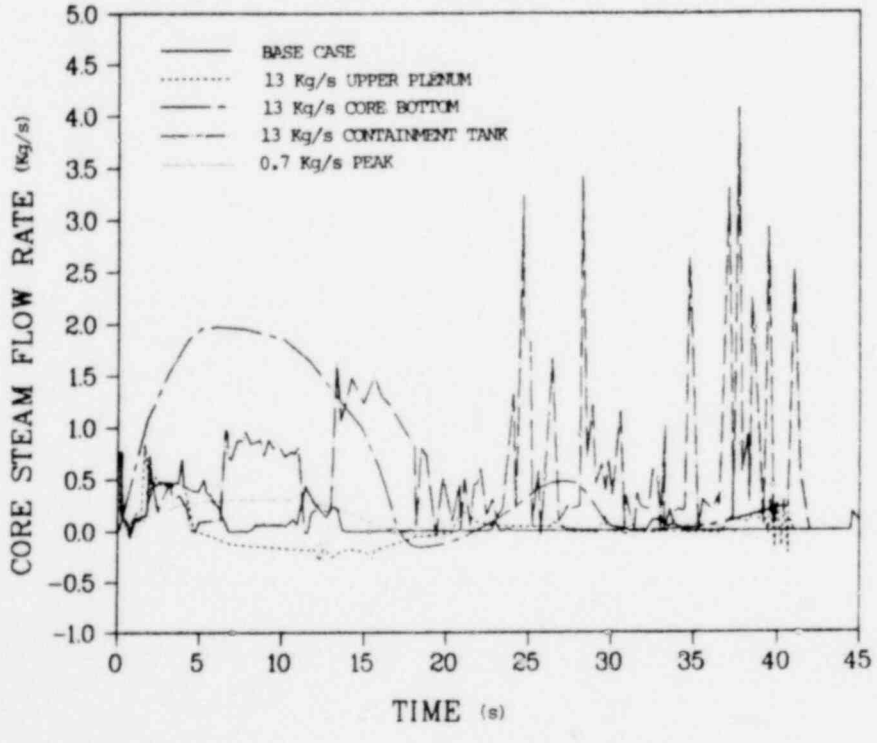


Fig. 12. SCTF core steam flow rate.

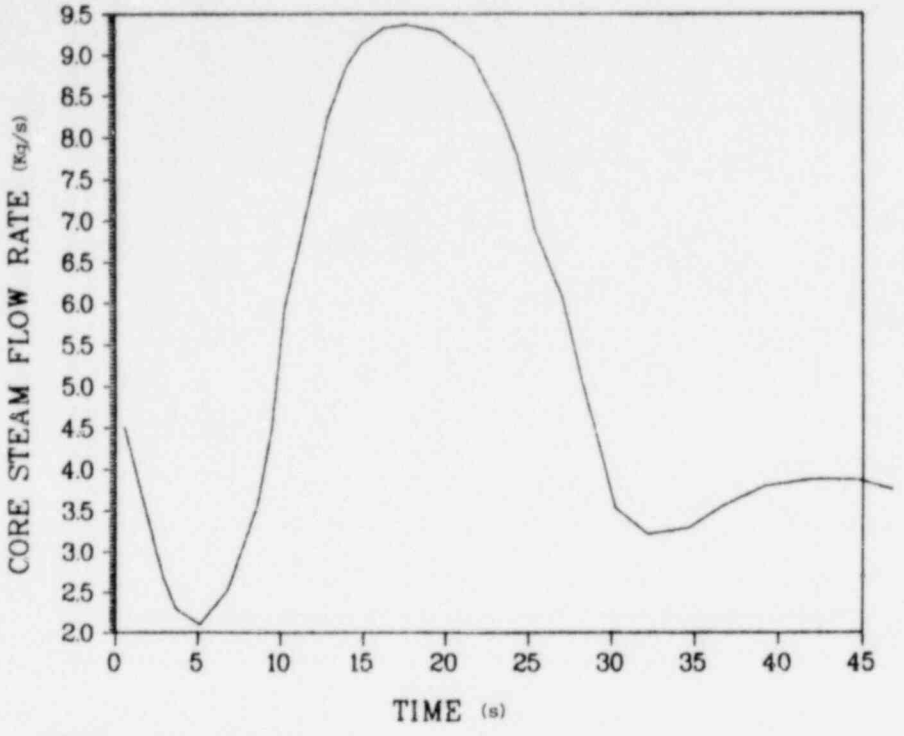


Fig. 13. GPWR core steam flow rate.

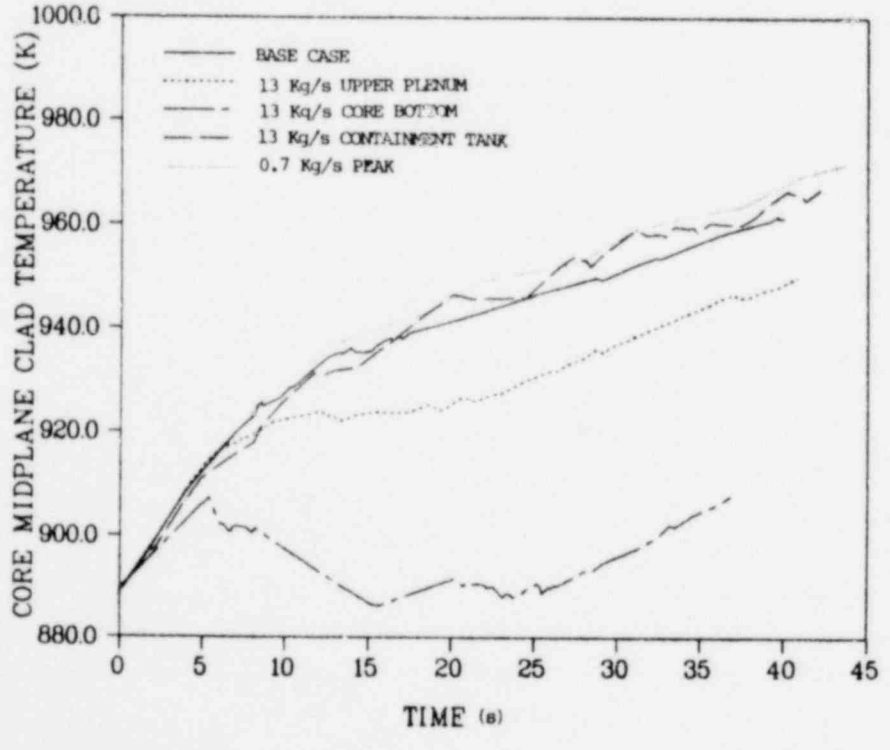


Fig. 14. SCTF core midplane clad temperature.

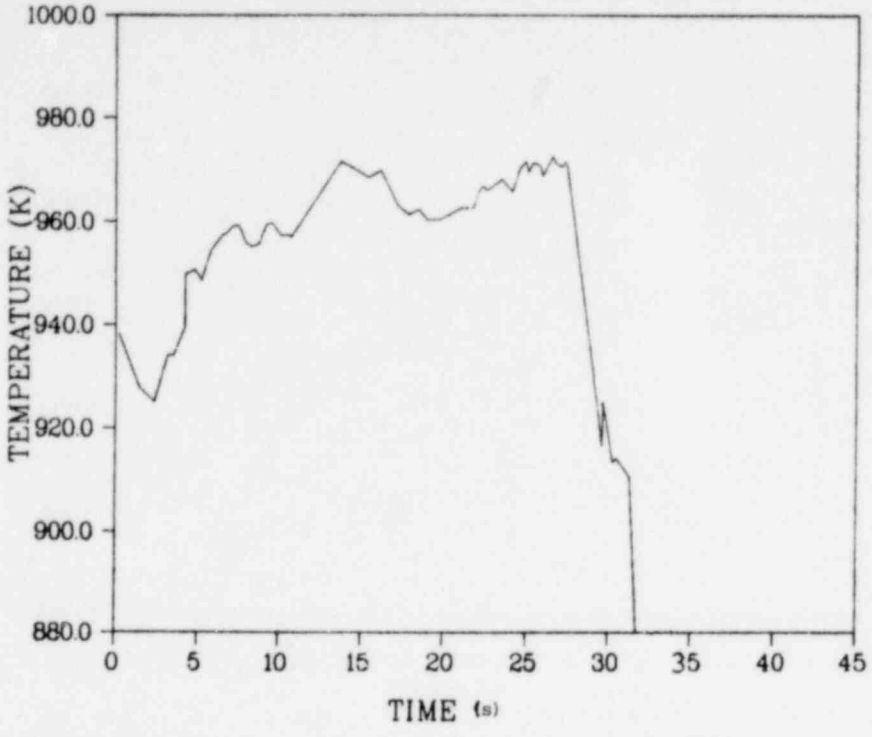


Fig. 15. GPWR average core midplane clad temperature.

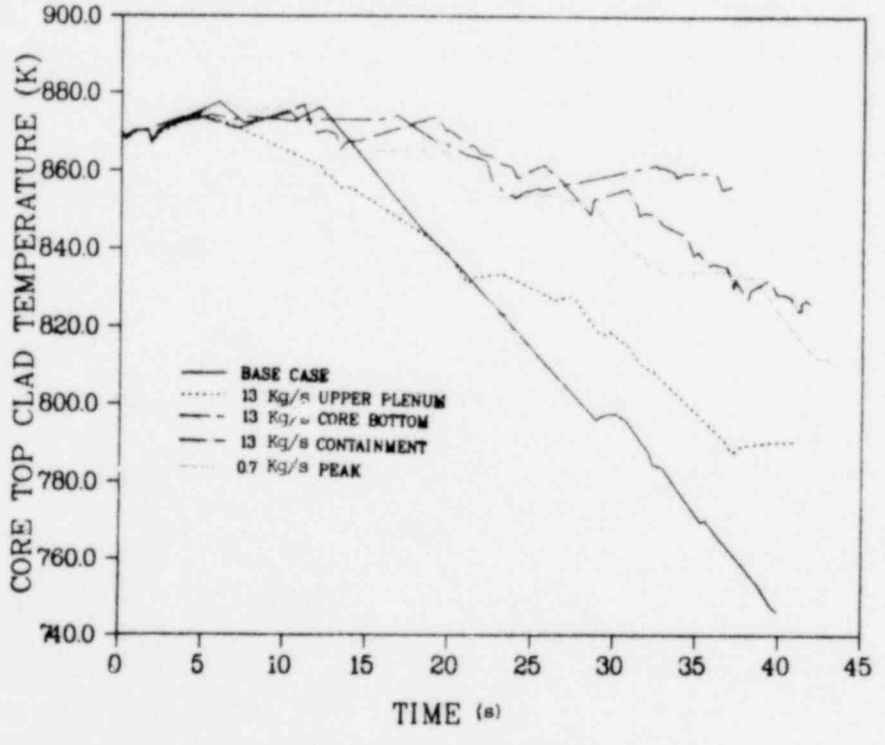


Fig. 16. SCTF core top clad temperature.

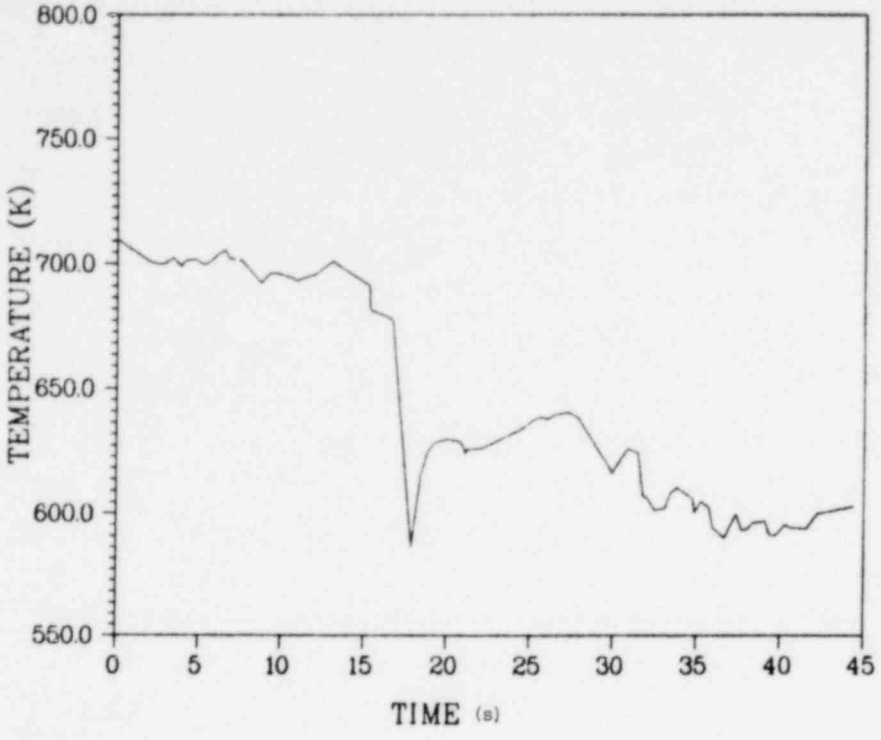


Fig. 17. GPWR core top clad temperature.

13 kg/s injection into the core midplane. None of the cases compares well with GPWR clad temperatures; the core midplane injection case provides more cooling than the other cases.

In conclusion, it is difficult to match most GPWR conditions for any feasible steam supply. Even though the steam supply strategies tried to date do not significantly improve on the base case, the incorporation of an extra steam supply is still recommended to provide flexibility in operation of the SCTF for both combined and cold-leg injection tests.

3. SCTF Instrument Ranging Study

(S. T. Smith, Q-6)

A TRAC study was performed to help determine the measurement range for the SCTF instrumentation. Both cold-leg injection and combined injection cases were run, and the extrema of selected parameters for each injection method were obtained for specified regions of the two-dimensional vessel. The results of these calculations were sent to INEL and ORNL as well as the NRC so that

these organizations can use this information for instrument design and ranging for the SCTF.

4. Rouths Storage Tank

(J. W. Spore, Q-6)

An estimate of the dimensions of the Rouths storage tank to be used in the 360° sector UPTF was obtained from MPR Associates, Inc. Final design dimensions and the transient boundary conditions have not yet been specified. The initial pressure will probably be approximately 20 bars with a final pressure of about 5 bars. It is not known what the time scale will be for the reduction of pressure downstream of the tank. The tank is designed to allow injection of steam from the primary loops into the tank below the height of the initial water level. The injection rates as a function of time are not known.

Based on the available information, preliminary calculations were performed to investigate level swell in the storage tank during a blowdown of the tank from 20 to 5 bars. The tank was simulated both with a TRAC vessel component and with a TRAC tee component. The TRAC vessel model of the storage tank indicates that the level in the tank will swell to the top of the tank. This is not the case with the tee model. The vessel model provides a better representation of the geometry of the tank than the tee model. However, the tee component resulted in a better comparison of the level swell data obtained from International Standard Problem 6 than the vessel component. Work is in progress to improve the vessel component comparison with International Standard Problem 6 level swell data.

The level swell calculations for the Rouths storage tank will be performed again after the improved vessel model has been developed and after the transient boundary conditions are known.

5. Pretest Prediction of CCTF Shakedown Test No. 4

(D. Dobranich, Q-6)

A TRAC pretest prediction for the Japanese CCTF Shakedown Test No. 4 was completed during the quarter. The actual test initial conditions for this calculation were not known, making it a "double-blind" prediction. The CCTF is a reflood facility which consists

of a cylindrical test vessel, one broken and three intact loops, simulated pump resistances, and associated steam generators and emergency core cooling injection systems. The vessel is full scale in the axial direction and is 1/5-scale in the radial direction. Within the vessel is the downcomer, upper and lower plena, and a core containing 2 000 full-length electrically heated rods.

The TRAC system description of CCTF is shown in Fig. 18 and the vessel noding is shown in Fig. 19. All 4 loops are modeled with a total of 27 one-dimensional components. The three-dimensional vessel contains 12 axial levels, 4 radial rings (corresponding to 3 core power zones and the downcomer), and 4 azimuthal sectors. A total of 312 mesh cells are used for the entire system.

Some of the initial conditions used for this calculation are shown in Table VIII. The system is at a constant initial pressure of 2.0 bars. The vessel walls are preheated to 473 K and the initial peak clad temperature is 873 K. All other structure in the system is initially at 392 K (which corresponds to the saturation temperature). The liquid level in the vessel extends 50 cm into the core at a temperature of 337 K starting at time zero. In the actual test, the lower plenum is filled with saturated water to the 0.9 m level and then 308 K water is used to complete the filling. The 337 K water temperature used reflects a mass weighted average temperature assuming uniform mixing. Figure 20 shows the initial clad temperatures in the core assuming the design radial and axial power distributions. Figure 21 gives the design ECC injection rates used to simulate the accumulator and low-pressure injection systems. At time zero, the ECC flow begins and the ANS decay power simulation is initiated.

Initially, much of the subcooled liquid entering the core reaches saturation and flashes to steam. The resulting pressure surge forces the liquid out of the core and into the downcomer. At approximately 20 and 30 s, large core pressure pulses occur causing the downcomer to fill and liquid to exit the broken cold leg. Except for an initial depletion, the lower plenum remains essentially full throughout the calculation. As seen in Fig. 22, approximately 1 200 kg of liquid is lost from the vessel due to

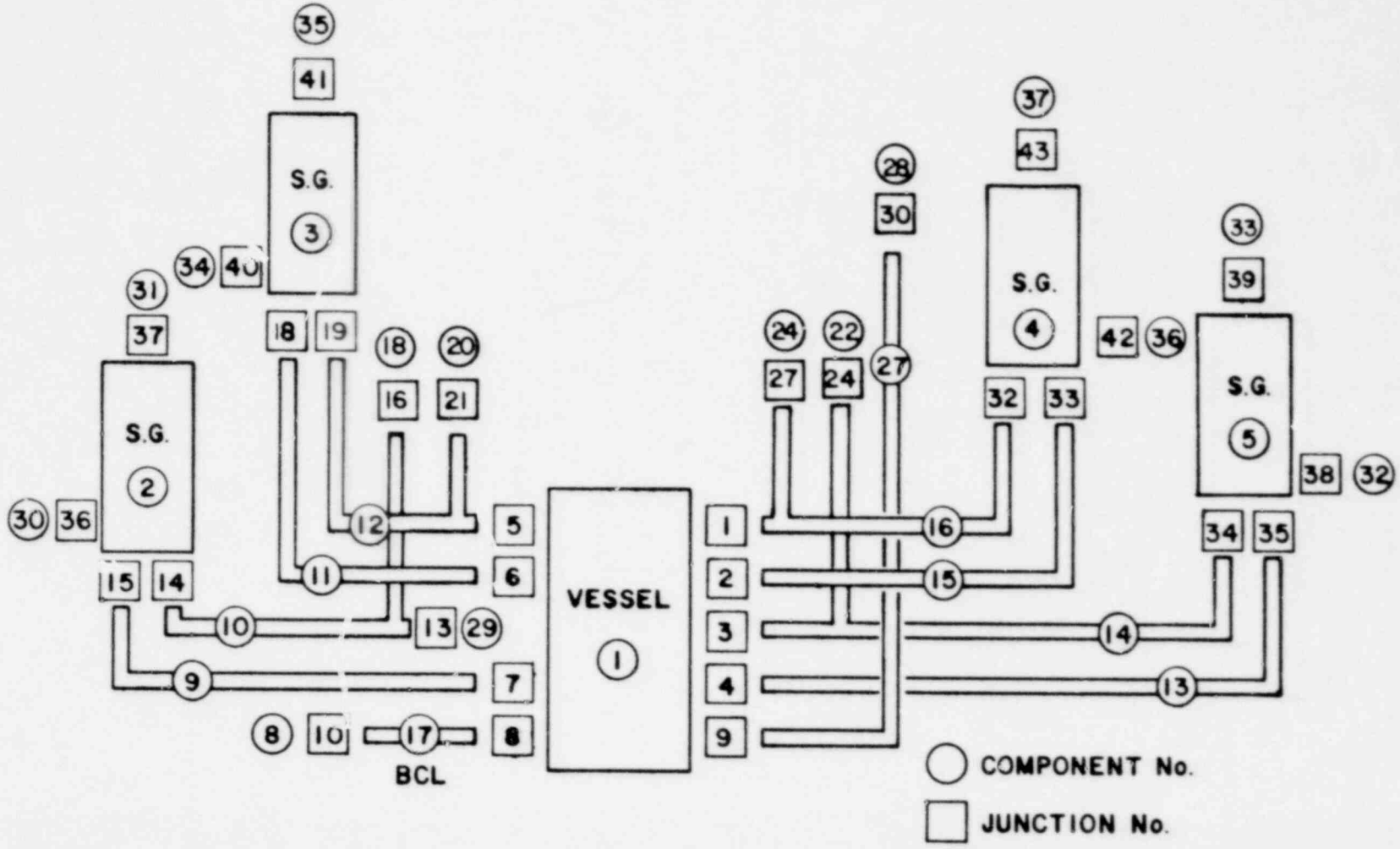


Fig. 18. TRAC component schematic of CCTF.

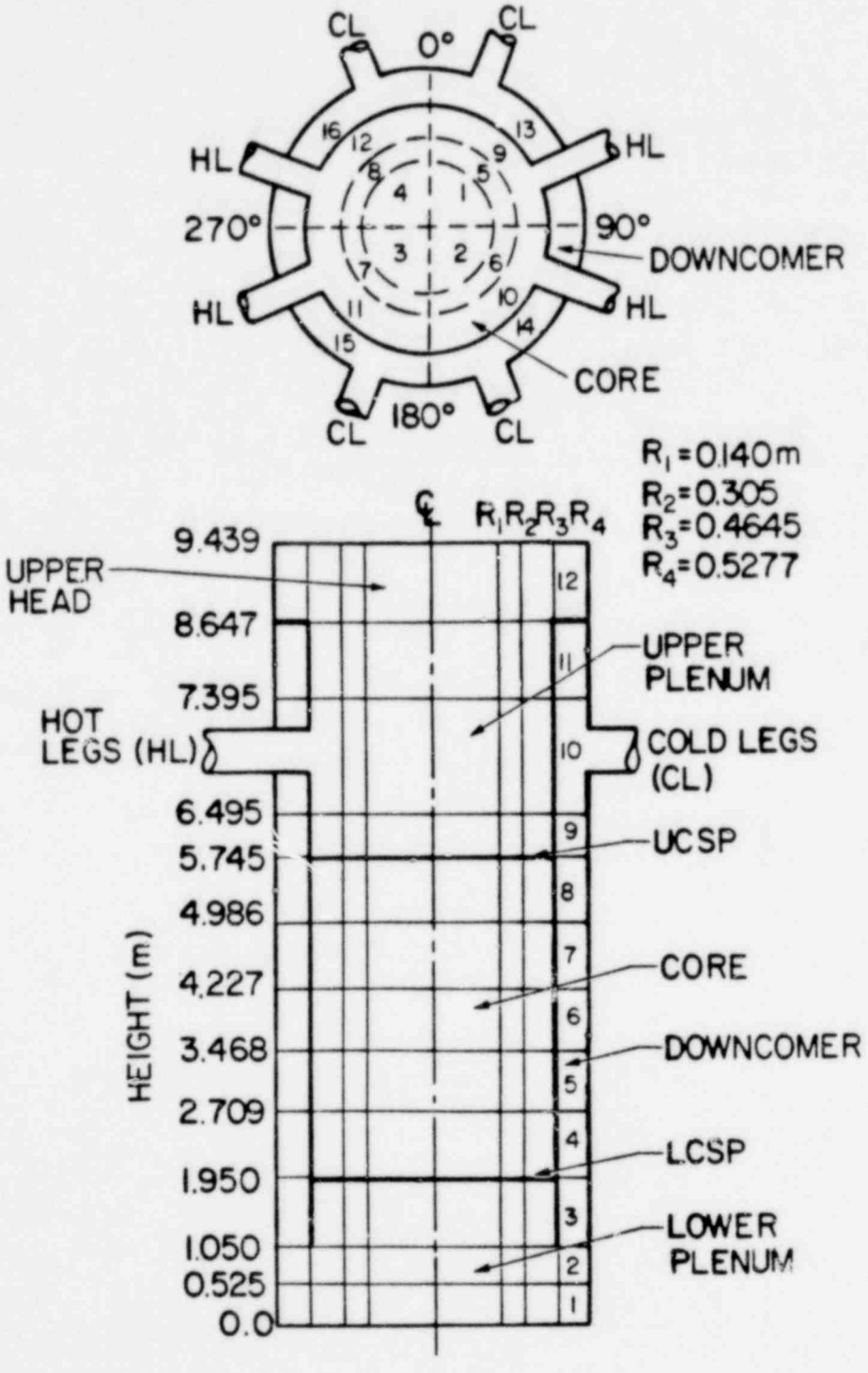


Fig. 19. TRAC noding for CCTF vessel.

TABLE VIII

CCTF INITIAL CONDITIONS

(Base Case)

| | |
|---|---|
| Power: | 8.37 MW (ANS Decay) |
| Radial Power Shape: | 1.15, 1.1, 0.89 |
| Axial Power Shape: | Chopped Cosine |
| Pressure: | System - 2.0 bars |
| | Break - 2.0 bars |
| | Steam Generator Secondary - 56.0 bars |
| Temperatures: | Peak Clad - 873 K |
| | Vessel Walls - 473 K |
| | Vessel Internals - 392 K (saturation) |
| | Primary Piping - 392 K |
| | ECC Liquid - 308 K |
| | Lower Plenum Liquid - 337 K |
| | Steam Generator Secondary - 543 K |
| Lower Plenum: | Full of Liquid |
| Core: | Liquid to 50 cm Level |
| Break: | 200% Cold Leg |
| ECC Injection Type: | Cold Leg |

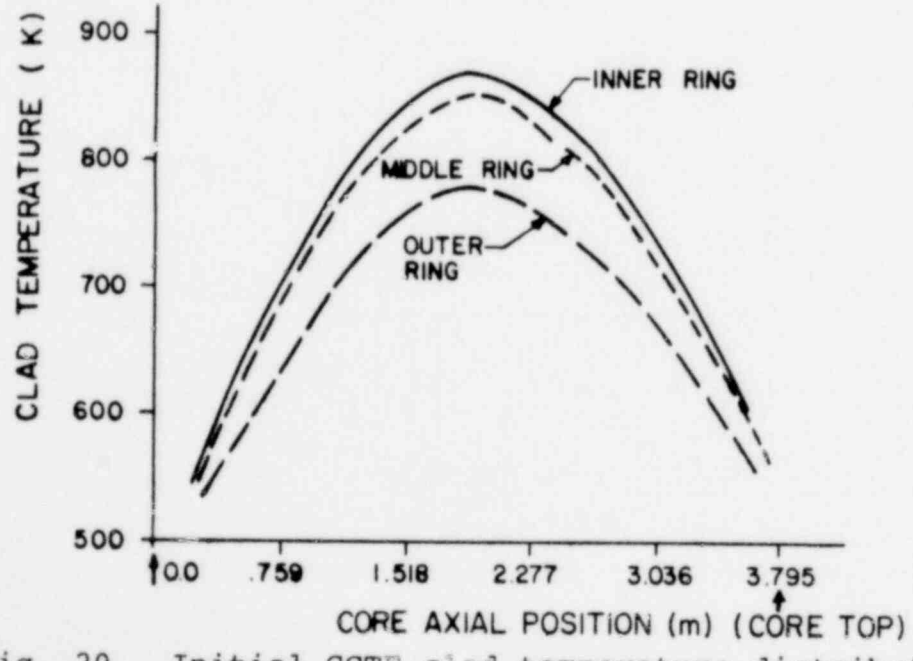


Fig. 20. Initial CCTF clad temperature distribution.

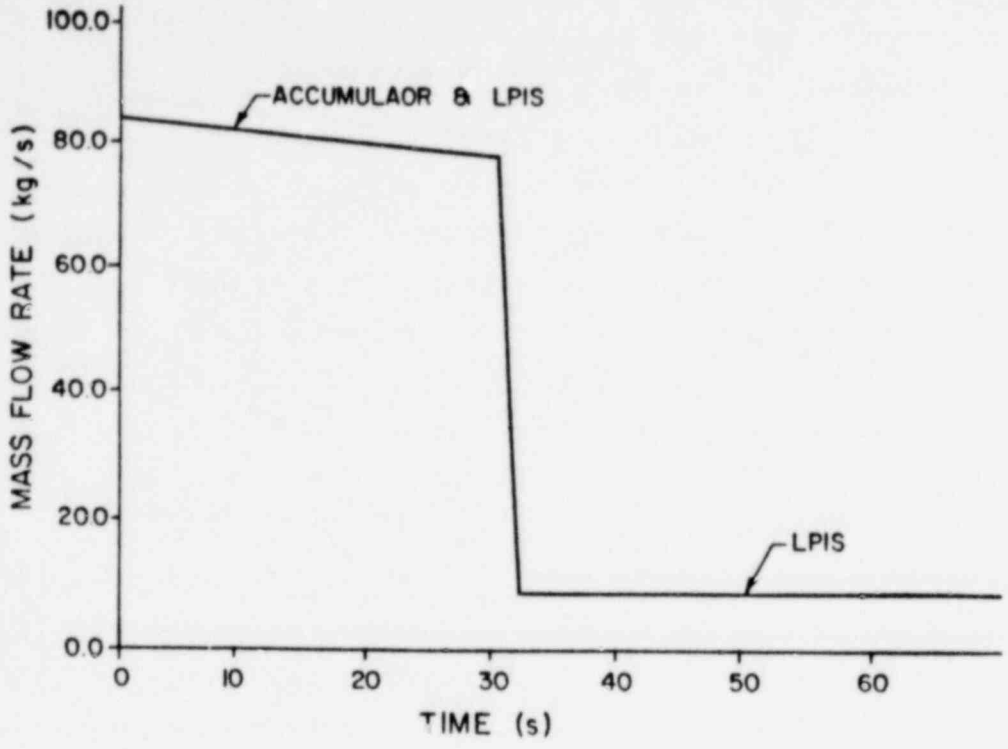


Fig. 21. CCTF ECC injection flow rates.

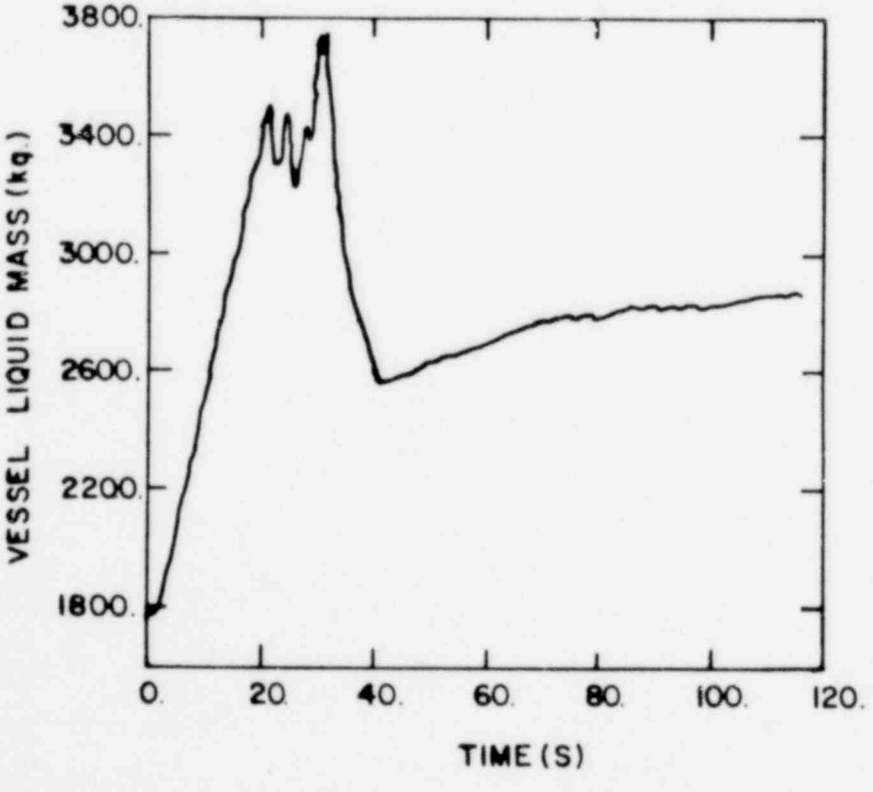


Fig. 22. CCTF vessel liquid mass.

partial core voiding after the accumulator flow has ended at 30 s. After approximately 40 s the vessel fills at a constant rate due to low-pressure injection with small out-of-phase oscillations occurring in the downcomer and core. Figure 23 shows the bottom quench front propagation in the highest powered rod. The rod quenches rapidly until 30 s (accumulators shut off) after which the quench front motion slows considerably but continues upward. Figure 24 shows that the core midplane reaches a peak temperature of 885 K after 3.0 s into the transient. After 60 s, the rod is quenched to the core midplane. The peripheral, low-power rods quench to the core midplane at about 30 s.

At 60.0 s the calculation predicts that the core midplane is about to quench while the upper level core temperatures are still rising. In the actual test run it is expected that precooling of the upper core will occur due to liquid carryover into the upper plenum and that the peak temperature will occur at the midplane and not in the upper core regions. Presently, TRAC inadequately calculates liquid carryover and this underestimates the precooling.

In summary, the results of this pretest calculation appear to be generally reasonable. The core midplane temperature peaked at 885 K after 3 s and the core quenched to the midplane at 60 s. A significant amount of liquid was lost out the break due to a core voiding phenomenon which also induced core downcomer oscillations. The major shortcoming of this calculation is the lack of liquid carryover into the upper plenum. Hence, precooling of the top of the core due to the carryover itself and to any resulting falling film was not predicted.

### 6. Faster Running German PWR Calculations

(J. L. Creel and C. E. Watson, Q-6)

A TRAC input deck has been prepared to model a typical German PWR using approximately 300 nodes, as opposed to 800 for the previous finely noded model.[10] The running time for a LOCA calculation using the intermediate noding has been reduced by a factor of 5 over the fine-node case. The LOCA calculation has been run to 109 s using this coarser-noded model.

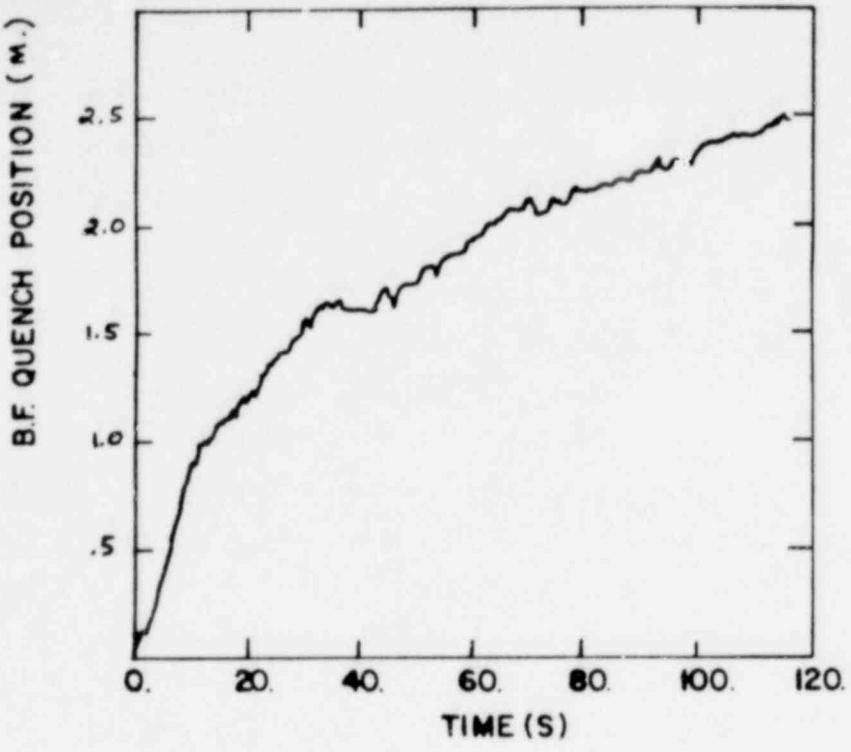


Fig. 23. CCTF quench front position in high-power rod.

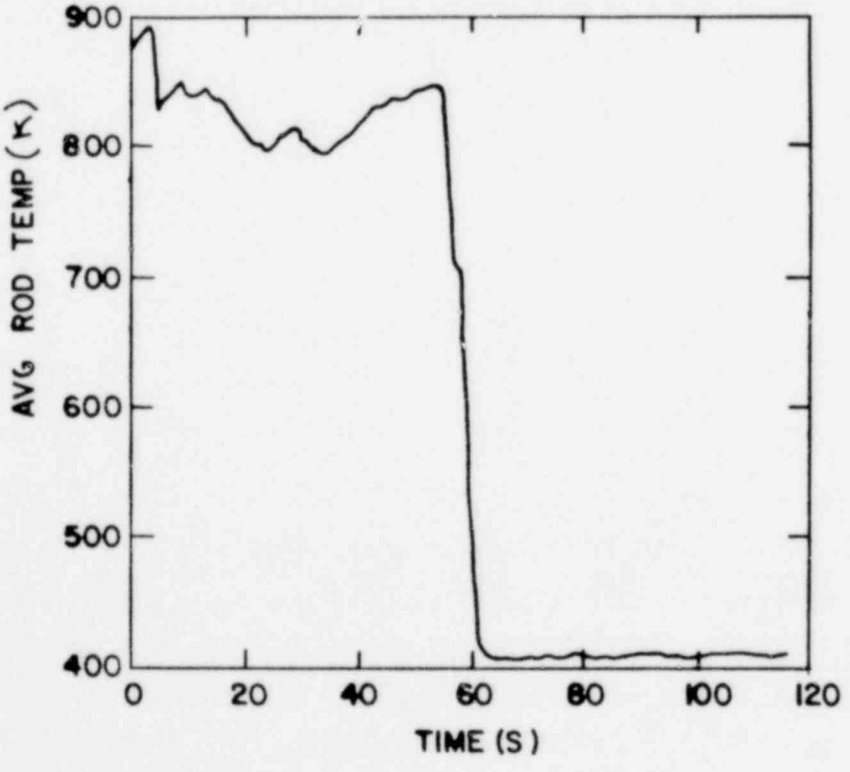


Fig. 24. Clad temperature for CCTF inner rod (core midplane).

The number of axial levels in the core was left identical to the fine-node case in an effort to obtain better agreement in the later stages of reflood than was obtained with the coarsely noded model of the USPWR. The same type of deviations is still seen, however. Work is under way to determine the source of the deviations. One approach is to better match steady-state conditions at the initiation of the transient calculation.

### 7. Experimental Data Processing and Analysis

(P. L. Rivera, Q-6)

A computer program is being developed to process data tapes from various experimental facilities and to prepare input files which can be used with the LASL TRAP code to overlay TRAC-calculated and experimental results. The program can now read data tapes in the format generated by the Semiscale facility. The LASL-defined format for the 2D/3D program is being implemented but is not yet checked out. A capability to process data in the NRC/RSR data bank format is also planned. Work is currently in progress to determine the feasibility of accessing the data bank directly from a LASL computer terminal.

A directory and storage structure for experimental data from all sources has been specified for the Common File System (CFS) at LASL. Finally, work is in progress on two programs for incorporation into a package that will be used for exporting TRAC graphics files.

## C. Independent TRAC Assessment

(J. C. Vigil, Q-6)

Independent assessment of TRAC mainly involves pretest and posttest predictions of tests in designated facilities using the publicly released and documented versions of TRAC. The primary objective of this activity is to determine the predictive capability of TRAC when applied to new tests involving different scales and experimental configurations. Facilities which are currently included are LOFT, Semiscale MOD-3, LOBI, PKL, FLECHT-SEASET, and Marviken III. The scope of the Independent Assessment Program

includes posttest analyses to resolve discrepancies between the code predictions and the test results. If required to resolve discrepancies, these analyses will include tests in other facilities. Recommendations for future code development or experiments and participation in the NRC standard problem exercises are also part of this activity.

During the quarter, pretest predictions were completed for LOFT nuclear LOCA test L2-3 and nonnuclear small-break test L3-0. Significant progress was made on the posttest prediction for Semiscale small-break test S-07-10B and the pretest prediction for LOBI blowdown test A1-01. Posttest analyses of PKL combined injection test K1.3 and Semiscale Mod-3 integral test S-07-6 were completed. Finally, TRAC-P1A was tested against air/water countercurrent flow tests in a vertical pipe. Further details of these analyses are given below.

## 1. Calculation of LOFT Test L2-3

(A. C. Peterson, Q-6 and K. A. Williams, Q-9)

A pretest double-blind calculation of LOFT nuclear test L2-3 was performed using the TRAC-P1A computer code. The TRAC model for this calculation was nearly identical to the model described in a previous quarterly report.[12] For the L2-3 calculation, the reflood assist lines in the broken loop were added to the TRAC model and the upper plenum volume was increased to correspond to a revised value obtained from the INEL.

Test L2-3 was a 200% cold-leg break experiment. The specified pretest conditions were a core power of 37.2 MW with a maximum linear heat generation rate of 39.4 kW/m, intact loop hot-leg temperature of 592 K, and a core $\Delta T$ of 35.8 K. The actual initial conditions were, within the uncertainty of the measurements, as specified.

The calculated rod cladding temperatures from TRAC-P1A and TRAC-P1A with the Iloeje rewet correlation, and the L2-3 experimental data, are shown in Sec. A.3. TRAC-P1A calculated a higher peak cladding temperature than was measured and did not calculate the hot-rod cladding rewet at about 6 s. At a lower power (peripheral)

location in the core, the rod cladding rewets were calculated and show a good agreement between the measured and calculated rod cladding temperatures.

When all of the experimental data become available, additional comparisons between measured and calculated results will be reported.

2. Calculations of LOFT Test L3-0

(A. C. Peterson, Q-6 and K. A. Williams, Q-9)

A pretest double-blind calculation of LOFT nonnuclear Test L3-0 was completed. The TRAC model for the calculation of Test L2-3 was modified so that fewer fluid mesh cells in the vessel and system piping were used for Test L3-0. This was done to speed up the calculation to handle the longer transient time of Test L3-0.

Test L3-0 was an isothermal blowdown of the LOFT system through the pressurizer relief valve. The TRAC calculation was completed for the entire transient which lasted about 40 min. When the experimental data become available, comparisons between measured and calculated results will be reported.

3. Semiscale Small-Break Test S-07-10B

(T. D. Knight, Q-6)

Semiscale Test S-07-10B simulates a small break (10%) in the cold leg of a PWR. The test was conducted in the Semiscale Mod-3 facility, and the break configuration is a communicative type (flow from hot leg to cold leg is permitted during the transient) with an orifice representing the break plane. ECC is only injected into the cold leg of the intact loop and is delayed until the system pressure reaches 1.45 MPa. During the transient, the secondary side of the broken loop steam generator is allowed to blow down.

A new TRAC input model of the Semiscale Mod-3 system was developed. It consists of 26 components and 30 junctions. There is a single vessel component to represent the inlet annulus and downcomer; the lower plenum, core, and upper plenum; and the upper head. The various components were developed and checked separately, and subsequently, were assembled into the system model. The loop resistances were adjusted to reflect the measured Semiscale Mod-3 resistances.

Comparisons were made to CISE Test 10 data (a CISE blowdown test with an orifice 5.4 mm in diameter -- approximately the same orifice diameter as in Semiscale Test S-07-10B). The comparison indicated that the TRAC calculation of critical flow through the orifice was high, and a form loss was applied to the orifice.[14]

The steady-state calculation has been run and the results are summarized in Table IX. Calculated initial conditions agree very well with measurements except for the pressure on the secondary side of the steam generators. The transient calculation is almost completed and will be reported in the next quarterly.

4. Initial LOBI Pretest Prediction

(C. E. Watson, Q-6 and A. B. Forge, C.E.A., France)

The TRAC-P1A model of LOBI blowdown test A1-01 consists of a vessel, two primary loops (one intact and one broken) with steam generators, and a pressurizer and accumulator connected to the intact cold leg. This configuration corresponds to the test apparatus. The intact loop simulates the lumped behavior of the three unbroken loops of a typical PWR and the broken loop simulates the single loop with the break. There are 22 components and approximately 150 fluid cells in the TRAC model. The vessel was modeled with 4 angular segments, 2 radial segments, and 12 axial levels.

A steady-state calculation was performed using the generalized steady-state option to obtain a consistent set of initial conditions. A comparison with the nominal initial conditions specified for the test is shown in Table X. As can be seen, the agreement is quite good (within 2%).

A calculation of the blowdown transient out to 24 s was performed using these calculated initial conditions. The mass flow rates from the vessel side and pump side of the break are shown in Figs. 25 and 26. The liquid mass inventory in the vessel is shown in Fig. 27. By about 20 s, the vessel has ceased to lose mass and is down to 60 kg of liquid. In Fig. 28, the accumulator mass flow rate is given. Flow starts at 16.3 s and rises to 2.4 kg/s at 23.7 s. This is approximately the rate of mass loss at the breaks although parts of the system other than the vessel are still emptying at this point. In Fig. 29 is shown the lower plenum pressure

TABLE IX

CALCULATED AND MEASURED INITIAL CONDITIONS FOR SEMISCALE MOD-3 TEST S-07-10B

| Parameter | Test Condition | TRAC |
|---|---|---|
| Upper Plenum Pressure | 15.700 MPa | 15.700 MPa |
| Cold-Leg Fluid Temperature | | |
| Intact Loop | 556 K | 555.7 K |
| Broken Loop | 556 K | 556.2 K |
| Hot-Leg Fluid Temperature | | |
| Intact Loop | 591 K | 591.6 K |
| Broken Loop | 591 K | 591.6 K |
| Flow Rate | | |
| Intact Loop | 7.45 kg/s | 7.541 kg/s |
| Broken Loop | 2.27 kg/s | 2.315 kg/s |
| Upper Head Bypass | 4.2% | 4.2 % |
| Total Core Power | 1.94 MW | 1.94 MW |
| Pump Speed | | |
| Intact Loop | 232 rad/s | 242 rad/s |
| Broken Loop | 1 438 rad/s | 1 372 rad/s |
| Steam Generator Secondaries | | |
| Intact Loop | | |
| Pressure | 5.650 MPa | 5.367 MPa |
| Temperature | 542.5 K | 541.5 K |
| Broken Loop | | |
| Pressure | 5.960 MPa | 5.483 MPa |
| Temperature | 546.6 K | 542.9 K |

which falls to 11 bars at 23.7 s. This is still above the assumed back pressure of 3.0 bars. Finally, the maximum average-rod temperature is given in Fig. 30. The peak temperature is 625 K reached at 1.0 s which is the time at which the power is switched from 100 to 0%.

TABLE X

CALCULATED AND NOMINAL INITIAL CONDITIONS FOR LOBI TEST A1-01

| Parameter | Nominal | TRAC |
|---|---|---|
| Power (MW) | 5.28 | 5.28 |
| ΔT (K) Core | 34.0 | 33.3 |
| T (K) Hot-leg Average | 597.0 | 596.3 |
| T (K) Cold-leg Average | 563.0 | 563.0 |
| P (bars) | 155.0 | 158.0 |
| W (kg/s) Intact Loop | 21.07 | 21.02 |
| W (kg/s) Broken Loop | 7.03 | 6.98 |

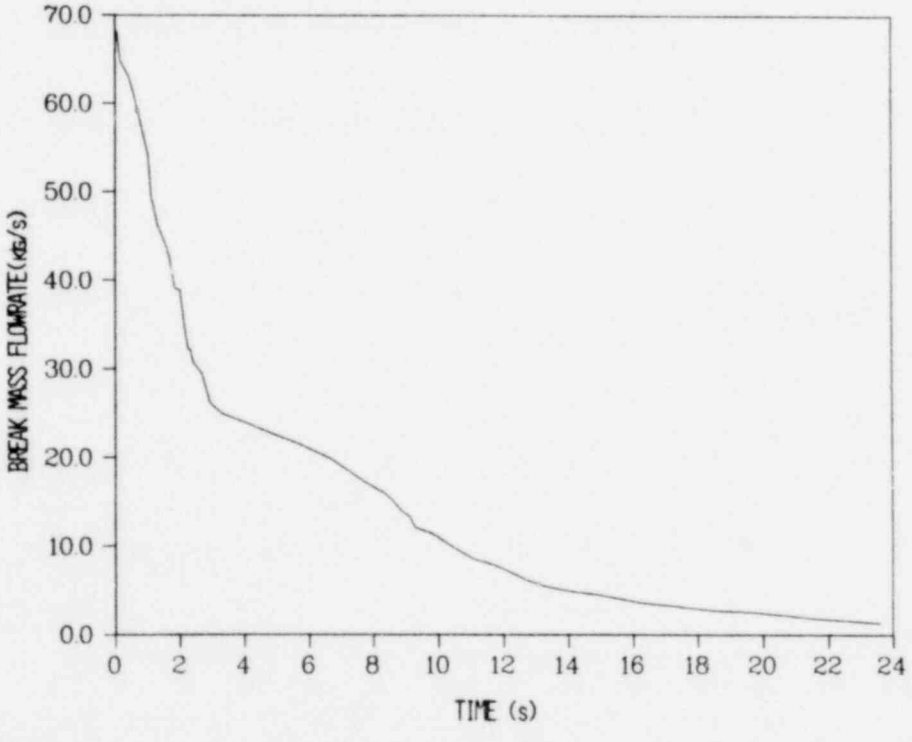


Fig. 25. Vessel side break mass flow rate for LOBI test A1-01.

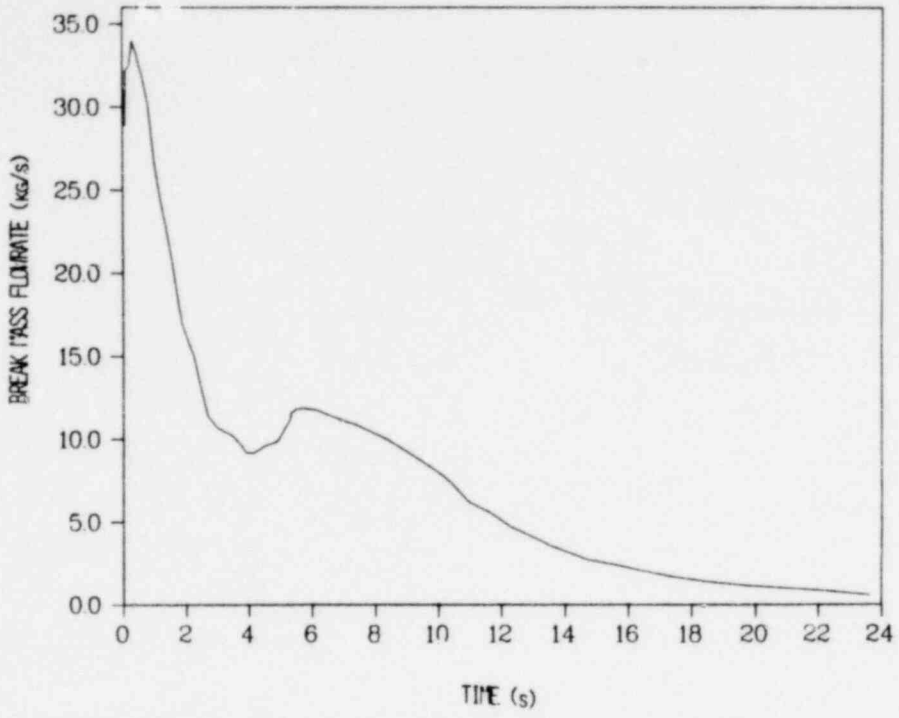


Fig. 26. Pump side break mass flow rate for LOBI test A1-01.

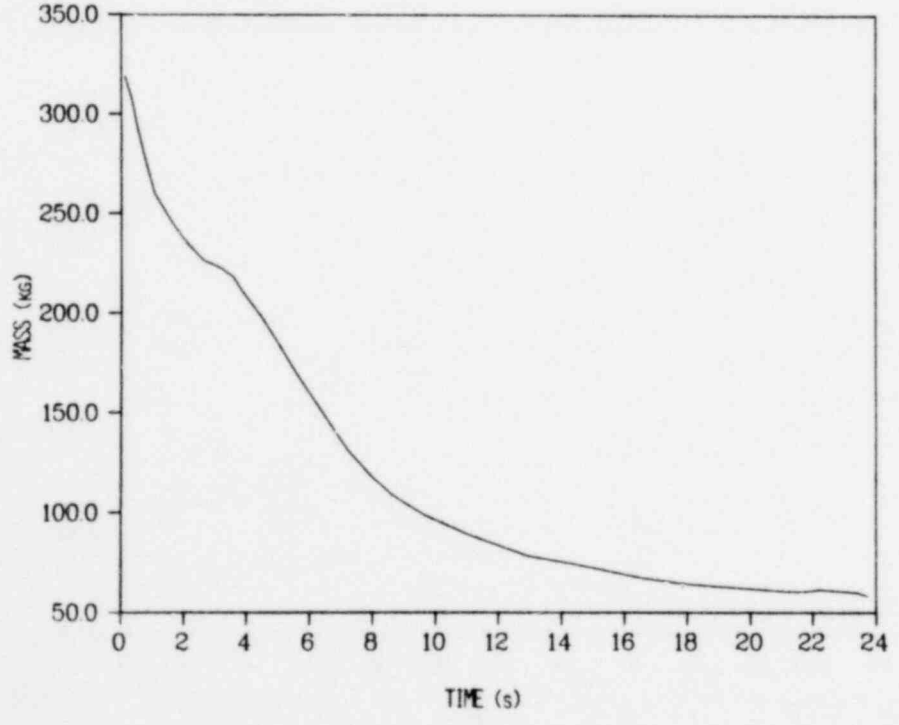


Fig. 27. Vessel liquid mass for LOBI test A1-01.

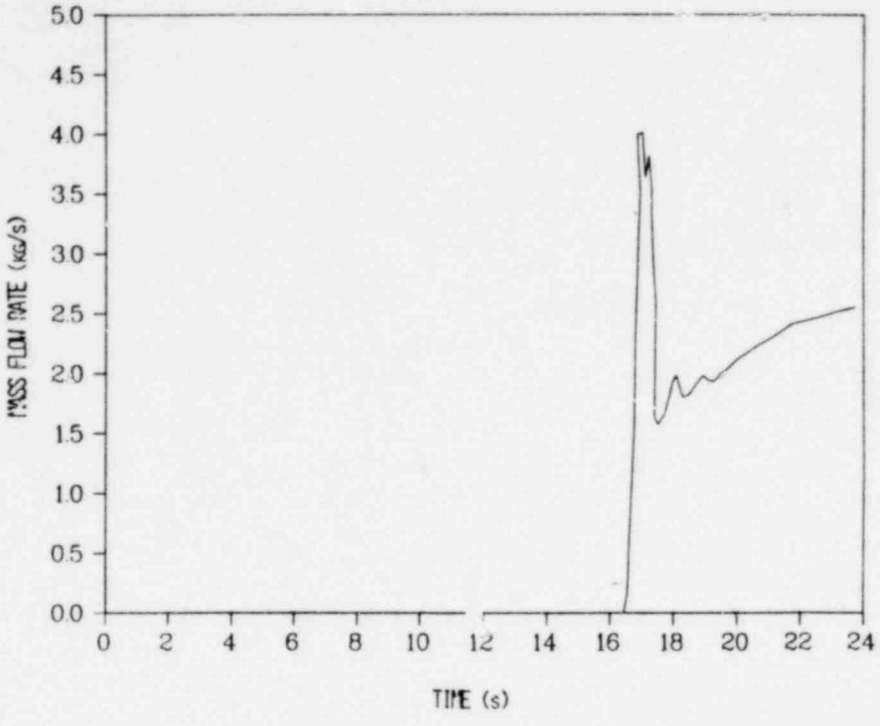


Fig. 28. Accumulator mass flow rate for LOBI test A1-01.

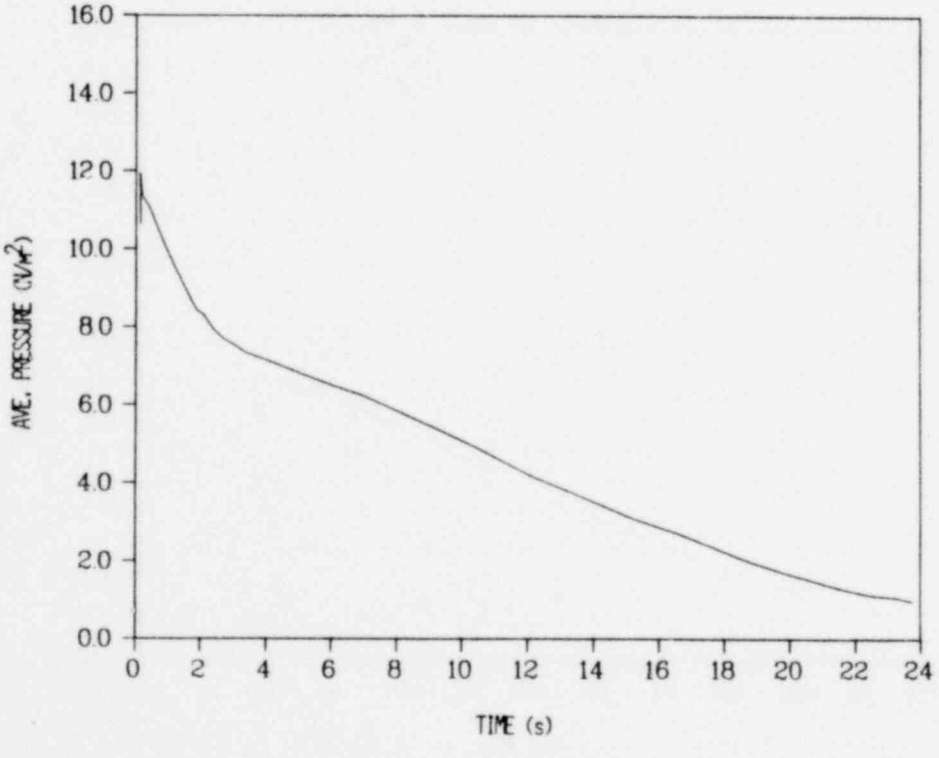


Fig. 29. Lower plenum pressure for LOBI test A1-01.

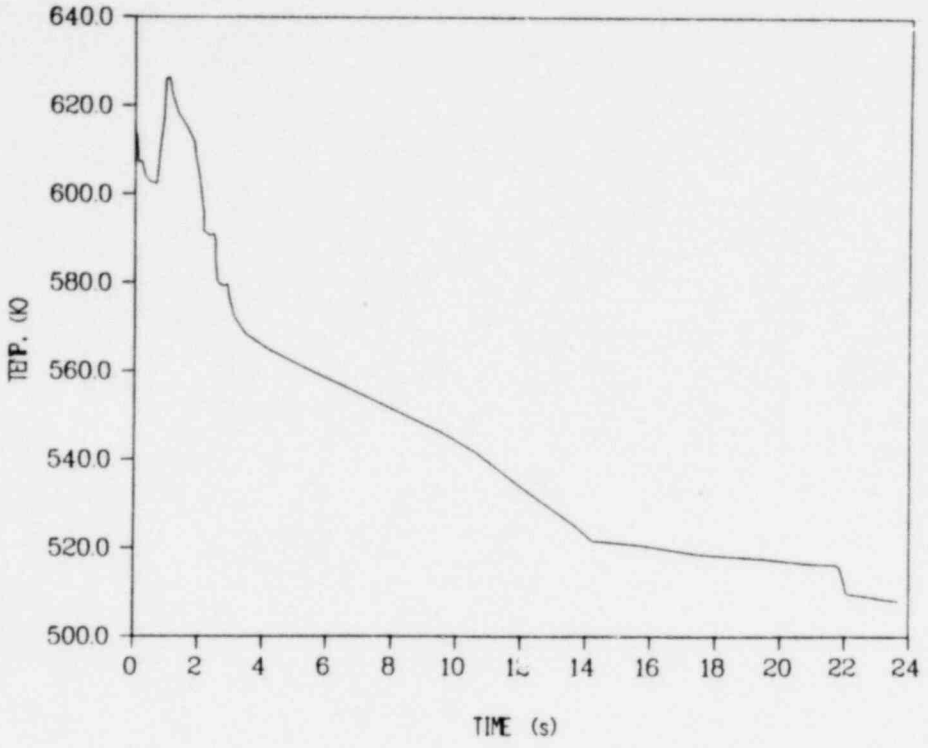


Fig. 30. Maximum average-rod temperature for LOBI test A1-01.

## 5. PKL Test K1.3 Posttest Analysis

(J. W. Spore, Q-6)

A posttest analysis of PKL combined injection test K1.3 was completed to 85.0 s with TRAC-P1A. The PKL test facility is located at Kraftwerk Union (KWU) in Erlangen, West Germany and is a reduced-scale thermal-hydraulics test facility for the study of integral effects during the refill and reflood stages of a LOCA. Significant features of the test facility are:

1. Full-height steam generators,
2. Downcomer simulated with two downcomer pipes,
3. Core containing 340 electrically heated rods in three different radial power zones.
4. Flow plate in the upper plenum, and
5. Three loops employed to simulate the primary system of a PWR.

Significant features of the K[illegible].3 test are:

1. Combined injection (two hot-leg injection points and one cold-leg injection point),

2. Peaked radial (1.21) and axial (1.19) power profiles, and

3. Cold-leg break simulation.

The TRAC model of the test facility consists of 560 cells of which 410 cells are used to model the vessel, external downcomer pipes, and external downcomer chamber. Each of the 3 simulated loops is modeled with 50 fluid cells. The downcomer pipes were modeled as two separate PIPE components. The downcomer chamber was modeled with a VESSEL component as was the main vessel which includes the core and the upper and lower plena.

The TRAC results indicate that several of the low-power and middle-power rods will quench within the first 50 s. This result is consistent with the test results. Early versions of TRAC were unable to predict this behavior. However, the calculated peak clad temperature in the high-power zone is continuing to rise at 85 s, which is inconsistent with the test data. Test data indicate a peak cladding temperature of 920 K at 40 s, at which time the measured cladding temperature decreased slowly to 853 K at 120 s, then quenched. The calculated cladding temperature for the location corresponding to the measured peak is 940 K at 85 s and still rising at 0.25 K/s. Possible sources for this discrepancy are:

1. The one-dimensional drift-flux fluid model employed in the downcomer pipes does not accurately model countercurrent flow, therefore has not allowed the lower plenum to refill at the appropriate rate. This problem will be corrected in later PKL TRAC models by representing the downcomer pipes within the vessel component.

2. The boron nitride thermal properties in TRAC-P1A are significantly different than the thermal properties of the magnesium oxide insulator used in the electrically heated rods.

3. The flow of a liquid film into the core from the upper plenum is retarded in TRAC-P1A due to the lumping of the entrained droplet shear coefficient with the wavy film shear coefficient when determining the average interfacial shear coefficient for annular flow. Later versions of the TRAC code which consider the droplets and the liquid film separately should eliminate this problem.

4. Errors in the TRAC-P1A reflood heat transfer package.

The insufficient penetration of ECC into the lower plenum from the downcomer pipes and into the core from the upper plenum also leads to calculated system pressure surges at several points in the transient which are not apparent in the data. These calculated pressure surges result from the accumulation of subcooled water in the upper plenum and downcomer chamber which eventually is carried to the steam generators. The flashing of this liquid in the steam generators results in the pressurization of the system. Resolution of the problems discussed previously should reduce or eliminate these pressure surges.

Because of the difficulties described above, the posttest analysis of PKL Test K1.3 with TRAC-P1A was discontinued. It is expected that the next release version, TRAC-P1A/MOD-1, will improve the results considerably.

## 6. TRAC Calculations of Semiscale Mod-3 Test S-07-6

(J. J. Pyun, Q-6)

The TRAC-P1A calculation of Semiscale Mod-3 integral LOCA Test S-07-6 was completed. The present TRAC model for this test is identical to that for test S-07-1 reported previously[15] except that the external downcomer distribution annulus and downcomer pipe are modeled within the three-dimensional VESSEL component along with the main reactor vessel. This was done so that countercurrent flow in the downcomer pipe can be treated with the two-fluid model.

The steady-state calculation was performed up to 33.0 s and the transient calculation was run up to 426.0 s. In general, the agreement between the TRAC calculations and experimental data was excellent for the steady-state calculation and the blowdown portion of the transient calculation. However, the TRAC calculation does

not agree with the experimental data very well during the reflood period of the transient calculation. In particular, it was found that the two-fluid hydrodynamic model of the external downcomer pipe, while showing marked improvement over the one-dimensional drift-flux model, still underpredicts the ECC liquid penetration rate into the lower plenum during the reflood period. This is because the interfacial shear coefficient in the two-fluid model is too high for low countercurrent flow velocities. Another factor is that the ECC penetration strongly depends on the heat transfer rate from the downcomer pipe wall to the fluid and this rate is not well known.

An attempt was made to correlate the interfacial shear coefficient for the two-fluid model by matching liquid penetration rate data obtained in air/water countercurrent flow experiments.[16] These calculations are described in the next section.

### 7. TRAC Calculation of Air/Water Countercurrent Flow Flooding Test

(J. J. Pyun, Q-6)

Air/water countercurrent flow flooding tests[16] in vertical tubes were conducted at Dartmouth College to investigate the validity of the Wallis correlation[17] relating gas and liquid fluxes in vertical tubes:

$$\sqrt{J_g^*} + \sqrt{J_\ell^*} = 0.7 \qquad (1)$$

where

$$J_g^* = \frac{\sqrt{\rho_g}\ J_g}{\sqrt{gD(\rho_\ell - \rho_g)}}$$

$$J_\ell^* = \frac{\sqrt{\rho_\ell}\ J_\ell}{\sqrt{gD(\rho_\ell - \rho_g)}}$$

$\rho_g$ = density of vapor phase
$\rho_\ell$ = density of liquid phase

$J_g$ = superficial vapor velocity
$J_\ell$ = superficial liquid velocity
g = gravitational force constant
D = pipe inner diameter (i.d.).

It is well known that this correlation is valid if the pipe i.d. is less than or equal to about 0.05 m. Analysis of these tests was initiated because TRAC calculates less liquid penetration than the experimental data during the reflood period of Semiscale Mod-3 Test S-07-6, even when the two-fluid model is used as discussed in the previous section.

The test facility consists of a vertical transparent pipe (i.e., a flooding tube) about 1.12-m-long and an upper and lower plenum. A 0.21 $m^3$ drum was connected to each and to form upper and lower plenum. Water enters through a 0.05-m pipe into the upper plenum at rates up to about 0.02 $m^3/s$. An overflow was cut out of the side of the upper plenum and excess water is drained away through a spillway. Air enters the side of the lower plenum through a 0.25-m pipe. The flooding tube i.d. was varied from 0.05-0.25 m. However, the present TRAC analysis was limited to the flooding test with a 0.05-m i.d. tube because the downcomer pipe i.d. in Semiscale Mod-3 is approximately 0.05 m.

The test was performed from initial conditions of 273 K and 1 bar. First, air is injected at a flow rate sufficient to stop all water penetration and then the water is turned on. Second, the air flow rate is decreased to allow water penetration into the flooding tube. Finally, the lower plenum water level is measured as a function of time.

Figure 31 shows a detailed TRAC noding diagram for this problem along with a TRAC arrangement of components and junctions. The system is modeled using 6 junctions and 7 components containing 16 fluid cells. The flooding tube is modeled using the two-dimensional VESSEL module containing 10 fluid cells. The air and water are injected by FILLS 7 and 5. The initial conditions were obtained by running a transient calculation in which air is injected at a specified rate until the system air flow rates, pressure, and

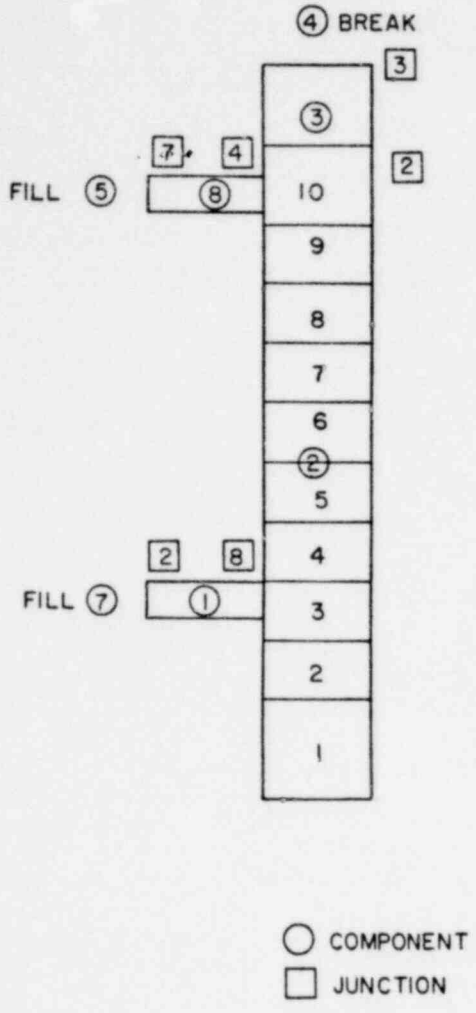


Fig. 31. TRAC noding diagram for air/water countercurrent flow flooding test.

temperature approach their steady-state values. The transient calculation was performed by restarting from the dump file obtained from the steady-state calculation but with water injection from FILL 5.

In general, the TRAC results did not agree very well with the experimental data. An effort is under way to improve the interfacial friction modeling at low relative velocities.

## D. Thermal-Hydraulic Research for Reactor Safety Analysis

(W. C. Rivard, T-3)

The research reported in this section focuses on a description of the FLX code for fluid-structure analysis of the German HDR experiments and on the dynamics of droplet spray flow.

1. The FLX code, which solves the three-dimensional elastic shell equations with finite differences, has been documented. FLX coupled with the three-dimensional K-FIX code has been released to the NESC.

2. Calculations of single cylinder capture efficiency have been made that include the effects of splash. Results show that the droplets that enter the airstream by splash are very unlikely to be recaptured in the cylinder water film, which is consistent with observations for single cylinders.

## 1. The FLX Code for Fluid-Structure Analysis

(W. C. Rivard, M. D. Torrey, and J. K. Dienes, T-3)

The numerical solution of the elastic shell equations for the coupled fluid-structure analysis of core support barrel dynamics is calculated with the FLX code. FLX has been coupled with the three-dimensional K-FIX code[18] and the combination known as K-FIX(3D,FLX) has been documented and released to the NESC for application to the full-scale HDR experiments.

The three-dimensional, linear-elastic, shell equations solved by FLX are:

$$\rho h \ddot{U} = N_\phi^0 + N_{\phi z}' - M_\phi^0/a + M_{z\phi}'/a + \rho h(\ddot{x} \sin\phi - \ddot{y} \cos\phi),$$

$$\rho h \ddot{V} = N_z' + N_{\phi z}^0 - \rho h \ddot{z}, \text{ and} \tag{2}$$

$$\rho h \ddot{W} = q - M_z'' + 2M_z^{0\prime} - M_\phi^{00} - N_\phi/a - \rho h(\ddot{x} \cos\phi + \ddot{y} \sin\phi),$$

where

$$N_z = C(V' + \nu U^0 + \nu W/a),$$

$$N_\phi = C(U^0 + W/a + \nu V'),$$

$$N_{\phi z} = C(1-\nu)(V^0 + U')/2, \tag{3}$$

$$M_z = D(W'' + \nu W^{00} - \nu U^0/a),$$

$$M_\phi = D(W^{00} + \nu W'' - U^0/a),$$

$$M_{z\phi} = -D(1-\nu)(W^{0\prime} - U'/a),$$

and

$$C = Eh/(1-\nu^2), \quad D = Eh^3/12(1-\nu^2). \tag{4}$$

In these equations, U, V, and W are the circumferential, axial, and radial displacements, respectively; $\rho$ is the density; h is the thickness; a is the radius of the middle surface; $\nu$ is Poisson's ratio; q is the differential pressure between the inside and outside of the core barrel (pressure inside-pressure outside); and E is Young's Modulus. The superscript prime denotes differentiation with respect to the axial coordinate z; the superscript zero denotes differentiation with respect to the circumferential coordinate $\phi$; and the dot denotes differentiation with respect to time t. The $\ddot{x}$ and $\ddot{y}$ terms describe two horizontal acceleration components and the $\ddot{z}$ term describes the vertical component of a seismic disturbance. The $\ddot{x}$ component lies in the $\phi = 0°$ plane and the $\ddot{y}$ component lies in the $\phi = 90°$ plane. Both are positive outward in their respective planes. The vertical component $\ddot{z}$ is positive upward. The coordinate directions coincide with those used to describe the three-dimensional fluid dynamics, i.e., the positive directions are counterclockwise, upward, and radially outward.

The accelerations $\ddot{U}$, $\ddot{V}$, and $\ddot{W}$ given by Eq. (2) determine the new velocity and displacement fields from the kinematic relations:

$$\dot{U} = \int \ddot{U} dt \ , \quad U = \int \dot{U} dt \ ,$$

$$\dot{V} = \int \ddot{V} dt \ , \quad V = \int \dot{V} dt \ , \text{ and} \tag{5}$$

$$\dot{W} = \int \ddot{W} dt \ , \quad W = \int \dot{W} dt \ .$$

The core barrel stresses are determined from the forces and moments per unit length in Eq. (3) as

$$\sigma_{zm} = N_z/h \ , \quad \sigma_{zb} = 6M_z/h^2 \ ,$$

$$\sigma_{\phi m} = N_\phi/h \ , \quad \sigma_{\phi b} = 6M_\phi/h^2 \ , \text{ and} \tag{6}$$

$$\sigma_{\phi zm} = N_{\phi z}/h \ , \quad \sigma_{z\phi b} = 6M_{z\phi}/h^2 \ .$$

The stresses with subscripts involving m are membrane stresses. These represent average stress values across the shell thickness in accord with the definitions

$$N_z \equiv \int_{-h/2}^{h/2} \sigma_z(\eta,z,\phi)d\eta \ ,$$

$$N_\phi \equiv \int_{-h/2}^{h/2} \sigma_\phi(\eta,z,\phi)d\eta \ ,$$

and

$$N_{\phi z} \equiv \int_{-h/2}^{h/2} \tau_{\phi z}(\eta,z,\phi)d\eta \ ,$$

where $\sigma_z$, $\sigma_\phi$, and $\tau_{\phi z}$ are local tensile and shear stresses. The stresses with subscripts involving b are bending stresses and provide information on the antisymmetric character of the stresses $\sigma_z$, $\sigma_\phi$, and $\tau_{\phi z}$ through the definitions

$$M_z \equiv \int_{-h/2}^{h/2} \eta\sigma_z(\eta,z,\phi)d\eta \ ,$$

$$M_\phi \equiv \int_{-h/2}^{h/2} \eta\sigma_\phi(\eta,z,\phi)d\eta \ ,$$

and

$$M_{z\phi} \equiv \int_{-h/2}^{h/2} \eta\tau_\phi(\eta,z,\phi)d\eta \ .$$

If, for example, we write the antisymmetric part of $\sigma_z$ as $\sigma_{z_2} = 2\eta\sigma_{zb}/h$ we obtain from the definition of $M_z$ that $\sigma_{zb} = 6M_z/h^2$, which is the result given in Eq. (6). The total stress at any

position across the core barrel thickness is the sum of the membrane and bending stresses.

The top boundary of the core barrel is modeled mathematically as a clamped or built-in boundary along which we require[19] that

$$U = V = W = W' = 0 \ . \tag{7}$$

The bottom of the core barrel is a free boundary along which forces and moments vanish. This boundary condition is described mathematically by

$$N_z = N_{\phi z} = M_z = 0 \text{ and}$$

$$M_z' - 2M^0_{z\phi} = 0 \ . \tag{8}$$

Equation (8) reduces to the classical Kirchhoff boundary conditions for the free edge of a plate where $N_z$ and $N_{\phi z}$ are identically zero and only lateral deflections (W-displacements) are considered.

The shell equations, Eqs. (2)-(5), are solved numerically by explicit integration of a system of finite difference equations. The middle surface of radius a is divided into many computational cells that form collectively the computing mesh. The circumferential dimension of each cell $\delta s = a\delta\phi$ is constant but the axial dimension $\delta z$ can vary from one row of cells to the next. The quantities W, $N_z$, $N_\phi$, $M_z$, and $M_\phi$ are located at the cell center, U is located at the center of the right boundary, V is located at the center of the top boundary, and $N_{\phi z}$ and $M_{z\phi}$ are located at the upper right corner as shown in Fig. 32.

The finite difference calculation begins by computing the forces and moments per unit length from the following finite difference approximations to Eq. (3).

$$(N_z)_{m,n} = C[(V_{m,n} - V_{m,n-1})/\delta z_n + \nu(U_{m,n} - U_{m-1,n})/\delta s + \nu W_{m,n}/a],$$

$$(N_\phi)_{m,n} = C[(U_{m,n} - U_{m-1,n})/\delta s + W_{m,n}/a + \nu(V_{m,n} - V_{m,n-1})/\delta z_n]$$

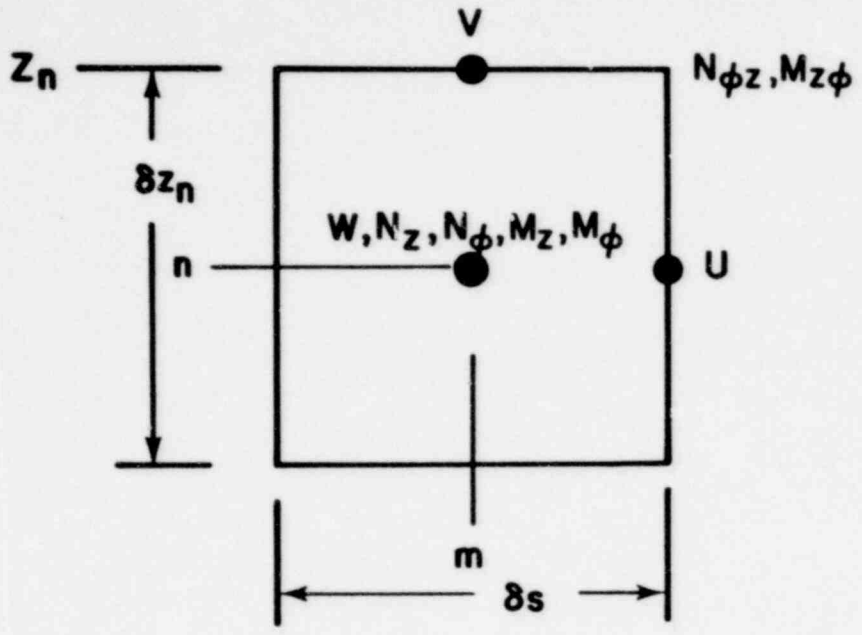


Fig. 32. Location of variables for computational cell (m,n).

$$(N_{\phi z})_{m+\frac{1}{2},n+\frac{1}{2}} = C(1-\nu)[(V_{m+1,n} - V_{m,n})/\delta s + 2(U_{m,n+1} - U_{m,n})/(\delta z_n + \delta z_{n+1})],$$

$$(M_z)_{m,n} = D\{2[(W_{m,n+1} - W_{m,n})/(\delta z_n + z_{n+1}) - (W_{m,n} - W_{m,n-1})/(\delta z_n + \delta z_{n-1})]/\delta z_n + \nu(W_{m+1,n} - 2W_{m,n} + W_{m-1,n})/\delta s^2 - \nu(U_{m,n} - U_{m-1,n})/a\delta s\},$$

$$(M_\phi)_{m,n} = D\{(W_{m+1,n} - 2W_{m,n} + W_{m-1,n})/\delta s^2 + 2\nu[(W_{m,n+1} - W_{m,n})/(\delta z_n + \delta z_{n+1}) - (W_{m,n} - W_{m,n-1})/(\delta z_n + \delta z_{n-1})]/\delta z_n - (U_{m,n} - U_{m-1,n})/a\delta s\},$$

and

$$(M_{z\phi})_{m+\frac{1}{2},n+\frac{1}{2}} = -2D(1-\nu)\{[(W_{m+1,n+1} - W_{m,n+1})/\delta s$$

$$- (W_{m+1,n} - W_{m,n})/\delta s$$

$$- (U_{m,n+1} - U_{m,n})/a\}/(\delta z_n + \delta z_{n+1}) .$$

The displacements in these expressions are all known from the solution at the previous cycle. Accelerations are computed from the following finite-difference approximations to Eq. (2).

$$\ddot{U}_{m,n} = (1/\rho h)\{[(N_\phi)_{m+1,n} - (N_\phi)_{m,n}]/\delta s$$

$$+ [(N_{\phi z})_{m,n} - (N_{\phi z})_{m,n-1}]/\delta z_n$$

$$- [(M_\phi)_{m+1,n} - (M_\phi)_{m,n}]/a\delta s$$

$$+ [(M_{\phi z})_{m,n} - (M_{\phi z})_{m,n-1}]/a\delta z_n\}$$

$$+ \ddot{x} \sin\phi - \ddot{y} \cos\phi ,$$

$$\ddot{V}_{m,n} = (1/\rho h)\{[(N_z)_{m,n+1} - (N_z)_{m,n}]/(\delta z_n + \delta z_{n+1})$$

$$+ [(N_{\phi z})_{m,n} - (N_{\phi z})_{m-1,n}]/\delta s\} - \ddot{z} ,$$

$$\ddot{W}_{m,n} = (1/\rho h)\Big(q_{m,n} - 2\{[(M_z)_{m,n+1} - (M_z)_{m,n}]/(\delta z_n + \delta z_{n+1})$$

$$- [(M_z)_{m,n} - (M_z)_{m,n-1}]/(\delta z_n + \delta z_{n-1})\}/\delta z_n$$

$$+ 2\{[(M_{z\phi})_{m,n} - (M_{z\phi})_{m-1,n}]/\delta s\,[(M_{z\phi})_{m,n-1}$$

$$- (M_{z\phi})_{m-1,n-1}]/\delta s\}/\delta z_n - [(M_\phi)_{m+1,n}$$

$$- 2(M_\phi)_{m,n} + (M_\phi)_{m-1,n}]/\delta s^2 - (N_\phi)_{m,n}/a\Big)$$

$$- \ddot{x} \cos\phi - \ddot{y} \sin\phi . \qquad (9)$$

New velocities and then new displacements are computed from the kinematic relations in Eq. (5) as

$$\dot{U}_{m,n} = \dot{U}_{m,n} + \delta t_s \ddot{U}_{m,n} \quad , \quad U_{m,n} = U_{m,n} + \delta t_s \dot{U}_{m,n} \ ,$$

$$\dot{V}_{m,n} = \dot{V}_{m,n} + \delta t_s \ddot{V}_{m,n} \quad , \quad V_{m,n} = V_{m,n} + \delta t_s \dot{V}_{m,n} \ , \quad \text{and}$$

$$\dot{W}_{m,n} = \dot{W}_{m,n} + \delta t_s \ddot{W}_{m,n} \quad , \quad W_{m,n} = W_{m,n} + \delta t_s \dot{W}_{m,n} \ ,$$

where $\delta t_s$ is the integration time step for the shell equations.

To enforce the boundary conditions in Eq. (7) in the computing mesh, we set

$$\begin{aligned} U_{m,NB2} &= - U_{m,NB1} \ , \\ V_{m,NB1} &= 0 \ , \text{ and} \\ W_{m,NB1} &= W_{m,NB2} = 0 \ , \end{aligned} \tag{10}$$

where n = NB1 refers to the row of cells around the top of the core barrel and n = NB2 refers to the row of cells above NB1, which are fictitious and only used for setting boundary conditions. Such fictitious cells surround the entire perimeter of the mesh. Equation (10) reflects our choice of $\delta z_{NB2} = \delta z_{NB1}$ in that the value of U at the core barrel top, obtained by arithmetic average, is zero.

The first three conditions in Eq. (8) are enforced in the computing mesh by appropriately setting the U, V, and W displacements in the fictitious row below the core barrel bottom. From the condition that $N_Z = 0$, we obtain

$$V_{m,1} = V_{m,2} + \delta z_2 \, \nu[(U_{m,2} - U_{m-1,2})/\delta s + W_{m,2}/a] \ , \tag{11}$$

from $N_{\phi Z}$ we obtain

$$U_{m,1} = U_{m,2} + \delta z_2 \, (V_{m+1,1} - V_{m,1})/\delta s \ , \tag{12}$$

and from $M_z = 0$, we obtain

$$W_{m,1} = W_{m,2} - 2\delta z_2 (W_{m,3} - W_{m,2})/(\delta z_2 + \delta z_3)$$

$$-\nu(\delta z_2)^2 \left[(W_{m+1,2} - 2W_{m,2} + W_{m-1,2})/(\delta s)^2\right.$$

$$\left. - (U_{m,2} - U_{m-1,2})/a\delta s\right] . \qquad (13)$$

Equations (11)-(13) reflect our choice of $\delta z_1 = \delta z_2$, which simplifies the equations. The final condition in Eq. (8) is satisfied by specifying $(M_z)_{m,1}$ through the relation

$$(M_z)_{m,1} = - 2\delta z_2 [(M_{z\phi})_{m,1} - (M_{z\phi})_{m-1,1}]/\delta s \qquad (14)$$

where we have used the fact that $(M_z)_{m,2} = 0$. $M_{z\phi}$ at n = 1 is evaluated using the displacements that have been determined by Eqs. (12) and (13).

The FLX code has been checked by comparisons with a variety of analytic solutions. The comparisons include calculations of added mass effects, core barrel torsional vibration modes and frequencies, lateral vibration frequencies that include effects of both shear and bending, and breathing mode vibrations. Limited comparisons with small-scale test data have also been made.

## 2. Collection Efficiency for Droplet Impingement in Circular Cylinders

(H. M. Ruppel and F. M. Harlow, T-3)

The capture efficiency for droplets impinging on one or several cylinders has been shown to depend on a variety of factors, some of which can be controlled by the experimentor and others of which depend on the detailed local-scale dynamics.

We have developed computational tools that enable us to examine both single cylinder and multicylinder capture efficiencies. Thus far, we have concentrated on conducting a detailed examination of the effects of several variables on single cylinder capture efficiency. The results of our investigation shed considerable light on the relative importance of the various factors and have

significant implications regarding the capture efficiency for an array of cylinders.

In the single-cylinder experiments, there are several conditions that are under direct control. The cylinder diameter, stand-off distance of the water nozzles, wind speed, and volumetric flux of water can be specified to whatever degree of accuracy is required. The droplet velocity and size spectrum, however, can be controlled only approximately, and estimates of their values are difficult.

After release from the nozzle, the trajectory of a water droplet will be affected in two ways by the wind, to an extent that depends upon the effectiveness of the wind-droplet momentum exchange. Ultimately, the crucial parameter in this interaction is the droplet size. The two effects of momentum exchange are, first, the tendency for the droplet and wind velocities to equilibrate; and, second, the tendency for the droplet to be deflected away from impingement on the cylinder by lateral forces in the region of the curved streamlines. Both of these momentum-exchange effects have been calculated with considerable accuracy, leading to a valid description of this primary-capture part of the collection efficiency. The neglect of collective effects among the droplets is an acceptable approximation for the current experimental circumstances, in which the mean-volume fraction of water is very small. For volume fractions well above 1%, however, these collective effects could become significant and must be included in any relevant analysis.

Once the droplet has contacted the cylinder surface or the film of water that coats most of the upstream part of that surface, the dynamical interactions become considerably more complicated. Part of the droplet water may join the film, ultimately splitting into a fraction that is permanently captured (i.e., falls to the collecting reservoir at the bottom of the cylinder) and a fraction that is lost (i.e., sheared or splashed from the film and reentrained into the wind). The remaining part directly splashes back into the wind, with a spectrum of fragment sizes and velocities that depends on film thickness, impingement angle, and the size and velocity of the impinging droplet. Detailed modeling of these

phenomena is beyond the scope of this investigation. For the present, we are studying the possibility of correlating the results by means of splash parameters, f, g, and h, describing the fraction of impingement velocity carried by the splash droplets, the fraction of size scale, and the fraction of total mass.

Detailed trajectory calculations for individual splash-back droplets show that under most circumstances they are permanently lost from the inventory of water that could be collected. Figure 33 shows several examples that we have calculated to demonstrate this almost inevitable loss of the splash-back droplets. Each example is characterized by the angle $\theta$ in radians that measures the departure of the impingement point from the leading edge. For these calculations, the splash-back droplets are injected into the stream along the normal to the cylinder surface at the impingement

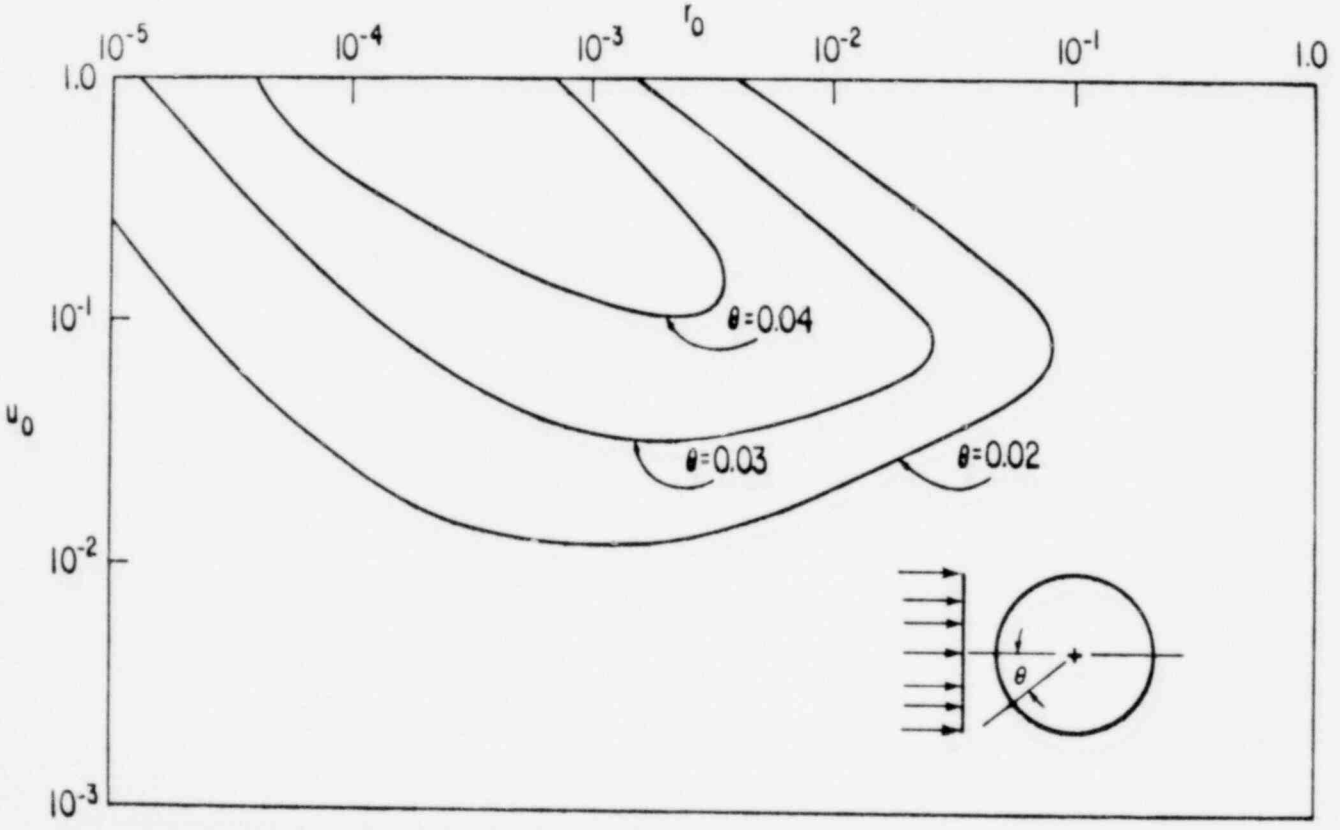


Fig. 33. Contours of the boundary between loss of recapture of a splash-back droplet, as a function of droplet radius, $r_o$, measured in cm, and the ratio of droplet splash-back speed to free-stream wind speed, $u_o$. Within each contour, characterized by the angle $\theta$ between the upstream wind direction and cylinder surface normal, the droplet is ultimately recaptured.

point. In the two-dimensional space of droplet speed and radius, there is only a very small region representing the droplets that subsequently impinge back onto the cylinder.

In general, for splash-back droplets that have a re-entry velocity in a direction other than the normal to the cylinder surface, there is a small range of injection angles for which reimpingement is possible. We have not yet calculated all possible circumstances, but the present tentative conclusion is that the contribution to one-cylinder collection efficiency from the recapture of splashed droplets is small.

The part of the impinging primary droplet that joins the adhering film commences to migrate with the film both downwards towards the collection reservoir and laterally towards the sides of the cylinder (i.e., the region that lies near 90° from the line of primary inflow of wind and droplets towards the cylinder). As the fluid approaches the sides, it becomes more and more susceptible to removal from the film, as a result of the splash from primary-droplet impingement and the interface instability and shear produced by the wind. Again, the detailed dynamics of the film rupture is of considerable complexity. Inclusion of an angular dependence in one or more of the splash coefficients may allow a satisfactory correlation of the results with the available experimental data.

At present, however, our principal interest is to extend our study of collection efficiency to an array of cylinders. Whereas the splash-back droplets from any one cylinder are unlikely to reimpinge on that same cylinder, their entrainment by the wind makes them an important consideration for subsequent impingement on other cylinders further downstream. The particular strength of our computing code is that it allows us to examine this specific aspect of the collection efficiency problem in considerable detail.

## E. LWR Experiments

(W. L. Kirchner, Q-8)

The objectives of LASL's LWR Safety Experimental Program remain to provide experimental support for model development activities and to develop advanced instrumentation techniques. The program is conducted in close cooperation with code and model development efforts at LASL and is coordinated with the multinational 2D/3D program for which rod lens systems are being provided.

The first rod lens viewing system was successfully tested in the PKL facility during this quarter. Fabrication and testing of a second unit to be used in the CCTF at Tokai, Japan, was essentially completed. Improved de-entrainment measurements were taken in the small wind tunnel and are presented below.

### 1. Upper Plenum De-entrainment Experiment

(J. C. Dallman, W. L. Kirchner, and D. B. Johnson, Q-8)

Additional measurements of dispersed flow droplet de-entrainment on single structures (cylindrical or square rods) have been completed for the range of parameters possible in the small wind tunnel (0-14 m/s air velocity and up to 45 kg/s water flow). Figures 34 through 36 give the results of these measurements for air velocities of 7 and 14 m/s. These results supercede those presented in Ref. 12. The spray capture efficiency, $\eta$, is the ratio of the liquid mass de-entrained to the total liquid mass intercepted by the cylinder. For mass flux rates greater than about 2 $kg/m^2s$, no substantial dependence of capture efficiency on tube diameter is evident; however, the 76.2-mm-square tube (with face perpendicular to mean flow) did exhibit a slightly higher de-entrainment efficiency. Air velocity, for the limited range available, does not appear to have a measurable effect on capture efficiency at high mass flux rates. Using estimates of mean-drop velocities, a weak dependence of capture efficiency is evident from a comparison of Figs. 34 through 36. A more complete analysis of these measurements is under way, and a full topical report is being prepared to detail these analyses.

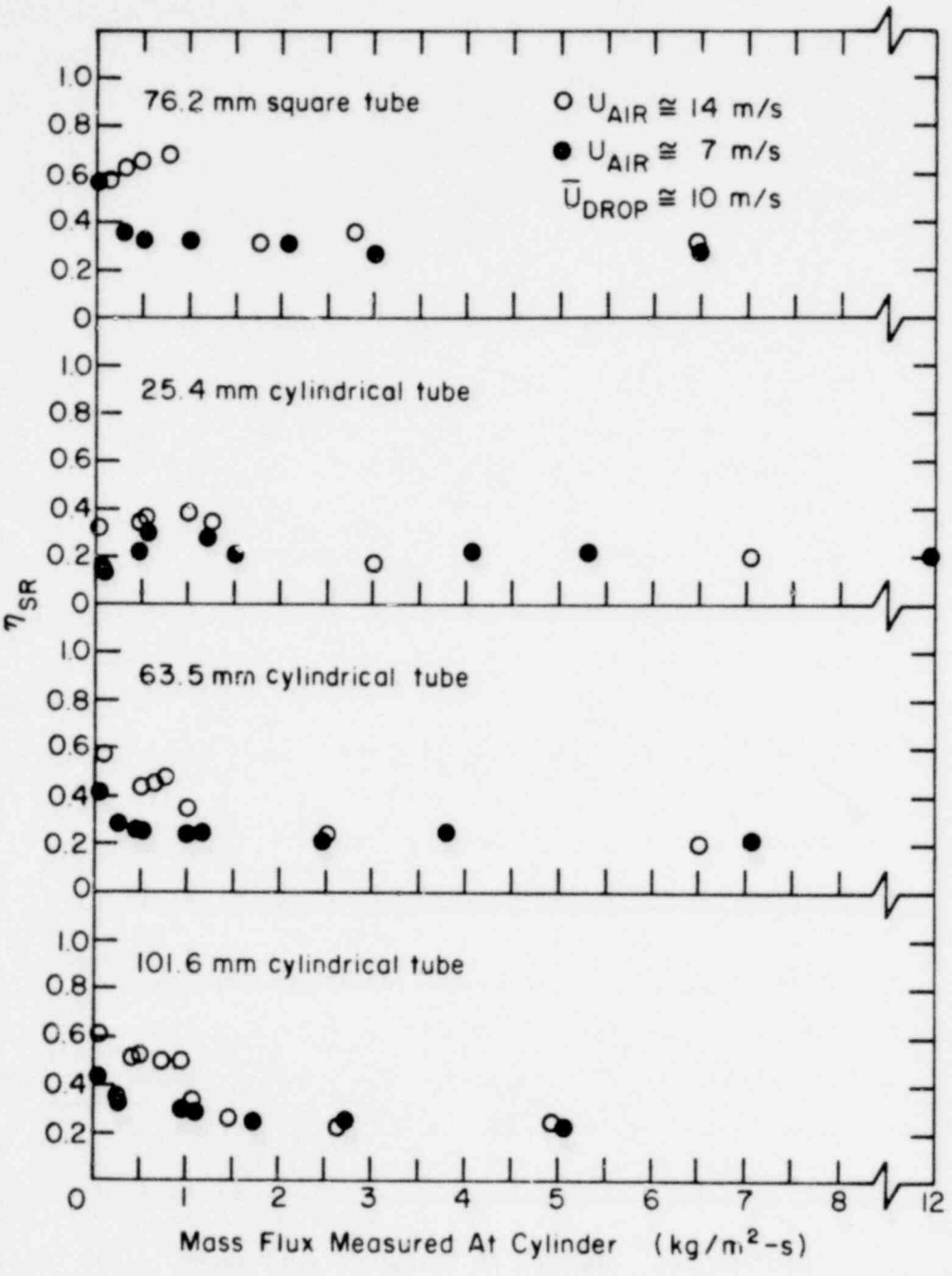


Fig. 34. De-entrainment efficiencies of isolated tubes in air-droplet cross flow with a mean-droplet velocity of approximately 10 m/s.

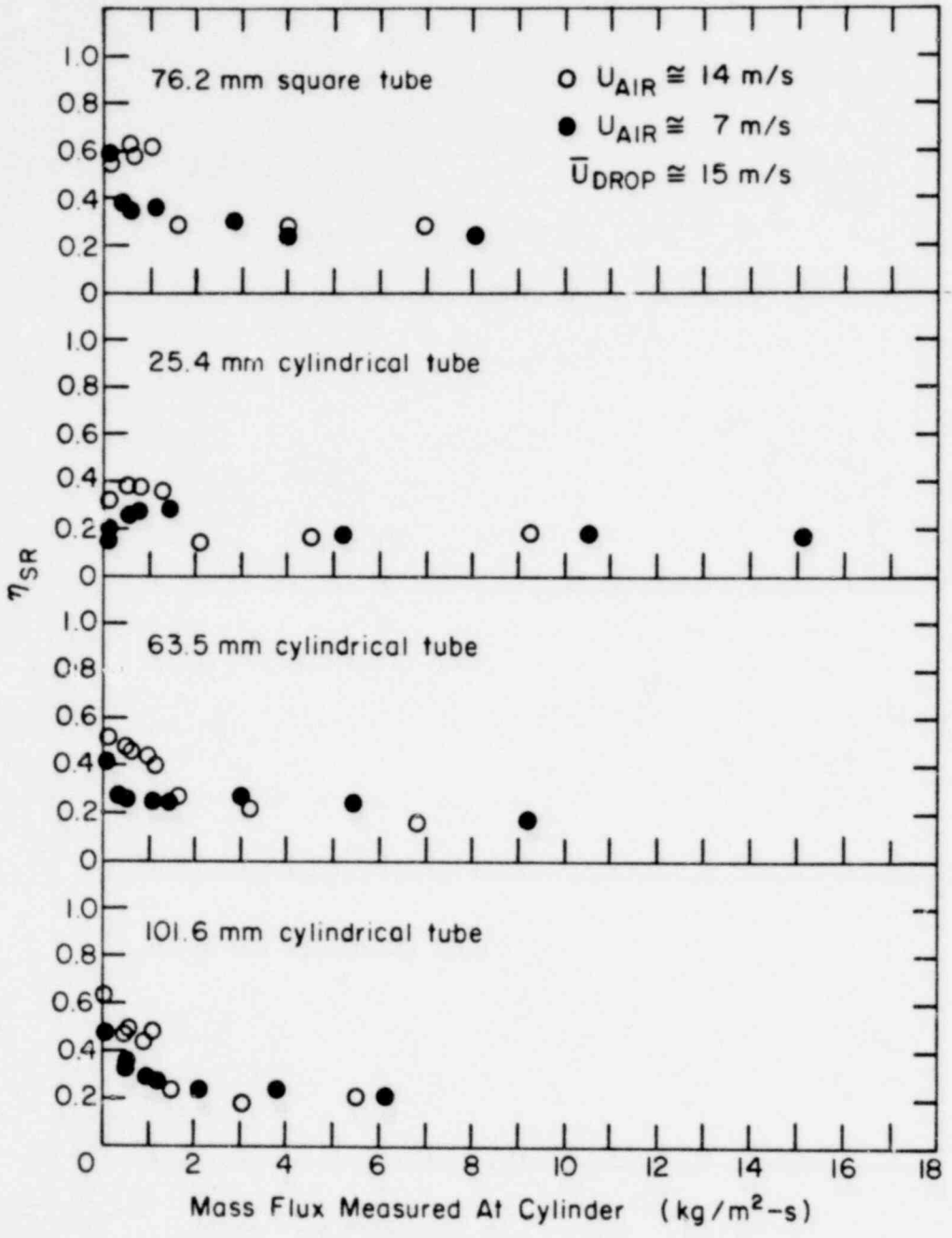


Fig. 35. De-entrainment efficiencies of isolated tubes in air-droplet cross flow with a mean-droplet velocity of approximately 15 m/s.

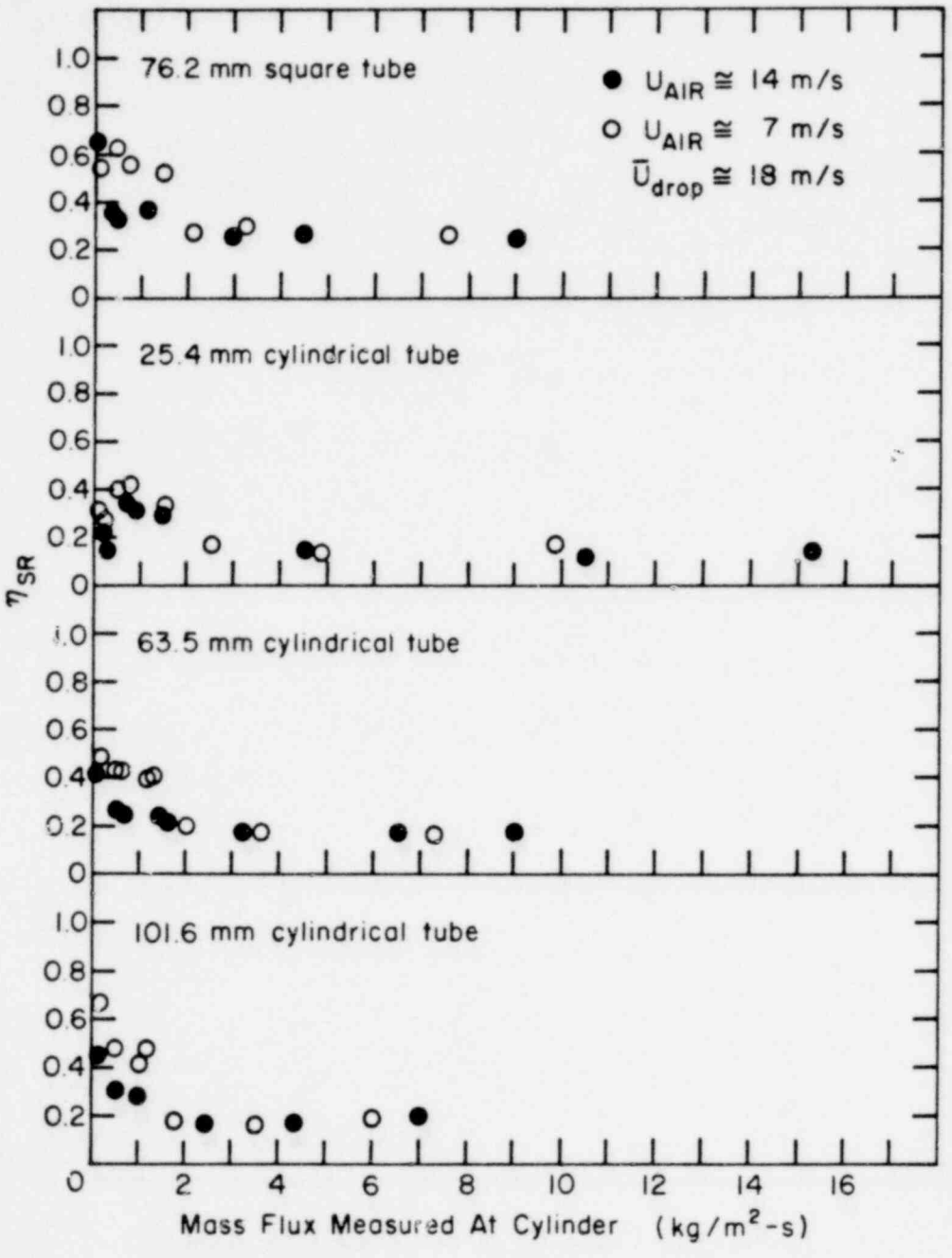


Fig. 36. De-entrainment efficiencies of isolated tubes in air-droplet cross flow with a mean-droplet velocity of approximately 18 m/s.

# III. LMFBR SAFETY RESEARCH

(M. G. Stevenson, Q-DO and J. E. Boudreau, Q-7)

The LMFBR safety research effort at LASL consists of several programs. In the first of these, the SIMMER code is being developed and applied to core disruptive accident (CDA) analysis with support from the Division of Reactor Safety Research (RSR) of NRC. SIMMER is a two-dimensional, coupled neutronics-fluid dynamics code intended for transition phase, core disassembly, and extended fuel-motion analysis. The second version of the code, SIMMER-II, has been completed and is now being used in the analysis of CDA problems.

In a separate, but closely related program funded by DOE, models are being developed for phenomena important to the progression and consequences of CDAs. Some of this work is basic research on phenomena, but in most cases the developed models will be included directly in accident analysis codes and, particularly, in SIMMER. Another part of this DOE program is focused on the application of the accident codes, particularly the SIMMER code, to the study of specific aspects of accident sequences. The work in the SIMMER code development and application area is reported in Sec. III.A.

Experimental investigation, including confirmation of reactor safety analysis methods, is an important part of safety research. Section III.B provides a summary of recent analytical and experimental work in a program funded by NRC/RSR to support SIMMER model development and testing.

## A. SIMMER Code Development and Applications

(L. L. Smith and C. R. Bell, Q-7)

Work in the energetics and single-subassembly transition-phase area is presented below. The single-subassembly transition-phase work is related to the need for a complete heatup, boiling, and disruption treatment of some channels in whole-core transition-phase assessments. The results of a SIMMER-II analysis presented

here indicate agreement with SAS3A is adequate to proceed with application of the SIMMER-II treatment to the whole-core problem. The energetics work provides a perspective for indicating the influence of real (nonideal) processes on the Clinch River Breeder Reactor (CRBR) tolerance for energetic accidents. This perspective also provides some insight on the influence of design features on the system tolerance.

### 1. SIMMER-II Analysis of CRBR Single-Subassembly Behavior in a Transient Undercooling Accident

(G. P. DeVault, Q-7)

SIMMER-II is being used to investigate the behavior and relocation of reactor materials within a single subassembly during a loss-of-flow (LOF) CDA. This one-dimensional analysis of the subassembly accounts for only axial variation of physical variables. Radial variations are not included; these are modeled by a lumped parameter formulation. For a geometric representation of the problem, see Fig. 37.

Preliminary calculations were made with SIMMER-II

1. to establish a given steady state and
2. to allow for pump or flow coastdown with the associated power bursts, voiding, melting, and material relocation well into the transition phase.

These calculations were used to establish a base case for future single-subassembly sensitivity analyses that will include variations in parameters and models.

Comparisons were made with the results of the SAS3A calculation for the CRBR Base Case 1, Channel 1.[20] The SAS3A code is quasi-three dimensional in its multichannel core treatment with detailed one-dimensional models for coolant voiding, cladding, fuel motion, and associated heat transfer in each channel. Boundary and initial conditions were required for our calculations and were inferred from the SAS3A base case. In particular, SAS3A gives initial axial distributions of pressure and average temperature for steady-state operation and the transient calculation provides the power and

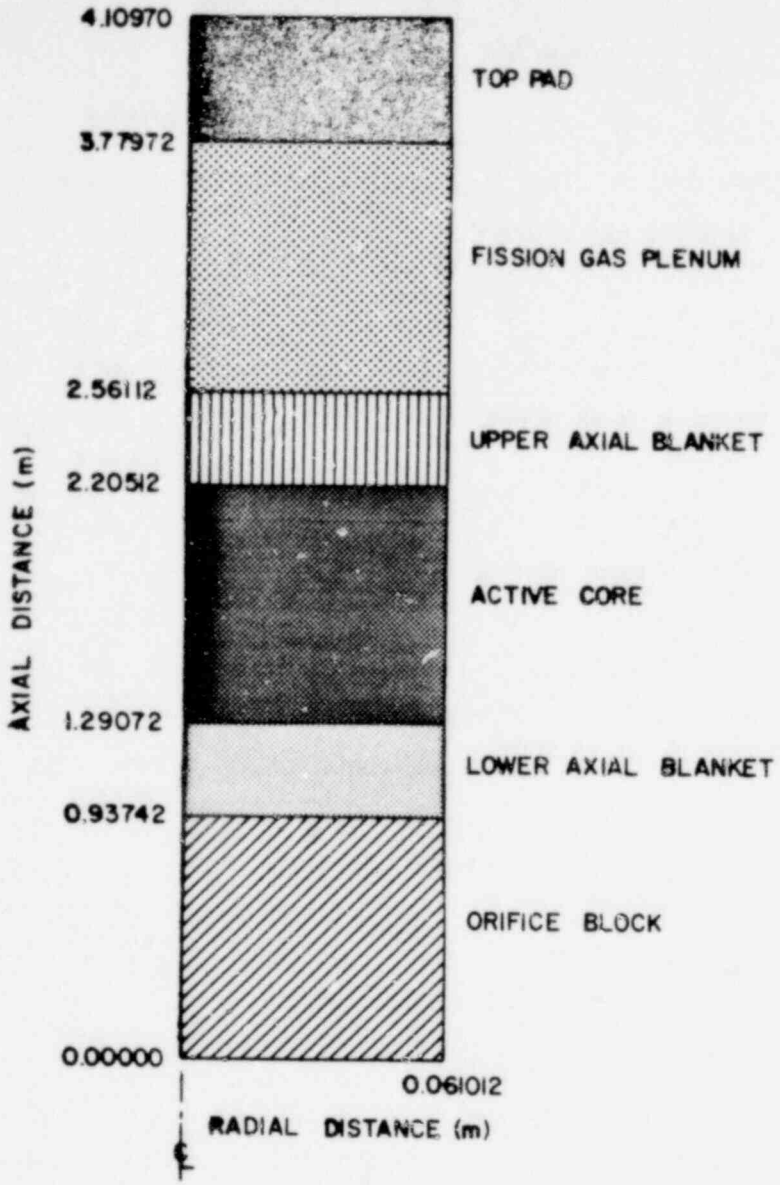


Fig. 37. Geometry of single-subassembly SIMMER-II calculation.

boundary pressure histories. Because SAS3A also uses temperature-dependent material properties, it was necessary to determine space-time average temperatures for the fuel, cladding, and coolant so that mean values of thermal conductivities and specific heats could be computed for use in SIMMER-II.

SAS3A starts its transient calculation from a steady-state single-phase coolant situation that is difficult to input and maintain in SIMMER-II. For example, the subassembly is filled initially with liquid sodium having a total mass flow equal to that of the SAS3A calculation. However, for SIMMER-II calculations, a specified

amount of vapor must be present even for such a single-phase flow. Thus, an analytic computation of values for the frictional-drag and orifice pressure-drop coefficients requires resolution of both the liquid and vapor momentum-conservation equations, which are coupled by an interfield drag force, to maintain velocity and pressure profiles.

Once an acceptable hydrodynamic steady state is found, the heat transfer processes may be made effective and constant nominal power can be turned on. The steady state now amounts to having the sodium carry heat away at the same rate it is being generated. It was necessary to include in the fuel pellet heat conductance a contribution from the fuel-cladding gap (the latter is about equal to the original pellet conductance). This effective pellet conductance then was varied within its error bounds to find a value that would hold the fuel temperature steady.

After achieving steady state, we applied the transient power and boundary pressures corresponding to pump coastdown. The resulting velocity coastdown to the start of sodium boiling agreed extremely well with the SAS3A calculation. Some minor adjustment was necessary to make the onset of voiding time of 11.8 s agree with SAS3A. During this period the system was always in a quasi-steady state (mild transient), so changing the pellet conductance had little effect on the start of boiling. Such a variation changed the fuel temperature, but the heat flux leaving the pellet remained very nearly the same. The controlling quantity was the coolant specific heat; it was necessary to decrease it by 4% below the average SAS3A value. Figure 38 gives a comparison of the cladding and fuel axial temperature profiles with the SAS3A results. The agreement is quite good, indicating the lumped-node heat transfer models of SIMMER-II are adequate in this application.

We continued the calculation to the initiation of cladding melting, which occurs in both SIMMER-II and SAS3A at 1.9 s after the onset of voiding. Figure 39 reflects the comparison of cladding and fuel temperature profiles for the two codes. The fuel temperatures agree very well, but there are some notable differences in the cladding profiles. First, the melting temperature of

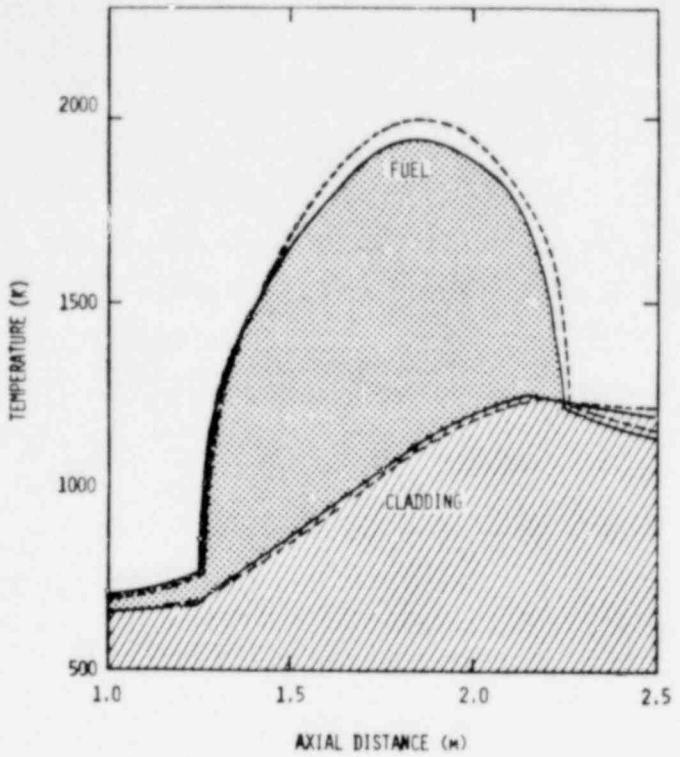


Fig. 38. Comparison of SIMMER-II and SAS3A temperature profiles at 0.1 s before the start of boiling, (SIMMER-II ——, SAS3A ---).

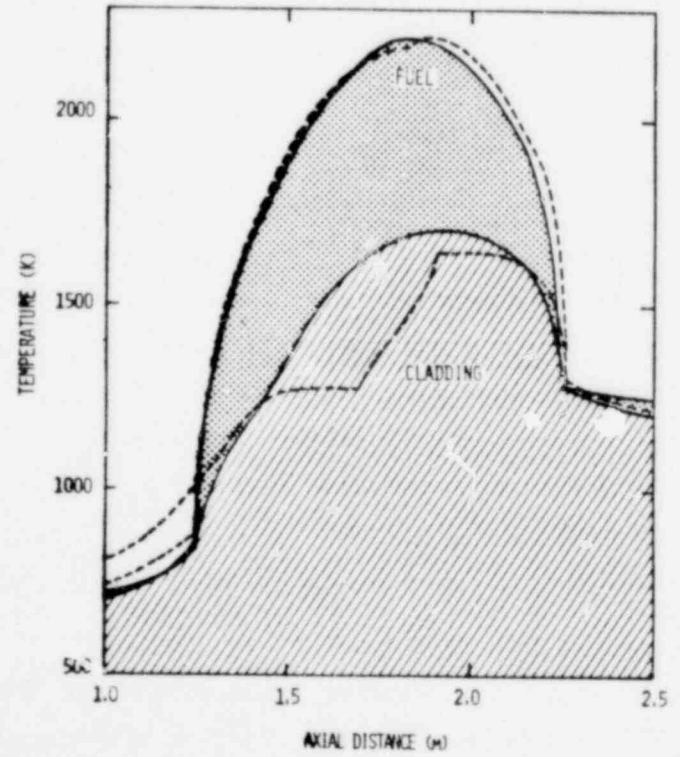


Fig. 39. Comparison of SIMMER-II and SAS3A temperature profiles at 1.> s after the start of boiling (SIMMER-II ——), SAS3A ---).

the cladding used by the two codes was not the same; the SAS3A calculation used 1 643 K while SIMMER-II used 1 700 K. Second, the SAS3A cladding temperature is higher in the lower axial blanket and becomes lower in the bottom half of the core. This seems to be related to the film boiling model used by SAS3A; as the voiding interface moves downward, it leaves a sodium film on the cladding that maintains very efficient heat transfer from the cladding until the film is gone. The resulting increase in pressure causes the interface to overshoot in its downward motion and chugging occurs. In subsequent SAS3A calculations not reported here, the interface chugging was removed by modifying the sodium film model to eliminate sodium film motion once cladding melting has started.[21]

### 2. Tolerance of LMFBR Containment Systems for Energetic Accidents

(C. R. Bell, Q-7)

The capacity of an LMFBR system to withstand energetic CDAs is related to many complex phenomena such as core expansion dynamics, thermal interactions, phase changes, coupled fluid/structure dynamics, primary system failure mechanics, sodium fires, missile generation and dynamics, and containment building failure mechanics. To claim true system tolerance, all these phenomena must be understood thoroughly by reactor designers. Because the level of understanding is directly related to research and development costs, judgments must be made to maximize the gain in system capability for limited allocation of resources. We must therefore determine the influence of various groups of energetic accidents on containment vessels and evaluate possible design changes to augment system tolerance.

Figure 40 qualitatively presents the impact of various nonideal processes during postdisassembly fuel expansion and reflects both design uncertainties and possible options in the CRBR.[22] The thermodynamic work potential shown on the abscissa can be considered either the result of an isentropic fuel-vapor or a Hicks-Menzies[23] sodium vapor expansion. The reactivity insertion rates that relate to the thermodynamic work potentials for the cases examined are

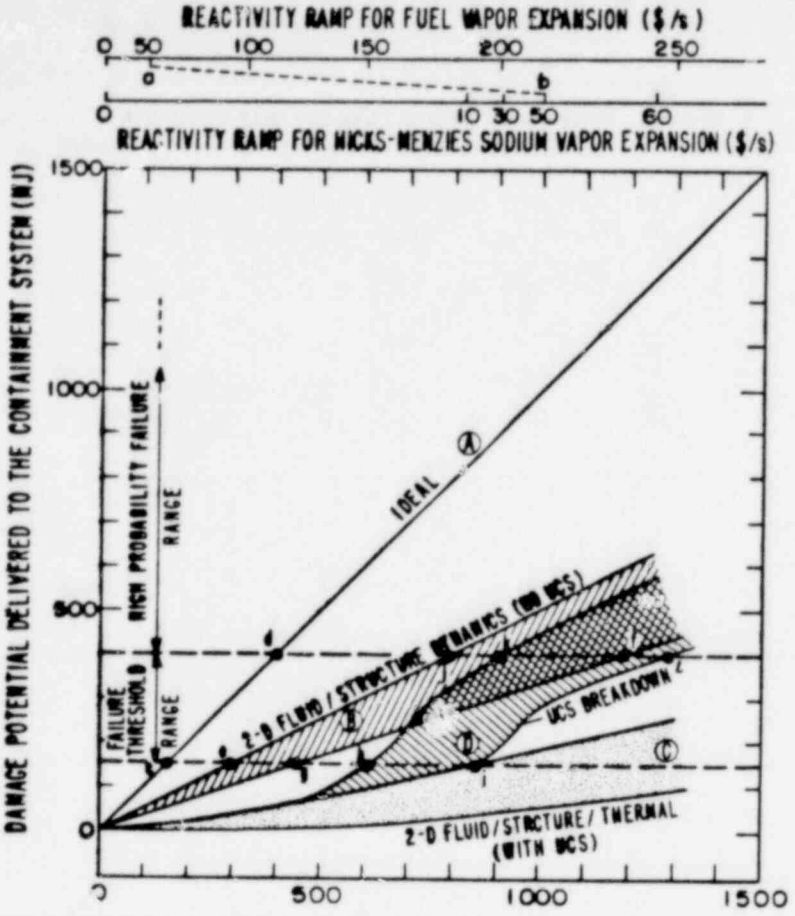


Fig. 40. Thermodynamic work potential (MJ) for expansion to the CRBR cover gas volume.

shown at the top of the figure. Transfer lines between the two scales (line a-b, for example) indicate constant reactivity insertion rates as a function of increasing sodium involvement in the expansion. (Sodium involvement is defined as the percentage of the optimum Hicks-Menzies work potential that can be produced.) The ordinate of Fig. 40 is pool kinetic energy at impact with the reactor closure system and can be interpreted loosely as damage potential. This kinetic energy may not correspond to real damage because the impact dynamics will strongly influence the transient forces developed in the system.

For CRBR, shown schematically in Fig. 41, a range may be estimated for impact kinetic energies leading to early primary heat transport system (PHTS) and reactor containment building (RCB) failure. The lower limit is conservative and may be associated with ideal sodium-fire pressurization of the RCB caused by sodium

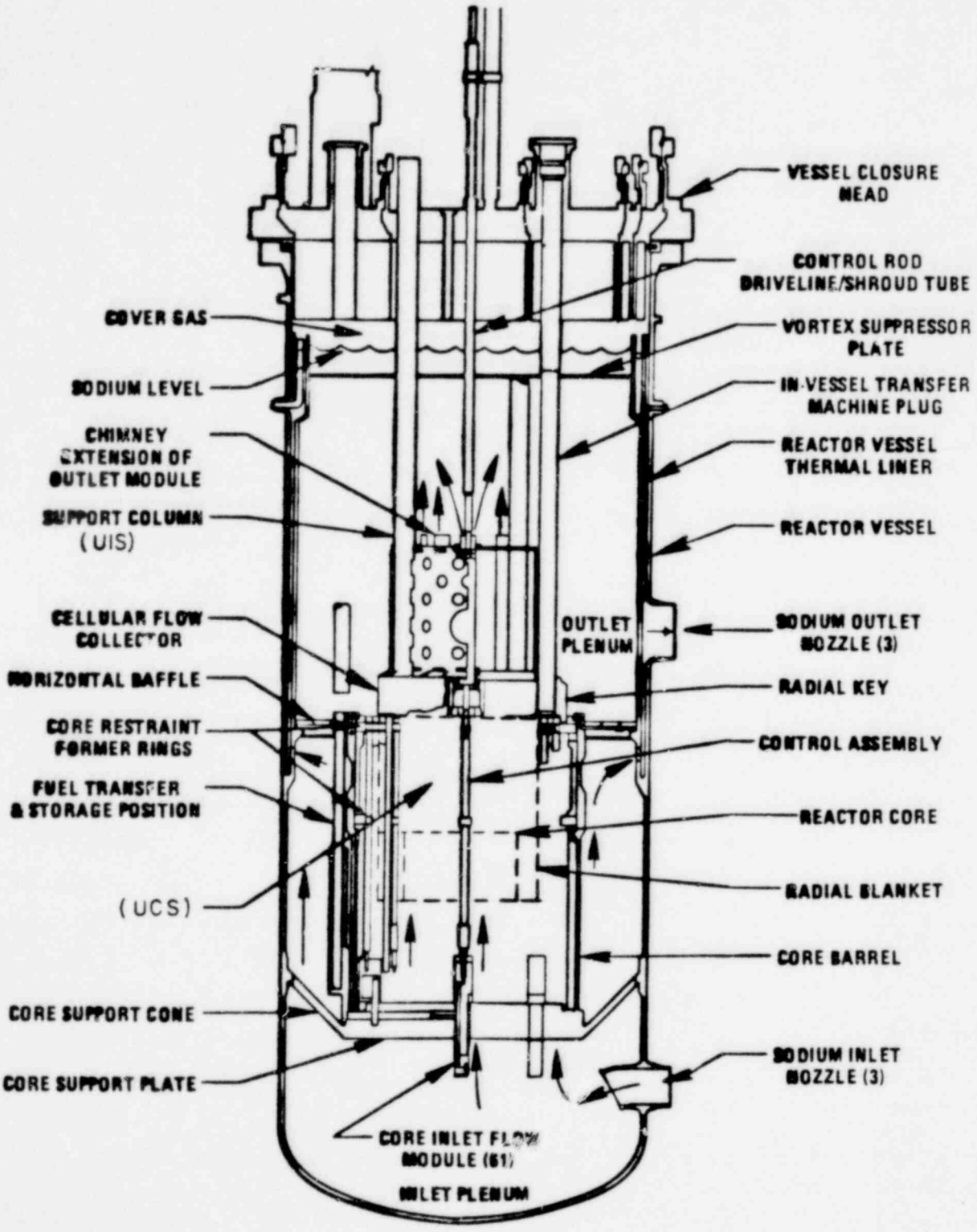


Fig. 41. CRBR schematic.[20]

1320 258

discharge through the reactor head and with "free body" missile generation. There is also a damage potential level at which the containment system will fail with higher certainty. We have estimated this level to be about 400 MJ (expansion to the cover gas volume) for the CRBR based on impact pressures at or above one-half the yield strength of the reactor head material. This level is uncertain but is selected primarily to evaluate whether different physical processes are important for two significantly different containment capabilities (150 vs 400 MJ). The width and position of the failure threshold range shown in Fig. 40 is a function of head failure modes (e.g., missile generation) and of sodium ejection paths. This design-dependent range can be affected through improved understanding of sodium burning, RCB pressurization, and RCB failure characteristics.

The "ideal" conversion process is shown as line A on Fig. 40. Point c is the conservative estimate of system tolerance for energetic CDAs. The figure shows that the system could withstand an accident ramp rate of $60/s involving only fuel vapor and considerably less with significant sodium augmentation. In moving from point c to d on Curve A, we assume that neither sodium fires nor missiles (such as ejected rotating plugs) cause secondary containment failure over this range of energetics. The maximum potential in system tolerance would be about $120/s if we are constrained to curve A and a pure fuel-vapor expansion.

If we exclude the above-core structures [upper-core structure (UCS) and upper internal structure (UIS)] and consider only effects of fluid dynamics and fluid/structure dynamics, we shift to zone B on Fig. 40. These expansions are characterized by

1. two-dimensional pool dynamics,
2. loss of work potential through plastic strain of the core barrel and vessel walls,
3. incomplete conversion of pool kinetic energy to loads on the vessel closure system because of incoherent pool impact, and

4. incomplete development of work potential because of the nonuniformity in the dynamic expansion.

These effects are fairly well understood and can be calculated to various degrees with computer codes such as REXCO,[24] SIMMER,[25] ICECO,[26] PISCES,[27] ASTARTE,[28] and SURBOUM.[29] Considerable experimental data have been accumulated in support of these fluid/structure effects[30-33] and more are being obtained on the nonuniform expansion behavior.[34] The bandwidth shown for region B arises from an assumed uncertainty of ± 20% around a nominal estimate.

As seen from Fig. 40, these effects reduce the conversion efficiency to about 50% of the ideal. This shifts the lower limit of system tolerance from $60/s (point c) to a range of $90-125/s. Of more importance is the potential for extending system tolerance to around 40/s if sodium fire and missile threats can be accommodated. The likelihood for severe fires and energetic missiles clearly increases as the reactivity ramp rate increases, however.

Work potential is diminished by heat losses from the working fluid. The heat transfer processes are coupled strongly to the structural behavior of the fluid dynamics and to the high heat capacity of the fast-response UCS. The combined effects of all the heat transfer processes (assuming the UCS and UIS remain in place and unplugged) are estimated[35] as region C in Fig. 40. It must be emphasized that region C represents not only heat transfer effects, but the combined result of severe fluid throttling in the UCS pin structure and heat transfer in the core, UCS, and sodium pool.

Region C cannot be accepted in the high work potential regime because the UCS and UIS are likely to fail dynamically under the higher core pressures. Recent experimental work at SRI International[36] shows large UIS translations for simulated isentropic fuel-vapor expansions in the range of 200 MJ (to the cover-gas volume). Because these were direct-loading experiments (i.e., there was no UCS between the core and UIS) and the flow passages of the UIS were blocked, the deformations of the columns are probably somewhat large compared to the real case. The effectiveness of the UCS could begin to deteriorate at approximately $150/s. The work

potential at which the mitigating effects of the UCS essentially disappear has not yet been determined but we estimate that the pins in the UCS probably would begin to buckle and flow passages would jam at approximately $200/s. UCS effectiveness as a heat sink would depend on the degree of interpenetration of core material before and during this mechanical jamming.

An estimated UCS breakdown zone is shown on Fig. 40 as region D. Some effect of thermal losses continues even in the work potential range beyond complete UCS breakdown because of heat transfer processes at the expansion zone/pool interface. Heat transfer processes in the core also will remain to some degree. Thus, the CRBR system tolerance for energetic accidents may be extended to the range of $150-200/s if fuel is the expanding fluid, a conservative containment failure threshold is used, and if heat transfer and above-core structure effects are included.

Figure 42 presents a summary of the CRBR system tolerance for energetic accidents in terms of reactivity ramp rate vs the expansion treatment used. The lower-case letters that designate various ranges are preserved from Fig. 40. The left band (points c, e, h, i, g, and c) represents the conservative limit of containment system tolerance and the band width represents an estimate of uncertainties. The magnitudes of the uncertainties may be questioned but the qualitative trends are valid. The right band (points d, j, k, l, f, and d) represents an upper limit of containment through increased understanding of the failure threshold and perhaps implementation of special design features to elevate the threshold.

Opposite curvature of the two bands is one feature of Fig. 42 that is very prominent and enforces our need to understand heat transfer and thermal losses in the above-core structure. The left (conservative) band indicates a substantial gain in system tolerance if the heat transfer processes are assessed and substantiated. The right (optimistic) band indicates marginal value for heat transfer effects in the high ramp-rate regime. This is mainly the result of the threshold nature of the UIS failure. In addition, the high ramp-rate expansions allow less time for heat transfer, thereby diminishing that influence.

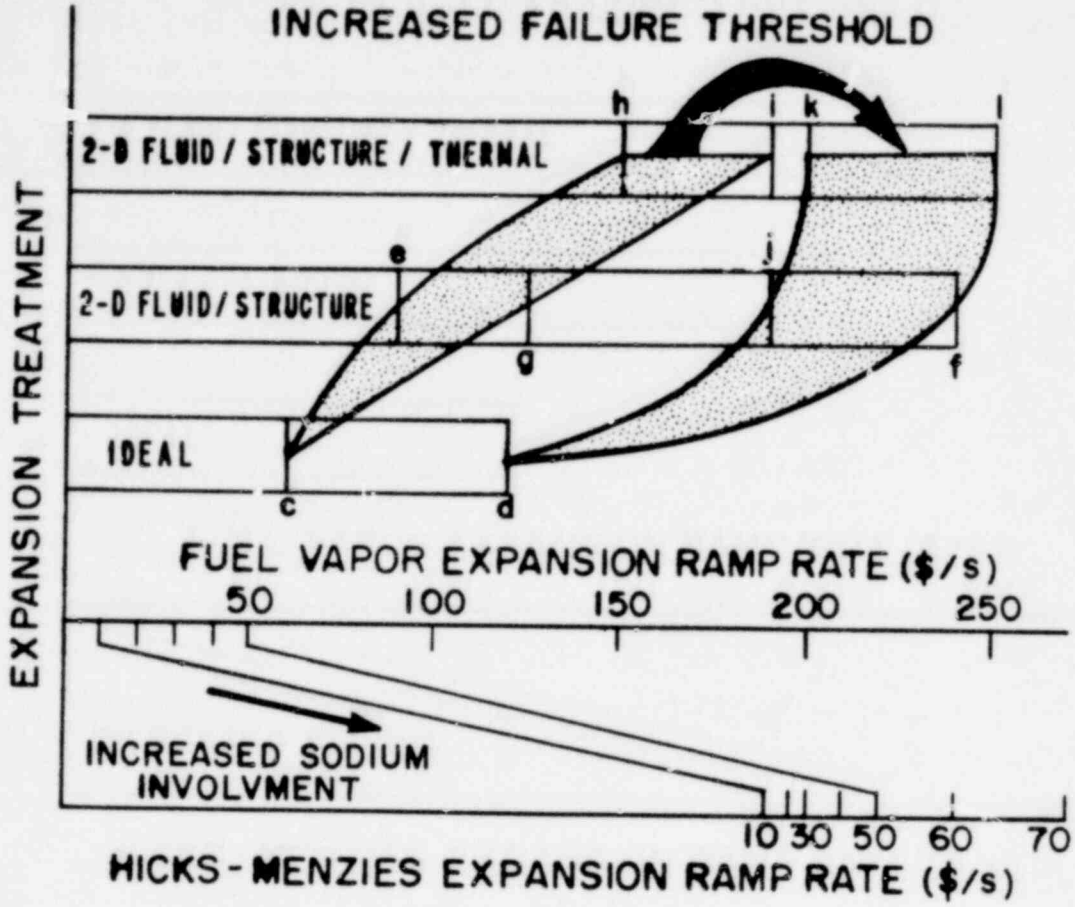


Fig. 42. Summary of CRBR tolerance for energetic accidents.

The second prominent feature of Fig. 42 is the inverse dependence of containment system tolerance on the degree of sodium involvement. Containment of even a mild accident requires low levels of sodium involvement. It is this characteristic of the liquid fuel-steel-sodium system that has provided the impetus for many years of international research in fuel-coolant interactions (FCIs).

A containment failure regime map that depends on reactivity ramp rate and effective sodium involvement is shown in Fig. 43 for the three sets of modeling assumptions that form the bases for regions A, B, and C in Fig. 40 (i.e., an ideal expansion, an expansion considering fluid-dynamic and structure effects only, and an expansion including both heat transfer and fluid dynamics effects). This failure map was derived from Fig. 42 using points c, e, and h as the containment failure thresholds for the three expansion treatments. For mild accidents (< $50/s) heat transfer may substantially

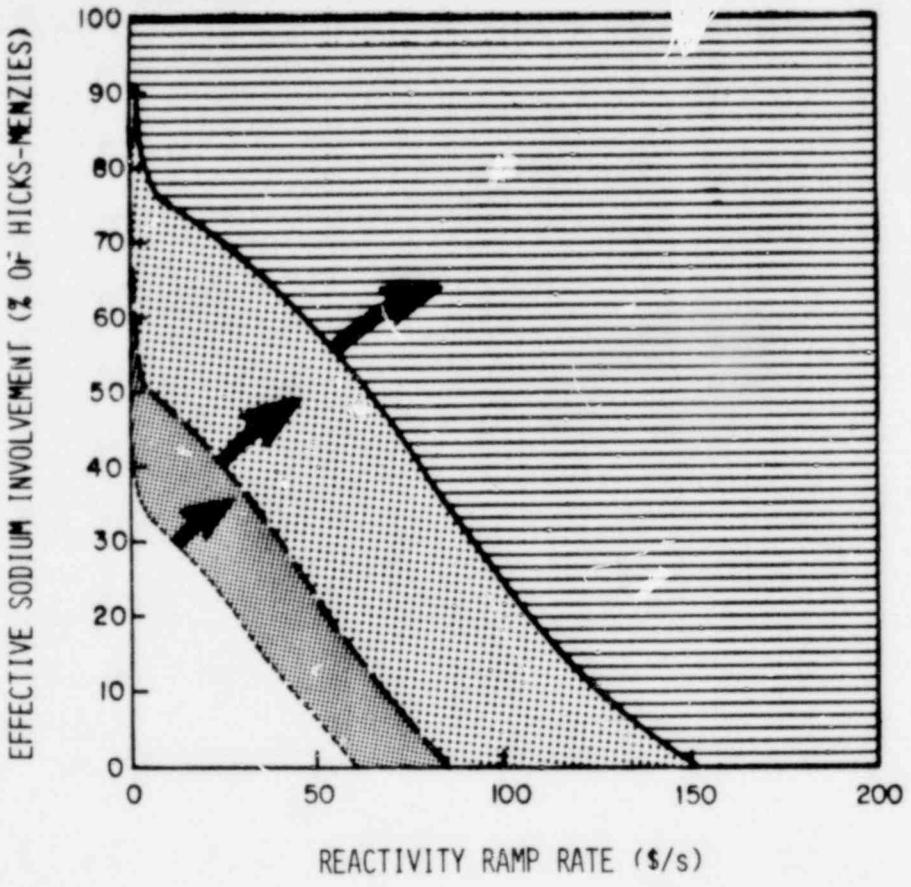


Fig. 43. Limits of effective sodium involvement for different accident severities and expansion treatments. Containability based on conservative limit of failure threshold and uncertainties in expansion treatments, line c, e, h in Fig. 40.

relax the requirement that we must demonstrate small effective sodium involvement. Heat transfer would also permit substantial sodium involvement in the intermediate ramp-rate range (\$50-150/s). In the higher ramp-rate range (about \$150/s), augmentation from sodium involvement can be tolerated only if uncertainties in UCS and UIS breakdown characteristics are resolved, the containment system failure threshold is increased, and/or specific design changes are made to shift the positions of regions B and D downward and to the right in Fig. 40.

Energetic expansions of high-temperature materials following postulated severe neutronic excursions in LMFBRs are complex, highly transient, and highly interactive. In addition, it is difficult to assess containment system failure thresholds. Therefore, these problems require consistent cost-benefit decisions regarding research and development needs, augmentation of safety-related design features, and approaches to formulating a defendable safety assessment. We have attempted to provide a perspective of this type for the CRBR. This can be translated partially to other designs but the estimated containment limits and the translations of ramp rates to work potentials are likely to be different.

3. A New Equation of State for Sodium

(G. I. Kerley, T-4)

A new equation of state (EOS) for liquid and vapor sodium has been developed for use in the SIMMER code and in other studies of LMFBR safety. Padilla has made a good compilation of sodium properties along the vapor-liquid coexistence curve.[37] However, a complete EOS surface (including the supercritical and metastable regions) is needed for detailed safety calculations. Although several good EOS models have been proposed, none have given satisfactory agreement with Padilla's tables.

We have used the CRIS model of fluids,[38,39] which is based upon thermodynamic perturbation theory, to compute an EOS for sodium. We also included the effects of molecular dimerization in the vapor phase. Our calculated coexistence properties compare well with Padilla's tables. In addition, our results agree with pressure-volume-temperature (PVT) measurements and other experiments

Recent work has shown that the structure of liquids is determined by repulsive forces and that the hard-sphere fluid provides a good model for this structure. In first-order perturbation theory, the entropy of the liquid is estimated by assuming the molecules to be hard spheres, and the internal energy is determined by averaging the intermolecular forces over the hard-sphere distribution. The hard-sphere diameter can be estimated by minimizing the Helmholtz free energy. In the CRIS model, it is assumed that

each liquid molecule is surrounded by a spherical shell of nearest neighbors and that the coordination number and nearest-neighbor distance vary from molecule to molecule. In this approximation, the dependence of the energy of a molecule on nearest-neighbor distance can be determined from the zero-temperature isotherm of the solid.

The first-order theory gave very good results when it was applied to argon and deuterium.[38] In studying liquid sodium and other metals, however, we found that terms beyond first order must be included to give satisfactory results for the vapor-liquid coexistence curve. We have extended the theory to include these corrections. The improved model gives very accurate results when compared with computer simulations on model liquids.[39] The method can be used to calculate the radial distribution function and the structure factor of a liquid as well as the thermodynamic properties.

In applying the CRIS model to sodium, we used static and shock-wave measurements to construct the zero-temperature isotherm in the compression region. We tried several methods to extrapolate the cold curve into the tension region and selected the one that gave the best fit to the vapor and liquid densities on the coexistence curve. The vapor pressure and the enthalpies on the cold curve were found to be fairly insensitive to the tension region. Band-theoretical calculations are being performed to verify the cold curve that we used.

In Figs. 44-46, we compare the calculated coexistence properties with measured results. Our vapor pressures (Fig. 44) are somewhat higher than experiment, the discrepancy ranging from 20% below 1 500 K to 50% near the critical point. This result is very good for a theoretical model; however, even better agreement may be needed for practical applications of the EOS. It should be possible to force agreement with experiment by making relatively small adjustments to the parameters used in creating the EOS. We plan to study this problem further.

The density on the coexistence curve is shown in Fig. 45. Experimental data are available up to 2 200 K.[40,41] At higher

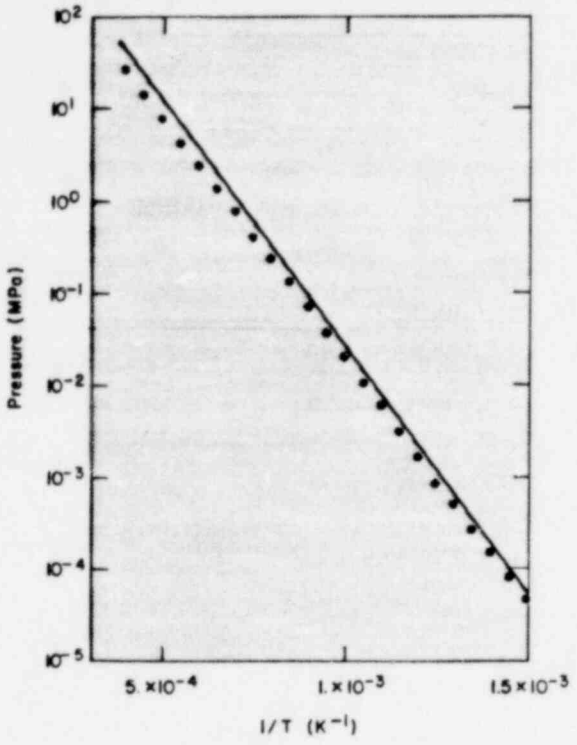


Fig. 44. Vapor pressure of sodium. The solid line is our calculation. Experimental data taken from Ref. 37.

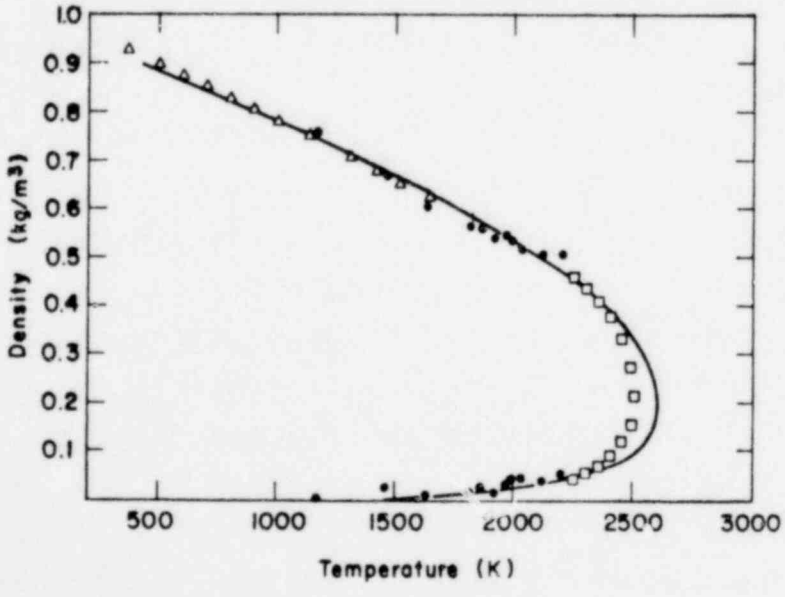


Fig. 45. Density of sodium on the coexistence curve. The solid line is our calculation. Data are taken from Refs. 40, 41, and 42.

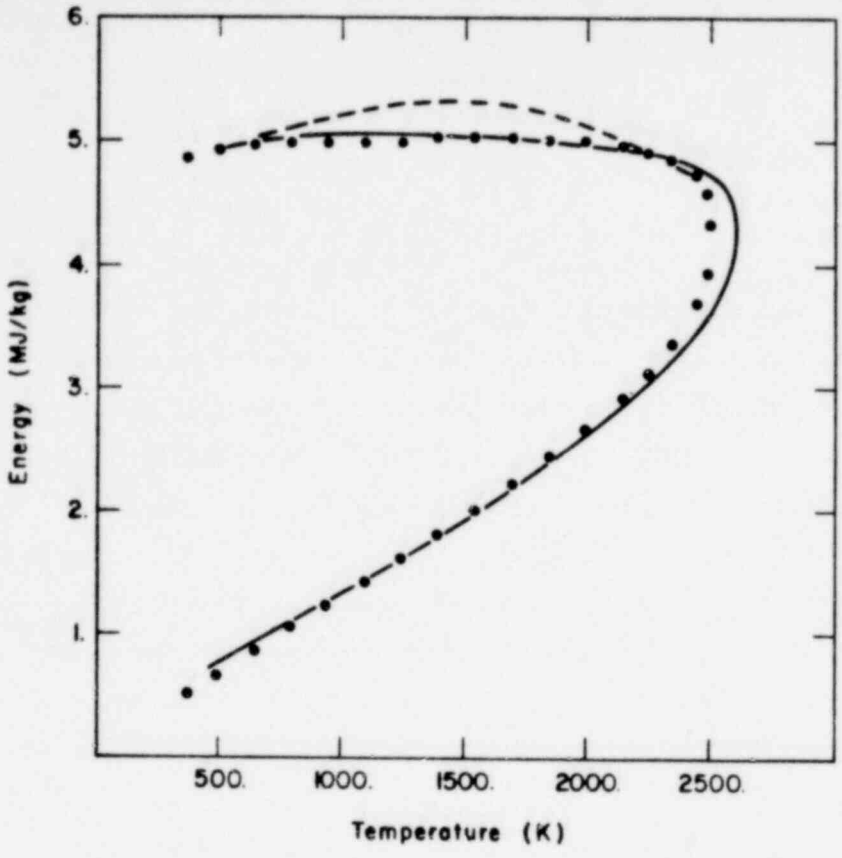


Fig. 46. Internal energy of sodium on the coexistence curve. The dashed line is our calculation without dimer formation and the solid line includes dimer effects. Data are taken from Ref. 37.

temperatures, we compared the estimates of Bhise and Bonilla, who used a corresponding states treatment.[42] The agreement is very good except near the critical point because long-range density fluctuations that are important in this region are not taken into account in our model. However, our critical temperature of 2 620 K is only 5% higher than the value obtained by Bhise and Bonilla.

The energy on the coexistence curve of Fig. 46 agrees well with Padilla's compilation. In this figure, we show calculations both with and without the formation of dimer molecules. The calculation that includes dimer effects shows the energy of the vapor phase to be nearly constant from 800-2 200 K, in good agreement with the experimental results. The theory also gives good results for the compressibility of the liquid, which has been measured to 2.3 GPa and for the structure factor. We have made exploratory

calculations of the viscosity and diffusion coefficient of liquid sodium, and the results are promising.

As mentioned above, we plan to make some studies of the sensitivity of the results to model parameters and to force agreement with experiment as much as possible. The final EOS table will be made available through the Sesame library.[43] A detailed description of this work will be published elsewhere.

Our new EOS gives a more complete and accurate description of sodium properties than is available from previous studies. For example, our calculations for the supercritical region predict pressures that are a factor of four less than those for ideal gas models currently in use. Our EOS gives a realistic description of the compressibility and thermal expansion of the liquid phase; these are either ignored or treated crudely in present calculations. It is likely that this more accurate description of the sodium EOS will be important in reactor safety evaluations, but calculations using SIMMER and other codes will be needed to determine the magnitude of the effects. Finally, our better understanding of sodium prepares the way for improvements in the modeling of FCIs, in the calculation of viscosities and other transport coefficients, and in applications of the liquid theory to steel and other materials.

4. Electronic Model for Gaseous $UO_2$ and the Effect on the $UO_2$ EOS

(J. D. Johnson, T-4)

During this reporting period, we formulated a computational model to account for the electronic excitations of the uranium dioxide ($UO_2$) molecule. This model was developed because we recognized that the specific heat of liquid $UO_2$ at ~ 3 200 K is approximately 134 J/mol·K;[44] at best, 75 J/mol·K can be explained by the translational, vibrational, and rotational modes of the molecule. The remaining 58 J/mol·K must be contributed by electron excitation. If such is the case for liquid $UO_2$, it is reasonable to expect a large contribution from electrons in the gaseous $UO_2$.

We therefore developed an electronic model that is essentially a Saha (chemical equilibrium) model.[45] Along the coexistence

curve for T ≤ 5 000 K, where we can neglect ionization of the electrons, this model has an electronic partition function

$$Q_e = Q^N \ , \tag{15}$$

where $Q_e$ is the electronic partition function of a single neutral molecule, N is the number of molecules, and $Q = \sum_{\alpha} e^{-\beta E_\alpha}$. The summation over $\alpha$ implies summing over electronic states and $\beta = 1/kT$, where k is the Boltzmann constant and T is temperature. The electronic levels in $UO_2$ are so dense that the sum can be replaced by an integral to obtain

$$Q = \int_0^{E_c} \rho(E) e^{-\beta E} dE \ , \tag{16}$$

where $\rho(E)$ is the density of electronic states for the molecule and $E_c$ is an appropriate energy cutoff.

The density of states is shown by the solid line of Fig. 47. Plotted on the same graph are the experimentally determined density of states for uranium[46] and a theoretical density of states for $UO_2$ obtained from a relativistic self-consistent field (RSCF) calculation.[47] When compared with the uranium, the magnitude of our $\rho(E)$ is reasonable. When compared with the RSCF calculation, $\rho(E)$ has the following features.

1. For $E \leq 15\ 000\ cm^{-1}$ the area under the line approximately equals the number of states found by the RSCF calculation.

2. At $E \simeq 15\ 000\ cm^{-1}$ the line is approximately equal to the RSCF number.

3. The RSCF calculation produces a sharp rise at $E \simeq 15\ 000\ cm^{-1}$ that supports the sharp rise in the solid line.

4. Above $15\ 000\ cm^{-1}$ the line has the same slope as the RSCF and diverges, as it should, at the ionization energy of $42\ 750\ cm^{-1}$.

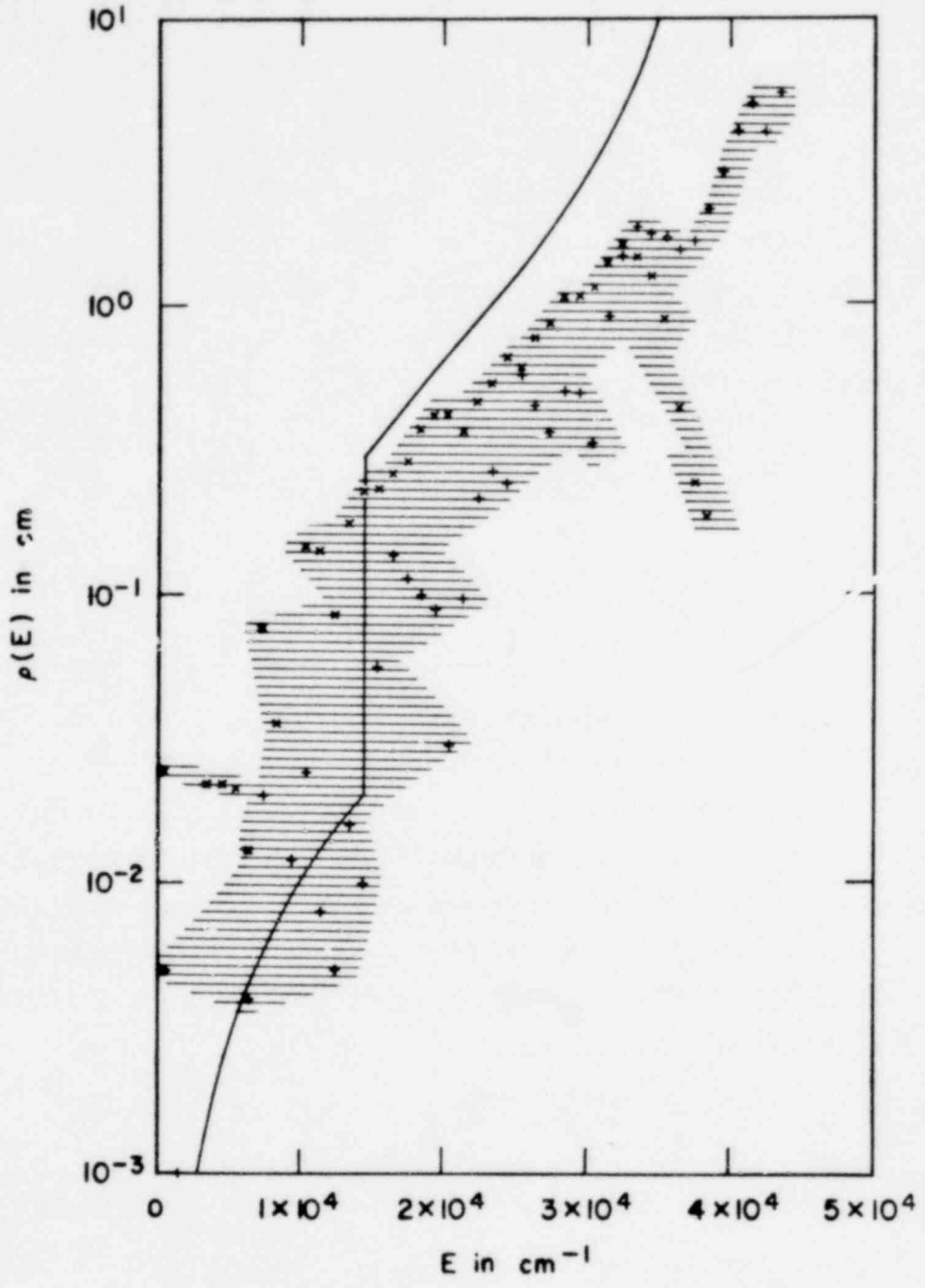


Fig. 47. Electronic density of states for neutral $UO_2$. The +'s are the theoretical density of states as given by a relativistic self-consistent field calculation.[48] The x's are the experimental data for neutral uranium.[49]

5. Our line is higher than the RSCF points for $E \geq 15\,000$ $cm^{-1}$.

For $E \geq 15\,000$ $cm^{-1}$, we feel our choice of $\rho(E)$ is better than the RSCF $\rho(E)$ for several reasons. First, the RSCF calculation that we used was a ground-state calculation; thus, for the excited states the calculation is not self-consistent. This leads to an unknown error in the $\rho(E)$, especially for the higher energies. Second, our $\rho(E)$ diverges at the ionization energy while the RSCF does not. Third, there are indications that some single-particle levels are missing in the RSCF calculation (in particular, 7 s and 6 d uranium levels). If only two levels are missing, the RSCF curve would more closely approximate our $\rho(E)$. Last, it seems reasonable that the density of states for $UO_2$ should be slightly higher than the uranium $\rho(E)$ for the higher energies.

For $E \leq 15\,000$ $cm^{-1}$, the smooth $\rho(E)$ is preferable to the detailed density of states from the RSCF calculation because of the uncertainties in the RSCF calculation.

This formulation for gaseous $UO_2$ for the range $T \leq 5\,000$ K is completed by adding in the other degrees of freedom, translational, vibrational, and rotational modes of the molecule. Our pressure is then

$$P = NkT/V \ , \tag{17}$$

where N is the number of molecules and V is the volume. Our enthalpy is

$$H = \frac{7}{2} NkT + H_e + Nk \sum_{i=1}^{4} \frac{\Theta_i}{e^{\Theta_i/T} - 1} \ . \tag{18}$$

$H_e$ is the electronic enthalpy and the last term is the enthalpy of the vibrational modes.[49] The $\Theta_i$ are the frequencies of the four vibrational modes of the linear $UO_2$ molecule. We take these frequencies to be 765.4 $cm^{-1}$ for the two stretching modes[48] and 178 $cm^{-1}$ for the two bending modes.[50]

We calculated the resulting enthalpy for gaseous $UO_2$ along the coexistence curve. The result shown by the solid curve in Fig. 48 is significantly different than the dashed line, which is the result for no electronic excitations.

This difference led us to calculate the vapor pressure $P_V$ because the enthalpy shown in Fig. 48 would tend to raise the high temperature $P_V$, thus producing better agreement with the data than has been obtained in the past.[51] We obtained the vapor pressure by integrating an approximate form of the Clasius-Clapeyron equation

$$\frac{d(\ell n\ P_V)}{dT} = \frac{H_g - H_c}{RT^2}\ , \tag{19}$$

where R is the gas constant, $H_g$ is the gas enthalpy, and $H_c$ is the condensed-phase enthalpy. For $T \leq 2\ 600$ K we obtained $H_c$ from the

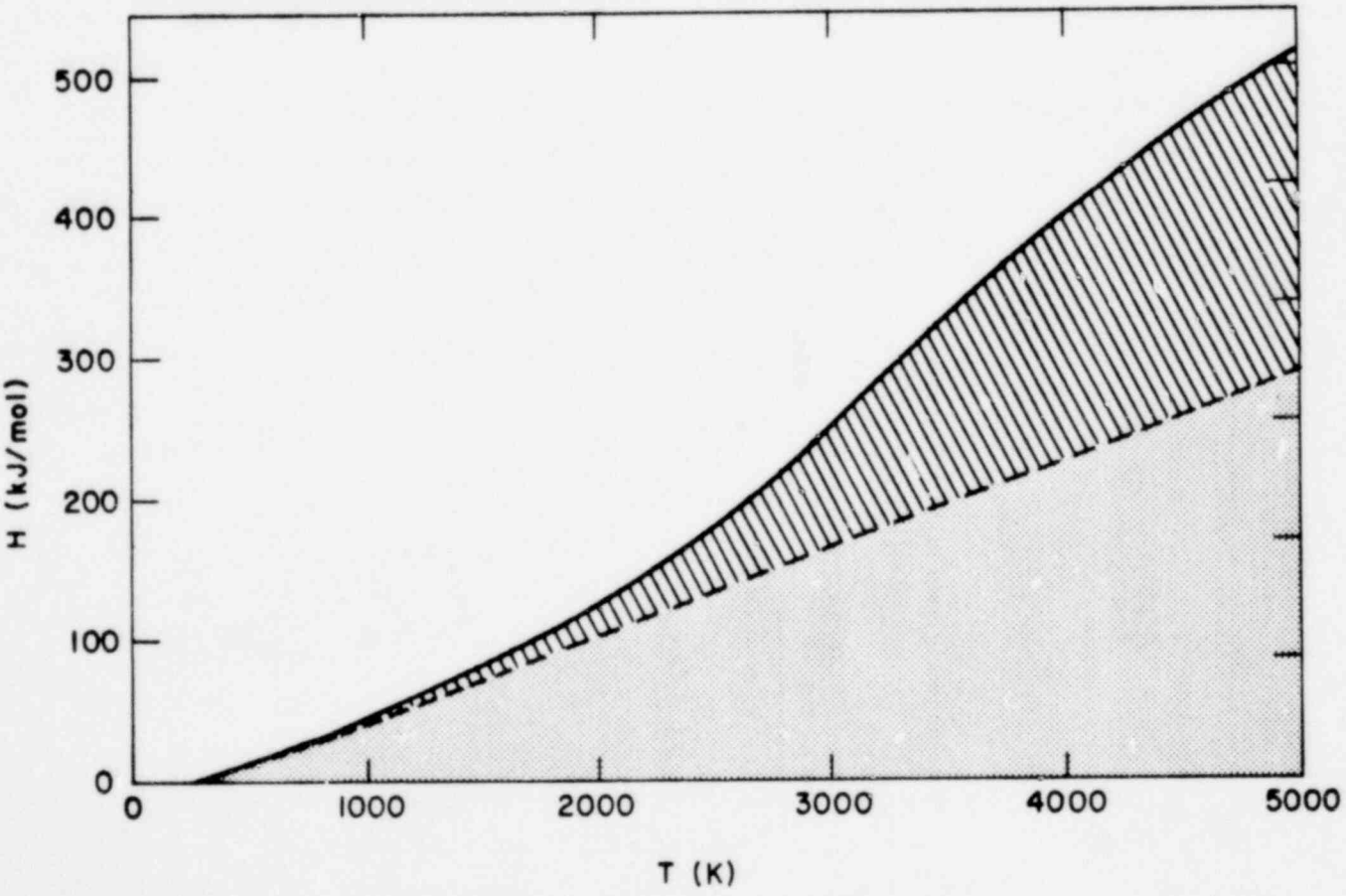


Fig. 48. Gas enthalpy along the coexistence curve.

paper of Rand, et al.[52] We performed a least-squares fit to the $H_c$ data[53] for 2 600 ≤ T ≤ 3 600 K and extrapolated linearly for high temperatures. To obtain Eq. (19), we eliminated the condensed-phase volume relative to the volume of the gas and made the ideal gas approximation. Two constants, $H_{g,298.15} - H_{c,298.15} = 0.626\ 23$ MJ/mol and the integration constant of Eq. (19), were chosen to give the best fit to the $P_V$ data.

The resulting $P_V$ is shown on Fig. 49 as a solid curve. The dashed curve is the International Atomic Energy Agency (IAEA) standard.[44,53-60] Our curve definitely gives a better fit to the data. We performed a least-squares fit to the log of the vapor-pressure data as a function of 1/T. For $T > T_{melt}$, we used the functional form $\ell n\ P_V = a + b/T$ and for $T < T_{melt}$, $\ell n\ P_V = c + d/T + e\ \ell n\ T$. We forced the two forms to match at $T = T_{melt}$ and to have the correct change in slope at $T_{melt}$. Our theoretical curve in Fig. 48 differs from this fit for $P_V$ by at most 5% over the temperature range 1 500 ≤ T ≤ 5 000 K. Thus, we have formulated a very reasonable electronic model for the gaseous $UO_2$ that gives a significantly different enthalpy when compared to the enthalpy without electronic excitations. The improvement of the vapor pressure is also significant.

We plan to include the above-described electronic model in a new EOS for uranium dioxide. The effects on reactor safety studies of this new EOS cannot be assessed until it is implemented and studies can be made. There is obviously a reasonable chance that the results will be influenced because the vapor pressure and gas enthalpy are increased significantly from older values. Such results may influence the uranium dioxide energetics at the high temperatures within the disrupted LMFBR core. However, even if the increased vapor pressure and gas enthalpy do not change the results of reactor safety studies, the work is justified by a better understanding of the uranium dioxide EOS.

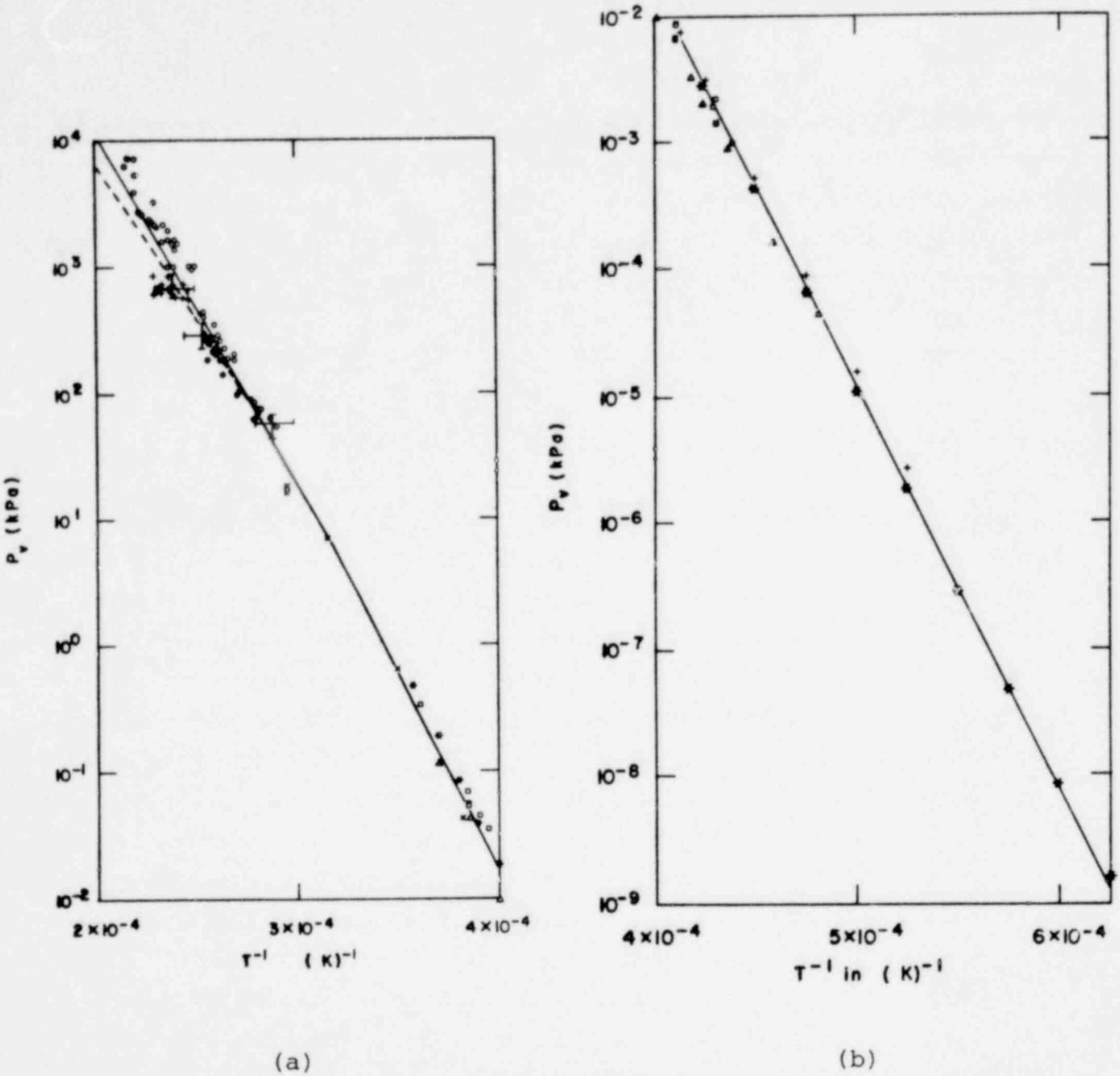


(a) (b)

Fig. 49. Comparisons of theoretical and experimental vapor pressures. Figure 49(a) gives the high-temperature results and Fig. 49(b) gives the low temperature. The data are from a variety of sources:

0 - Ohse, et al.[54]

+ - on Fig. 49(a) - Bober, et al.[55]

x - Reedy and Chasanov[56]

□ - Ohse[57]

Δ - Tetenbaum and Hunt[58]

* - Ackermann, et al.[59]

+ - on Fig. 49(b) - Pattoret et al.[60]

## B. SIMMER Verification

(J. H. Scott, Q-7)

During this quarter, work continued in the areas of advanced momentum-exchange modeling. Significant progress is being made toward the goal of implementing a generalized momentum-exchange model in SIMMER.

The major emphasis in the SIMMER validation effort has been to verify the SIMMER fluid-dynamics treatment. Various relevant experiments have been analyzed, including interfield area and drag experiments and flashing-fluid expansion experiments performed at SRI International and Purdue University. In general, SIMMER results are good; however, several model uncertainties related to flow regimes persist. This conclusion is emphasized by the statistical sensitivity studies performed in support of the SRI International experiment analyses.

Continued progress is evident in the area of experimental support of SIMMER, especially in the upper structure dynamics (USD) experiment. Much of our current effort has been expended toward an assessment of the adequacy of the USD rupture diaphragm for Series-II tests.

Finally, at the request of Hanford Engineering Development Laboratory (HEDL), we have performed a fuel-failure analysis for a reference overpower transient in Fast Test Reactor (FTR). Other organizations are performing similar calculations, and HEDL will make code result comparisons and assess the importance of differences.

### 1. Interfield Area and Drag Experiment Analysis

(P. E. Rexroth, Q-7 and V. S. Starkovich, Q-8)

The interfield drag program has permitted us to evaluate the treatment of drag between a continuous vapor phase and either liquid droplets or solid particles. (A general description of this aggregate fluidization experiment and analysis program can be found in Ref. 61. Earlier results and suggestions for a modified calculation of the drag coefficient are included in Ref. 15.) During

this quarter, the analysis has been modified to utilize SIMMER-II rather than SIMMER-I. We have also expanded the experimental program by including the variables of particle size and density. In going from SIMMER-I to SIMMER-II, it was necessary to modify the boundary flow conditions. SIMMER-II no longer permits a constant-velocity inlet flow; therefore, a constant pressure drop across the tube was chosen such that the desired time-average vapor velocity was obtained. This boundary condition is more representative of the experiment than that used before.

In earlier experiments,[15] 3-mm-diam glass beads ($\rho$ = 2 200 kg/$m^3$) were used for the bed material. The vapor flow and initial bed depth were variable quantities. More recently, experiments have been conducted using three sizes of glass beads and two sizes of aluminum spheres ($\rho$ = 2 700 kg/$m^3$). The calculated and measured oscillation periods for the experiments performed this quarter are given in Table XI.

TABLE XI

EXPERIMENTAL RESULTS

| Bead Material | Particle Diameter (mm) | Superficial Vapor Velocity (m/s) | Initial Bed Depth (mm) | Experimental Oscillation Period (s) | Calculated Oscillation Period (s) |
|---|---|---|---|---|---|
| Glass | 3 | 2.5 | 160 | 0.72 | 0.87 |
| Glass | 3 | 3.0 | 160 | 0.89 | 0.46 |
| Glass | 3 | 3.25 | 160 | 0.92 | 1.04 |
| Glass | 3 | 3.0 | 120 | 0.71 | 0.80 |
| Glass | 3 | 3.0 | 200 | 1.02 | 1.09 |
| Glass | 4 | 3.0 | 160 | 0.96 | 0.90 |
| Glass | 6 | 3.0 | 160 | 0.96 | 0.84 |
| Aluminum | 3 | 3.0 | 160 | 0.94 | 0.94 |
| Aluminum | 4 | 3.0 | 160 | 0.84 | 0.86 |

This data set revealed many interesting points. First, SIMMER underpredicts the period for all cases using 3-mm glass beads. The calculational and experimental results are consistent in indicating a trend toward longer periods with higher vapor velocity and greater initial bed depth. However, the experimental results show no clear trend of the effect of particle size on period for the glass beads. The calculations show a drop in period with increased particle size. This trend would be expected because drag force per unit mass decreases with increased particle radius. The experiments and calculations are consistent in showing this trend for the aluminum spheres. SIMMER also calculates a lower period for aluminum than glass when the other variables are held constant. The experiment shows this result only for the 4-mm spheres.

Considering these inconsistencies, the experimental data from the glass bead experiments must be viewed with caution. The beads are not extremely uniform in either shape or size, and they chip and break up somewhat during the experiment. These effects may explain the unexpected SIMMER results. We feel that the data obtained from experiments using the aluminum spheres are more reliable because of their quite uniform size and shape.

The overall behavior of the interfield drag experiment is calculated well by SIMMER. The calculated oscillation periods for those using aluminum spheres agree to within a few per cent with the experimental values. These positive results indicate sound general methodology of the SIMMER momentum-exchange formulation. The correlation used to calculate the exchange coefficient provides excellent results for the flow regime observed in these experiments. When more dynamic flow or liquid-dominated flow is encountered, this correlation may not be adequate; and this uncertainty should be taken into account when assessing the results of such calculations.

## 2. Advanced Momentum-Exchange Models

(E. J. Chapyak, Q-7)

As a part of our continuing effort to extend the KACHINA drag formulation to include bubbly flow regimes, we have generalized SIMMER's momentum equations to include the effects of virtual mass

(i.e., bubbly flow) and acceleration-dependent drag terms (i.e., Basset forces). These equations were presented in a previous report[10] and are repeated below for convenience. The nomenclature is that used in Ref. 10.

$$\bar{\rho}_p[1 + \tfrac{1}{2}\alpha_p(1 + \bar{\rho}/\bar{\rho}_p)]\left[\frac{\partial \vec{u}}{\partial t} + (\vec{u} \cdot \vec{\nabla})\vec{u}\right] = -\frac{3}{2}\alpha_p \vec{\nabla}_p - \bar{\rho}_p \vec{g}[1 + \tfrac{1}{2}\alpha_p(1 + \bar{\rho}/\bar{\rho}_p)] + \alpha\alpha_p \quad \text{(Drag)}, \tag{20}$$

$$\bar{\rho}[1 + \tfrac{1}{2}\alpha_p(1 + \bar{\rho}/\bar{\rho}_p)]\left[\frac{\partial \vec{v}}{\partial t} + (\vec{v} \cdot \vec{\nabla})\vec{v}\right] = -\alpha\vec{\nabla}p\left(1 + \frac{1}{2}\frac{\rho}{\rho_p}\right) - \rho\vec{g}[1 + \tfrac{1}{2}\alpha_p(1 + \bar{\rho}/\bar{\rho}_p)] - \alpha\alpha_p \quad \text{(Drag)}, \tag{21}$$

where

$$\text{Drag} = \frac{-9}{2}\rho\frac{\nu}{R^2}(\vec{u} - \vec{v}) - \frac{3}{8}C_d\frac{\rho(\vec{u} - \vec{v})|\vec{u} - \vec{v}|}{R} - \frac{9}{2}\frac{\rho}{R}\frac{\sqrt{\nu}}{\pi}\int_{-\infty}^{t}\left|\frac{\partial \vec{u}}{\partial \tau} + (\vec{u} \cdot \vec{\nabla})\vec{u} - \left[\frac{\partial \vec{v}}{\partial \tau} + (v \cdot \vec{\nabla})\vec{v}\right]\right|\frac{d\tau}{\sqrt{t - \tau}},$$

and bars over the densities indicate macroscopic variables. The subscript p refers to either droplet or bubble properties and unsubscripted variables refer to the continuous (either vapor or liquid). Because these equations are rigorous only in the low particle-density limit (i.e., $\alpha_g \to 1$), an empirical extension to other $\alpha$ values is required for practical applications in SIMMER. Thus, for the liquid field, we would have

$$\bar{\rho}_\ell[1 + \tfrac{1}{2}\alpha_g\alpha_\ell(1 + \alpha_\ell\frac{\bar{\rho}_\ell}{\bar{\rho}_g} + \alpha_g\frac{\bar{\rho}_g}{\bar{\rho}_\ell})]\left(\frac{\partial v_\ell}{\partial t} + \vec{v}_\ell \cdot \vec{\nabla}\vec{v}_\ell\right) = -\alpha_\ell\vec{\nabla}p - \tfrac{1}{2}\alpha_\ell\alpha_g(\alpha_\ell\frac{\bar{\rho}_\ell}{\bar{\rho}_g} + \alpha_g)\vec{\nabla}p$$

$$- \bar{\rho}_\ell \, g[1 + \tfrac{1}{2} \alpha_g \alpha_\ell (1 + \alpha_\ell \frac{\bar{\rho}_\ell}{\bar{\rho}_g} + \alpha_g \frac{\bar{\rho}_g}{\bar{\rho}_\ell} - \alpha_\ell \alpha_g \, (\text{Drag}), \quad (22)$$

and for the vapor field,

$$\bar{\rho}_g[1 + \tfrac{1}{2} \alpha_g \alpha_\ell (1 + \alpha_\ell \frac{\bar{\rho}_\ell}{\bar{\rho}_g} + \alpha_g \frac{\bar{\rho}_g}{\bar{\rho}_\ell})](\frac{\partial \vec{v}_g}{\partial t} + \vec{v}_g \cdot \nabla \vec{v}_g) = = \alpha_g \nabla p$$
$$- \tfrac{1}{2} \alpha_\ell \alpha_g (\alpha_g \frac{\bar{\rho}_g}{\bar{\rho}_\ell} + \alpha_\ell) \nabla p - \bar{\rho}_g \vec{g}[1 + \tfrac{1}{2} + \alpha_g \alpha_\ell \frac{\bar{\rho}_\ell}{\bar{\rho}_g} + \quad g \frac{\bar{\rho}_g}{\bar{\rho}_\ell})]$$
$$- \alpha_\ell \alpha_g \, (\text{Drag}), \quad (23)$$

where the drag term should be generalized as in Ref. 62. Note that in the limit $\alpha_\ell \to 1$ or $\alpha_g \to 1$, Eqs. (22) and (23) reduce to Eqs. (20) and (21). Their validity for general $\alpha$ is unknown and in all probability could be improved by making the coefficient of virtual mass (i.e., the factor of one-half above) a function of the $\alpha$'s and by generalizing the drag term. These modifications will be investigated soon.

Our momentum-exchange derivation has been extended to include SIMMER's energy equations. The result is simply that, in the dispersed bubbly flow ($\alpha_\ell \to 1$) regime, the term $K_{g\ell}(\vec{v}_\ell - \vec{v}_g)^2$ in the SIMMER vapor energy equation should appear instead in the liquid energy equation. Thus, this term should be replaced by a term like $\alpha_g \, K_{g\ell}(\vec{v}_\ell \, \vec{v}_g)^2$ in the vapor equation, and a term like $\alpha_\ell \, K_{g\ell}(\vec{v}_\ell - \vec{v}_g)$ (Ref. 63) should be added to the liquid equation. No other changes are required, however, provided that $K_{g\ell}$ is generalized as in Ref. 63 and a Basset force term is added to $K_{g\ell}$, if desired. Further improvements in drag modeling for general $\alpha$ will be the subject of future investigation.

The objective of this work is ultimately to arrive at a generalized treatment for momentum exchange that can be incorporated in SIMMER. If this objective is met, the numerical transition from dispersed to bubble flow regimes will be eased considerably and we can more readily evaluate the importance of flow-regime modeling in accident analysis.

## 3. SIMMER-II Analysis of Flashing Water Experiments

(A. J. Suo-Anttila and P. E. Rexroth, Q-7)

Part of the SIMMER-II verification program includes both pre- and posttest analysis of several related experiments. These include the analysis of Purdue, SRI-E001,[33] and Edwards-O'Brien[64] flashing water experiments. The latter two experiments were analyzed posttest; that is, the answer was known before the computer simulation was made. However, these analyses help us determine SIMMER-II's accuracy and also aid as we modify the existing code to match the results of both experiments. After developing a version of SIMMER that reproduces the results of both experiments without parameter variations, the pretest analysis of the Purdue flashing water experiment was performed.

The SRI-E001 flashing water experiment was very similar to the high-pressure SRI-D006 nitrogen experiment[33] with the exception that the high-pressure nitrogen was replaced with hot (571 K) saturaged water at 7.15 MPa. The geometry of the system was the same as the earlier nitrogen-series experiments, that is, a 1/30-scale CRBR.

Several SIMMER analyses were performed on the SRI International flashing water experiment. The results of these analyses indicated that the computed result is very sensitive to liquid density variation with temperature and to models of phase-transition rates. The temperature range encountered in the experiment (290-571 K) results in water densities varying from 730-1 000 kg/m$^3$. If constant density is used throughout the problem, late impact times result, even though the pressure levels in the system are correct. This problem was overcome by using a two-component system, each component having the thermophysical properties of either hot or cold water.

The phase-transition rate models determine both the shape and the amplitude of the pressure trace in the lower core. The actual vaporization-condensation model has been verified from a number of experiments with longer time scales. The fundamental assumption in this model is that the vapor-liquid interface remains in thermodynamic equilibrium. This assumption is probably violated to a

small extent in that the time scale of these experiments is short enough (on the order of 3 ms) for nonequilibrium conditions to persist. However, the error introduced by this assumption is negligible compared to other sources of error.

The major deficiencies in the phase-transition rate models come from the flow-regime model. It is the flow-regime model that provides input to the vaporization-condensation model. The inputs involved are the vapor- and liquid-side heat transfer coefficients and the interfacial area for phase change. Variations in these parameters can greatly alter the predicted phase-transition rates because the product of the heat transfer coefficient and interfacial area determines the rate of phase transition. Because of the flow-regime sensitivities, several different flow-regime models were tested. The results of three of these models are presented here for the SRI-E001 experiment.

The first calculation is an untuned, off-the-shelf SIMMER analysis. The dispersed droplet flow-regime model in this case is documented in the SIMMER manual.[25] The result of this calculation is an equilibrium expansion of the hot water (see Fig. 50). The impact time in this case is earlier than that encountered in the SRI International experiment. The kinetic energy is less than the isentropic value because of nonuniform expansion effects and condensation of the hot water vapor upon the cold water in the upper pool.

The second flow-regime model is a constant bubble-drop size model. In this model, the number of bubbles or drops is determined by the volume fraction of vapor or liquid within a computational cell and the initially specified bubble or drop size. The bubble-drop size was varied to match head impact time exactly (3.15 ms). The corresponding pressure trace for the lower core is shown in Fig. 50 (labeled version II).

The third flow regime tested was a number density model. In this model, the number density of nucleation sites is specified in a cell-wise manner. Each nucleation site will transform into a single bubble whenever a cell becomes two phase. If the cell vapor-volume fraction exceeds 50%, each bubble will be transformed into a droplet. The most important aspect of this model is the

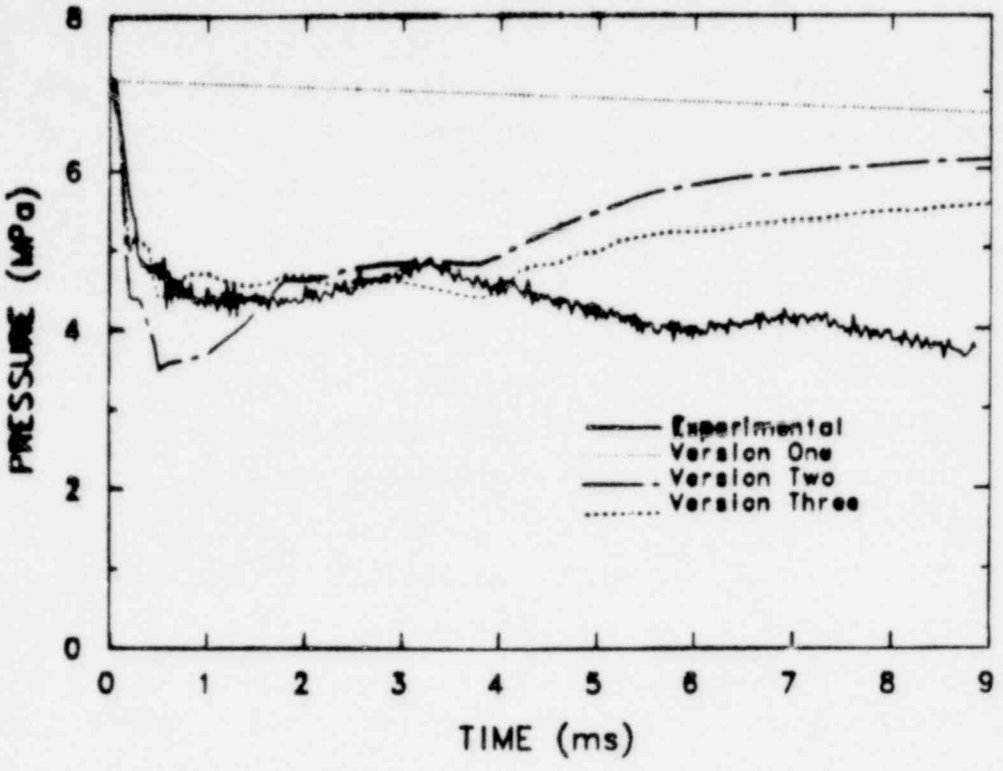


Fig. 50. Lower core pressure, experiment SRI-E001.

computation of movement of nucleation sites, vapor bubbles, or liquid droplets. We recognized intuitively that motion of the nucleation sites could not be ignored; therefore, two number density continuity equations were added to SIMMER to account for convection. The first continuity equation calculates the convection of the bubbles or nucleation sites by utilizing the vapor velocity. In the second equation, the droplets are convected by the liquid velocity, which is identified in SIMMER as a distinct velocity field.

In the calculation, shown in Fig. 50, the number density of nucleation sites was varied to match the head impact time exactly. The corresponding lower core pressure trace is labeled version III.

The calculated lower core pressures following head impact for all the models diverge from the experimental pressure trace partly because of numerical effects caused by the use of two components to simulate hot and cold water. Another reason, evident from the

SRI International experiment films,[33] is elimination of some of the bubbles in the pool due to condensation. These effects are not currently included in the flow-regime models.

Using the number density flow-regime model in SIMMER, the impact time of the SRI-E001 experiment can be obtained while maintaining the good agreement between measured and calculated lower core pressures indicated in Fig. 50. Before performing a predictive analysis on the large-scale Purdue flashing water expansion experiments, we felt that further confirmation of this flow-regime model was desirable. The Edwards horizontal pipe blowdown[64] was chosen primarily because the dimensions of the experiment are large enough to bring out any major scale-related effects of the model. The apparatus consisted of a straight steel pipe 4.1 m in length and 0.073 m inside diameter. The tube was water-filled, pressurized, and heated. When the desired initial conditions were attained, a glass rupture disk at one end of the pipe was broken, initiating the blowdown. Seven pressure transducers, spaced along the tube, recorded the progress of the blowdown. Experiments were performed with initial pressures of 6.9 and 10.3 MPa. The water was subcooled in both cases.

The lower pressure experiment was chosen for SIMMER analysis. The problem was first tried using the standard flow-regime model. The particle size cutoffs were set to $10^{-10}$ and 10 m, respectively, so that they would not arbitrarily affect the determination of particle size. Extremely small particle sizes and resultant high evaporation rates resulted, forcing the time step to an unacceptably low value. As with the SRI International analysis, this problem can yield acceptable results, but the minimum drop size ($10^{-10}$) must be chosen judiciously to virtually constrain the drop size. The simulation was then run using the number density flow-regime model with the same initial nucleation-site number density used for SRI-E001. Figures 51 and 52 show comparisons of the measured and calculated pressures at the gauge locations nearest the ends of the pipe. The agreement at gauge station 1 is quite good, but that is expected because this pressure is determined primarily by the exit friction coefficient that must be chosen arbitrarily. The reasonable

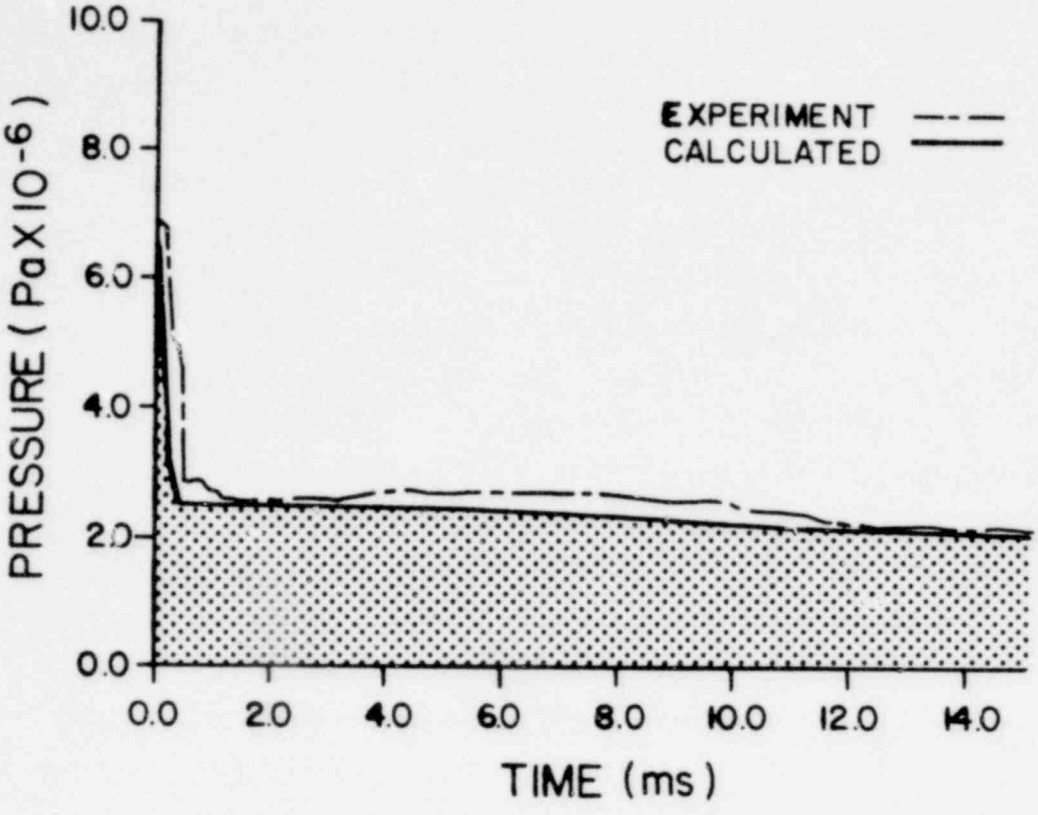


Fig. 51. Edwards pipe blowdown gauge station 1.

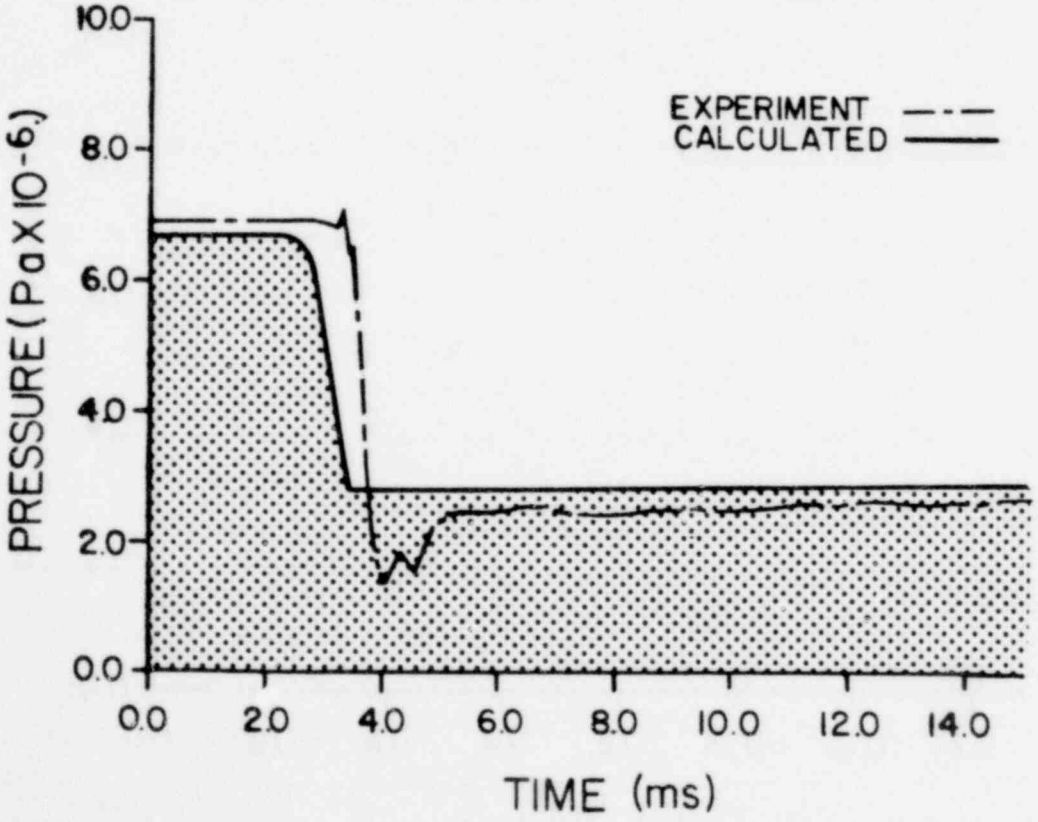


Fig. 52. Edwards pipe blowdown gauge station 7.

agreement at gauge station 7 located near the closed end of the tube, is much more indicative of the efficacy of the number density flow-regime model for this particular analysis.

Because of the reasonable success of the number density flow-regime model in the analysis of the SRI International and Edwards blowdown experiments, it was chosen for the predictive analysis of the first Purdue flashing water experiment.[63] Dimensionally, this experiment is a 1/7-scale model of the CRBR vessel. A schematic of the vessel is shown in Fig. 53. The pressure vessel initially is filled partially with saturated water (2.07 MPa, 468 K). Just before breaking the diaphragm, nitrogen gas is injected into the pressure vessel, providing sites for vapor nucleation. Like the SRI International experiments, pressure transducers are located in the pressure vessel, the throat, and on the upper lid. A SIMMER

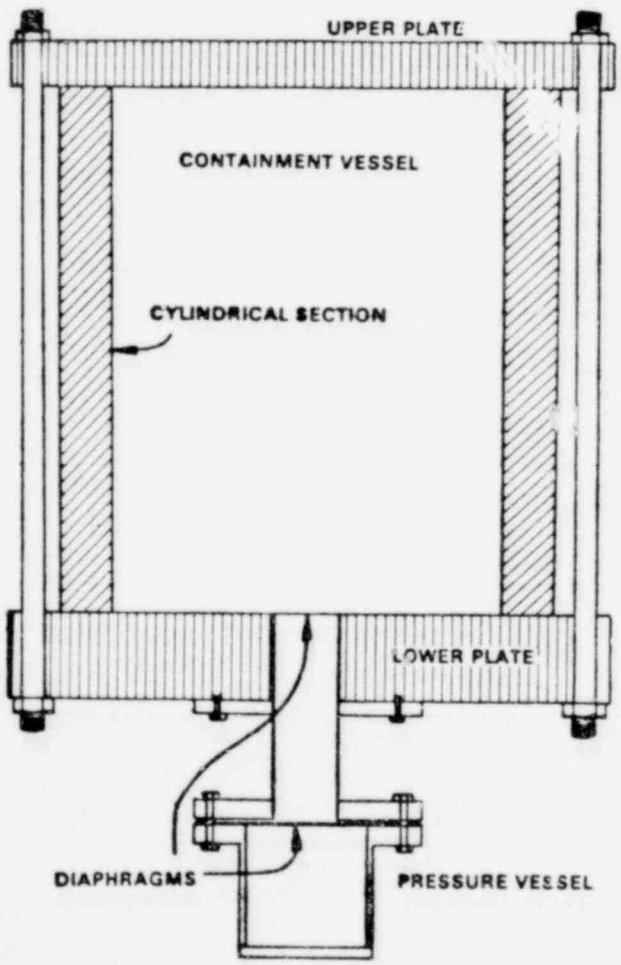


Fig. 53. Scaled schematic of the experimental apparatus including terminology of the major components.

analysis of this experiment predicted the time to head impact as 15 ms. This value has not been compared yet to the actual value nor has the error band on the head impact time been determined, as the sensitivity analysis is still in progress.

These flashing water analyses are being performed as part of the verification of the SIMMER analysis of the CRBR energetics. The impact of flow-regime modeling on that problem is uncertain. Because the results of calculations like those of the SRI International and Purdue experiments seem to be sensitive to flow regime, we are doing further studies to quantify that sensitivity and recommend that these be extended to include studies of the full-scale CRBR case.

4. Upper Structure Dynamics Experiment Analysis

(E. J. Chapyak, Q-7)

A major concern in the USD experiments is the performance of the rupture disks that release pressurized core materials through the UCS. Two performance characteristics that a priori appear to be important are the maximum opening angle of the petals and the time required to achieve this maximum angle. Excessively long opening times or poor opening angles would necessitate the use of an explosively driven valve to replace the rupture-disk system -- an option requiring considerable manpower and funding. A phenomenological model for rupture-disk petal dynamics has been developed and the significance of incomplete rupture was addressed with the SIMMER code. On the basis of this analysis, we recommend that use of the rupture disks be continued.

The forces that tend to rupture the disk's petals are differential pressure, which is dominant at early times, and drag forces, which may be of some importance at later times. In this model, we will neglect (conservatively) drag forces. The basic features of differential loading involve a rarefaction wave, which propagates into the high-pressure material and reduces the pressure on the high-pressure side of the diaphragm, and a compression wave, which propagates into the low-pressure material and increases the loading on the low-pressure side (both of these effects are caused by petal motion). In addition, there are inherently two- and

three-dimensional release waves that propagate through the slit openings between petals and encourage pressure equilibration across their surfaces.

Assume that the scored lines in the disk crack instantaneously at t = 0, and that subsequently, a bending line is formed at the base of each of the four petals. Equating angular acceleration to the torque exerted on each petal, we have

$$I\ddot{\theta} = \int \Delta p \; y \; dA - \delta^2 Y \ell \; , \tag{24}$$

where I is the moment of inertia about the bending line ($I = \rho\delta\int y^2 dA$ where $\rho$ is the petal density), $\ddot{\theta}$ is the petal's angular acceleration, $\Delta p$ is the pressure differential across the petal, y is the perpendicular distance from the bending line, dA is an area element on the petal, $\delta$ is the thickness of the petal, Y is a characteristic stress in the bending zone, and $\ell$ is the length of the bending line. Further, we approximate the pressure below (subscript b) and above (subscript t) the diaphragm, respectively, as

$$P_b = P_c\left[1 - \left(\frac{\gamma - 1}{2}\right)\frac{u}{a_b}\right]^{2\gamma/\gamma-1} \simeq P_c\left(1 - \frac{\gamma u}{a_b}\right) \; , \tag{25}$$

$$P_t = P_o + \rho_t \, a_t \, u \; ,$$

where $P_c$ is the core pressure, $P_o$ is the above-core pressure, a denotes sound speed, $\gamma$ is the ratio of specific heats for the above-core gas, and u is the petal velocity. Here, we have tacitly ignored the two- and three-dimensional release waves referred to above, treated the core material as a constant gamma gas, and used an acoustic approximation for the compression wave generated in the above-core region. The use of the linearized forms of $P_b$ and $P_t$ is a reasonable approximation for the cases treated below. Performing the area integrations in Eq. (24) and substituting Eq. (25) into Eq. (24), we have

$$\ddot{\theta} = \frac{P_c - P_o}{\rho\delta r}\frac{4}{\sqrt{2}} - \frac{24}{\rho\delta r}\frac{\delta^2 \ell Y}{r^3} - \frac{\dot{\vartheta}}{\rho\delta}\left(\rho_b a_b + \rho_t a_t\right), \qquad (26)$$

where $\rho_t$ and $\rho_b$ are the above-core and core gas densities, respectively, $a_t$ and $a_b$ are the above-core and core sonic speeds, respectively, and r is the radius of the petal. Posttest examination of rupture disks used in the first USD experiment suggests that the bending moment term in Eq. (26) in effect increased $P_o$ by about 101 kPa. With this generalization of $P_o$, we can express Eq. (26) as

$$\ddot{\theta} = \frac{P_c - P_o'}{\rho\delta r}\frac{4}{\sqrt{2}} - \frac{\dot{\vartheta}}{\rho\delta}\left(\rho_b a_b + \rho_t a_t\right),$$

which has as a solution satisfying $\theta(0) = \dot{\theta}(0) = 0$,

$$\theta = \frac{P_c - P_o'}{\rho_b a_b + \rho_t a_t}\frac{2\sqrt{2}}{r}\left\{t - \frac{\rho\delta}{\rho_b a_b + \rho_t a_t}\left[1 - e^{\frac{t}{\rho\delta}\left(\rho_b a_b + \rho_t a_t\right)}\right]\right\}.$$

Calculated rupture-disk opening times (defined when $\theta = \pi/2$) for various core materials are presented in Table XII. The above-core material is assumed to be air at 101 kPa. Input parameters are:

$P_o' = 2.0 \times 10^5$ Pa,

$P_c = 2.0 \times 10^6$ Pa,

$\rho = 8.0 \times 10^3$ kg/m$^3$,

$\delta = 2.5 \times 10^{-4}$ m,

$T_c = 4.5 \times 10^2$ K, and

$T_a = 3.0 \times 10^2$ K,

where $T_c$ is the core temperature and $T_a$ is the air temperature above the disk. These parameters describe the approximate conditions for the first USD experiment.

TABLE XII

RUPTURE DISK OPENING TIMES FOR VARIOUS MATERIALS

| Description | Opening Time (s) | Relief Time (s) | Sound Speed in Core (m/s) | $\gamma$ (if gas) | Gram Molecule wt. (if gas) | Acoustic Impedence In Core ($kg/m^2/s$) |
|---|---|---|---|---|---|---|
| He | $1.9 \times 10^{-4}$ | $1.9 \times 10^{-4}$ | $1.25 \times 10^{3}$ | 1.67 | 4 | $2.67 \times 10^{3}$ |
| Typical USD simulant vapor phase | $2.0 \times 10^{-4}$ | $3.1 \times 10^{-4}$ | $3.12 \times 10^{2}$ | 1.3 | 50 | $8.3 \times 10^{3}$ |
| Freon 113 | $2.2 \times 10^{-4}$ | $4.4 \times 10^{-4}$ | $1.73 \times 10^{2}$ | 1.2 | 150 | $1.39 \times 10^{4}$ |
| Complex Molecule | $3.3 \times 10^{-4}$ | $9.3 \times 10^{-4}$ | 64 | 1.1 | $10^{3}$ | $3.44 \times 10^{4}$ |
| Biological Molecule | $8.2 \times 10^{-4}$ | $2.7 \times 10^{-3}$ | 19.4 | 1.0 | $10^{4}$ | $1.03 \times 10^{5}$ |
| Water (liquid) | 0.01 | $1.8 \times 10^{-4}$ | $1.5 \times 10^{3}$ | | | $1.5 \times 10^{6}$ |

Note that for all the gases listed, the opening time is equal to or less than the release time (here approximated as $t_r = 2r(1/a_b + 1/a_t)$. This would suggest that the opening times listed are roughly correct (i.e., the two- and three-dimensional effects are not too significant). For water, however, the opening time is about two orders of magnitude larger than the release time. Here, the rupture disk barely cracks open before release waves equilibrate the pressure difference across the disk and stop the petals from unfolding.

Preliminary SIMMER calculations of the first USD experiment suggest two important findings. First, rupture-disk opening times of less than about 1 ms appear to be adequate because the leading edge of the core material takes about 1 ms to move through the rupture disk structure when an instantaneous release is assumed. Thus, with opening times less than 1 ms, the petals move away fast enough for unimpeded core material motion. Second, partial openings

of the disk do not seem to affect the results significantly provided the flow area through the disk is larger than the opening in the UCS. For example, Fig. 54 shows the pressure drop across the UCS as a function of time for a fully open case and partially open case, with the available flow area reduced by a factor of four. Figures 55 and 56 show the velocity and density exiting the UCS for the fully open and partially open case, respectively. Clearly, no significant difference in these variables is observed between the two cases.

This analysis has suggested that rupture disks provide adequate opening times and angles if the core materials interacting with the rupture disk are primarily gases. We believe that this will be the case if flashing core simulants are used. We may, however, have difficulties with nonflashing core simulants when most of the core material is liquid.

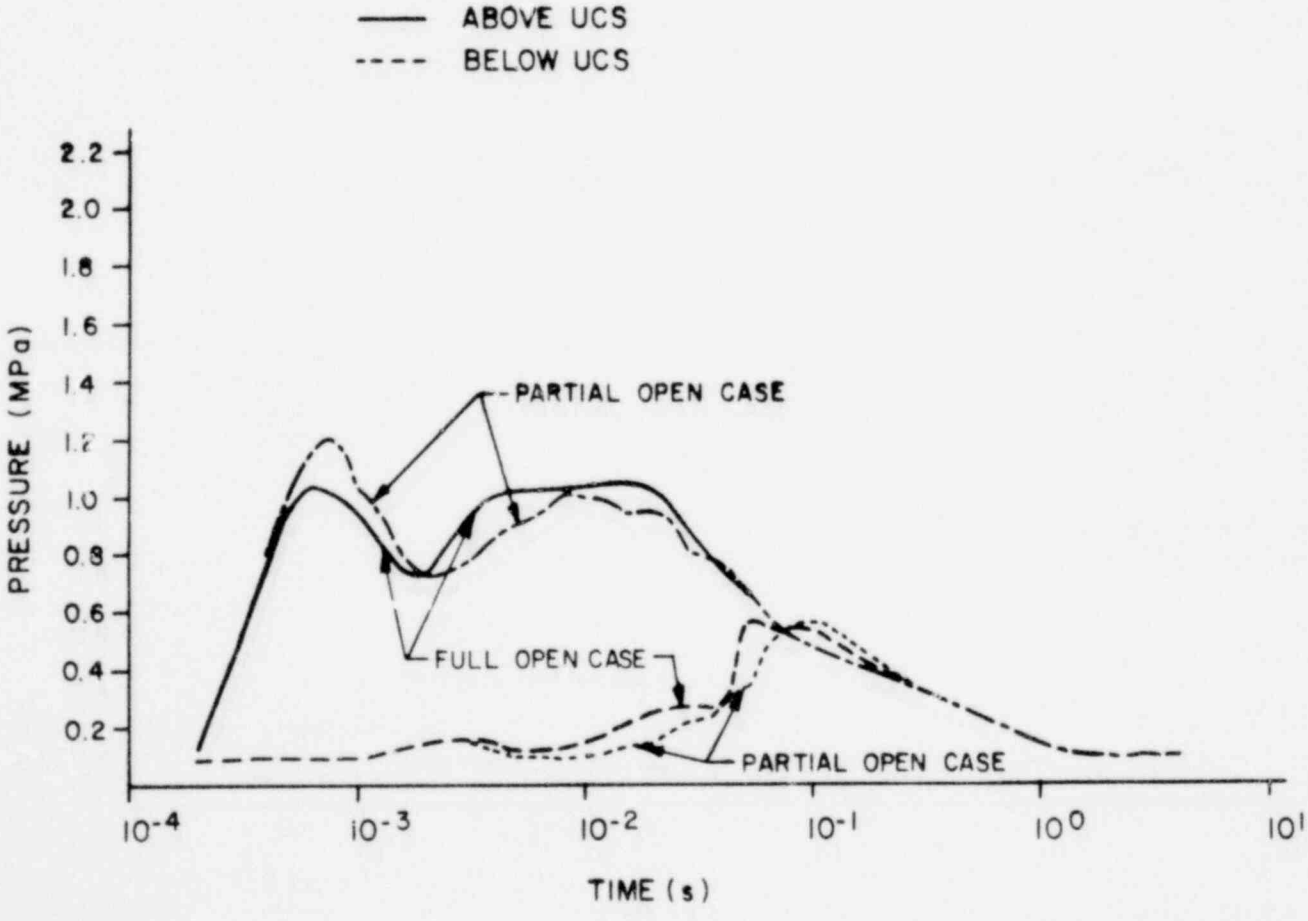


Fig. 54. SIMMER predictions of pressure drop across the UCS.

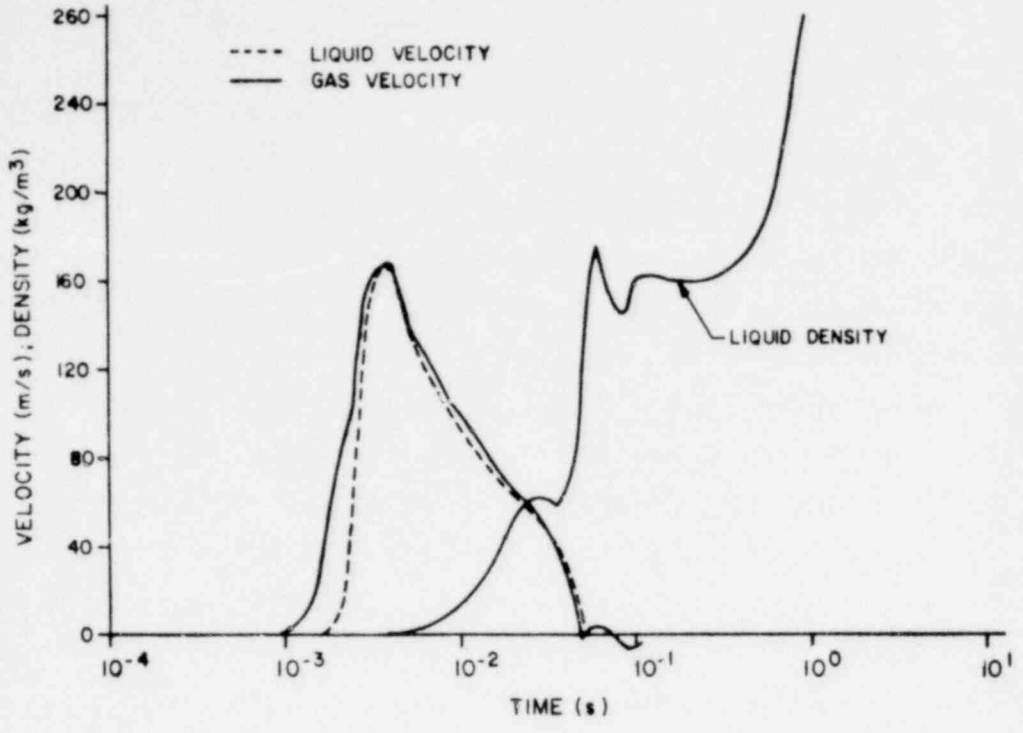


Fig. 55. SIMMER predictions of velocity and density at top of UCS.

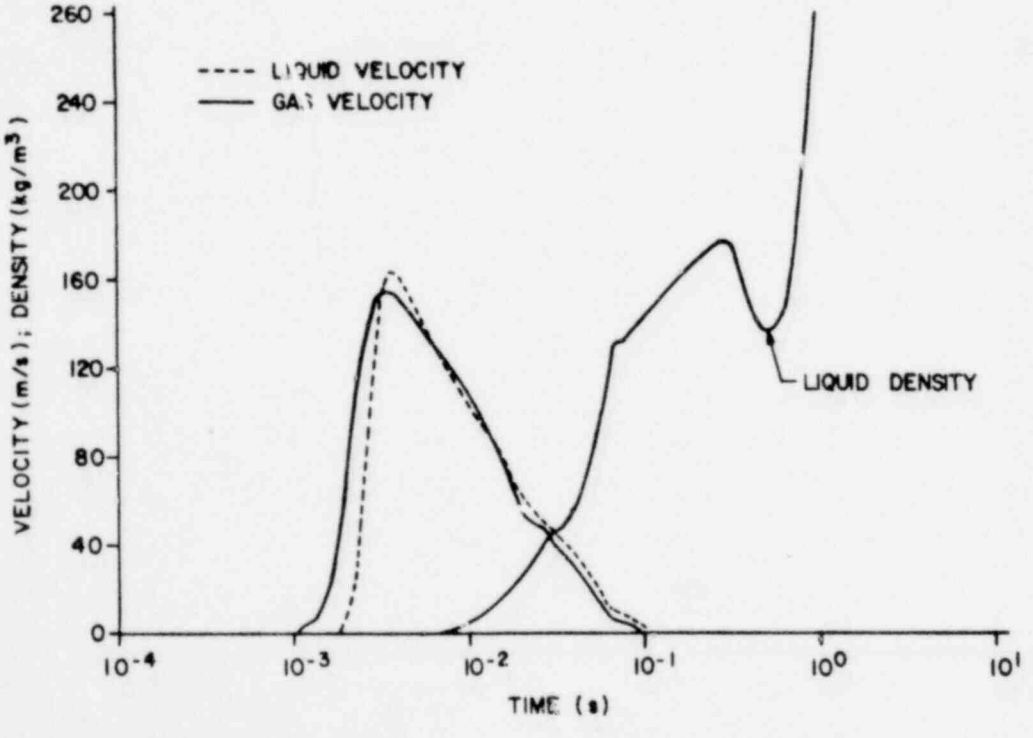


Fig. 56. SIMMER predictions of velocity and density at top of UCS for the partially open case.

## 5. USD Experimental Design

(V. S. Starkovich and L. A. Mondy, Q-8; and E. J. Chapyak, Q-7)

Instrumentation of the experimental hardware, including assuring the operability of the signal conditioning and signal recording electronics, was completed for the USD experiment. In addition, fabrication of the remaining hardware items was completed and all of the sensors and simulant materials needed for the Phase I and Phase II experiments were received.

Approximately 15 data channels are being employed on the experiment, including 5 temperature measurements, 5 pressure measurements, and 3 channels devoted to determining the velocity of the movable piston. The purpose of the movable piston[1] is to simulate the inertial loading of the sodium pool above the expanding two-phase core material in the accident analysis case. Although the piston itself has not been instrumented, the viewing chamber through which the piston moves has been equipped with three displacement transducers positioned along its axial length to permit time-of-flight (TOF) measurements to be done on the piston. In addition to calibration traces, actual pressure and temperature signals from each data channel have been recorded on FM tape and transmitted to hard copy.

Two of the hardware components that have received the most attention are the liquid level indicating apparatus, which allows initial core conditions to be measured, and the pin bundle for the scaled-down UCS, which is about 80% complete. The inner aluminum walls of the UCS will eventually be insulated to simulate more accurately the heat transfer rate that would occur in a thin-walled stainless steel subassembly can.

In addition, a mixing fixture was fabricated for the purpose of determining the optimum propeller type, size, and angular velocity for mixing of the liquid simulants in the multiple component Phase-II experiments. These simulants are ethylene glycol, n-propanol, and ammonia. We are investigating whether these simulants are chemically compatible with each other and physically compatible with the experimental hardware under the desired temperatures and pressures.

## 6. Assessment of Uncertainties in SIMMER Experiment Analysis

(R. D. Burns, Q-7)

During this reporting period we performed a sensitivity analysis to determine if SIMMER-II results were consistent with experimental observation. This work was preceded by a performance analysis in which parameters controlling numerical calculations were optimized.[10] The experiment we analyzed involved an LMFBR core-disruptive accident simulated with air and water and in scaled geometry.[65] The experiment was performed by SRI International.

Our approach employed variations in SIMMER-II input values that affect the magnitude of computed results. Because many input values are not known precisely and any of several different values may be equally likely, we expected several possible sets of calculated results. If the experimentally observed results are encompassed among the possible calculated outcomes, the experimental and calculational results coincide. If the range is narrow, agreement between observation and calculation can be claimed. If the range is wide, input uncertainties contributing to the magnitude of the range need to be reduced. A method of statistical sensitivity analysis has been developed to identify dominating uncertainties.[15,66]

In the present work, the experiment preceded the analysis. A nominal SIMMER-II calculation using best estimates for all input values yielded a set of results for a pressure history in the simulated reactor core and for the impact time of the simulated sodium pool with the reactor vessel head. The results deviated from the experimental observations. To explain the deviations, certain input values were speculated to be inaccurate in some SIMMER-II models. These include models for liquid-droplet size determination, water EOS, and heat transfer involving liquid water.

Fifteen independent input value variations were selected to encompass the range of possibly correct values. Some variations covered as many as four orders of magnitude. Widest uncertainty was assumed in the heat transfer models, while the least was in the water EOS. While the ranges of variation are continuous, they were discretized for purposes of this study. This resulted in 19 discrete values, all equally likely for each of the 15 independent variations. This amounts to $19^{15}$ (over $10^{19}$) possible calculated outcomes to be compared with the experimental observations.

From a sampling of the possible input sets we selected 19 to represent the domain of all possible outcomes. These translate into 19 SIMMER-II calculations, each with different values for the 15 uncertainties. The total CRAY-1 computational time for all runs was about 4 h. The number 19 was selected because it provides a high confidence (99%) that even weak correlations between input and output value variations will be detected (signal-to-noise ratio = 3).[10]

Results of the calculations showed widely varying system behavior, which is measured in terms of core pressure, impact time, and system kinetic energy. Because of the strong (inverse) correlation between pressure and impact time, no combination of both parameters was found to match observed values. If pressure is comparable, impact time is too early; if impact time is comparable, pressure is too high. Experimentally observed results were not consistent with those of SIMMER-II even when accounting for wide input uncertainty; we then determined that a systematic error existed in problem input for SIMMER-II in describing the correct amount of water present in the core. The correction resulted in better agreement between the nominal calculation and the experiment.

In further evaluation of the results, we discovered three regions of behavior. The first high-energetics region is characterized

by slowly decaying core pressure and early impact times. The SIMMER-II runs that exhibited this behavior tended to have large areas for water heat transfer resulting in rapid vapor generation. A second, intermediate-energetics region involves rapid decay to about half the original core pressure from rapid vapor expansion followed by pressure recovery as vaporization becomes important. A third, low-energetics region is characterized by rapid, almost total decay of core pressure with very small system accelerations because of no pressure recovery from vaporization. The SIMMER-II runs exhibiting this behavior had small areas for water heat transfer.

The variation in behavior is attributed to flow-regime and droplet-size uncertainties. The behavior observed in the experiment was that of intermediate energetics; thus, the uncertainty in input parameters was reduced to preclude the high and low ranges. To reduce uncertainty within the intermediate region and thereby achieve better agreement with the experiment, statistical sensitivity analysis indicated the need for improvements in models involving vaporization calculations. With these improvements we achieved agreement between the experiment and the SIMMER-II results (Ref. 67 and Sec. III.B.3 above).

7. LAFM Analysis of HEDL 50¢/s TOP Reference Base Case

(P. K. Mast, Q-7)

At the request of HEDL, we have analyzed a hypothetical 50¢/s transient overpower (TOP) accident involving an FTR-type pin (50¢/s TOP reference base case) using the Los Alamos Fuel Model (LAFM) code.[68] The specified initial conditions (Table XIII)[69,70] are representative of a pin with a goal burnup of 80 000 MWd/kg. A constant inlet coolant temperature of 589 K and constant inlet coolant flow of 0.118 kg/s were assumed in the analysis.

The 50¢/s power transient was simulated by using a power-time history given by

$$P/P_o = e^{0.613\ t},$$

where t is in seconds. All of the energy was assumed to be deposited in the fuel using a flat radial power profile.

TABLE XIII

PIN CHARACTERISTICS

| | |
|---|---|
| Peak Burnup | 80 000 MWd/kg |
| Peak Fluence | $1.2 \times 10^{23}$ n/cm$^2$ (E > 0.1 MeV) |
| Fuel-Cladding Gap | 0.0 m |
| Peak Pin Power | 41.01 kW/m |
| Plenum Pressure | 1.4 MPa |

---

Cladding properties (Larson-Miller parameter, yield stress) at a goal fluence of $1.2 \times 10^{23}$ n/cm$^2$ are not available. There is, however, some experimental evidence to suggest that cladding damage saturates[71] (or possibly starts to recover[72]) above a fluence of ~ $6 \times 10^{22}$ n/cm$^2$. Thus, the cladding properties used in the analysis are those for a fluence of $6 \times 10^{22}$ n/cm$^2$.

The calculated sequence of events for this 50¢/s transient began with a closed fuel-cladding gap (see summary in Table XIV). Solid fuel-cladding differential thermal expansion occurs as soon as the power starts to increase (shortly after time 0.0). At 1.23 s into the transient, permanent cladding deformation begins (starting at an axial height of ~ 0.69). At this time, the cladding loading mechanism is still strictly differential thermal expansion (fission gas pressure is too low to be important).

Fuel-cladding differential thermal expansion is calculated to continue until ~ 2.75 s into the transient. At that time, the calculated cladding-life fraction[68] at a height of ~ 0.86 (the eventual failure location) is 0.18 (failure occurs at a life fraction of 1.0). From 2.76-2.85 s, fission gas pressurization of the pin is the dominant cladding loading mechanism. During this time, the life fraction at a height of ~ 0.86 increases from 0.18-0.34. This fission gas pressure in the pin reaches a peak value of ~ 50 MPa.

At 2.85 s into the transient, fuel melting and the subsequent expansion of the molten fuel is calculated to deplete the available fuel porosity. The subsequent pressurization of the molten fuel volume is assumed to cause cladding failure shortly thereafter at

TABLE XIV

CALCULATED SEQUENCE OF EVENTS

| Time (s) | Description |
|---|---|
| 0.00-2.75 | Fuel cladding differential thermal expansion is calculated. |
| 1.23 | Permanent cladding strain begins at a relative height of ~ 0.69. |
| 2.64 | Melt fraction of 50% is reached at a relative height of ~ 0.55. |
| 2.75 | Calculated life fraction at a relative height of ~ 0.86 is 0.18. |
| 2.75-2.84 | Fission gas pressurization is dominant cladding loading mechanism. |
| 2.84 | Calculated life fraction at a relative height of ~ 0.86 is 0.34. |
| | Peak cladding strain (at a relative height of ~ 0.86) is 0.34%. |
| | Pin fission gas pressure is ~ 50 MPa. |
| | Cladding temperature (at a relative height of 0.86) is 1 150 K. |
| 2.85 | Fuel porosity collapse and subsequent molten fuel pressurization leads to pin failure. |

---

an axial location of ~ 0.86 (the location of peak life fraction at that time).

It is interesting to note that the peak fuel melt fraction at the best estimate failure time is 58% (at an axial height of ~ 0.64) A peak melt fraction of 50% was reached at 2.64 s at an axial height of ~ 0.55. Thus, a 50% melt fraction criterion would have predicted failure within 200 ms of the best estimate failure time but at an axial height of 0.55 instead of 0.86. This reflects the difficulty in using the 50% melt fraction criterion to predict the location of pin failure in hypothetical TOP accidents.

This analysis indicates that for the goal burnup of the specified FTR-type pin, initial pin failure during a hypothetical 50¢/s TOP accident will occur near the top of the active core at a time when a substantial amount of pressurized molten fuel exists

in the pin. The ultimate outcome of such a TOP event depends largely on the degree of fuel effusion (vs blockage) of the coolant channels. However, previous analyses[20] have indicated the late, top-of-core, pin failure scenario results in the most benign potential TOP accident consequence.

## C. Evaluation of LMFBR Fuel and Clad-Motion Diagnostics

(A. E. Evans, M. B. Diaz, B. Pena, E. E. Plassmann, and W. L. Talbert, Jr., Q-14)

Previous studies using the scanning hodoscope with the PARKA critical assembly have been directed predominantly toward the study of fast-neutron images of the $UO_2$ pellets in arrays of FTR fuel pins. These fast-neutron images have been found to suffer less than gamma-ray images from the effects of scattering and self-absorption of radiation in the test samples and in such necessary intervening material as the steel walls of the test assembly capsule. However, there is still an interest in gamma-ray imaging and some groups plan to use this technique as a fuel-motion diagnostic. An example is the coded aperture systems being developed at Sandia Laboratories.[73] Furthermore, it has been proposed that high-energy gamma radiation from neutron capture in iron can be used to image cladding in the test section, at least to a point where blockage formation might be detected.[74]

Already reported gamma-ray imaging studies were completed using stilbene,[75] NE102, and NaI(Tl)[76] scintillators. These studies have been limited because of poor counting efficiency when discriminators are set for energy thresholds of greater than 1 MeV. Background shifts, caused by reactor fission product activity and, in the case of NaI(Tl) detectors, the buildup of $^{128}I$ activity during the hour or so required to scan a test assembly, also impeded these studies. We now find that the newly available bismuth germanate (BGO) scintillators offer an opportunity to improve the gamma-ray imaging data which the PARKA nodoscope can measure. This is possible because the BGO full-energy-peak efficiency is much less precipitously dependent upon photon energy than

that of the other detectors. Response of BGO detectors to gamma radiation from 0.12-8.28 MeV was measured and reported during the previous quarter.[10]

We first needed to determine whether the BGO detectors would show effects of activation or radiation damage in the environment in which PARKA hodoscope detectors operate. Accordingly, the previously used 12.8 x 12.8-mm detector was mounted in front of one of the collimator slots while PARKA was operated at 5 mW/g $^{235}U$ for 4 h with a 37-pin FTR test assembly in the test hole. The collimator slot was held fixed on the center of the test assembly and the counting rate from the detector, biased at 1 MeV, was taken every 5 min., starting at the time the reactor reached full operating power. The resulting data are shown in Fig. 57, together with those obtained simultaneously from a stilbene detector and the results of a prior run using a NaI(Tl) detector. The counting ratio of the BGO and stilbene detectors remained constant over the entire 4-h run, suggesting that the 13% buildup in count rate in both detectors was related to the radiation environment rather than to the detectors, and is probably associated with fission-product buildup in the test section. The departure of the NaI(Tl) data from this behavior is obvious.

A pulse-height distribution from our 38-mm BGO detector mounted in front of one of the collimator slots is shown in Fig. 58. For this measurement, the collimator was pointed at the edge of the test area which had a 22-mm-thick steel test sleeve in place. In this position, the detector was "seeing" a total thickness of 154 mm of steel. We identified the observed high-energy radiation as capture-gamma rays from iron. The peaks indicated on the figure correspond to available data.[77] The 7.64-MeV peak is from radiation to the ground state of $^{57}Fe$ after thermal-neutron capture by $^{56}Fe$. Higher energy transitions, 9.30 and 10.16 MeV, due to neutron capture in $^{54}Fe$ and $^{57}Fe$, were too weak to be useful for these studies. The spectrum displayed was accumulated in 3 000 s with PARKA again operating at a power level of 5 mW/g $^{235}U$.

Removing the steel test sleeve reduced the intensity of the high-energy radiation by only 15%. By moving the detector to one

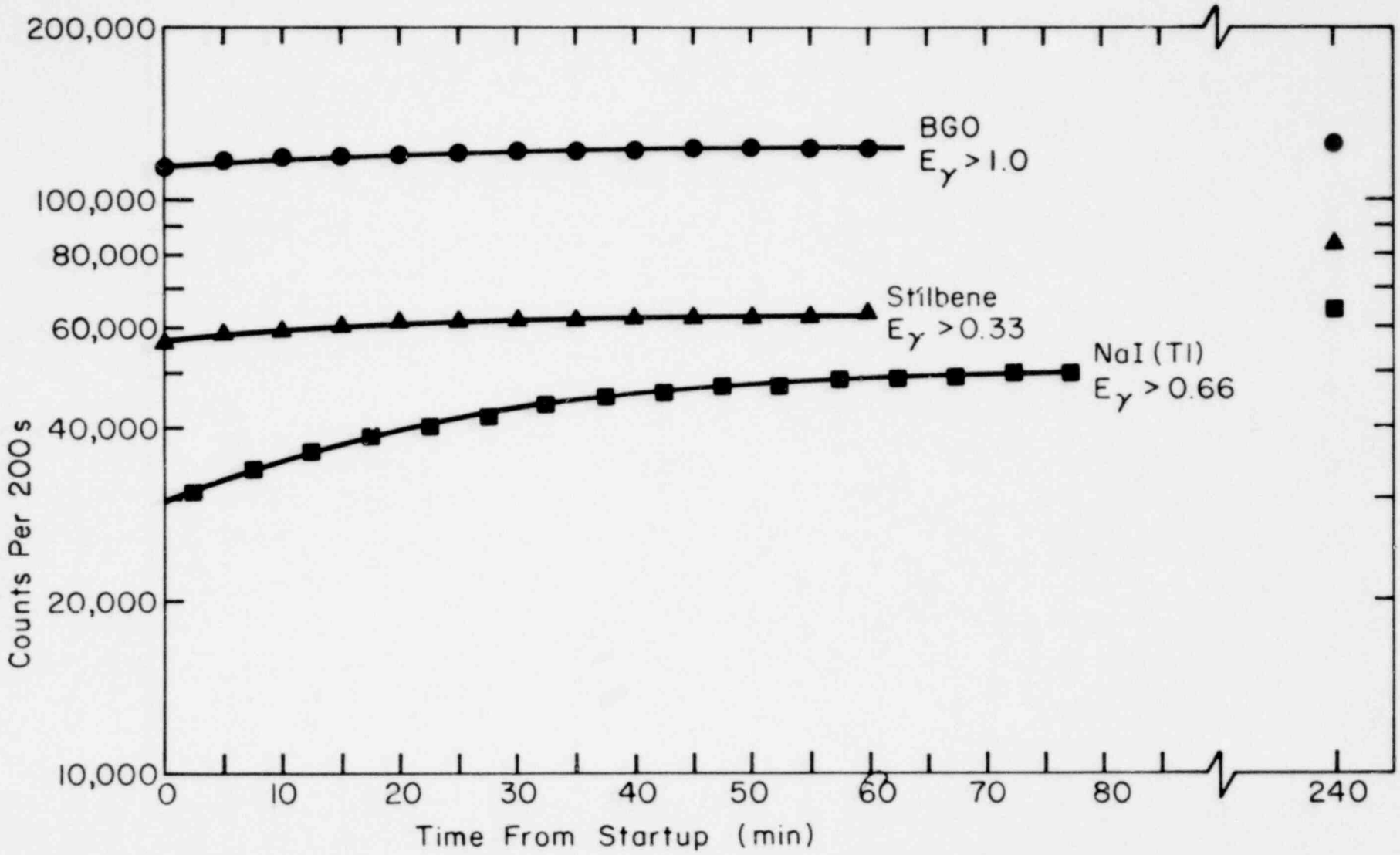


Fig. 57. Counting rate buildup in BGO, stilbene, and NaI(Tl) scintillators when used as detectors for the PARKA hodoscope system.

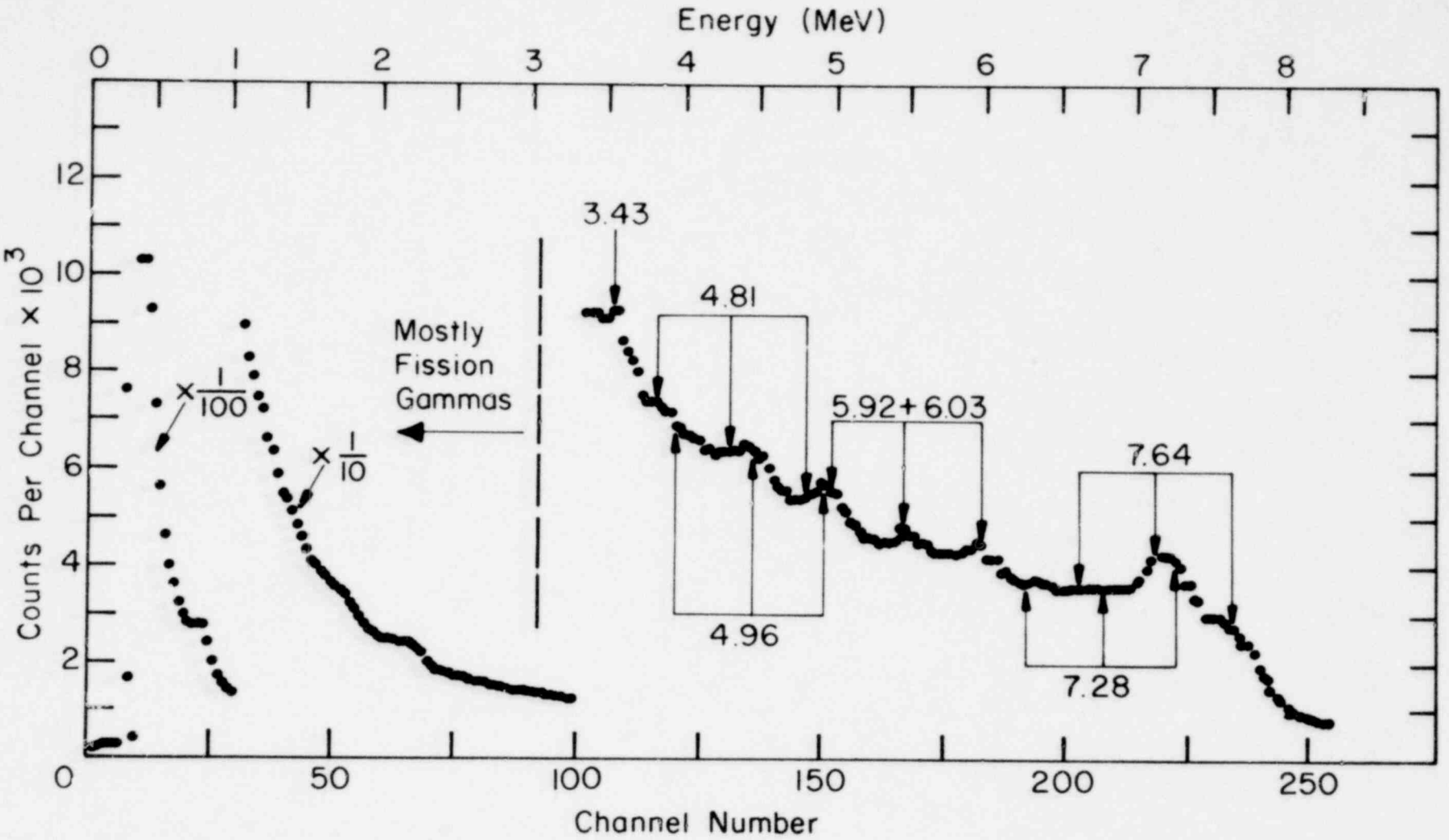


Fig. 58. Gamma-ray pulse-height distribution from the PARKA hodoscope, using a 38-mm x 38-mm bismuth germanate scintillator. Identified transitions from thermal neutron capture in iron are from Ref. 77.

side of the collimator slot, we were able to determine that 3/4 of the observed iron capture-gammas originated in steel near the detector, i.e., from capture of thermal neutrons in the steel of the collimator near the detector end. After switching to the 12.5-mm BGO detector, this high-energy background was reduced to about 23% of the total signal.

Thimbles for tests in the upgraded TREAT Reactor at Idaho Falls are expected to have steel walls with thicknesses of up to 45 mm. Thus, a collimator slot centered on one of these test assemblies will also be looking at radiation from at least 90 mm of steel. Using a mass removal coefficient[78] of 0.030 $cm^2/g$ for 7.6-MeV gamma rays in steel, which translates into a linear cross section $\Sigma$ of 0.236 $cm^{-1}$, the signal from steel in the test region will be attenuated to exp(-0.236 x 4.5) or 35% of its original strength. However, one must consider the effect of all of the steel in view of the collimator. Considering the steel jacket as a uniformly radiating source of 7.6-MeV gamma rays, the count rate R at the detector from gamma rays originating in the jacket steel will be (ignoring absorption in the test assembly),

$$R = \int_0^T s(x)\, e^{-\Sigma x}\, dx \ ,$$

where T is the total thickness of steel being observed (i.e., twice the wall thickness), s(x) is the intensity of 7.6-MeV gamma rays emitted at position x (which to simplify our argument, we shall assume to be a constant, S), and $\Sigma$ is the linear removal cross section for these gamma rays. Integrating,

$$R = \frac{S}{\Sigma}\,(1 - e^{-\Sigma T}) \ ,$$

which approaches a saturation value $R_o = S/\Sigma$ for an infinite slab. Furthermore, the signal $\delta R$ from a small additional quantity of steel anywhere in line with the collimator, as for instance in the test region, will be $\Sigma R_o \exp(-\Sigma T)dx$. For a vessel with 4.5-cm-thick

walls or a total thickness of 9.0-cm steel, $R = 0.88\ R_o$ and $\delta R = 0.028\ R_o\ cm^{-1}$. A clad blockage 1 cm thick in the test assembly would therefore be expected to increase the number of 7.6-MeV gamma rays reaching the detector by ≈ 3%.

This somewhat simplified calculation may be compared with hodoscope collimator data taken of the test region in PARKA with varying quantities of steel. As one goes from the center to the edge of the test section, the thickness of steel seen by the collimator increases. Taking measurements at the center and edge of the test region gives us values of 11.2 and 12.7 mm of steel with the removable 22-mm sleeve withdrawn, and 54 and 98 mm with this sleeve in place. Counts of pulses corresponding to an energy interval of from 6.2-8.1 MeV (with noncollimated background subtracted) are shown in Table XV. Comparison with the uniform source model discussed above shows the effect of thermal neutron flux depression in the steel. These results are interpreted to indicate that a 1-cm-thick steel blockage in the test assembly would cause an increase in count rate of capture gamma rays of the order of 1% with the test assembly enclosed in a 45-mm-thick steel capsule.

We have already shown that fissioning fuel may be imaged with gamma-ray sensitive detectors. Now we find that the signal-to-background ratio of gamma-ray images of fuel can be enhanced by selection of the gamma-radiation energy interval used to form the image. This is indicated in Fig. 59, which is derived from pulse-

TABLE XV

OBSERVATION OF 7.6-MeV GAMMA RADIATION FROM SEVERAL THICKNESSES OF STEEL IN PARKA

| Steel Thickness (mm) | Measured Net Counts (1 000 s) | Computed Counts/1-exp(-ΣT) |
|---|---|---|
| 11.2 | 2 507 | 10 806 |
| 12.7 | 2 817 | 10 876 |
| 54 | 3 443 | 4 781 |
| 98 | 4 162 | 4 619 |

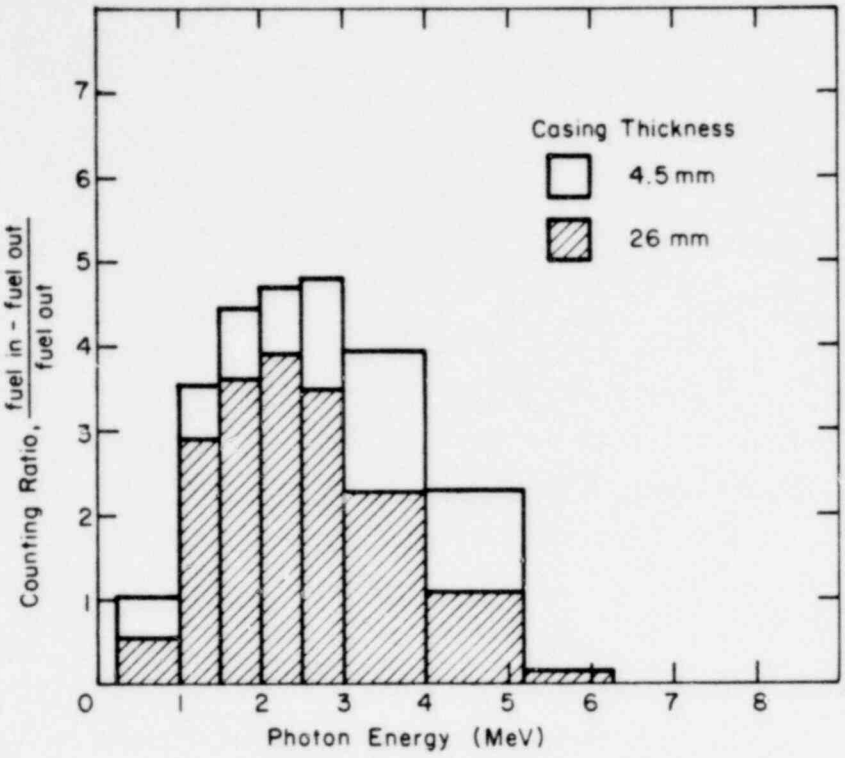


Fig. 59. Gamma-ray signal-to-background ratio as a function of pulse height for a 37-pin FTR test assembly in PARKA, with the test assembly surrounded by 5.6- and 26-mm-thick steel casings.

height distributions using the 12.5-mm BGO detector to scan across flats of a 37-pin test assembly and across a voided section of the test region, both with and without the 22-mm removable steel shell. The results show that photons of energies above 3 MeV will produce images with poorer signal-to-background ratios than those in the energy range from 1-3 MeV. This points out the desirability of using an upper level, as well as a threshold discriminator for fuel motion imaging with gamma sensitive detectors. We can also conclude that nonenergy-dispersive detectors, such as gamma sensitive fluors used for direct imaging of self radiation from a test assembly, should, if possible, also have an energy-dependent response tailored to maximum sensitivity in the 1-3-MeV range.

## IV. HTGR SAFETY RESEARCH PROGRAM

(M. G. Stevenson, Q-DO)

Under the sponsorship of the NRC/RSR, LASL is conducting a program of research in High-Temperature Gas-Cooled Reactor (HTGR) safety technology in the following task areas:

- Structure Evaluation
- Phenomena Modeling, Systems Analysis, and Accident Delineation

Progress for this quarter in these two areas is reported below.

### A. Structural Evaluation

(C. A. Anderson, Q-13)

Work during the past quarter has been concentrated on the seismic program with preparations for a final series of seismic tests on the two-dimensional core block model at the White Sands Missile Range (WSMR) and the participation of R. C. Dove in the seismic testing of a 1/2-scale model of the Very High-Temperature Reactor (VHTR) core at the Takasago Laboratory at Takasago, Japan. The activity is reported in detail below. Work on development of a prestressed concrete reactor vessel (PCRV) analysis capability is being carried at a low level with the main activity being a review of concrete constitutive relations; no report on this activity is included here.

#### Seismic Program

(R. C. Dove and W. E. Dunwoody, Q-13)

The two-dimensional HTGR core block model has been scheduled for a final series of tests at the WSMR during the period July 30-August 3. This final test series will investigate the effect of side wall and dowel pin clearances on the core forces developed during a seismic event.

During the present quarter, R. C. Dove worked with the VHTR Design Group at the Tokai Establishment of the Japanese Atomic Energy Research Institute (JAERI). The period of March 17-May 12, 1979 was selected because during this period a 1/2-scale model of the VHTR core was being seismically tested. This particular model represented a vertical slice of the VHTR core, and as such, contained 121 hexagonal core blocks, plus side reflectors, side wall spring packs, and plenum caps. This model was constructed by the Mitsubishi Heavy Industries (MHI) and tested at the MHI Takasago Laboratory. Figure 60 illustrates this 1/2-scale model.

The testing of this model began in February, 1979 and is scheduled to be completed by October 15, 1979. A visit to the Takasago Laboratory during the period of March 27-April 10, 1979 was carried out to observe one complete series of tests on the model. This series involved the use of bilinear springs to support the side reflectors. The model was well instrumented with displacement, force, acceleration, and strain transducers. The measuring, recording, and test equipment was of high quality. During these tests the model was subjected to both sinusoidal sweep and simulated earthquake tests.

In the nuclear reactor field the Mitsubishi Takasago Laboratory has conducted simulated earthquake tests on:

1. a 1/12-scale model of the containment proposed for the "MONJU" fast breeder reactor,
2. a scale model of the "JOYU" experimental fast-reactor pressure vessel,
3. a full-size mockup of the double-walled piping to be used in the "MONJU" primary,
4. a full-size residual heat removal (RHR) pump and piping used in the Japanese PWR-type reactors, and
5. a full-size mockup of the scram rod system to be used in the "MONJU."

The last item is still undergoing tests. It is a very large system since it includes the rod drive mechanism, the full-sized

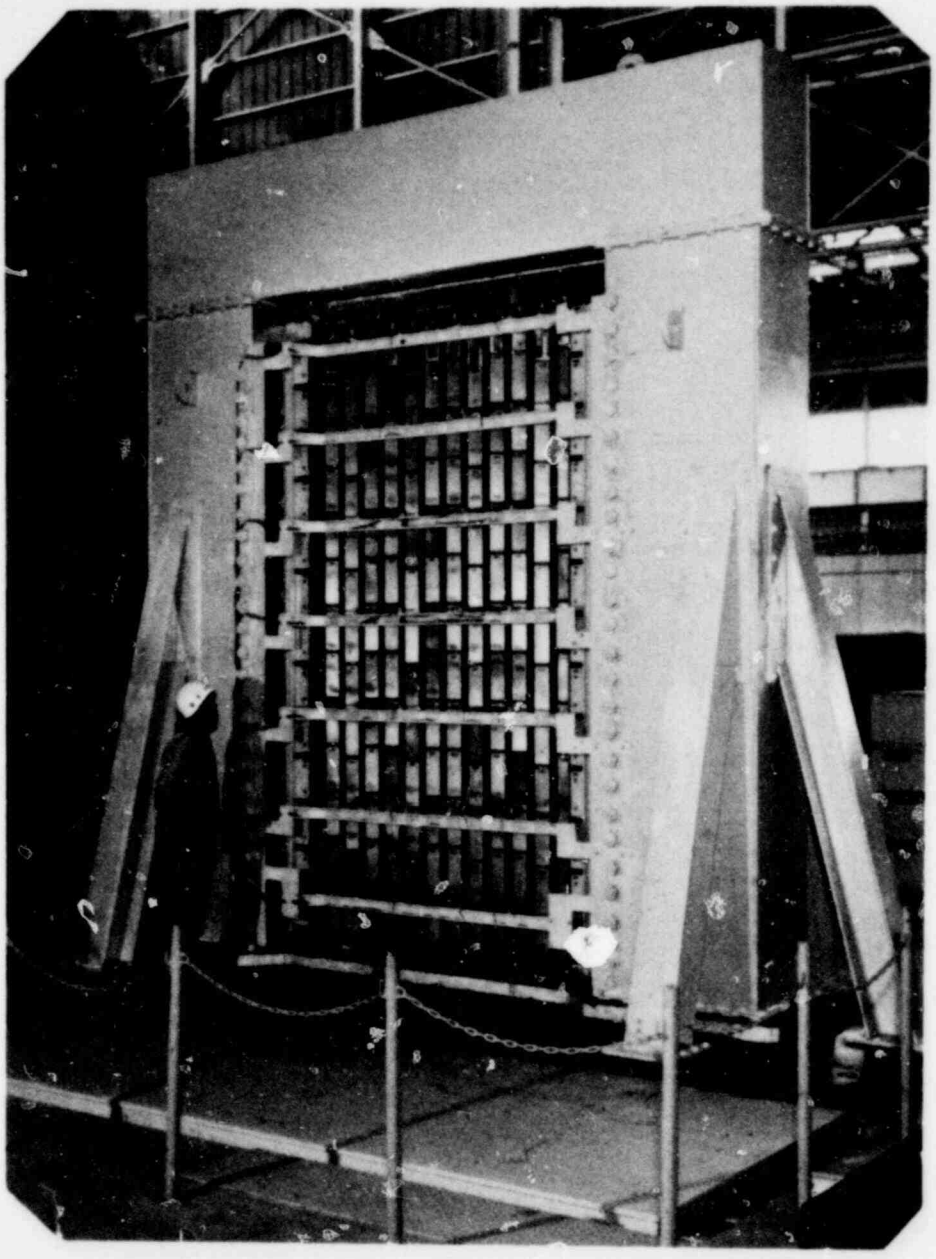

Fig. 60. Half-scale HTGR model at Takasago Technical Institute.

rod, and a 19-element fuel region immersed in water. The total test element height is about 27 m. Because of the very large size and mass, this test is not being conducted on a conventional servo-hydraulic shaking table. Instead, this entire system is mounted on rollers and is excited by two hydraulic shakers positioned at top and bottom of the assembly. This test is sponsored by the Power Reactor and Nuclear Fuel Development Corporation (PNC).

Following the visit to the Takasago Laboratory, Dr. Dove returned to the JAERI Tokai Establishment and participated in the analysis of the VHTR model test results, comparison of experimental and analytical results, and discussion of the plans for additional VHTR model tests. After the conclusion of these VHTR model tests, a report will be prepared by Dr. Ikushima of JAERI.

Other activities while at the JAERI Tokai Establishment included:

1. Work with Dr. Takeo Uga on the translation of a report on the seismic testing of an RHR pump. This report should be available (in English) in June 1979.

2. Review and discussion of a preliminary report prepared by Muto Institute of Structural Mechanics on the "Candu Core Seismic Test." A paper based on these tests will be presented by Dr. Muto at the 5th International SMIRT Conference to be held in Berlin, Germany, on August 13, 1979.

3. Preparation and delivery of a lecture titled, "Scale Model Theory." This lecture was designed to emphasize fluid-structure interaction since JAERI engineers in the Reactor Safety Division who are working on the emergency core cooling tests expressed special interest in this topic.

## B. Phenomena Modeling, Systems Analysis, and Accident Delineation

(K. R. Stroh, Q-6)

### Fission Product Release and Transport

(J. L. Lunsford, Q-6)

Results from some of the LASL fuel particle heatup and failure experiments have been reported in earlier quarterly reports. The experiments were stopped in 1978 and a formal report describing the results is being published. A summary of this work is provided here.

#### a. Experimental Results

Six types of fuel particles were present in the beads received from the General Atomic Company (GAC). Table XVI summarizes fuel particle histories in the shipment. Table XVII summarizes the test results.

TABLE XVI

FUEL PARTICLE IRRADIATION HISTORIES

| Capsule | Coating | Kernel | Irradiation Conditions: Temperature (°C) | Irradiation Conditions: Fast Fluence ($10^{21}$ n/cm$^2$) | Irradiation Conditions: Kernel Burnup (% FIMA) |
|---|---|---|---|---|---|
| HB-5 | TRISO | $U(C_{3.0}O_{0.5})$ | 700 | 4.9 | 59.0 |
| FTE-14 | TRISO | $UC_2$ | 1 000 | 1.2 | 23.0 |
| F-30 | TRISO | (Th/U)C | 1 251 | 9.1 | 18.2 |
| P13R | BISO | $ThO_2$ | 1 000 | 11.4 | 4.4 |
| P13S | BISO | $ThO_2$ | 940 | 11.6 | 4.1 |
| HT-28 | BISO | $ThO_2$ | 900 | 6.4 | 7.2 |

During the course of the work, some 66 experiments were conducted. Some of these experiments were thermal runs made without a fuel particle in the furnace, some were room temperature experiments with fuel particles broken with a piston device *in situ* in the furnace liner, while most were thermal runs made with a fuel

TABLE XVII

FUEL PARTICLE TESTING RESULTS

| Capsule | Total Number Received | Number Tested at Room Temperature | Number Tested at Elevated Temperature | Total Number Tested |
|---|---|---|---|---|
| HB-5 | 30 | 0 | 1 | 1 |
| FTE-14 | 50 | 6 | 2 | 8 |
| F-30 | 50 | 0 | 31 | 31 |
| P13R | 20 | 3 | 13 | 16 |
| P13S | 20 | 0 | 1 | 1 |
| HT28 | 10 | 0 | 0 | 0 |
| Totals | 180 | 9 | 48 | 57 |

particle in place in the furnace. In most cases, thermal runs to temperatures above 2 200°C caused bead failure as detected by the appearance of $^{85}Kr$ in the ionization chamber.

In actual testing, the question arises as to whether or not the appearance of an ionization current peak indicates instantaneous and catastrophic failure of a fuel particle. The way in which the krypton escapes the particle and travels to the ionization chamber, through the outlet gettering furnace and the associated plumbing, determines what interpretation will be placed on the shape of the current trace. It is instructive, therefore, to examine the simplest possible case: namely, the current peak resulting from a mechanical crushing at room temperature of a fuel particle located in the center of the furnace. This was accomplished with a small piston device that was designed to crush and grind a single fuel particle. The mechanical breaker, which was hand-operated, could be inserted through a vacuum seal in line with the furnace liner tube. To operate the breaker, a fuel particle was placed in the chamber, the device was inserted into the furnace, helium flow was established with both the inlet and outlet gettering furnaces in operation, and the bead was broken in situ. Figure 61 (Run No. 58) shows the resultant current trace for a TRISO particle. The dotted line represents the beginning of the current peak as determined by monitoring the most sensitive scale of the electrometer voltmeter. The time delay for the appearance of the krypton in the ionization chamber was measured at 11.8 min. for this case of a TRISO/FTE-14 break with 150 ft of copper tubing and a flow rate of 1 cc/s through a 250 cc ion trap into a 1 000 cc ionization chamber. For a BISO particle, Fig. 62 (Run No. 63) indicates the response of the ionization current for a mechanical P13R break with 150 ft of copper tubing and a flow rate of 1 cc/s through a 250 cc ion trap into a 1 000 cc ionization chamber. Because the current levels for the BISO are reduced an order of magnitude from those for the TRISO, these data suggest that a large reduction of the krypton concentration does little to change the relative shape of the response curve of the ionization chamber.

Thermal failure in TRISO fuel particles was accompanied by a current trace having much the same appearance as for the mechanical

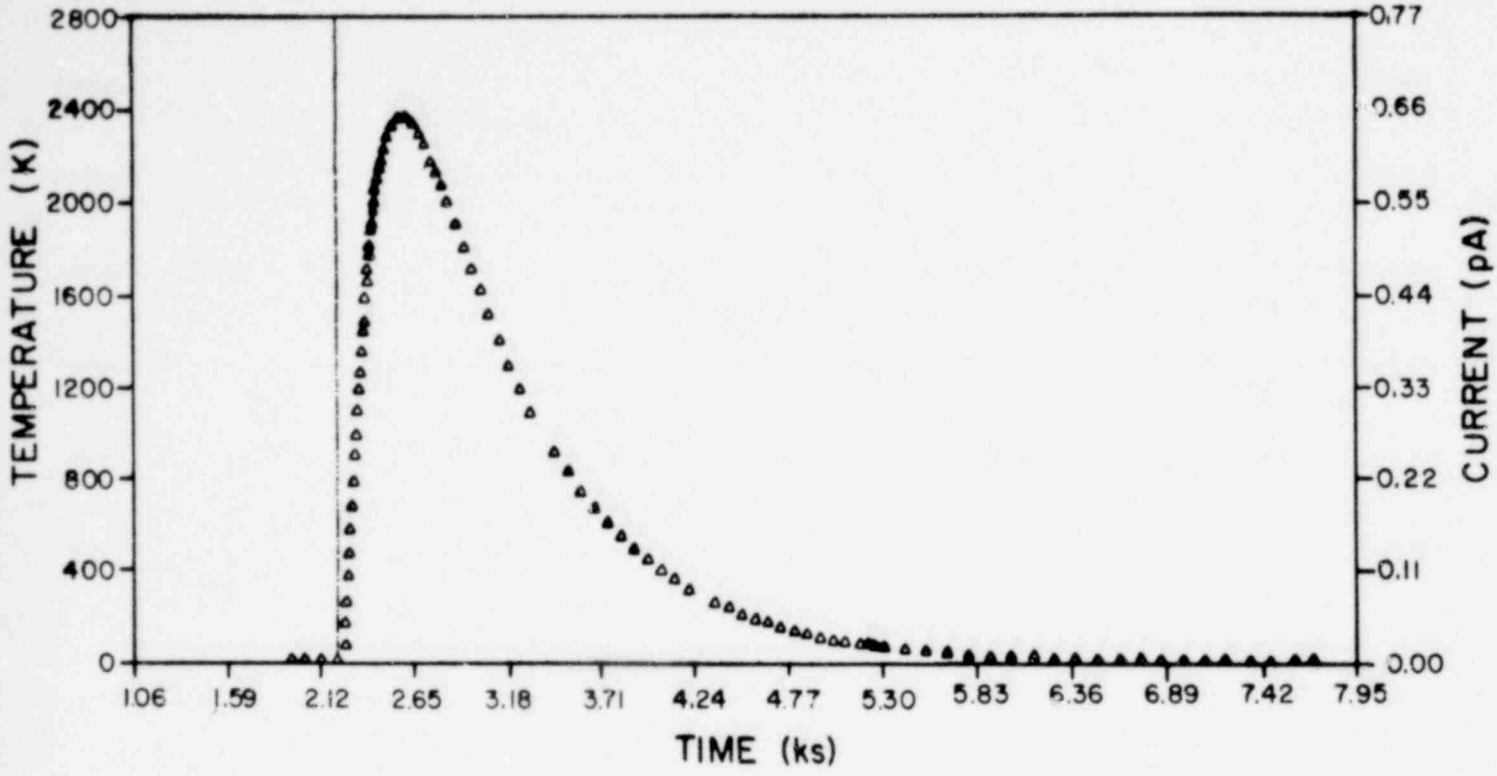


Fig. 61. Room temperature break of a TRISO/FTE-14 fuel particle with 150 ft of tubing and 1 cc/s sweep rate through a 250 cc ion trap into a 1 000 cc ionization chamber.

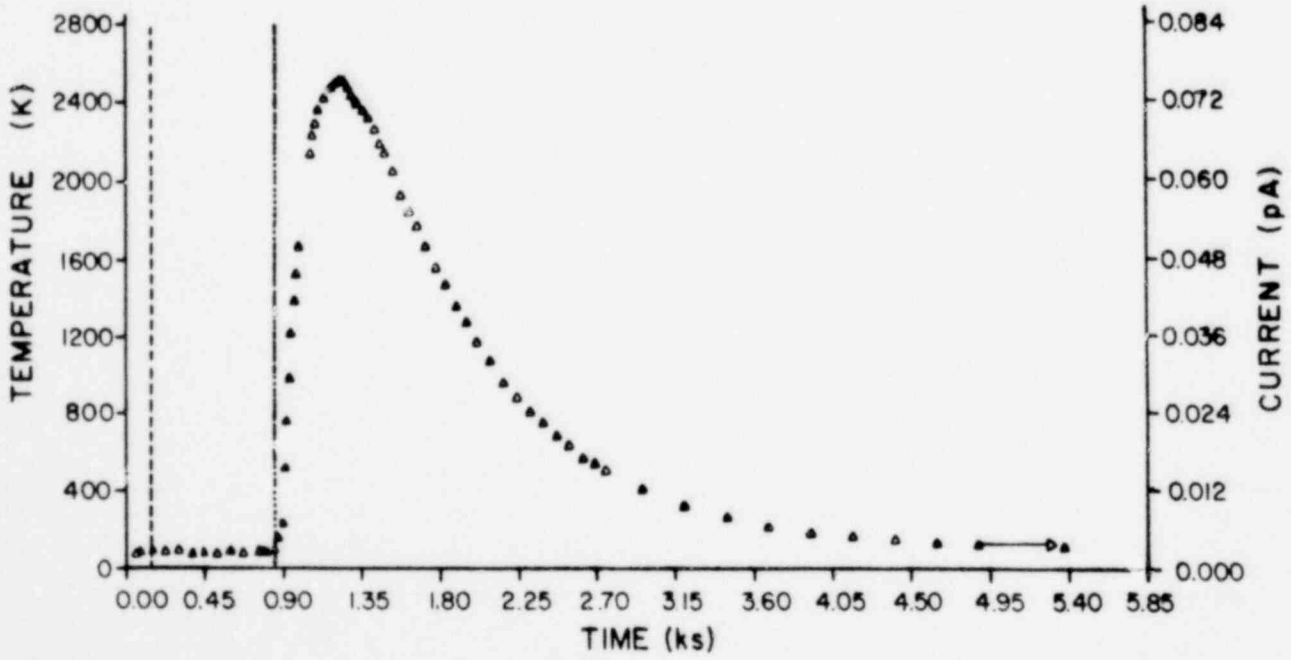


Fig. 62. Room temperature break of a BISO/P13R fuel particle with 150 ft of tubing and a 1 cc/s sweep rate through a 250 cc ion trap into a 1 000 cc ionization chamber.

break at room temperature. Figure 63 (Run No. 53) shows the current trace for a TRISO/F-30 bead. (The tantalum liner tube breached during the run and the gas flow was adjusted twice to compensate for bypass leakage. The times corresponding to these two adjustments are indicated by the vertical dashed lines. The solid line indicates the start of the power rampdown.) The room temperature break was carried out with 150 ft of tubing and a 1 cc/s sweep rate through a 250 cc ion trap into a 1 000 cc ionization chamber. The break at temperature occurred in a test with 50 ft of tubing and a 0.5 cc/s flow rate through a 250 cc ion trap into a 1 000 cc ionization chamber. Furthermore, the thermally induced turbulence in the liner tube at 2 500°C is appreciable. Nevertheless, the appearance of the response at temperature tends toward that of the mechanical break at room temperature. More important is the fact that the power ramp down at 12 ks did not perturb the

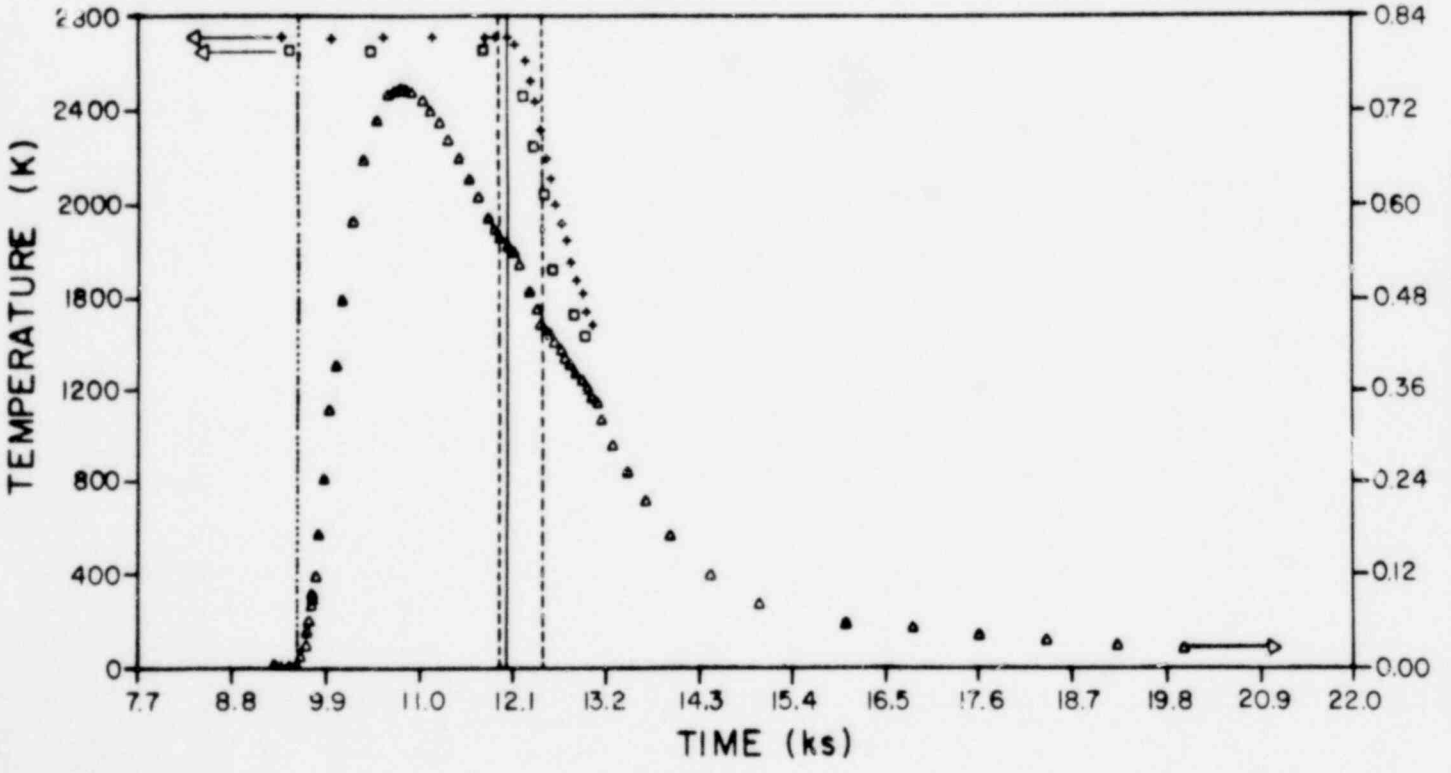


Fig. 63. Thermal break of a TRISO/F-30 fuel particle with 50 ft of tubing and a 0.5 cc/s sweep rate through a 250 cc ion trap into a 1 000 cc ionization chamber. Squares indicate boat temperatures; crosses indicate cavity temperatures.

krypton release curve. Consequently, we favor an interpretation that the TRISO particles were failing instantaneously.

Thermal failure in BISO fuel particles was accompanied by a current trace having a totally different appearance from the mechanical break at room temperature. Figure 64 (Run No. 66) shows the current trace for a BISO/P13R bead. (The curve has clearly been interrupted by the power-down ramp after more than 6 h into the run and 4 h at temperature. The vertical chain-dotted lines indicate changes in the power program.) Both of the runs were conducted with 150 ft of tubing and a sweep rate of 1 cc/s through a 250 cc ion trap into a 1 000 cc ionization chamber. The appearance of the two curves is totally different. More important, the shape of the curve clearly implies that the release of krypton is diffusion-controlled as a temperature drop of 260°C at 21 ks caused a decrease in the krypton release rate of a factor of 6.3, and a subsequent drop of 180°C at 26 ks caused a drop in the release

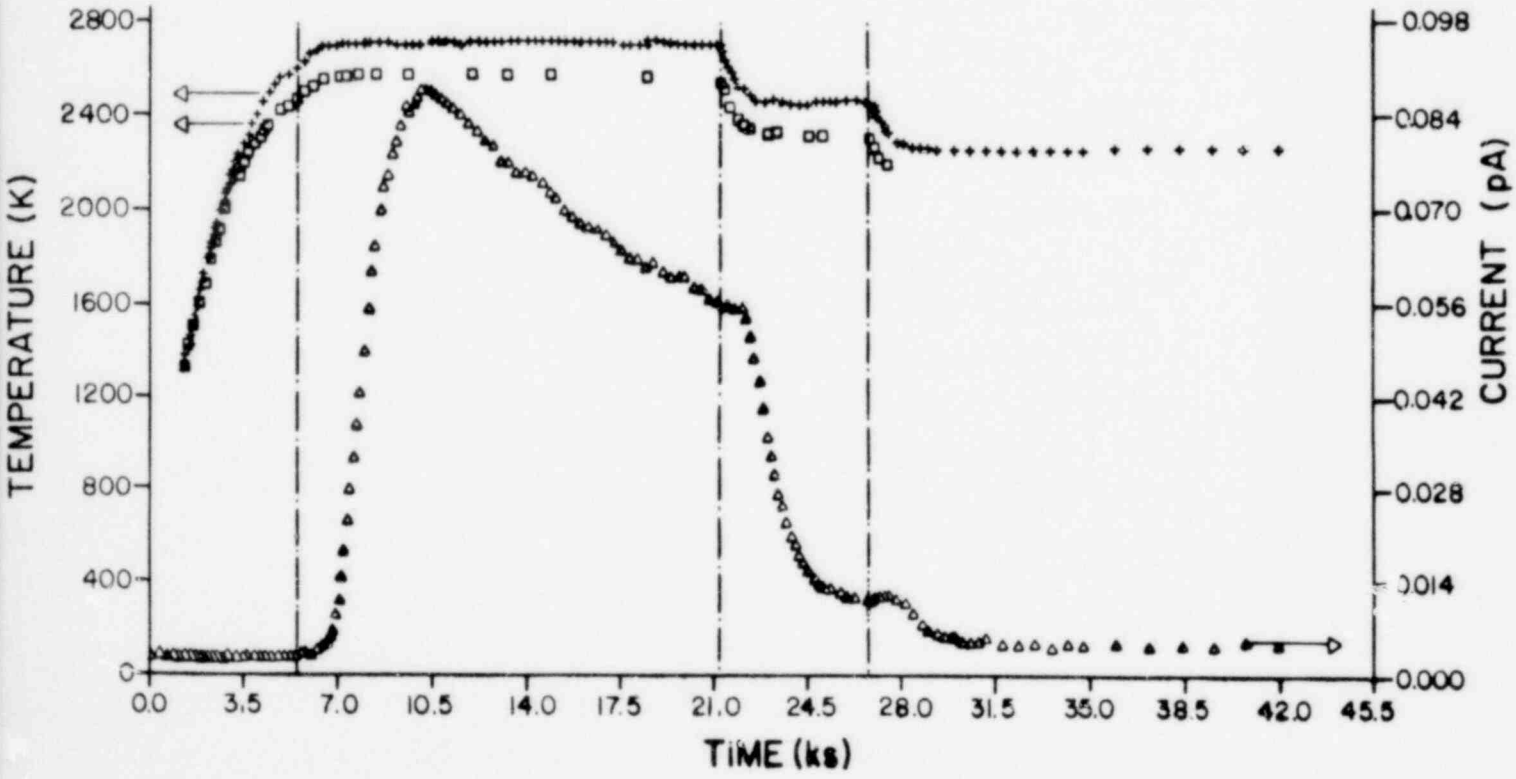


Fig. 64. Thermal break of a BISO/P13R fuel particle with 150 ft of tubing and a 1 cc/s sweep rate through a 250 c ion trap into a 1 000 cc ionization chamber. Squares indicate boat temperatures; crosses indicate cavity temperatures.

rate by a factor of 5.3. Consequently, we favor an interpretation that the BISO fuel particles were not failing instantaneously, but were losing krypton by diffusion.

b. Statistical Results

As indicated in Table XVII, the test results for the TRISO bead are most numerous for the F-30 fuel particle. For the 31 F-30 particles tested at temperature, 5 were conducted with background levels of sufficient magnitude as to render interpretation impossible. For the remaining 26 runs, the data are consistent with the interpretation of instantaneous failure as depicted in Fig. 63. Before and after failure, different release mechanisms will give rise to different release constants. In an attempt to quantify the transition from prefailure to postfailure mechanisms, we chose to examine an Arrhenius rate expression of the form

$$e^{-\frac{Q}{RT}}, \tag{27}$$

where Q is an activation energy in joules, R is the universal gas constant in joules/mol K, and T is the absolute temperature in K. If one assumes that thermal damage is exponentially related to temperature, and if one advances the notion of a damage limit independent of temperature, then the integral of Eq. (27) becomes a criterion for transition from prefailure to postfailure release mechanisms. Thus, we are interested in the statistical distribution of the quantities

$$x_n = \int_0^{t_o} e^{-\frac{Q}{RT}} dt \ , \ n = 1, \ldots, N \ , \tag{28}$$

where the integral is evaluated from zero to the time of failure $t_o$ for the bead (n) under test for each of the N thermal runs. When the number of beads tested becomes sufficiently large, the repeated evaluation of Eq. (28) for successive tests generates a density function f(x). The quantity of interest to the code developer is

the fraction of fuel particles surviving. Denoting this distribution as F, we have

$$F(x) = 1 - \int_0^x f(x')\, dx' \quad . \tag{29}$$

In this sense, F(x) is the complement of the cumulative distribution of the density function f(x).

In order to calculate F(x), it is necessary to evaluate Eq. (28). This, in turn, requires the determination of $T_n(t)$, the temperature history of each bead as a function of time throughout the test. Figure 65 (Run No. 10) shows a fit to a thermal run with a TRISO fuel particle. The chain-dotted line indicates where the

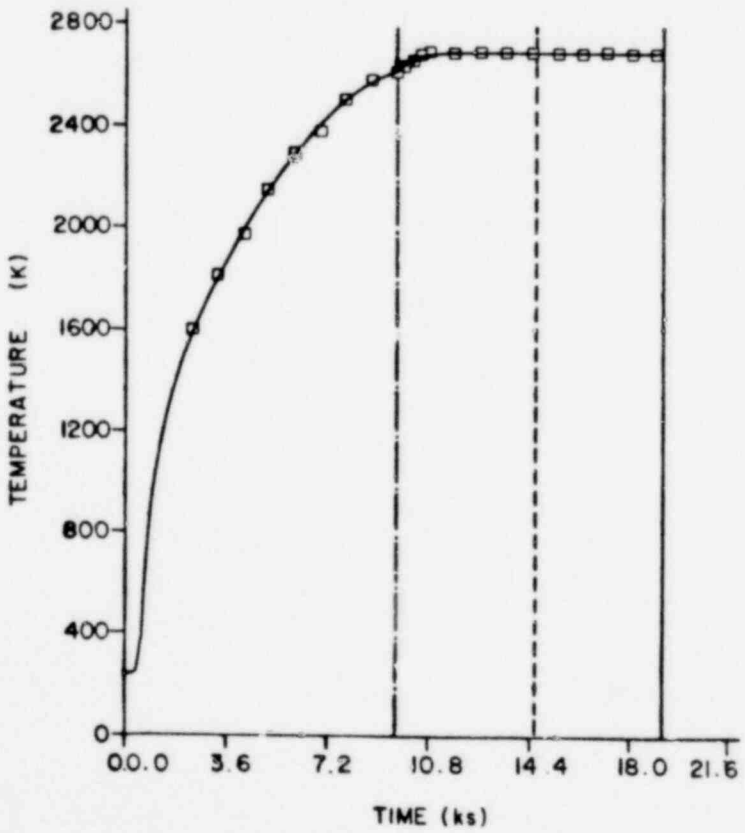


Fig. 65. Nonlinear least-squares fit to the temperature data of Run No. 10. The vertical chain-dotted line at 9.6 ks indicates where the programmer was turned off and the power set point was increased manually.

power program was halted and the power set point was manually increased. The dotted line represents the time at which the fuel particle failed, and the solid line represents the initiation of the power rampdown.

In order to calculate the survival distribution F(x), it is first necessary to assign a value to the activation energy Q in Eq. (28). In isothermal testing, a value of activation energy could be revealed by plotting the logarithm of a function of the rate against the reciprocal of the absolute temperature. As the testing carried out in this work was nonisothermal, no such procedure is available. Instead, it was decided to use that value of activation energy Q which would minimize some statistical property of the distribution f(x).

For any distribution, the mean is defined

$$\mu = \frac{1}{N} \sum_{N=1}^{N} x_n \ , \tag{30}$$

the variance is defined

$$\nu = \frac{1}{N} \sum_{N=1}^{N} (x_n - \mu)^2 \ , \tag{31}$$

and the coefficient of dispersion is the ratio

$$r = \frac{\sigma}{\mu} \ , \tag{32}$$

where $\sigma$ is the standard deviation

$$\sigma = \sqrt{\nu} \ . \tag{33}$$

Figure 66 contains a plot of the coefficient of dispersion (chain-dashed line) as a function of the activation energy Q. Here, Q is varied from zero to 1 600 kJ. The values near zero are clearly

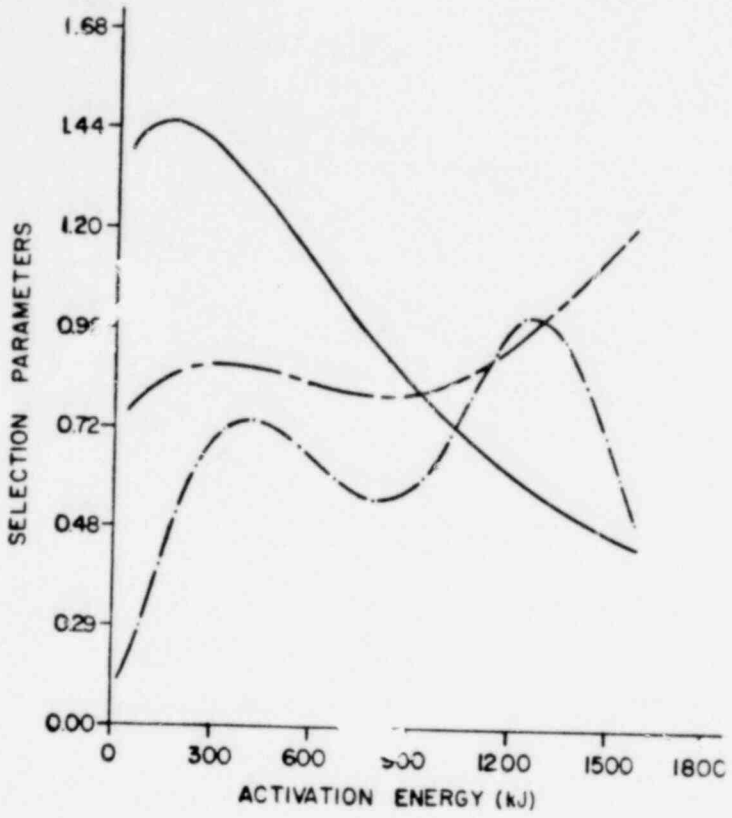


Fig. 66. Plot of the coefficient of dispersion (chain-dashed line), the $\alpha$ of the incomplete gamma function (solid line), and the significance level of the composite hypothesis (chain-dotted line) against the activation energy Q. The coefficient of dispersion goes through a minimum around 825 kJ; the $\alpha$ of the incomplete gamma function is one at about 722 kJ.

nonphysical and generate a limb of the curve that is of no interest. The plot indicates a minimum in the coefficient of dispersion in the vicinity of 825 kJ. However, the minimum is extremely broad, indicating that the goodness of fit is relatively insensitive to the activation energy Q.

In order to calculate F(x) from Eq. (29), it is necessary to approximate f(x) in some way. We elected to fit the density function f(x) to the incomplete gamma function. This distribution is of the form

$$\gamma(x) = \frac{x^{(\alpha-1)} \, e^{-\frac{x}{\beta}}}{\beta^{\alpha} \, \Gamma(\alpha)} \qquad (34)$$

where the $\alpha$ and $\beta$ are the two disposable constants for the gamma distribution with zero origin. The form is extremely general, taking on a wide variety of shapes as determined by the constants $\alpha$ and $\beta$. When $\alpha = 1$, the distribution reduces to the exponential distribution

$$e(x) = \frac{1}{\beta} e^{-\frac{x}{\beta}} , \qquad (35)$$

where the $\beta$ of Eq. (35) is the $\beta$ of Eq. (34).

The calculation of the parameters of the incomplete gamma function was carried out using a method of maximum likelihood estimators.[79] The $\beta$ of Eq. (34) is a scale factor and is uninteresting in the context of the present discussion. The parameter $\alpha$ calculated as indicated above is plotted in Fig. 66 as the solid line. It is interesting to note that the value of $\alpha$ is close to one over the range of the minimum in the coefficient of dispersion. When $\alpha$ is close to one, the resultant distribution is close to exponential. The exponential distribution is highly desirable because of its nearly ideal properties in statistical problems. Consequently, it was considered interesting to calculate a test for goodness of fit of the data to an exponential distribution. This was done using a method outlined elsewhere,[80] and the significance level of the exponential hypothesis is plotted in Fig. 66 as a chain-dotted line. (A significance level below 0.1 would be said not to support the exponential hypothesis.) Because the plot of the significance for the test for exponentiality is in excess of 0.5 over the entire range of Q, it was deemed to be acceptable to represent the data as an exponential distribution by selecting a value of activation energy Q for which the $\alpha$ of Eq. (34) is one. This corresponds to an activation energy of 722 kJ.

The density function f(x) for an activation energy Q of 722 kJ is listed in Table XVIII. The survival distribution F(x) for this density function is plotted in Fig. 67. Also plotted is the exponential fit to the data with a value for β of 2.82E-11. The entire test program for the F-30 fuel particle is thereby reduced to two constants.

The calculation of the survival fraction for the TRISO/F-30 fuel particle becomes quite simple. For any differential region, one may calculate the fraction of particles in the pre- and post-failure regimes by first calculating the reaction coordinate

$$x = \int_{o}^{t_o} e^{-\frac{Q}{RT}} dt \ , \qquad (36)$$

and then calculating the fraction surviving as

$$F(x) = e^{-\frac{x}{\beta}} \qquad (37)$$

where the activation energy Q is 722 kJ, the exponential constant β is 2.82E-11, and the integral of Eq. (36) is carried out over the time-temperature profile T(t) for the region in question.

The derivation of the survival distribution F(x) proceeded from physical assumptions regarding an Arrhenius rate function with

TABLE XVIII
DISTRIBUTION OF $x \cdot 10^{11}$
(Q = 722 kJ)

| Col. 1 | Col. 2 | Col. 3 | Col. 4 | Col. 5 |
|---|---|---|---|---|
| 0.011 42 | 1.051 05 | 1.576 92 | 3.132 26 | 4.286 75 |
| 0.029 07 | 1.212 70 | 1.831 39 | 3.312 86 | 4.343 72 |
| 0.319 92 | 1.301 29 | 1.900 70 | 3.773 15 | 4.898 64 |
| 0.654 85 | 1.342 96 | 2.308 35 | 3.936 56 | 5.519 51 |
| 0.798 27 | 1.479 95 | 2.897 06 | 4.101 62 | 8.086 16 |
| | | | | 9.308 71 |

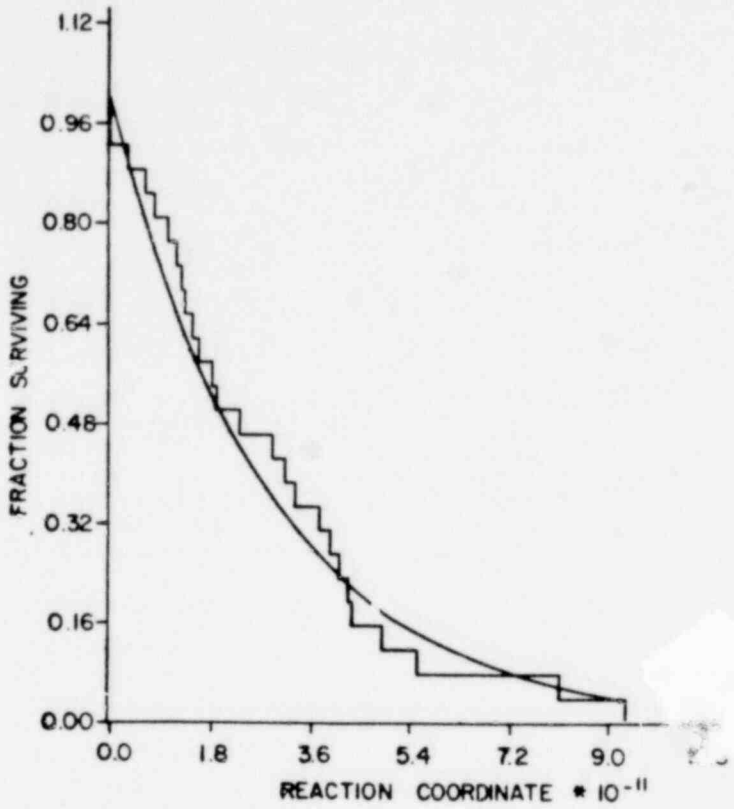


Fig. 67. Survival statistics for the TRICO/F-30 test data. The stepped line is the plot of the experimental data with an assumed activation energy of 722 kJ. The smooth line is the exponential fit to the experimental data for a value of $\beta$ of 2.82E-11.

a single activation energy and a damage limit for the individual fuel particle, both independent of temperature. If such assumptions are correct, they will make the resultant model more physical. However, the accuracy of the final fit as carried out here is unaffected by the correctness of these presumptions. In this sense, a physically correct model may be superior under conditions of extrapolation, but will give equivalent answers under interpolation. In other words, the validity of the data representation given here does not depend in any way upon the validity of the physical model to which the data were fitted.

c. Comparison with the Analytic Fuel Failure Model

A comparison was made between the experimental results of this study and the analytic fuel failure model used in other studies at LASL.[81] For this purpose, the accident trajectory following the loss-of-forced cooling (LOFC) was selected as the computational medium.

The analytic fuel failure model, which is independent of time, is given by the relations

$$F(T) = 1.0 \ , \ T < T_1 \ , \tag{38}$$

$$F(T) = C_0 + C_1 T \ , \ T_1 < T < T_2 \ , \tag{39}$$

and

$$F(T) = 0.0 \ , \ T > T_2 \ , \tag{40}$$

where T is the maximum temperature that the fuel particles have experienced and the constants $C_0$ and $C_1$ are selected to linearly scale the distribution between one and zero as a function of the temperatures $T_1$ and $T_2$, respectively. The temperatures used in the comparison calculation were taken for fuel material burned less than 0.12 y; namely

$$T_1 = 1\,858.15 \text{ K} \ , \tag{41}$$

and

$$T_2 = 1\,998.15 \text{ K} \ . \tag{42}$$

The core temperature profile for the LOFC accident is tabulated in the LARC-1 report for the first 20 h after the initiation of the accident.[81] This distribution was used to calculate LOFC survival distributions for both the experimental and analytical models. The results of the calculations are plotted in Fig. 68. The solid line represents the results of the calculation using the analytical model of Eqs. (38)-(42). The dashed line is the same calculation with the fuel failure model of Eqs. (36) and (37). The fuel particle population as calculated with the experimental model

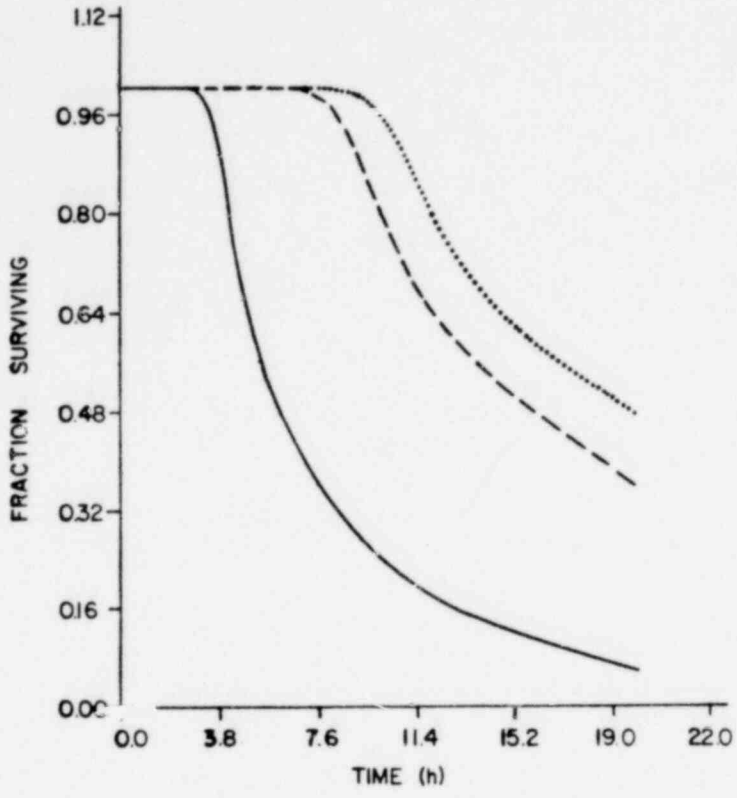


Fig. 68. Fuel particle survival distributions for analytical (solid line), experimental (dashed line), and hypothetical (dotted line) fuel particle failure models during the accident trajectory for an LOFC accident.

is seen to remain intact for some 4 h longer than is the case for the analytical model. The dotted line represents a hypothetical fuel failure model with a statistical distribution identical to that for the F-30, but with a temperature characteristic raised some 200 K, indicating that an increase in thermal resistance has postponed the onset of fuel particle failure by some 2 h in the LOFC accident trajectory. This suggests a rule of thumb that -- relative to the F-30 Ft. St. Vrain prototypical fuel performance in an LOFC accident -- an increase in the thermal resistance of 100 K will result in a 1 h increase in the onset of fuel failure.

The use of the analytical model definitely constitutes a conservative estimate of fuel particle behavior. This is indicated in Fig. 68 and again in Fig. 69, where the rate of fuel failure is

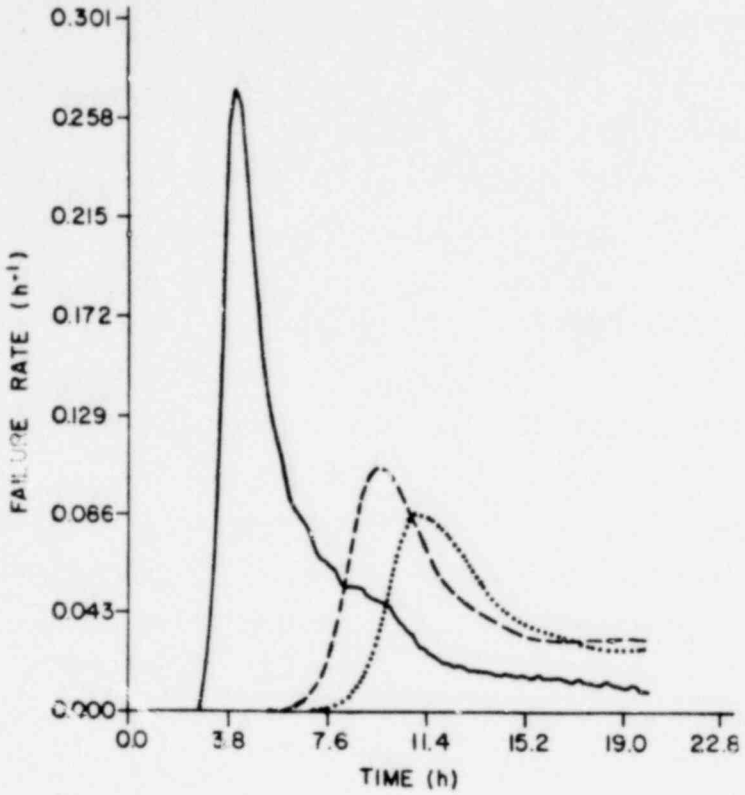


Fig. 69. Fuel particle failure rates for analytical (solid line), experimental (dashed line), and hypothetical (dotted line) fuel particle failure models during the accident trajectory for an LOFC accident.

plotted for the two fuel particle models. The peak for the experimental model is delayed, reduced in amplitude, and broadened relative to the analytical model -- all by a factor of 2.5. The plot of the failure rate of the hypothetical fuel particle (dotted line) suggests that enhanced resistance to thermal failure will markedly reduce peak failure rates.

## V. GAS-COOLED FAST REACTOR LOW-POWER SAFETY EXPERIMENTS

(D. L. Hanson, Q-13)

The basic assembly module of the GCFR is a subassembly comprising 264 fuel rods, 6 corner support rods, 1 central rod (instrumented), and their surrounding duct. The duct is a right hexagonal cylinder. The purpose of this out-of-pile experimental program is to demonstrate the behavior of the GCFR core module in the event of a loss-of-core coolant flow or pressure and subsequent shutdown of reactor power to the level resulting from decay heat alone. The loss-of-flow accident (LOFA) will be simulated in the steel melting and relocation test (SMRT) and the loss-of-pressure accident will be simulated in the depressurzied accident condition (DAC) test. These experiments require the development of an electrically heated fuel rod simulator capable of delivering 2 kW of power while operating at surface temperatures exceeding 1 650 K, and the development of a fixture that will permit operation of an ensemble of 450 such rods (1 core module thermally guarded by segments of the 6 surrounding modules) at helium pressures up to 9.1 MPa. This guarded core module (GCM) fixture will be the largest in a sequence of four test fixtures developed in the course of this program. The others are:

- Ten-inch, single rod fixture,
- One-meter, seven rod fixture, and
- Full-length subgroup (FLS) 37-rod fixture.

The GCM fixture will be used first for the SMRT and subsequently for the DAC test.

### A. Program Planning

(D. L. Hanson, Q-13)

In a meeting at the GAC on April 11, 1979, representatives of LASL and Oak Ridge National Laboratory (ORNL) were apprised of the

decision to reverse the direction of coolant flow in the GCFR core. The ducts and fuel rods will now be bottom-supported and the helium will flow upward. With this new configuration, the duct fallaway mechanism is inappropriate for preventing recriticality in LOFA. Since the duct melting and fallaway test (DMFT) has been the cornerstone of the LASL core disruptive test program, the decision to reverse the direction of coolant flow requires a major redirection of the LASL program. Toward this end, it has been decided that:

1. The title of the LASL program will be changed from "Core Disruptive Test" to "Low-Power Safety Experiment." This may offer more experimental latitude, especially the inclusion of natural convection experiments.

2. The DMFTs will be eliminated. Instead, there will be two SMRTs. The first test assembly in the GCM test fixture in the high bay will be designated SMRT 1. Operation of this assembly is tentatively scheduled for June 1980 (we will try to do it sooner), with the follow-on test, SMRT 2, to be scheduled no later than April 1981.

3. We will plan to provide upflow preheat to the SMRT 1 test assembly.

4. The June 1980 date for SMRT 1 and the reduction from 6 DMFTs to 2 SMRTs may allow:

   a. Completion of FLS testing, including an FLS 3, if necessary, or

   b. Interleaving of FLS tests and SMRTs.

   This appears to obviate the need for a separate new FLS-type pressure vessel for use as the pressure vessel for the GCM preheater. Consequently, we will plan to use the FLS pressure vessel for the preheater. The preheater pressure vessel funding allocation will be applied to accelerating the design and fabrication of SMRT 1 hardware in this FY. If it proves necessary, a new vessel could be fabricated in FY 80.

5. 0.15 m of heater rod fallaway motion is no longer appropriate or desirable (it would seriously alter the power gradient distribution during subsequent steel relocation). We will therefore limit heater rod fallaway displacement to 0.025 m.

In addition to this substitution of SMRT for DMFT, program planning for DAC tests is continuing and planning for natural convection tests is anticipated.

## B. Analysis

(F. Ju, J. G. Bennett, and C. A. Anderson, Q-13)

### Analysis of Rod Bending and Spacer Grid Interaction

FLS-1 showed us that the thermomechanical interaction of the GCFR heater rods and the spacer grids produces forces and/or rod deflections that severely limited the time period during which full decay power could be applied to the heater rods. In order to assess this interaction, a finite element beam column model has been developed and tested with thermal moments and spacer grid constraints representative of the FLS experiments. Coupling of the rod model with a fluid flow and heat transfer model will give us a design capability for low-power experiments that is currently lacking.

A finite element model has been designed for the evaluation of the thermoelastic deformation of a heater (fuel) rod, especially extended to cases where the deformation of the rod results in binding with the spacers. Only two finite elements over a span provide reasonable accuracy in prediction of the deformation of the rod, the axial force in the rod due to restriction of free thermal expansion, and the torque being transmitted to the spacer when free rotation at the spacer is being restricted. Existing finite element codes require many elements between supports in order to obtain the needed accuracy. Thus, when heater rods have multiple spacer supports, as in the GCFR, the number of elements per rod becomes large and calculations prohibitively expensive for a complete fuel assembly.

For the initial design of the element, the heater or fuel rod was assumed to be elastic and satisfy the Euler-Bernoulli condition. The development of the finite element model of the rod, though assuming moderately small displacement gradients, employs the full quadratic expression of the strain-displacement relationship.

Virtual work principles are used in establishing the stiffness matrix. The result is a fully nonlinear and nonsymmetric stiffness matrix, which is itself a function of force and displacement parameters.

The beam-column element has been tested against the analytical (exact) solution of a simple heater rod thermal constraint problem. In the problem, only two spacers at the two ends are used. The thermal gradient across the rod causes thermal bending. Since the clearance at the spacer does not allow unlimited slope there, binding results. Subsequent axial thermal strain causes further lateral deformation due largely to the development of axial force from the axial constraint against free expansion. The problem is also solved with single-element and two-element finite element models. Against varying axial thermal strain, the axial force (S), the mid-span deflection (w), and the total moment (M) at the ends are plotted in Fig. 70. From Fig. 70, it can be deduced that two finite elements are sufficiently accurate to predict the thermo-elastic deformation of a constrained GCFR heater rod.

## C. Design

(J. Churchman, A. J. Giger, and R. Robinson, Q-13)

### 271-Rod GCM Experiment

The support frame was redesigned to use an external PV manifold (PV = pressure vessel). Design was completed for electrical shunts that indicate power by rows in the main duct. Instrumentation pass-throughs were designed for the top PV cover (224 channels). Layout design was completed for the expansion end of the heater electrodes (and alumina sleeves) and detailing of parts in this region was started.

In a major revision, the layout of the GCM experiment was inverted so that it now simulates an up-flow core. Even though the GCM support frame was completely detailed, the flexibility of its design is such that no modifications were required.

Drawings were completed and released for fabrication for the following:

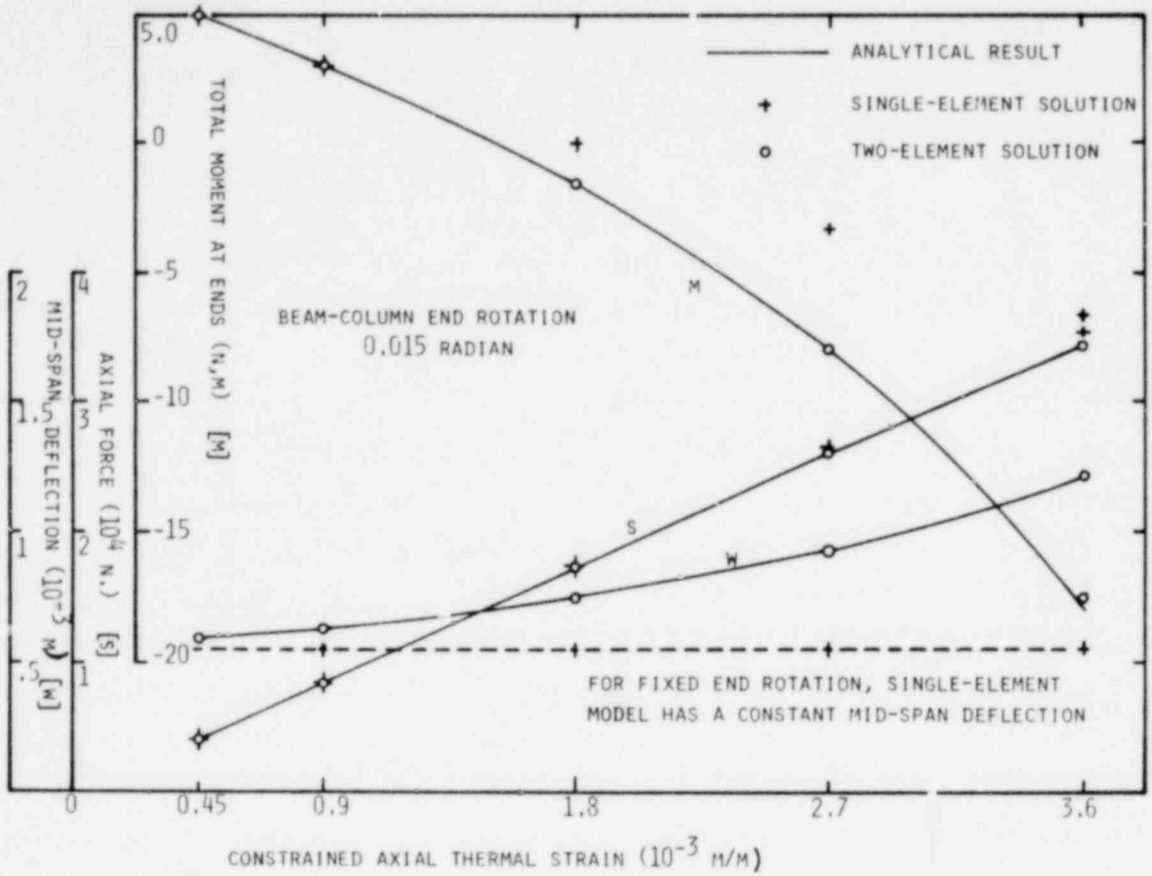


Fig. 70. Moment, force, and deflection on a constrained and heated rod.

GCM support frame

GCM experiment support plate (cooled)

Spline plate and fittings

Core support plate

Main duct weldment

A specification for 6.3-mm-o.d. by 4.6-mm-i.d. alumina sleeves was prepared that will be used to procure 1 265 m of insulation for the first GCM test.

Shop drawings were prepared for the shell of the guard heaters.

1320 328

## D. Procurement and Fabrication

(A. J. Giger, D. R. Bennett, and W. E. Dunwoody, Q-13)

### 1. Data Acquisition System

The Hewlett Packard 9825 and 3052A data acquisition system is to be shipped after July 9, 1979.

### 2. High Bay Addition to Test Cell 1

The outer structure of the high bay addition to test cell 1 has been completed as indicated in Fig. 71. Interior work has commenced and should be finished within several weeks. The removable roof feature will be utilized for crane installation.

### 3. Overhead Crane

Delivery of the 10-ton overhead bridge crane has not been confirmed but is expected to be after August 1, 1979.

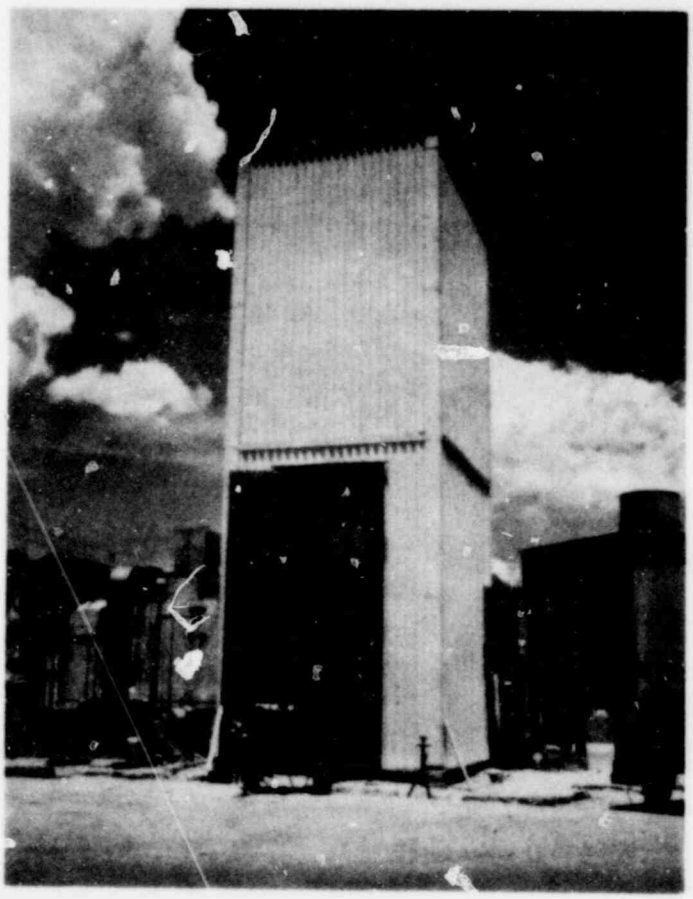

Fig. 71. High bay addition to test cell 1.

4. GCM Pressure Vessel

The fabrication of the guarded core pressure vessel has fallen behind schedule by about five weeks because of the late delivery of the main cylinder material from Kaiser Steel.

The main cylinder has been machined inside and outside and all six nozzles have been welded on the cylinder. The radiographs of the nozzle welds indicate that four weld repairs must be made to meet specifications.

The top and bottom flange covers have been rough machined and should be completed in two weeks. The six nozzle covers have been machined except for drilling the bolt holes in three covers.

The small port covers are nearly 50% complete.

The design of the vessel support is completed and fabrication drawings are being made.

5. 271-Rod GCM Experiment

(A. J. Giger and J. Churchman, Q-13)

After the bidding process, orders were placed for the following:

| Item | Vendor | Price ($K) | Delivery (Wks) |
|---|---|---|---|
| GCM support frame | Schneebeck Industries | 17 000 | 15 |
| GCM support frame insulation | Zircar Products, Inc. | 4 890 | 8 |
| Alumina insulating sleeves | Coors Porcelain | 9 671 | 12 |

Additionally, an order for 10 Nitronic-33 forgings was placed with G. O. Carlson. These are required for support frame fittings and instrumentation pass-throughs.

The cooled version of the GCM experiment support plate was placed for bids.

Some GAC-supplied 316 SS sheet was placed in the main LASL shop for the first guard heater fabrication.

## E. Assembly, Installation, and Checkout

(R. E. Ortega, J. H. Anderson, D. R. Bennett, and D. L. Hanson, Q-13)

### 1. FLS 2 Assembly

The completed FLS 2 test package was inserted in the pressure vessel on June 12, 1979. A number of changes from the FLS 1 configuration have been made, primarily for the purpose of extending heater rod life. These changes are summarized in Table XIX, together with their anticipated benefits. The four-component flow impedance device (three baffles and a leaf-spring seal) and the duct port blocking band are shown installed on the duct in Fig. 72. These are the principal devices for inhibiting convection outside the test bundle.

Thermocouple locations on the test assembly are given by the following convention. Axial locations are specified by alphabetic station as shown in Fig. 73. Duct and rod thermocouple positions are specified by their axial station (measured downward from the top of the upper axial blanket), their radial distance from the center of the test assembly, and by the clockwise angle rotation from the viewport axis (as viewed from the top of the assembly).

Rod thermocouples are also designated by their position in the hexagonal array of rods. The rod bundle is divided into six equal sectors as shown in Fig. 74, where the sector (1) outer flat is perpendicular to the viewport axis. Sector, row, and position numbering for each sector are as indicated. The center rod is designated as sector 0, row 0, position 1. The direction of a line between the center of the rod and the thermocouple on its surface is the angular rotation (again reckoned clockwise, viewed from the top) from a rod's zero direction line, which is perpendicular to its sector outer flat.

FLS 2 software differs from that in the FLS 1 tests in two major respects. First, because the system benchmark tests have significantly improved data acquisition rates, interleaving of power control and data acquisition has been eliminated. Second, power control of the experiment has been changed to allow for the

# TABLE XIX

## DIFFERENCES BETWEEN FLS 1 AND FLS 2

| COMPONENT, REGION, OR PROCESS | CHANGE | ANTICIPATED BENEFIT |
|---|---|---|
| Rod internal insulation | 1. Stricter i.d. and o.d. acceptance criteria | Looser fits of alumina sleeve in cladding and heater rod in alumina sleeve for reduced frictional interaction during thermal transients. Reduced likelihood of rod disassembly. |
| | 2. Deliberately avoid coincidence of alumina sleeve joints in the neighborhood of heater rod lands | Preclude engagement of the rod lands by the alumina sleeves during sleeve expansion. Reduced likelihood of rod disassembly. |
| Spacer Grids | 1. Configuration changed from mockup-prototype to wave-spring | Increased rotational compliance. Eliminate lockup and consequent rod bowing and/or breaking. |
| Duct | 1. Changed from circular to hexagonal | Satisfy GA request. Should decrease internal convection (but increase external convection). |
| | 2. Closed the duct viewports | Eliminate internal-to-external convection paths. |
| Duct gas ports | 1. Blocked, except for small leakage path | Eliminate convection between rod bundle and upper plenum of pressure vessel. |
| Duct-to-insulation gap | 1. Added a four-component flow impedance. | Impede natural convection outside duct. Reduce duct bowing, temperature, asymmetry, spacer grid cocking and, possibly, rod breakage. |
| Insulation viewports | 1. Blocked ports through Mo shield | Block thermal radiation through the Mo shield and convection between the gaps on opposite sides of the shield. |
| | 2. Deliberately misaligned ports through SS and alundum components | Block thermal radiation and convection to the vessel wall region. |
| Pressure vessel pass-thru | 1. Changed from water-cooled Cu to uncooled Mo | Increase strength and reduce heat-sink effects. |
| Power control | 1. Changed from constant-current only to constant-current with voltage limiting override | Limit power in case of rod failures. |
| Test Sequence | 1. Six convection tests plus one destruct test changed to one destruct test. | Reduce the number of thermal expansion cycles. Increase rod life. |
| Thermocouples | 1. Improve mechanical stability of external connection. | Increased thermocouple reliability. |

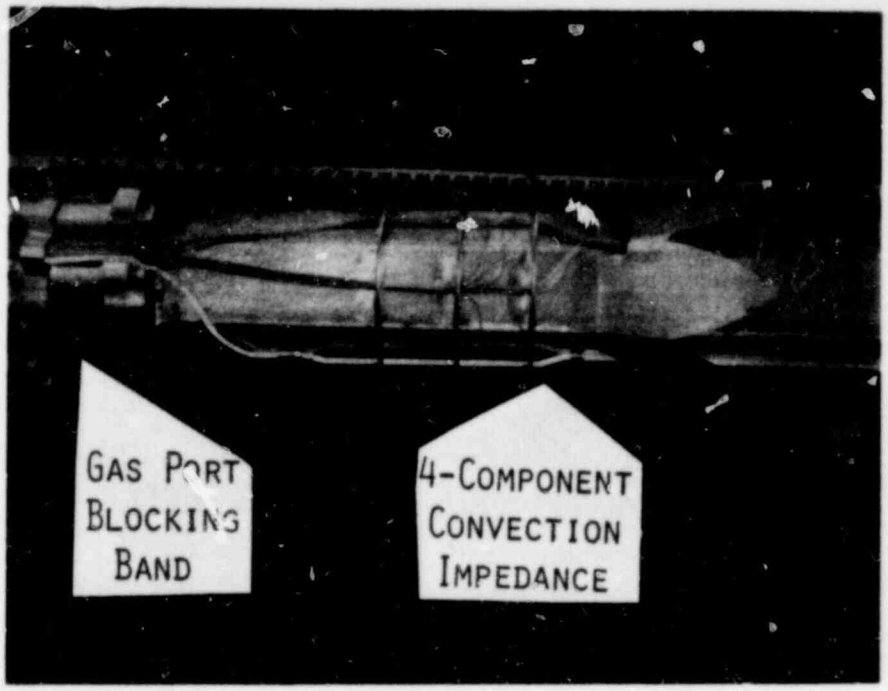


Fig. 72. Convective flow impedances on FLS 2 duct.

possibility of rod breakage and the subsequent change in assembly resistance. The power demand, which is specified as a current demand and then converted to an analog voltage signal by the computer, follows an asymptotic exponential schedule for five time constants and then switches to a constant power level. The associated current demand is then adjusted in response to the resistance of the test assembly so as to maintain constant power input.

2. FLS 2 Installation

The installation of FLS 2 in Test Cell 1 was completed on June 14, 1979.

3. FLS 2 Checkout

Simulated operations for the vacuum bakeout and the FLS 2 test were run on the dummy load fixture in Test Cell 1 in order to investigate the new power control strategy and data acquisition rates. In both cases, the 2.5 MW Westinghouse generator operated

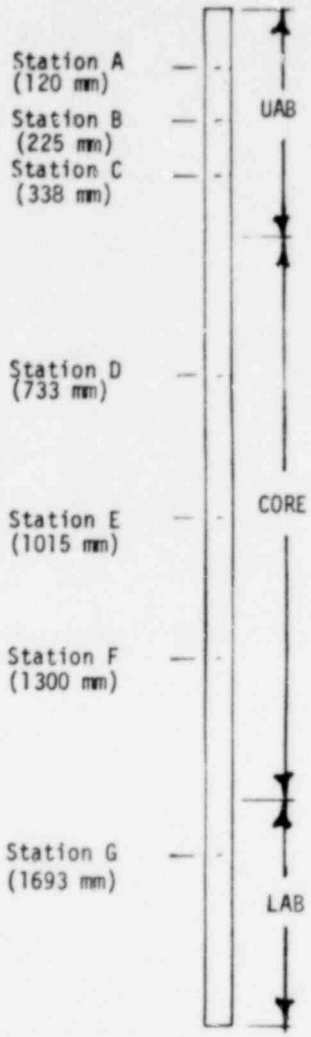


Fig. 73. FLS 2 axial thermocouple stations.

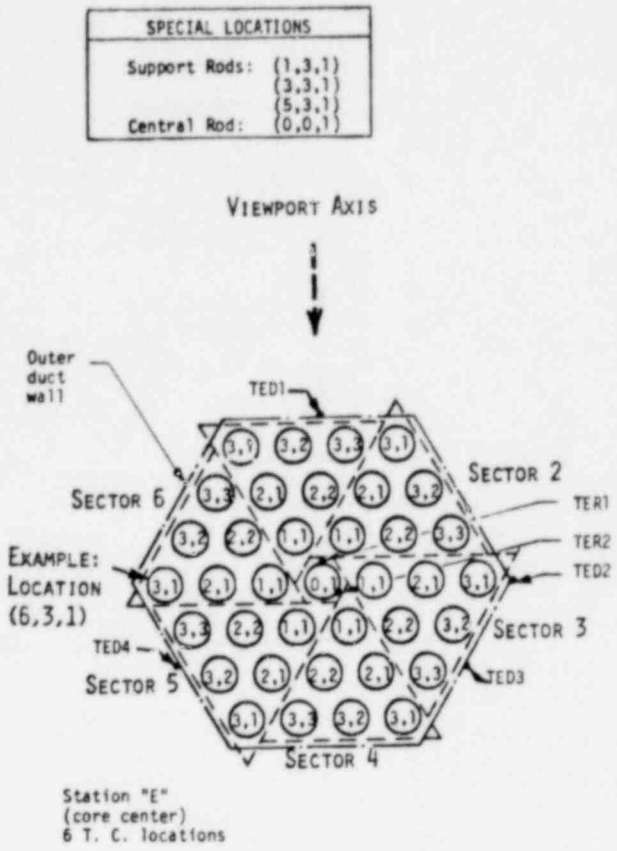


Fig. 74. FLS 2 sector designations, viewing from the top.

under a current demand. The results were as expected except in a minor discrepancy between the current demanded from the generator and the current observed in the load. The cause of this discrepancy is being studied.

## F. Testing

(R. E. Ortega, J. H. Anderson, D. R. Bennett, and D. L. Hanson, Q-13)

1320 334

1. FLS 2 Vacuum Bakeout

The first vacuum bakeout procedure was completed on the FLS 2 test assembly on June 19, 1979. Pressure at the beginning of the test was 2.8 Pa. The power input schedule was a rough stairstep approximation to a 5 000 s half-period sine wave. Maximum power input was 455 W and the maximum temperature observed was 538 K. This temperature then decayed with a time constant of $1.4 \times 10^4$ s.

Sixteen thermocouples exhibited opposite trends from expectations. This behavior was ultimately traced to a single shipment of thermocouple wire. The vendor apparently had inadvertently supplied type J wire instead of the type K that was requested. The 16 affected channels have now been retrofitted with type J lead wires and reference junction.

2. GCM Instrumentation Pass-Through

Upon disassembly of FLS 1, it was discovered that the thermocouple sheaths were badly distorted by the lavite packing material in the pass-through fittings. Comparative tests have now been performed with 12- and 16-hole Conax fittings at 12.4 MPa and ambient temperature using neoprene and teflon as packing materials. The results of these tests indicate that neoprene is acceptable, but teflon is not. The ability of neoprene to withstand the expected operating temperatures in the GCM fixture is still in question. We are using silicone rubber packing in the 4-hole pass-through in FLS 2. These were custom-molded by LASL Group CMB-6.

## VI. CONTAINMENT SYSTEMS

(R. G. Gido, Q-6)

The following sections summarize the progress from the area of Containment Systems Safety funded by the NRC, Division of Systems Safety (DSS).

### A. Containment Subcompartment Analysis

(R. G. Gido, Q-6 and J. S. Gilbert, Q-9)

Modeling procedures for nuclear power plant containment subcompartment analysis have been developed. Previously, comprehensive standard modeling procedures did not exist. Standardization reduces the extent of modeling input parameter studies normally required to establish an acceptable model.

Containment subcompartment analysis is the evaluation of the thermodynamic consequences of a postulated pipe rupture in a subcompartment. The subcompartment is a fully or partially enclosed volume within the containment that houses or adjoins high-energy piping systems and restricts the flow of fluid to the bulk containment volume from a postulated pipe rupture. The water mass and energy release from the pipe rupture generates pressure waves that propagate throughout the subcompartment. Pressure differences across components and shield wall are developed and force and moment loads result. The maximum pressure differences usually occur in less than 1 s and are relieved by the ultimate distribution of flow to the bulk containment volume ($1\text{-}8 \times 10^4 m^3$).

Examples of subcompartments include reactor cavity, steam generator, and pressurizer compartments. As the reactor cavity subcompartment [see Fig. 75) incorporates most of the modeling input requirements for subcompartment analysis, several reactor cavity subcompartments were selected for the sensitivity studies performed.[82] The modeling procedures are constrained by available subcompartment codes,[83,84] NRC guidelines,[85] and current practice. As it is an area of major concern, nodalization of subcompartment

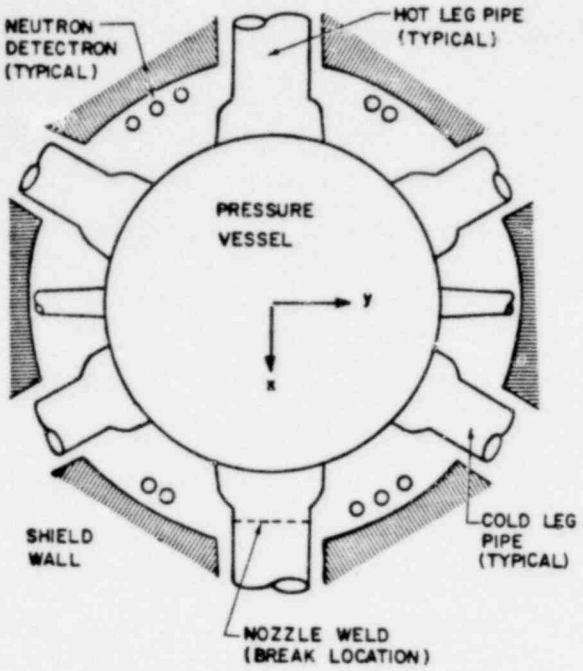


(a)

Horizontal (x-y) cross section of reactor cavity subcompartment.

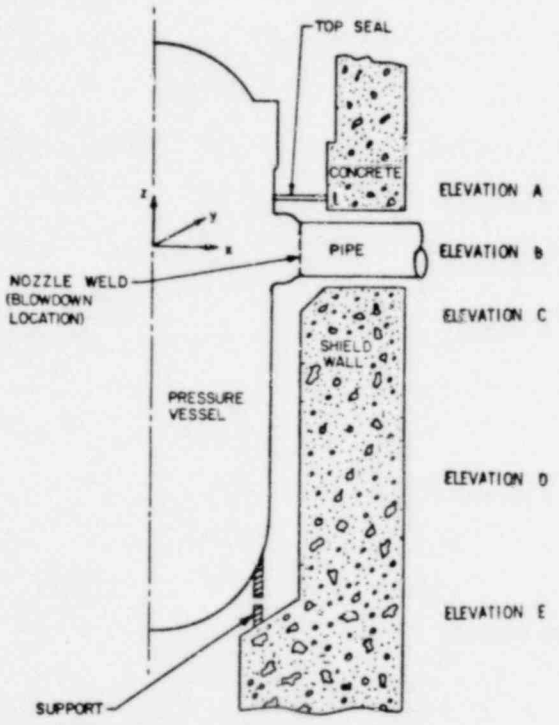


(b)

Vertical (x-z) cross section of reactor cavity subcompartment.

Fig. 75. Reactor cavity subcompartment.

geometry is described in detail below. Other modeling procedures are itemized.

Subcompartment nodalization must represent the physical geometry and flow paths consistent with assumptions of subcompartment analysis codes.[83,84] To accomplish this, control volume boundaries for junctions or vent paths must be located at minimum flow areas where geometric influences create pressure differentials. Examples of such locations are reactor vessel nozzles, piping and supports; neutron detector tubes; shield blocks, plugs, and rings; variations in reactor vessel diameter and variations in profile of primary shield wall; and shield wall penetration entrances and exits. Under certain conditions it is also necessary to define nodal boundaries in regions of constant cross-sectional area to account for frictional (f·L/D) or inertial (L/A) effects. The nodal model shown in Fig. 76 represents a 180° span of the reactor cavity subcompartment pictured in Fig. 75(a) and (b). The boundaries at elevation A represent a sealed top above the reactor cavity annulus. Two geometric discontinuities result in additional nodal boundaries. They are the flow area change past the hot and cold legs of the reactor coolant system at elevation B and the flow area change past the shield wall diameter variation at location C. The nodal boundaries at elevation D were established midway between elevations C and E to account for the pressure gradient in the long constant area annular region below the reactor vessel nozzles. The junctions at elevation E correspond to the area transition to the lower reactor cavity. Our sensitivity studies show that it is permissible to eliminate the horizontal boundary at elevation D for certain cavity designs when the boundary is established in the absence of geometric restrictions. These studies determined that the resultant forces and moments calculated about a horizontal axis through the nozzles (elevation B) changed by less than 5%.

In estab ishing vertical boundaries to account for pressure differentials created by circumferential flow about the reactor vessel, two locations of geometric variations were used. These locations correspond to the flow area past the piping of the reactor coolant system and the flow area past the neutron detector tubes.

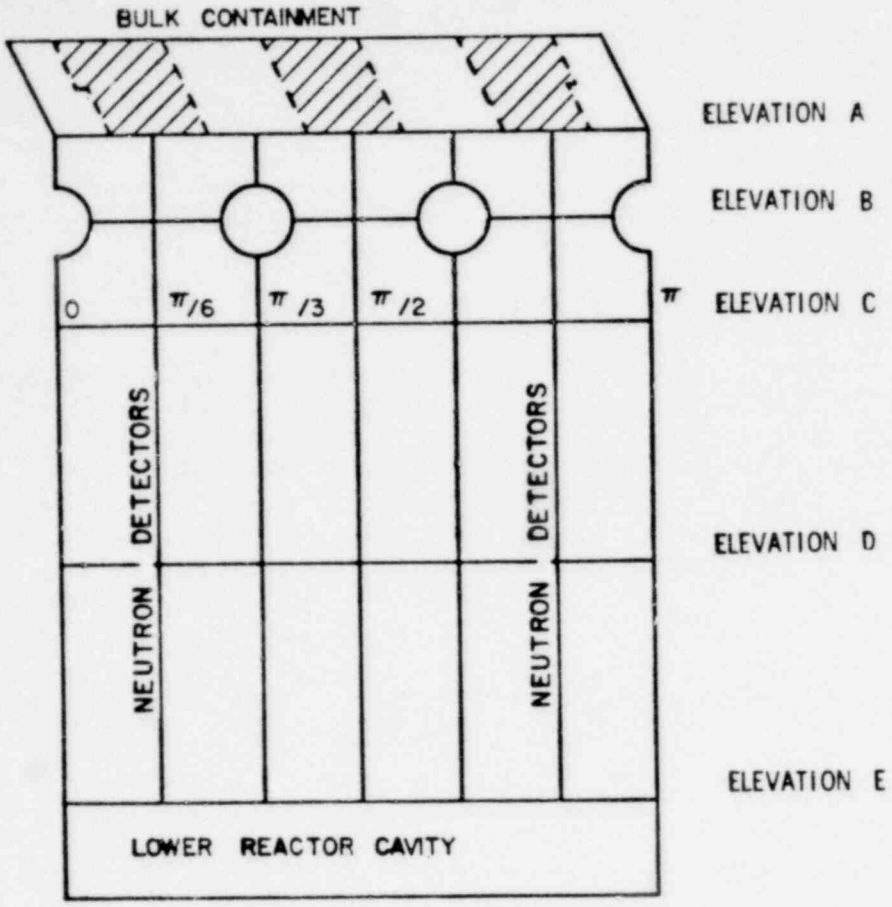


Fig. 76. Reactor cavity subcompartment annular region nodalization schematic showing shield wall penetrations and neutron detector locations.

Therefore, the control volumes in Fig. 76 encompass equal 30° segments. This noding detail was retained in areas below the nozzle region. Sensitivity studies demonstrated that circumferential nodalization could be made coarser without substantial changes to the calculated peak loads and moments on the reactor vessel.

A critical aspect of modeling is nodalization of the volume into which the break effluent mass and energy is released. In particular, the effects of break jetting and delayed liquid vaporization must be considered. For the model in Fig. 76, blowdown was assumed to enter the four control volumes surrounding the ruptured pipe.

In addition to standard nodal models, the following modeling procedures are recommended:

1. Homogeneous equilibrium thermodynamics of control volume constituents,

2. Accounting for the presence of air,

3. Complete water entrainment in the flow mixtures,

4. Subsonic flow calculations based on the incompressible momentum equation,

5. A minimum vent flow based on the lower of either the subsonic or the critical flow calculation, and

6. Critical flow calculation based on the homogeneous equilibrium model or the Moody correlation with a 0.6 multiplier.

## B. Analysis of Containment Long-Term Accident Response

(D. E. Lamkin, Q-6 and A. Koestel, Consultant)

The qualification of equipment exposed to a Main Steam Line Break (MSLB) has recently become a matter of concern because containment bulk temperatures of about 478 K (400°F) can be calculated. This is considerably in excess of the current qualification value of 422 K (300°F). In response to this concern, we have investigated the technical bases for such calculations and the equipment thermal boundary conditions, in general, to establish appropriate test qualification requirements.[86]

The equipment environment can be partitioned into two regions. One region is that outside and the other is that within the MSLB jet. The region outside the jet can be represented by the containment overall bulk conditions. To determine boundary conditions within the MSLB jet, thermodynamic and compressible flow calculations were performed for a highly underexpanded perfect gas.

Our investigation revealed that current procedures[87] for the determination of the bulk conditions were subject to improvement in several areas pertaining to the energy removed by passive heat sinks. In particular, we recommend that

1. the bulk temperature be used as the driving potential for heat trasnfer,

2. the condensed mass removal associated with the heat transfer follow the procedures recommended in Ref. 88, and

3. better data than the currently used values of Tagami[89] and Uchida[90] be obtained.

Use of the bulk temperature, instead of the saturation temperature corresponding to the bulk steam partial pressure, is recommended because the heat transfer is a mass-transfer-limited process due to the vapor-air boundary layer as shown in Fig. 77. This boundary layer results in the condensation effect being limited to that from the temperature at the interface to the wall temperature. However, the interface temperature is only slightly greater than the wall temperature because the steam partial pressure at the interface is very much lower than that for the bulk. This is due to

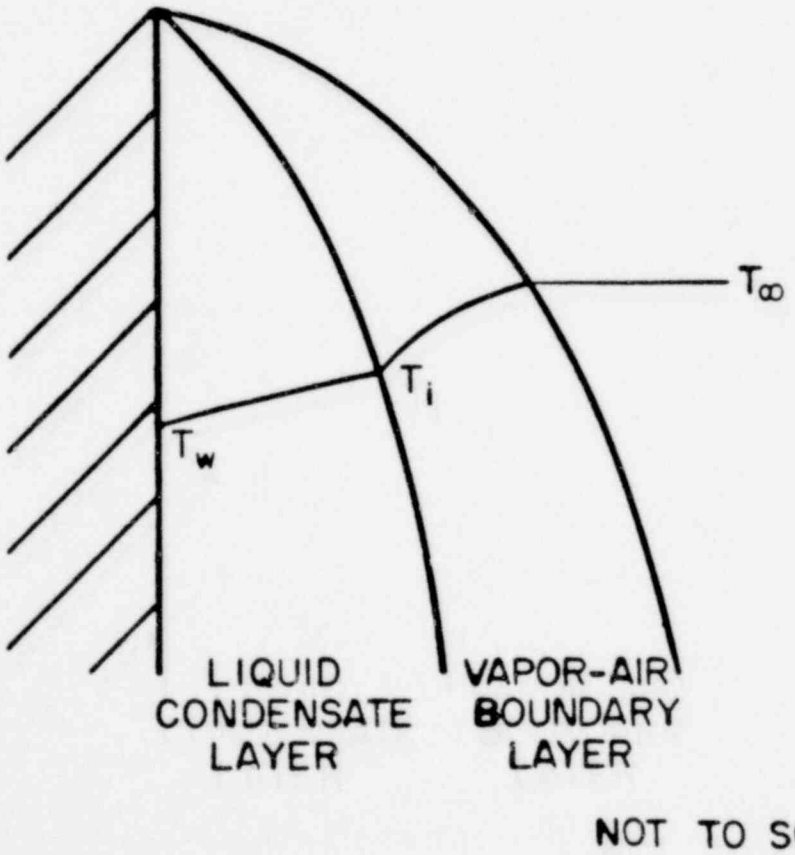


Fig. 77. Condensation of steam in the presence of air.

the accumulation of the noncondensible air near the interface. Recommendation 2 is a further result of the vapor-air boundary layer. That is, the energy required to cool the air and steam in the vapor-air boundary layer must be acknowledged.[88] The impact of recommendations 1 and 2 is demonstrated by the comparisons of Table XX.

TABLE XX

EFFECT OF NEW CONDENSED MASS REMOVAL AND DRIVING TEMPERATURE ON MSLB PRESSURES AND TEMPERATURES

Effect of condensed mass removal model on Carolinas and Virginia Tube Reactor (CVTR) MSLB calculated temperatures and pressures -- measured values are 0.225 MPa (32.6 psia) and 387 K (237°F).

(a)

| Mass Removal Ref. | MR[a] | Max. Pressure MPa | Max. Pressure psia | Max. Temperature K | Max. Temperature °F |
|---|---|---|---|---|---|
| 87 | NA | 0.190 | 27.6 | 421 | 298 |
| 87 | 1.0 | 0.210 | 30.5 | 407 | 273 |
| 88 | 0.5 | 0.223 | 32.3 | 396 | 253 |
| 88 | 0.33 | 0.230 | 33.4 | 390 | 243 |
| 88 | 0.17 | 0.225 | 34.5 | 376 | 217 |

Effect of condensed mass removal model and driving temperature (TD) for a typical MSLB analysis.

(b)

| Mass Removal Ref. | MR[a] | TD | Peak Pressure MPa | Peak Pressure psia | Peak Temperature K | Peak Temperature °F |
|---|---|---|---|---|---|---|
| 87 | NA | sat. | 0.241 | 35.0 | 468 | 383 |
| 87 | NA | bulk | 0.192 | 27.9 | 449 | 348 |
| 88 | 1.0 | bulk | 0.193 | 28.0 | 440 | 332 |
| 88 | 0.33 | bulk | 0.197 | 28.6 | 416 | 289 |
| 88 | 0.2 | bulk | 0.199 | 28.9 | 405 | 269 |

[a]MR = fraction of steam mass entering vapor-air boundary layer that is condensed.

Table XX(a) comparisons show the effect of the mass condensation recommendation. For the recommendation,[88] the fraction of steam entering the vapor-air boundary layer that is condensed (MR) is varied. Reference 87 result is the current approach. The new mass removal model provides a better comparison with the CVTR[91] measurements for all values of MR. A value of 0.33 gives the best comparison. Table XX(b) shows the impact of applying recommendations 1 and 2. Note that use of the bulk temperature results in a reduction in temperature with further reduction resulting from inclusion of the new condensed mass model.

The physical situation within the MSLB jet is depicted in Fig. 78. After the jet exit, there is a region of adjustment to the back pressure. In this region, the Mach number reaches high values and a normal shock results. This is followed by a constant pressure jet region with a potential core that is gradually diminished by mixing with the surrounding fluid. Application of the procedures developed[92] produced the following representative results for a saturated steam source at 8.27 MPa (1 200 psia), enthalpy of 2.76 MJ/kg (1 185 Btu/lb), and isentropic exponent of 1.1 expanding into still air at 322 K (120°F) and 0.101 MPa (14.7 psia). The normal shock occurs a distance of 14 R (R is the break radius) from the break, the shock radius is 13 R, the break exit Mach number is 3.1, and the Mach number just upstream of the shock is 4.4. Downstream of the shock, a potential core extends for a distance of 63 R. In the core, the Mach number is 0.3 and the temperature is 411 K (280°F). The relatively low temperature results from the isenthalpic process assumed to occur.

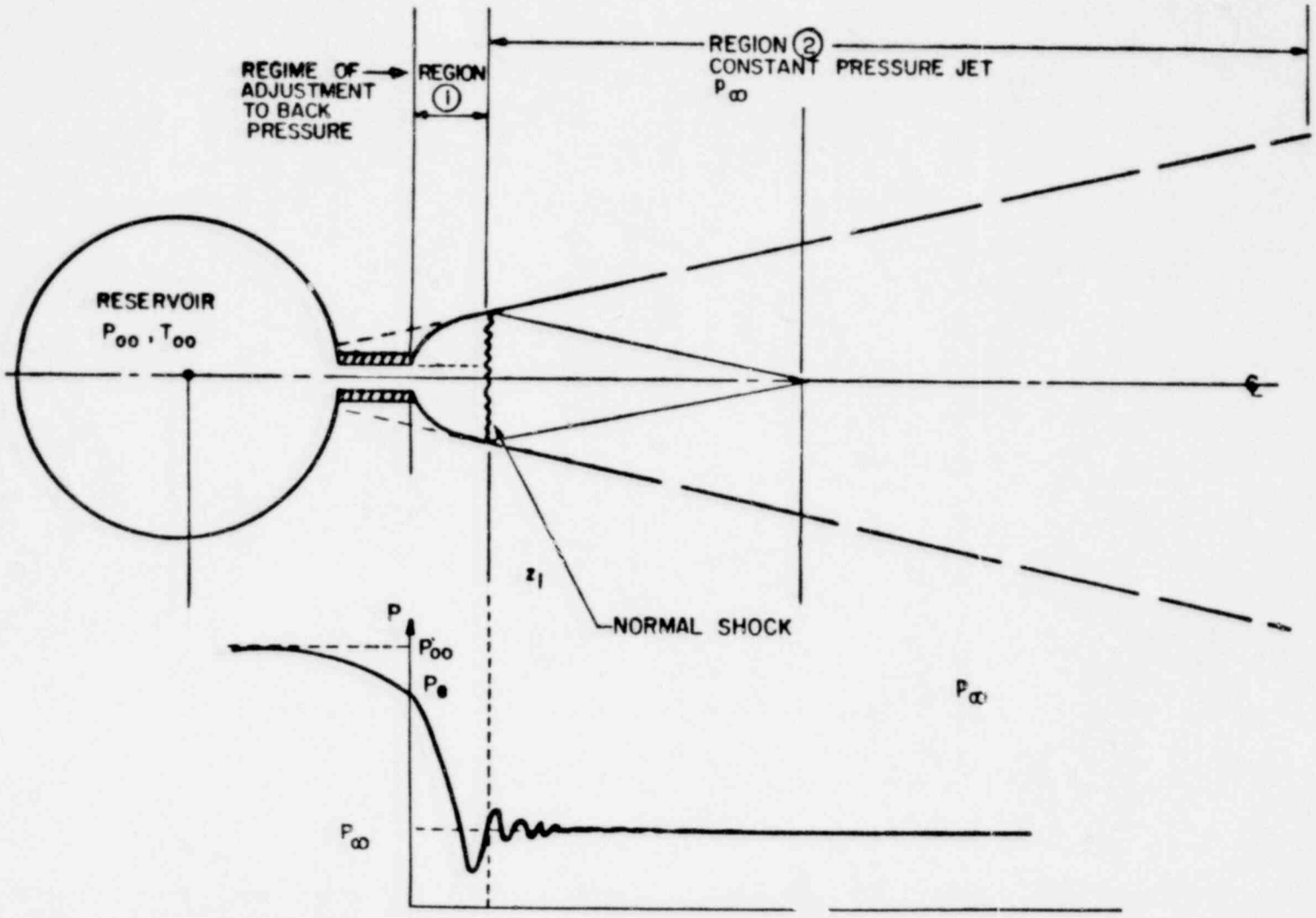


Fig. 78. Idealized representation of a MSLB jet showing the pressure variation and normal shock that result from the large underexpansion.

REFERENCES


1. G. A. Berna, M. P. Bohn, and D. R. Coleman, "FRAPCON-1: A Computer Code for the Steady-State Analysis of Oxide Fuel Rods," EG&G Idaho, Inc. report CDAP-TR-78-032-R1 (November 1978).

2. J. M. Sicilian, TRAC Newsletter, No. 1 (June 1979).

3. D. A. Mandell, K. A. Williams, and W. L. Kirchner, "TRAC Minimum Film Boiling Sensitivity Study," presented at the NRC Workshop on Rewet Phenomena (Denver, Colorado, April 1979).

4. L. B. Thompson and Y. Y. Hsu, Minutes of the Denver Meeting on Rewet Phenomena, U.S. Nuclear Regulatory Commission (April 1979).

5. J. A. Findlay, General Electric Co., San Jose, California, Private Communication (June 1979).

6. G. Yadigaroglu, Nuclear Safety, 19, 1 (1978).

7. "Reactor Safety Research Program, Quarterly Report for the Period July 1-September 30, 1978," Battelle Pacific Northwest Laboratories, NUREG/CR-0546, PNL-2653-3 (1978).

8. R. B. Duffey and D. T. C. Porthouse, Nuclear Engineering and Design, 25 (1973).

9. J. F. Jackson and M. G. Stevenson, "Nuclear Reactor Safety Quarterly Report for the Period January 1-March 31, 1977," Los Alamos Scientific Laboratory report LA-NUREG-6842-PR (May 1977).

10. J. F. Jackson and M. G. Stevenson, "Nuclear Reactor Safety Quarterly Report for the Period January 1-March 31, 1979," Los Alamos Scientific Laboratory report NUREG/CR-0868, LA-7867-PR (June 1979).

11. O. C. Iloeje, D. N. Plummer, W. M. Rohsenow, and P. Griffith, "An Investigation of the Collapse and Surface Rewet in Film Boiling in Forced Vertical Flow," J. of Heat Transfer, 166-172 (May 1975).

12. J. F. Jackson and M. G. Stevenson, "Nuclear Reactor Safety Quarterly Report for the Period October 1-December 31, 1978," Los Alamos Scientific Laboratory report NUREG/CR-0762, LA-7769-PR (May 1979).

13. C. J. Crowley, J. A. Block, and C. N. Cary, "Downcomer Effects in a 1/15-Scale PWR Geometry-Experimental Data Report," Creare, Inc. report NUREG-0281 (1977).

14. J. F. Jackson and M. G. Stevenson, "Nuclear Reactor Safety Quarterly Report for the Period April 1-June 30, 1977," Los Alamos Scientific Laboratory report LA-NUREG-6935-PR (August 1977).

15. J. F. Jackson and M. G. Stevenson, "Nuclear Reactor Safety Quarterly Report for the Period April 1-June 30, 1978," Los Alamos Scientific Laboratory report NUREG/CR-0385, LA-7481-PR (October 1978).

16. H. J. Richter and T. W. Lovell, "The Effect of Scale on Two-Phase Countercurrent Flow Flooding in Vertical Tubes," Dartmouth College report (August 1978).

17. G. B. Wallis, One-Dimensional Two-Phase Flow (McGraw-Hill, New York, NY, 1969).

18. W. C. Rivard and M. D. Torrey, "THREED: An Extension of the K-FIX Code for Three-Dimensional Calculations," Los Alamos Scientific Laboratory report LA-NUREG-6623, Suppl. II (January 1979).

19. S. Timoshenko, Theory of Plates and Shells (McGraw-Hill, New York, NY, 1940).

20. W. R. Bohl, H. K. Fauske, D. R. Ferguson, R. J. Henninger, and R. W. Ostensen, "An Analysis of Transient Undercooling and Transient Overpower Accidents Without SCRAM in the Clinch River Breeder Reactor," Argonne National Laboratory report 75-29 ANL/RAS (1975).

21. W. R. Bohl and T. J. Heames, "Fuel-Coolant-Interaction, Cladding- and Fuel-Motion Model Development," Argonne National Laboratory report ANL-RDP-49 (1976).

22. Project Management Corporation, "Clinch River Breeder Reactor Preliminary Safety Analysis Report" (July 1975).

23. E. P. Hicks and D. C. Menzies, "Theoretical Studies on the Fast Reactor Maximum Accident," Proc. Conf. Safety Fuels and Core Design in Large Fast Power Reactors, ANL-7120 (October 1965).

24. Y. W. Chang, J. Gvildys, and S. H. Fistedis, "Two-Dimensional Hydrodynamics Analysis for Primary Containment," Argonne National Laboratory report ANL-7498 (1969).

25. L. L. Smith, "SIMMER-II: A Computer Program for LMFBR Disrupted Core Analysis," Los Alamos Scientific Laboratory report NUREG/CR-0453, LA-7515-M (October 1978).

26. C. Y. Wang, "ICECO - An Implicit Eulerian Method for Calculating Fluid Transients in Fast Reactor Containment," Argonne National Laboratory report ANL-75-81 (December 1975).

27. S. L. Hancock, "Finite Difference Equations for PISCES-2DELD, A Coupled Lagrange Continuum Mechanics Computer Program, TCAM 76-2," Physics International Co. report (April 1976).

28. M. S. Cowler, "ASTARTE - 2-D Lagrangian Code for Unsteady Compressible Flow: Theoretical Description," TRG report 2527 (R/X)(March 1974).

29. M. Namias and A. Lamotte, "Description of the "SURBOUM" Programme," Belgonucleaire report 308.39/177/n/040 (May 1972).

30. R. J. Tobin and D. J. Cagliostro, "Experimental Simulation of a Hypothetical Core Disruptive Accident in 1/30-Scale Models of the Clinch River Breeder Reactor," SRI International report 4 (October 1978).

31. N. E. Hoskin and M. J. Lancefield, "The COVA Programme for the Validation of Computer Codes for Fast Reactor Containment Studies," Nuclear Eng. and Design 46 1 (March 1978).

32. M. Egleme, J. P. Fabry, H. Lamotte, "Nuclear Accident Simulation in a 1/6-Scale Model of the SNR-300 Fast Breeder Reactor," Nuclear Eng. and Design 42, 1, 115 (1977).

33. R. J. Tobin and D. J. Cagliostro, "Effects of Vessel Internal Structures on Simulated HCDA Bubble Expansions," SRI International report 5 (November 1978).

34. T. G. Theofanous and D. Christopher, "The Termination Phase of Core Disruptive Accidents in LMFBRs," Purdue University report PNE-78-126 (February 1978).

35. C. R. Bell and J. E. Boudreau, "SIMMER-I Accident Consequence Calculations," ANS Trans. 27, 555 (1977).

36. D. J. Cagliostro, C. M. Romander, and R. J. Tobin, "Experimental Studies in Attenuation of Radiological Consequence of CDA Energetics," SRI International quarterly progress report No. 15 (November 1978).

37. A. Padilla, Jr., "High-Temperature Thermodynamic Properties of Sodium," Hanford Engineering Development Laboratory report HEDL-TME 77-27 (February 1978).

38. G. I. Kerley, "A New Model of Fluids," Los Alamos Scientific Laboratory report LA-4760 (December 1971).

39. G. I. Kerley, "Perturbation Theory and the Thermodynamic Properties of Fluids," Los Alamos Scientific Laboratory report (to be published).

40. J. P. Stone, C. T. Ewing, J. R. Spann, E. W. Steinkuller, D. D. Williams, and R. R. Miller, "High-Temperature Properties of Sodium," Naval Research Lab report NRL-6241 (September 1965).

41. I. G. Dillon, P. A. Nelson, and B. S. Swanson, "The Measurement of Densities and Estimation of Critical Properties of the Alkali Metals," J. Chem. Phys. 44, 4229 (1966).

42. V. S. Bhise and D. F. Bonilla, "The Critical and High-Temperature Equilibrium Phase Densities of Sodium and Potassium," Proc. of the Seventh Symposium on Thermophysical Properties, National Bureau of Standards (Gaithersburg, Maryland, May 1977).

43. B. I. Bennett, J. D. Johnson, G. I. Kerley, and G. T. Rood, "Recent Developments in the Sesame Equation-of-State Library," Los Alamos Scientific Laboratory report LA-7130 (February 1978).

44. L. Leibowitz, M. G. Chasanov, L. W. Mishler, and D. F. Fischer, "Enthalpy of Liquid Uranium Dioxide to 3500 K," J. Nucl. Mate. 39, 115 (1971); also R. A. Hein and P. N. Flagella, "Enthalpy Measurements of $UO_2$ and Tungsten to 3260 K," General Electric Co. report GEMP-578 (February 1968).

45. L. H. Aller, Astrophysics: The Atmospheres of the Sun and Stars (The Ronald Press Co., New York, NY, 1963).

46. R. Engleman, Jr., Los Alamos Scientific Laboratory, private communication (December 1978; also J. Blaise and L. J. Radziemski, Jr., "Energy Levels of Neutral Atomic Uranium (UI)," J. Opt. Soc. Am. 66, 644 (1976).

47. A. M. Boring, Los Alamos Scientific Laboratory, private communication (January-April 1979).

48. S. D. Gabelnick, G. T. Reedy, and M. G. Chasanov, "Infrared Spectra of Matrix-Isolated Uranium Oxide Species. I. The Stretching Region," J. Chem. Phys. 58, 4468 (1973).

49. T. L. Hill, An Introduction to Statistical Thermodynamics (Addison-Wesley Publishing Co., Reading, Massachusetts, 1960).

50. D. W. Green, Argonne National Laboratory, private communication (May 1979).

51. Preliminary Report of the IAEA Specialist's Meeting on Equations of State of Materials of Relevance to the Analysis of Hypothetical Fast Breeder Reactor Accidents, A.E.R.E., Harwell, United Kingdom (June 1978).

52. M. H. Rand, R. J. Ackermann, F. Grønvold, F. L. Oetting, and A. Pattoret, "The Thermodynamic Properties of the Urania Phase," to be published in Rev. Int. Htes. Temper. et Refract.

53. R. A. Hein, L. H. Sjodahl, and R. Szwarc, "Heat Content of Uranium Dioxide from 1200 to 3100 K," J. Nucl. Mate. 25, 99 (1968); also L. Leibowitz, L. W. Mishler, and M. G. Chasanov, "Enthalpy of Solid Uranium Dioxide from 2500 K to its Melting Point," J. Nuc. Mate. 29, 356 (1969).

54. R. W. Ohse, J. F. Babelot, C. Cercignani, P. R. Kinsman, K. A. Long, J. Magill, and A. Scotti, "Application of Laser Pulse Heating for the Study of High-Temperature Vapours, Phase Transitions and Equation of State," Proc. 10 Materials Research Symposium on Characterization of High Temperature Vapors and Gases, National Bureau of Standards (Gaithersburg, Maryland, September 1978).

55. M. Bober, W. Breitung, H. U. Karow, and K. Schretzmann, "Evaporation Studies of Liquid Oxide Fuel at Very High Temperatures Using Laser Beam Heating," KFK report 2366 (1976); also M. Bober, H. U. Karow, and K. Schretzmann, "Vapor Pressure Measurements of Oxide Fuel Between 3000 and 5000 K Using Laser Heating," Nucl. Tech 26, 237 (1975).

56. G. T. Reedy and M. G. Chasanov, "Total Pressure of Uranium-Bearing Species Over Molten Urania," J. Nucl. Mate. 42, 341 (1972).

57. R. W. Ohse, "High-Temperature Vapor-Pressure Studies of $UO_2$ by the Effusion Method and Its Thermodynamic Interpretation," J. Chem. Phys. 44, 1375 (1966).

58. M. Tetenbaum and P. D. Hunt, "Total Pressure of Uranium-Bearing Species Over Oxygen-Deficient Urania," J. Nucl. Mate. 34, 86 (1970).

59. R. J. Ackermann, P. W. Gilles, and R. J. Thorn, "High-Temperature Thermodynamic Properties of Uranium Dioxide," J. Chem. Phys. 25, 1089 (1956).

60. A. Pattoret, J. Drowart, and S. Smoes, "Etudes Thermodynamiques par Spectrometrie de Masse sur le Systeme Uranium-Oxygene," Proceedings IAEA Symposium on Thermodynamics of Nuclear Materials (Vienna, Austria, 1967), p. 613.

61. J. F. Jackson and M. G. Stevenson, "Nuclear Reactor Safety Progress Report for the Period July 1-September 30, 1977," Los Alamos Scientific Laboratory report LA-7039-PR (January 1978).

62. F. H. Harlow and A. A. Amsden, "Flow of Interpenetrating Material Phases," J. Comp. Phys. 18, 440-464 (1975).

63. T. G. Theofanous, M. Saito, D. Cristopher, and J. Beecher, "The Termination Phase of Core Disruptive Accidents in LMFBRs," Third Quarterly Progress Report, Purdue University report PNE-78-138 (November 1978).

64. A. R. Edwards and T. P. O'Brien, "Studies of Phenomena Connected with the Depressurization of Water Reactors," J. of British Nucl. Energy Society 9, 125-135 (April 1970).

65. P. E. Rexroth and A. J. Suo-Anttila "SIMMER Analysis of SRI High Pressure Bubble Expansion Experiments," presented at Specialists' Workshop on Predictive Analysis of Material Dynamics in LMFBR Safety Experiments (Los Alamos Scientific Laboratory, March 1979).

66. J. F. Jackson and M. G. Stevenson, "Nuclear Reactor Safety Progress Report for the Period July 1-September 30, 1978," Los Alamos Scientific Laboratory report NRUEG/CR-0522, LA-7567-PR (December 1978).

67. A. J. Suo-Anttila, "Analysis of Postdisassembly Expansion Experiments," to be presented at International Meeting on Fast Reactor Safety Technology (Seattle, Washington, August 1979).

68. P. K. Mast, "The Los Alamos Failure Model (LAFM): A Code for the Prediction of LMFBR Fuel Pin Failure," Los Alamos Scientific Laboratory report LA-7161-MS (March 1978).

69. J. E. Hanson, Hanford Engineering Development Laboratory, private communication (February 9, 1979).

70. R. E. Baars, Hanford Engineering Development Laboratory, private communication (February 9, 1979).

71. G. D. Johnson and C. W. Hunter, "Mechanical Behavior of Fast Reactor Fuel Pin Cladding Subjected to Simulated Overpower Transients,"Hanford Engineering Development Laboratory report HEDL-TME-78-13 (1978).

72. G. D. Johnson and C. W. Hunter, "Mechanical Properties of Transient-Tested Irradiated Fast Reactor Cladding," Trans. Am. Nucl. Soc. 30, 195 (November 1978).

73. J. G. Kelly and K. T. Stalker, "ACPR Upgrade Fuel Motion Detection System," in "Transactions of the Second Technical Exchange Meeting on Fuel and Clad-Motion Diagnostics for LMFBR Safety Test Facilities," Argonne National Laboratory report ANL/RAS 76-34 (1976).

74. C. L. Fink, A. DeVolpi, and G. Stanford, "Advances in Clad Glockage Detection," in "Trans. of the Second Technical Exchange Meeting of Fuel- and Clad-Motion Diagnostics for LMFBR Safety Test Facilities," Argonne National Laboratory report ANL/RAS 76-34 (1976).

75. A. E. Evans, Jr., J. D. Orndoff, and W. L. Talbert, Jr., "Evaluation of LMFBR Fuel-Motion Diagnostics with PARKA," IEEE Trans. on Nuclear Sci. 1, NS-26, 815 (February 1979).

76. J. F. Jackson and M. G. Stevenson, "Nuclear Reactor Safety Progress Report for the Period October 1-December 21, 1977," Los Alamos Scientific Laboratory report LA-7195-PR (April 1978).

77. L. V. Groshev, A. M. Demidov, L. N. Lutsenko, and V. I. Pelekhov, "Atlas of γ-Ray Spectra From Radiative Capture of Thermal Neutrons, International Series of Monographs on Nuclear Energy," eds. P. A. Charpie and J. V. Dunworth, Division IV, Vol. 1 (Pergamon Press, New York, NY, 1959).

78. G. W. Grodstein, "X-Ray Attenuation Coefficients from 10 keV to 10 MeV," National Bureau of Standards Circular 583 (1957).

79. N. L. Johnson and S. Kotz, Continuous Univariate Distributions-1 (Houghton Mifflin Co., New York, NY, 1970), 160-190.

80. S. S. Shapiro and M. B. Wilk, "An Analysis of Variance Test for the Exponential Distribution (Complete Samples)," Technometrics 14, 2 (May 1972).

81. L. M. Carruthers and C. E. Lee, "LARC-1: A Los Alamos Release Calculation Program for Fission Product Transport in HTGRs During the LOFC Accident," Los Alamos Scientific Laboratory report LA-NUREG-6563-MS (November 1976).

82. R. G. Gido, J. S. Gilbert, and C. G. Tinkler, "Subcompartment Analysis Procedures," Los Alamos Scientific Laboratory report (to be published).

83. R. G. Gido, J. S. Gilbert, R. G. Lawton, and W. L. Jensen, "COMPARE-MOD 1: A Code for the Transient Analysis of Volumes with Heat Sinks, Flowing Vents, and Doors," Los Alamos Scientific Laboratory report LA-7199-MS (March 1978).

84. R. L. Curtis and W. H. Lee, "Containment Supplement to: RELAP 4 - A Computer Program for Transient Thermal-Hydraulic Analysis," Aerojet Nuclear Co. report I-214-75-03 (June 1975).

85. "Standard Review Plan for the Review of Safety Analysis Reports for Nuclear Power Plants," Sec. 6.2.1.2, Office of Nuclear Reactor Regulation, U.S. Nuclear Regulatory Commission report NUREG-75/087 (September 1975).

86. D. E. Lamkin, A. Koestel, and R. G. Gido, "Containment Main Steam Line Break Equipment Qualification," Los Alamos Scientific Laboratory report (to be published).

87. L. L. Wheat, "CONTEMPT-LT: A Computer Program for Predicting Containment Pressure-Temperature Response to a Loss-of-Coolant Accident," Aerojet Nuclear Co. report ANCR 1219 (June 1975).

88. D. E. Lamkin, "A New Condensation Mass Removal Model for Containment Analysis," Trans. ANS 1978 Winter Meeting (Washington, DC, December 1978).

89. T. Tagami, "Interim Report on Safety Assessments and Facilities Establishment Project in Japan for Period Ending June 1965 (No. 1)," unpublished work (February 1966).

90. H. Uchida, A. Oyama, and T. Togo, "Evaluation of Postincident Cooling Systems of Light-Water Power Reactors," Proc. of the Third International Conf. on the Peaceful Uses of Atomic Energy held in Geneva, August 31, 1964, Vol. 13 [New York, United Nations, 1965 (A/Conf. 28/10/436)](May 1964).

91. R. C. Schmitt, G. E. Bingham, and J. A. Norberg, "Simulated Design Basis Accident Tests of the Carolinas Virginia Tube Reactor Containment Final Report," Idaho Nuclear Corporation report IN-1403 (December 1970).

92. A. H. Shapiro, The Dynamics and Thermodynamics of Compressible Fluid Flow (The Ronald Press Co., New York, NY, 1953).

DISTRIBUTION

| | Copies |
|---|---|
| Nuclear Regulatory Commission, Categories R-4, R-7, and R-8 | 888 |
| Technical Information Center, Oak Ridge, Tennessee | 2 |
| Los Alamos Scientific Laboratory | 200 |
| | 1090 |

1320 353

☆U.S. Government Printing Office: 1979 — 677-013/159

1320 354


Available from
US Nuclear Regulatory Commission
Washington, DC 20555

Available from
National Technical Information Service
Springfield, VA 22161

Microfiche $3.00

| | | | | | | | | | |
|---|---|---|---|---|---|---|---|---|---|
| 001-025 | 4.00 | 126-150 | 7.25 | 251-275 | 10.75 | 376-400 | 13.00 | 501-525 | 15.25 |
| 026-050 | 4.50 | 151-175 | 8.00 | 276-300 | 11.00 | 401-425 | 13.25 | 526-550 | 15.50 |
| 051-075 | 5.25 | 176-200 | 9.00 | 301-325 | 11.75 | 426-450 | 14.00 | 551-575 | 16.25 |
| 076-100 | 6.00 | 201-225 | 9.25 | 326-350 | 12.00 | 451-475 | 14.50 | 576-600 | 16.50 |
| 101-125 | 6.50 | 226-250 | 9.50 | 351-375 | 12.50 | 476-500 | 15.00 | 601-up | |

Note: Add $2.50 for each additional 100-page increment from 601 pages up.